Electronic Structure of CuMnAs, an Antiferromagnetic Dirac Semimetal Candidate, and Progress Towards ARPES on Optically Driven Superconductivity

by

A. Garrison A. Linn

B.S., Birmingham-Southern College, 2015

M.S., The University of Alabama at Birmingham, 2017

A thesis submitted to the

Faculty of the Graduate School of the

University of Colorado in partial fulfillment

of the requirements for the degree of

Doctor of Philosophy

Department of Physics

2023

Committee Members:

Daniel S. Dessau, Chair

Dmitry Reznik

Rahul Nandkishore

Tanja Cuk

Charles Rogers

Linn, A. Garrison A. (Ph.D., Physics)

Electronic Structure of CuMnAs, an Antiferromagnetic Dirac Semimetal Candidate, and Progress Towards ARPES on Optically Driven Superconductivity

Thesis directed by Prof. Daniel S. Dessau

The field of spintronics has long sought to make better computing devices by harnessing the electron spin. Meanwhile the growing field of topology in electronic band structures has been at the forefront of many recent developments in our basic understanding of materials physics. CuMnAs is at the intersection of these two fields, combining control over Antiferromagnetic (AFM) order with novel changes in electron band structure and topology. Because the latter is mediated by the AFM order, CuMnAs is predicted to host a new topological metal insulator transition that can be controlled at THz speeds. Thus, CuMnAs opens paths to faster [$\mathcal{O}(1000x)$] computing devices and controlled studies of ultrafast topology changes. My work provides the first direct test of the density functional theory that underlies the above predictions in CuMnAs, including measuring the electronic band structure in CuMnAs using angle-resolved photoemission spectroscopy (ARPES).

For over a hundred years, physicists have dreamt of a room temperature superconductor, which would change the world through numerous technologies. Yet, to this day, room temperature superconductivity remains an unrealized dream. However, in recent years, studies have found signatures in THz reflectivity measurements of a transient superconducting state at, or even above, room temperature. The state is induced by excitation with an intense mid-infrared, ultrafast laser pulse. Because the state is so short lived [$\mathcal{O}(\text{ps} - \text{ns})$], the primary signatures of superconductivity—0 DC resistance and the Meissner-Ochsenfeld effect—have not been measured conclusively. Therefore, I have set out to measure the transient state using time-resolved ARPES, which would have other signs of superconductivity and could even directly test some of the alternate hypotheses and proposed theories. While my measurements will come after the completion of this thesis, I will discuss my work to improve our measurement system, enabling the future measurements.

Dedication

To my family, mentors, and friends past, present, and future.

Acknowledgements

First and foremost, I would like to thank my family, including my fiancé—Claire Zain, for their unwavering and abundant love and support and sparking in me the intellectual curiosity to pursue physics. Claire in particular has been critical to making it through the stressful points of my PhD, and without my parents, I would not be, let alone have been able to pursue a PhD.

I would also like to thank my PhD advisor, Dan Dessau, for supporting me, enabling my work, and teaching me how to be an experimental physicist. I very much enjoyed our discussions of physics and conducting research with you, and I appreciate that you created a path for me.

This work would not have been possible without so many collaborators: P. Wadley et al. who made the tetragonal CuMnAs samples studied, L. Šmejkal et al. who put forth the theoretical proposals, the synchrotron facilities and staff at ALS (particularly J. Denlinger) and Diamond (particularly T. Kim and C. Cacho), and my lab mates/collaborators: P. Hao, B. Berggren, K. Gordon, and D. Narayan. And my work continues to build off of S. Parham and J. Griffith's work, with support from H. Whitelock and A. Shackelford. Discussing physics with H. Li was a blessing!

I have been blessed to have so many mentors, coaches, and professors that believed in and supported me over the years. I cannot thank them all, but I must acknowledge my Master's advisor, David Hilton, for introducing me to ultrafast optics and research, and of the many amazing professors, I want to acknowledge those that first taught me physics, not only in the classroom but in countless office hours, M. Rupright, D. Pontius, R. Kawai, and I. Perakis.

To my many friends that I have made over this journey (BB, DC, CK, KG, YL, NY, SM, DB, GG, CM, OC, ...), I will cherish the memories forever and look forward to making more.

Contents

Figures

Figure

Chapter 1

Introduction

In this dissertation, I will discuss my two primary contributions during my time as a PhD student at the University of Colorado at Boulder. The first is my measurement of the experimental electronic structure of tetragonal CuMnAs. Antiferromagnetic CuMnAs is an exciting new material with unique symmetries that enable the electric control of the Néel vector, which mediates electric control over Dirac quasiparticle masses, including tuning through zero mass. This was first noted in theoretical work by Šmejkal et al. [1], and they went on to derive the topological charge of the massless Dirac points in a minimal model of CuMnAs, opening the possibility of electric control of topology through electric control of the masses of the Dirac quasiparticles. Finally, the opening and closing of mass gaps at various Dirac points as a function of the orientation of the antiferromagnetic vectors opens the possibility of a new form of topological-magnetoresistance with a greatly enhanced magnitude over what is presently possible. Together, these facts have brought a lot of attention to CuMnAs; however, prior to my work, no direct measurement of the electronic structure had been made, meaning much of the theoretical work was untested. Although the theoretical work included density functional theory (DFT) studies and DFT is usually a good approximation of the electronic structure, DFT is not always reliable, particularly when electronic correlations are present, which is to be expected for a magnetic transition metal like Manganese. Therefore, my angle-resolved photoemission spectroscopy (ARPES) measurements provided a critical and robust test of the theoretical foundations, underpinning the excitement in CuMnAs.

My second contribution is the redesign and improvement of our time-resolved ARPES system

to enable studies of light induced superconductivity. In recent years, Cavalleri and his teams have made bold claims of light induced superconductivity, seeing signatures consistent with superconductivity above room temperature [2]. There work primarily utilizes extremely intense mid-IR laser pulses to induce a transient state, which they probe with THz optical reflectivity measurements. These measurements show signatures of superconductivity, but they are not able to measure a Meissner-Ochsenfeld effect nor a conclusive zero DC resistivity, opening up their work to intense debate and alternative explanations that are not superconductivity. Thus, there is a need for additional experimental probes of their transient state, and not only can time-resolved ARPES measure a superconducting gap, it has the chance to test specific alternative explanations and proposed theories, making a high quality time-resolved ARPES measurement on the transient states extremely enticing. And while our lab has the necessary equipment to conduct the tests, the experimental demands on the system are extremely challenging, and time-resolved ARPES is generally a very difficult technique to begin with. Therefore, I made several significant improvements to our experimental system to enable the desired measurements on the transient states studied by Cavalleri et al., and I intend to make the measurements immediately following my defense.

This dissertation is organized as follows. To put my work into context and enable the reader to follow the primary contributions, in Ch. 2 I will discuss the background physics relevant to CuMnAs: Dirac semimetals, anisotropic magnetoresistance, and spin-orbit torques. Then, I will discuss the experimental technique at the center of this dissertation, ARPES, in Ch. 3, covering the theoretical interpretation of the data, experimental details, and the extension to time-resolved measurements. Next, I will dive into my work on CuMnAs in Ch. 4. Then, I will introduce superconductivity and discuss Cavalleri's work on light induced superconductivity in Ch. 5. Finally, I will briefly discuss what time-resolved ARPES can reveal about the light induced superconductivity and the demands on the system to perform such studies, and then I will describe our time-resolved ARPES setup, including a theoretical background and my contributions to the new and improved system in Ch. 6.

Chapter 2

Background Physics Relevant to CuMnAs

CuMnAs can form a tetragonal or orthorhombic crystal that becomes antiferromagnetic (AFM) below $\sim$ 480 K [3] for the tetragonal phase and $\sim$ 350 K [4] for the orthorhombic phase. In the AFM phase of both structural phases, CuMnAs posses a special set of symmetry operations that give rise to the interesting electronic properties: 1) the existence of Dirac quasiparticles, 2) electric currents apply a torque on the antiferromagnetic Néel vector, and 3) the Dirac quasiparticles have a mass that depends on the direction of the Néel vector, which can lead to huge changes in the resistance to currents. Additionally, in some cases, the zero mass and finite mass states have different topological indexes, meaning that tuning the mass can drive topological transitions.

In this chapter, I will introduce the broader field of Dirac semimetals followed by a discussion of a minimal model of CuMnAs's electronic structure, showing the symmetries that protect a 4-fold Dirac crossing and mediate the Dirac mass. Then, I will discuss the means to control the Néel vector, namely spin-orbit torques. Finally, I will discuss the anisotropic magnetoresistance (AMR), including the predicted topological AMR, which is important to device physics in CuMnAs.

2.1 Dirac Semimetals

There has been a huge amount of interest in Dirac physics in solid-state systems of which CuMnAs is just one of the newer developments. This might be surprising, because relativity is often neglected in the study of crystalline materials due to the fact that electrons are typically travelling $< 1\%$ the speed of light. So, the goal of this section is to show how Dirac physic shows up in

crystalline materials by deriving a low energy theory of graphene, which we will see is described by a massless Dirac equation. Then, I will explicitly show how parity, $\mathcal{P}$, and time reversal, $\mathcal{T}$, symmetries protect a 4-fold band crossing, constituting a Dirac point, in graphene. Next, I will give a general argument based on symmetry that explains why these symmetries protect band crossings in two-level systems, such as graphene. Finally, I will briefly discuss interesting paths of inquiry based on breaking various symmetries, which will lead us to AFM Dirac semimetals that break $\mathcal{P}$ and $\mathcal{T}$ but preserve their combined symmetry, $\mathcal{PT}$.

Graphene is the prototypical example of Dirac physics emerging in solid-state systems, and CuMnAs, at least in a minimal model, is very analogous to the graphene model [1]. Of course, there has been much very important theoretical work on graphene [5–7] (to name just a few) and experimental work claiming a Nobel prize [8]. Additionally, there are great resources that work through graphene in an approachable method, which I draw on heavily in the following [9–11].

Graphene is a 2D sheet of carbon atoms forming a hexagonal lattice (see Fig. 2.1), and each carbon atom is bound to its three neighbors by a strong sigma bond. Since carbon has only four electrons in its outer shell, three are sp^2 bonded, leaving one electron in the π orbitals, which form the valence and conduction bands. Thus, it is sufficient to consider a single tight binding orbital on each carbon atom, and therefore, the electronic band structure to lowest order can be described by a nearest neighbor tight binding Hamiltonian, where electrons on A sites hop to neighboring B sites and vice-versa:

$$H = -t \sum_{\vec{R},\vec{\delta}} A^\dagger(\vec{R}) B(\vec{R} + \vec{\delta}) + h.c., \tag{2.1}$$

where t is real and represents the hopping strength, $\vec{R}$ is a 2D vector to lattice sites, and $\vec{\delta}$ is a 2D displacement vector to the nearest neighbor carbon atoms. A, B are annihilation operators for the tight binding orbital on the A, B carbon atoms.

Since we are working on a lattice, it makes sense to work in momentum space. The Hamiltonian may be transformed by using the standard Fourier transform of the operators,

$$A(\vec{R}) = \sum_{\vec{k}} A(\vec{k}) \exp\left(i\vec{k} \cdot \vec{R}\right). \tag{2.2}$$

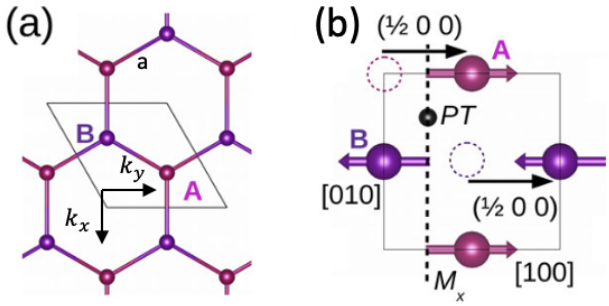

Figure 2.1: Depiction of the 2D unit cell of graphene (a) and effective 2D representation of CuMnAs Mn atoms (b). b) "PT" highlights the point about which the system is $\mathcal{PT}$ symmetric, and the dashed line shows the mirror plane while the arrows exhibit the translation of the nonsymmorphic glide mirror plane symmetry, $\mathcal{G}_x = \{M_x : \frac{1}{2}, 0, 0\}$. Copied from [1].

Substituting this into Eqn. 2.1 and using $\sum_{\vec{R}} \exp(i\vec{R}\cdot(\vec{k}-\vec{k}')) = \delta_{\vec{k},\vec{k}'}$, the Hamiltonian becomes

$$\begin{aligned} H &= -t\sum_{\vec{k},\vec{\delta}} \left(A^\dagger(\vec{k})B(\vec{k})\exp\left(i\vec{k}\cdot\vec{\delta}\right) + B^\dagger(\vec{k})A(\vec{k})\exp\left(-i\vec{k}\cdot\vec{\delta}\right)\right) \\ &= \sum_{\vec{k}} \left(f(\vec{k})A^\dagger(\vec{k})B(\vec{k}) + f^*(\vec{k})B^\dagger(\vec{k})A(\vec{k})\right). \end{aligned} \tag{2.3}$$

This Hamiltonian can be represented in the pseudospinor representation, $\psi = (A, B)^T$, as

$$\begin{aligned} H(\vec{k}) &= \psi^\dagger(\vec{k}) \begin{pmatrix} 0 & f(\vec{k}) \\ f^*(\vec{k}) & 0 \end{pmatrix} \psi(\vec{k}) \\ &= \psi^\dagger(\vec{k}) h(\vec{k}) \psi(\vec{k}) \end{aligned} \tag{2.4}$$

which is summed over $\vec{k}$ to produce the full Hamiltonian, H. $h(\vec{k})$ is referred to as the Bloch Hamiltonian.

This Hamiltonian can be easily diagonalized, yielding

$$E_\pm(\vec{k}) = \pm|f(\vec{k})|, \tag{2.5}$$

which has two bands because there are two atoms (two states) in each unit cell. And the eigenvectors in the pseudospin representation are

$$\psi_\pm = \frac{1}{\sqrt{f^*(\vec{k})}} \begin{pmatrix} \pm\sqrt{f(\vec{k})} \\ \sqrt{f^*(\vec{k})} \end{pmatrix}. \tag{2.6}$$

$f(\vec{k})$ can be found directly, by noting that $\delta = \frac{a}{2}(1, \pm\sqrt{3})$ and $a(-1, 0)$ for all nearest neighbors (see Fig. 2.1). Setting $a = 1$ and thus working with $k_x, k_y \in (-\pi, \pi]$,

$$f(\vec{k}) = -t\left(\exp\left(-ik_x\right) + 2\exp(i\tfrac{k_x}{2})\cos\tfrac{\sqrt{3}}{2}k_y\right) \tag{2.7}$$

Thus, we have found the band structure for graphene. Since graphene has a periodic structure in real space, the system, including the band structure, will be periodic in momentum space. Specifically, the repeating hexagonal lattice in real space produces a repeating hexagonal lattice in momentum, and therefore, we need only examine the band structure in the first Brillouin zone—the hexagon

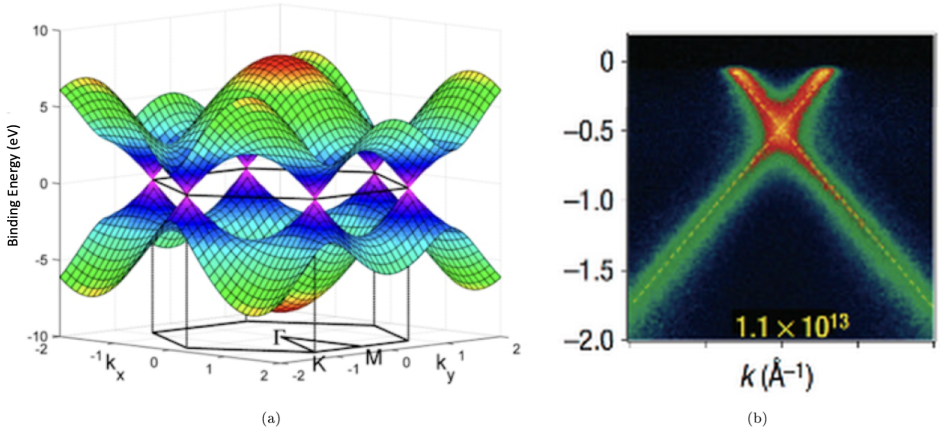

(a) (b)

Figure 2.2: Electronic dispersion in graphene. (a) shows the band structure and the Brillouin zone for graphene. (b) shows an ARPES spectrum through the Dirac point. Adapted from [9].

centered at zero momentum (see Fig. 2.2 for a plot of the band structure in the first Brillouin zone).

Next, we want to find a theory for the low energy excitations out of the ground state, which is the filled Fermi sea. Note that there are two electrons in each unit cell. Therefore, accounting for spin degeneracy of each band, the lower band is exactly filled. Additionally, notice that the top of the lower band touches the bottom of the upper band, forming degeneracy points anywhere that $f(\vec{k}) = 0$. Since the Fermi level will be at these degeneracy points, the Hamiltonian of the low energy theory can be found by expanding the full Hamiltonian around the degeneracy points for small momenta, $\vec{q}$.

First, find the degeneracy points. Setting $f(\vec{k}) = 0$ and with a bit of rearrangement of Eqn. 2.7, the following condition yields degeneracy points:

$$\exp\left(-i\frac{3}{2}k_x\right) = -2\cos\left(\frac{\sqrt{3}}{2}k_y\right) \tag{2.8}$$

Since the right hand side is purely real, the imaginary part of the left hand side must be 0. This gives the condition that $k_x = 0, \pm\frac{2\pi}{3}$. Then, solving the real part of the above equation for k_y in each case, the degeneracy points are found to be at $(k_x, k_y) = \{\pm\frac{2\pi}{3}(1, \frac{1}{\sqrt{3}}), \pm\frac{2\pi}{3}(1, \frac{-1}{\sqrt{3}}), (0, \pm\frac{4\pi}{3\sqrt{3}})\}$. These are, in fact, the 6 corners of the hexagonal Brillouin zone, and due to the overall C_3 symmetry of the lattice, there are only 2 distinct degeneracy points, which can each be connected to 2 others by reciprocal lattice vectors, making 6 total crossings. So, it is sufficient to consider only the distinct points in k-space, commonly referred to as $K = \frac{2\pi}{3}(1, \frac{1}{\sqrt{3}})$ and $K' = \frac{2\pi}{3}(1, \frac{-1}{\sqrt{3}})$.

Second, expand around both K and K' to find the full theory; however, we can start with K' and draw several important conclusions before moving on to K. To leading order in $\vec{q}$,

$$f(K' + \vec{q}) \approx -\frac{3t}{2}e^{i\pi/3}\left(q_y + iq_x\right) \tag{2.9}$$

Plugging this into $h(\vec{k})$,

$$h(K' + \vec{q}) = -\frac{3t}{2}\begin{pmatrix} 0 & e^{i\pi/3}\left(q_y + iq_x\right) \\ e^{-i\pi/3}\left(q_y - iq_x\right) & 0 \end{pmatrix}. \tag{2.10}$$

Now, by rotating the phases of the A and B operators, which means changing the relative phases of those electronic states, this Bloch Hamiltonian can be brought to the form [9],

$$h(K' + \vec{q}) = \hbar v_{\mathrm{F}} \vec{\tau} \cdot \vec{q}, \tag{2.11}$$

where $\vec{\tau} = (\tau_x, \tau_y)$, which are the usual Pauli matrices acting on the pseudospin space, and $v_{\mathrm{F}} = \frac{3t}{2}$ is the Fermi velocity. Eqn. 2.11 represents the low energy Bloch Hamiltonian for the electrons around the K' point.

Now, we can make the comparison to Dirac physics. For reference, the Dirac equation can be written in the form:

$$H_{\mathrm{Dirac}} = c \sum_i \alpha_i p_i + \beta m c^2, \tag{2.12}$$

where the matrices, α, β satisfy the conditions:

$$\begin{aligned} \beta^2 &= 1 \\ \{\alpha_i, \alpha_j\} &= 2\delta_{ij} \\ \{\alpha_i, \beta\} &= 0. \end{aligned} \tag{2.13}$$

Since the Pauli matrices satisfy the anticommutation relation above and $\tau^2 = 1$; in 2D, the matrices can be chosen as $\alpha_1 = \tau_x$, $\alpha_2 = \tau_y$, and $\beta = \tau_z$. Thus, it is clear that eqn. 2.11 is the 2D massless Dirac equation with the speed of light replaced by the Fermi velocity. Alas, it is shown that relativistic Fermions can show up as quasiparticle excitations of a non-relativistic condensed matter system. Thus, the degeneracy points are called Dirac points.

Before worrying about the rest of the low energy Hamiltonian around the K point, let's discuss the symmetries in graphene and the important role that they play. For starters, one normally expects crossings in band structures to hybridize and open a gap, but clearly that does not happen in graphene. The reason is symmetry. Looking at Fig. 2.1(a), it is clear that the lattice is symmetric under parity, $\mathcal{P}$, about the center of the hexagons. Under this parity, $A(\vec{\delta}) \leftrightarrow B(-\vec{\delta})$, which implies that in momentum space, $\mathcal{P}f(\vec{k}) \rightarrow f(-\vec{k})$, $\mathcal{P}A(\vec{k}) \rightarrow B(\vec{k})$, and similar for B. Applying $\mathcal{P}$ to eqn. 2.3, one can see that $\mathcal{P}H(\vec{k}) = H(\vec{k})$, provided that $f(-\vec{k}) = f^*(\vec{k})$, which is

the case for graphene as can be seen from eqn. 2.7. This means that $[H(\vec{k}), \mathcal{P}] = 0$, i.e. the energy eigenstates are also parity eigenstates. In the pseudospin representation, $\mathcal{P}\psi(\vec{k}) \rightarrow \tau_x \psi(-\vec{k})$ since the A and B operators swap under parity as mentioned above. Looking at eqn. 2.6, applying the $\mathcal{P}$ operator and taking advantage of $f(-\vec{k}) = f^*(\vec{k})$, the parity eigenvalues of $\psi_\pm(\vec{k})$ can be found:

$$\begin{aligned}
\mathcal{P}\psi_\pm(\vec{k}) &= \tau_x \frac{1}{\sqrt{f^*(-\vec{k})}} \begin{pmatrix} \pm\sqrt{f(-\vec{k})} \\ \sqrt{f^*(-\vec{k})} \end{pmatrix} \\
&= \frac{1}{\sqrt{f(\vec{k})}} \begin{pmatrix} \sqrt{f(\vec{k})} \\ \pm\sqrt{f^*(\vec{k})} \end{pmatrix} \\
&= \pm\frac{\sqrt{f^*(\vec{k})}}{\sqrt{f(\vec{k})}} \left(\frac{1}{\sqrt{f^*(\vec{k})}} \begin{pmatrix} \pm\sqrt{f(\vec{k})} \\ \sqrt{f^*(\vec{k})} \end{pmatrix} \right) \\
\mathcal{P}\psi_\pm(\vec{k}) &= \pm\frac{\sqrt{f^*(\vec{k})}}{\sqrt{f(\vec{k})}} \psi_\pm(\vec{k}). \qquad (2.14)
\end{aligned}$$

So, the important point is that the eigenstates representing the upper and lower bands in graphene have different eigenvalues under parity, which forbids them from hybridizing, since doing so would make them no longer $\mathcal{P}$ eigenstates as they must be due to $[H_k, \mathcal{P}] = 0$.

The other important symmetry in graphene is time reversal symmetry, $\mathcal{T}$. To obey time reversal symmetry, $\mathcal{T}h(\vec{k}) = h^*(-\vec{k}) = h(\vec{k})$. This is easily seen to be true in eqn. 2.4, because $f^*(-\vec{k}) = f(\vec{k})$. When spin is taken into account, each band is doubly degenerate due to Kramer's degeneracy. So, the time reversal symmetry is critical to protecting the full four-fold crossing.

Now returning to constructing the full low energy theory in graphene, note that under $\mathcal{T}$ $K \leftrightarrow K'$. This implies the $h(K + \vec{q}) = \mathcal{T}h(K' + \vec{q}) = h^*(K + \vec{q}) = \hbar v_{\mathrm{F}} (\vec{\tau} \cdot \vec{q})^*$. This can be represented in the basis $\Psi = [A(K + \vec{q}), B(K + \vec{q}), A(K' + \vec{q}), B(K' + \vec{q})]^T$ as

$$\begin{aligned}
h &= \hbar v_{\mathrm{F}} \begin{pmatrix} (\vec{\tau} \cdot \vec{q})^* & 0 \\ 0 & \vec{\tau} \cdot \vec{q} \end{pmatrix} \qquad (2.15) \\
&= \hbar v_{\mathrm{F}} (\tau_x q_x - \varsigma_z \tau_y q_y), \qquad (2.16)
\end{aligned}$$

where ς_z is a Pauli matrix in the (K, K') space. Finally, the above Hamiltonian describes the full

low energy theory in graphene.

Having shown that Dirac physics emerges in the low energy physics of graphene and that $\mathcal{T}$ and $\mathcal{P}$ play a critical role in protecting the Dirac points in graphene, let's now look at a more general argument for why $\mathcal{P}$ and $\mathcal{T}$ protect the crossings of a two level system [10]. In general, any Hamiltonian for a two level system can be written as a linear combination of Pauli matrices. Thus, a general two band Bloch Hamiltonian may be written as

$$h(\vec{k}) = \begin{pmatrix} g(\vec{k}) & f(\vec{k}) \\ f^*(\vec{k}) & -g(\vec{k}) \end{pmatrix}, \tag{2.17}$$

where similar to graphene, $f(\vec{k})$ accounts for terms proportional to τ_x and τ_y, but in general there is also another term, $g(k)\tau_z$.

Now, let's study the constraints on $f(\vec{k})$ and $g(\vec{k})$ under $\mathcal{P}$ and $\mathcal{T}$ symmetry. First, impose that the system is symmetric under parity, i.e. $\mathcal{P}h(\vec{k}) = h(\vec{k})$. As we discussed above,

$$\begin{aligned} \mathcal{P}h(\vec{k}) &= \tau_x h(-\vec{k})\tau_x \\ &= \begin{pmatrix} -g(-\vec{k}) & f^*(-\vec{k}) \\ f(-\vec{k}) & g(-\vec{k}) \end{pmatrix}. \end{aligned} \tag{2.18}$$

This is only equal to the original $h(\vec{k})$, i.e. symmetric under parity, if $g(-\vec{k}) = -g(\vec{k})$ and $f(-\vec{k}) = f^*(\vec{k})$. Second, impose time reversal symmetry, i.e. $\mathcal{T}h(\vec{k}) = h(\vec{k})$. As mentioned before,

$$\begin{aligned} \mathcal{T}h(\vec{k}) &= h^*(-\vec{k}) \\ &= \begin{pmatrix} g^*(-\vec{k}) & f^*(-\vec{k}) \\ f(-\vec{k}) & -g^*(-\vec{k}) \end{pmatrix}. \end{aligned} \tag{2.19}$$

This is equal to the original $h(\vec{k})$ only if $g^*(-\vec{k}) = g(\vec{k})$ and $f^*(-\vec{k}) = f(\vec{k})$. If a system has both $\mathcal{P}$ and $\mathcal{T}$, then notice that $f(\vec{k})$ has the same condition on it, which can obviously be satisfied as shown explicitly in the case of graphene. However, $g(\vec{k})$ has the following two conditions:

$$g(-\vec{k}) = -g(\vec{k}) \text{ and} \tag{2.20}$$

$$g^*(-\vec{k}) = g(\vec{k}). \tag{2.21}$$

Combining these $g(-\vec{k}) = -g(\vec{k}) = -g^*(-\vec{k})$, which means that $g(\vec{k})$ must be purely imaginary. However, Hamiltonians are, of course, observable and thus are Hermitian, requiring that $g(\vec{k})$ be purely real. Alternatively, $g(\vec{k}) = 0$ satisfies the conditions.

So, it is shown that a two level system with both parity and time reversal symmetry must have no term proportional to τ_z. This is what enables the crossing, because in general, there are 3 Pauli matrices and thus 3 degrees of freedom, but in 2D there only 2 degrees of freedom to tune, k_x and k_y. So, only in the absence of one of the Pauli matrices, can we tune the two level energy gap to 0.

There is a rich history of important physics that comes from opening a gap at the Dirac points by breaking parity and/or time reversal symmetry. As noted above, in 2D $\beta = \tau_z$ in the Dirac equation 2.11, which means that breaking either time reversal or parity allows a term proportional to τ_z, adding a mass gap to the Dirac dispersion. This can be done, for example, by adding different on-site energy terms for the A and B atomic sites, which breaks parity. On the other hand, time reversal symmetry can be broken by adding a complex hopping term, as Haldane did [5], which famously lead to a zero field quantum Hall state and played an important role in the emerging field of topological materials. Kane and Mele [6] found a way to open a gap while preserving parity and time reversal symmetry by adding a spin-orbit term, that makes the two level system a 4 level system by introducing spin. This led to the discovery of topological insulators.

2.1.1 Antiferromagnetic Dirac Semimetals

One might wonder, given the emphasis of parity and time-reversal symmetry in the previous section, whether it would be possible to have a 4-fold crossing in an antiferromagnet at all, because time-reversal symmetry will be broken by the magnetic order, and it is possible, depending on the magnetic order, that parity will be broken as well. In CuMnAs, it is the case that both of these symmetries are broken; however, the system remains invariant to the combined parity and time-reversal, i.e. the system is invariant under $\mathcal{PT}$. This means the bands are Kramer's pairs, i.e. doubly degenerate. However, this is only one symmetry and cannot protect the crossing of the

doubly degenerate bands, as parity did in graphene. So, in CuMnAs or any $\mathcal{PT}$ symmetric AFM, there must be yet another symmetry to protect the crossing of the doubly degenerate bands if there is to be a 4-fold crossing similar to graphene. Of particular interest is any symmetry that can be controlled externally, as this would allow control of the mass term of the Dirac fermions.

In this section, a minimal model for CuMnAs will be motivated and solved, demonstrating the protection of the 4-fold crossing by a nonsymmorphic glide mirror plane symmetry, which can be controlled by the direction of the Néel vector. And the topology of the system will be studied as well. This model is only to illustrate the physics. Full Density Functional Theory (DFT) is needed to accurately describe the electronic structure.

The first approximation is to consider only the Mn atoms in one plane as a 2D system [see Fig. 2.1(b)], focusing on only the highest energy valence electron state on the Mn atoms. This is justified because the Mn atoms form a crinkled 2D plane [see Fig. 2.7(c)] and the distance between these planes is greater than second nearest neighbor. Then the physics will include hopping, an AFM exchange interaction, and because of the broken inversion symmetry on each Mn atom, a spin-orbit interaction with the out of plane electric field (Rashba spin-orbit). Since a $\mathcal{PT}$ symmetry connects all nearest neighbors, the electric field must be antisymmetric along the path connecting nearest neighbors. This means that there is no Rashba type spin-orbit interaction connecting nearest neighbors. So, we will consider interactions up to second nearest neighbors for hopping and spin-orbit coupling. Thus, our minimal Hamiltonian is

$$H = H_{\text{hopping}} + H_{\text{AFM}} + H_{\text{R}}. \tag{2.22}$$

Let's now derive the Hamiltonian in momentum space piece by piece, starting with H_{hopping}. The nearest neighbor contribution to the hopping portion of the Hamiltonian is identical to graphene's in equation 2.3 but with a different $f(k)$. In CuMnAs the nearest neighbors are at $\delta = (0.5, \pm 0.5)a$ and $(-0.5, \pm 0.5)a$, where a is the lattice constant/length of the edges of the square unit-cell. This yields $f(k) = -4t\cos(\frac{a}{2}k_x)\cos(\frac{a}{2}k_y)$, which is purely real and thus only contributes as τ_x in the pseudospin representation. For the next nearest neighbor term, the derivation will be similar to

the nearest neighbor term. However, notice that the next nearest neighbor is A to A and B to B hopping, and that both A and B sites have the same $\delta = (\pm a, 0)$ and $(0, \pm a)$ to all next nearest neighbors [see Fig. 2.1(b)]. So, the next nearest neighbor hopping term will take the form

$$\sum_k \left(f_2(k) A^\dagger(k) A(k) + f_2(k) B^\dagger(k) B(k) \right), \tag{2.23}$$

where f_2 must be real because $(A^\dagger A)^\dagger = A^\dagger A$. And analogous to $f(k)$, $f_2(k) = -t' \sum_\delta \exp(ik\delta)$, where t' is the strength of the next nearest neighbor hopping. Given the above mentioned δ vectors, $f_2(k) = -t'(\cos(k_x a) + \cos(k_y a))$. Notice that this term is proportional to the identity matrix in the pseudospinor representation. Putting this all together in the pseudospin representation,

$$\begin{aligned} H_{\text{hopping}} &= \sum_k \psi^\dagger(\vec{k}) \left(\tau_x f(\vec{k}) + \tau_0 f_2(\vec{k}) \right) \psi(\vec{k}) \\ &= \sum_k \psi^\dagger(\vec{k}) \left(-4t \cos(\frac{a}{2} k_x) \cos(\frac{a}{2} k_y) \tau_x - t'(\cos(k_x a) + \cos(k_y a)) \tau_0 \right) \psi(\vec{k}), \end{aligned} \tag{2.24}$$

where τ_0 is the identity operator on the pseudospin space.

The AFM exchange coupling term comes from a nearest neighbor exchange interaction

$$\begin{aligned} H_{\text{AFM}} &\sim \sum_{\langle \vec{R}, \vec{R}' \rangle} \vec{\sigma}_{\vec{R}} \cdot \vec{\sigma}_{\vec{R}'} \\ &\sim \sum_{\langle \vec{R}, \vec{R}' \rangle} A^\dagger_\alpha(\vec{R}) A_\beta(\vec{R}) \vec{\sigma}_{\alpha,\beta} \cdot \vec{\sigma}_{\gamma,\rho} B^\dagger_\gamma(\vec{R}') B_\rho(\vec{R}'), \end{aligned} \tag{2.25}$$

where the second line is the representation of the first line in second quantization. The σ matrices are the Pauli matrices acting on the spin degree of freedom. The repeated Greek indices are understood to be summed over $\uparrow, \downarrow$. The next step is to make the standard mean field approximation to turn this quartic term into a bilinear term that may be diagonalized analytically:

$$\begin{aligned} & A^\dagger_\alpha(\vec{R}) A_\beta(\vec{R}) B^\dagger_\gamma(\vec{R}') B_\rho(\vec{R}') \\ \approx\ & \langle A^\dagger_\alpha(\vec{R}) A_\beta(\vec{R}) \rangle B^\dagger_\gamma(\vec{R}') B_\rho(\vec{R}') + A^\dagger_\alpha(\vec{R}) A_\beta(\vec{R}) \langle B^\dagger_\gamma(\vec{R}') B_\rho(\vec{R}') \rangle \\ -\ & \langle A^\dagger_\alpha(\vec{R}) A_\beta(\vec{R}) \rangle \langle B^\dagger_\gamma(\vec{R}') B_\rho(\vec{R}') \rangle . \end{aligned} \tag{2.26}$$

The last term is just a scalar function that sums to a constant term in the Hamiltonian, which may be removed by shifting the definition of the zero energy point. Note that $\langle A^\dagger_\alpha(\vec{R}) A_\beta(\vec{R}) \rangle \vec{\sigma}_{\alpha,\beta}$

is just the expectation value of the spin moment on the A Mn atoms, and we are looking for a Hamiltonian deep in the AFM phase, so $\langle A^\dagger_\alpha(\vec{R})A_\beta(\vec{R})\rangle\,\vec{\sigma}_{\alpha,\beta} \propto \vec{n}$, where $\vec{n}$ is the Néel vector, taken to point parallel to the moment on the A sites and thus antiparallel to the moment on the B sites. Putting this together,

$$H_{\mathrm{AFM}} = J_n \sum_{\vec{R}} \left(A^\dagger(\vec{R})A(\vec{R})\vec{\sigma}\cdot\vec{n} - B^\dagger(\vec{R})B(\vec{R})\vec{\sigma}\cdot\vec{n} \right), \tag{2.27}$$

where J_n characterizes the overall strength of the AFM exchange interaction and the spin indices are suppressed/implicit. The sum over nearest neighbors is replaced by a sum over all lattice sites, because the 4 nearest neighbors to each site contribute equally, and the factor of 4 can be absorbed into J_n. The minus sign reflects that the moments on the B sites are antiparallel to the Néel vector. The Fourier transform of the field operators do not introduce phase factors since they are on the same site. So, Fourier transforming this and moving to the pseudospinor representation,

$$H_{\mathrm{AFM}} = \sum_k \psi^\dagger(\vec{k})\tau_z J_n \vec{\sigma}\cdot\vec{n}\psi(\vec{k}). \tag{2.28}$$

The spin-orbit coupling accounts for the interaction of the elctron's spin and motion through an out of plane electric field. In the electron's frame, there is a magnetic field $\vec{B} \sim \vec{p}\times E\hat{z}$, that contributes a Zeeman term to the Hamiltonian,

$$H_{\mathrm{R}} \sim E\vec{\sigma}\cdot\vec{p}\times\hat{z} = E\left(p_y\sigma_x - p_x\sigma_y\right). \tag{2.29}$$

Representing this in second quantization,

$$H_{\mathrm{R}} \sim E_{\mathrm{eff}} \int d^3r \Psi^\dagger(\vec{r})\left(p_y\sigma_x - p_x\sigma_y\right)\Psi(\vec{r}), \tag{2.30}$$

where $\Psi(\vec{r})$ is the annihilation operator of a spinless electron state at $\vec{r}$. Although, in general, E is a complicated function of position, this derivation is only concerned with the form of the interaction and an overall constant will be added to capture the strength, so E can be treated as a constant and pulled out of the integral as, E_{eff}, which contributes to the overall strength. $\Psi(\vec{r})$ can be represented in the A, B basis as $\Psi(\vec{r}) = \sum_{\vec{R}} C(\vec{R})w(\vec{R}-\vec{r})$, where C is A or B, depending

on the Mn atom at $\vec{R}$ and $w(\vec{R})$ is the Wannier state on the A, B site. So, in this basis

$$H_{\rm R} \sim E_{\rm eff} \int d^3r \sum_{\vec{R},\vec{R}'} C^\dagger(\vec{R}) w^*(\vec{R}+\vec{r}) \left((-i\partial_y)\sigma_x - (-i\partial_x)\sigma_y\right) C(\vec{R}') w(\vec{R}'+\vec{r}), \tag{2.31}$$

where the position representation of the momentum operator is used, $\vec{p} = -i\vec{\nabla}$. The derivative operators operate on the Wannier functions, and looking at one term,

$$\begin{aligned} \partial_x w(\vec{R}'+\vec{r}) &= \hat{x}\cdot\vec{\nabla} w(\vec{R}'+\vec{r}) \\ &= lim_{\vec{\delta}\to 0} \frac{w(\vec{R}'+\vec{r}+\vec{\delta}) - w(\vec{R}'+\vec{r})}{\delta} \hat{\delta}\cdot\hat{x} \\ &\approx \frac{w(\vec{R}'+\vec{r}+\vec{\delta}) - w(\vec{R}'+\vec{r})}{\delta} \frac{\delta_x}{\delta}, \end{aligned} \tag{2.32}$$

where in the approximation $\vec{\delta}$ is the displacement vector to neighboring lattice sites. Note that the Wannier states are orthonormal, using this fact the position integral of one term can be evaluated:

$$\begin{aligned} \int d^3r w^*(\vec{R}+\vec{r}) \partial_x w(\vec{R}'+\vec{r}) &\approx \int d^3r w^*(\vec{R}+\vec{r}) \frac{w(\vec{R}'+\vec{r}+\vec{\delta}) - w(\vec{R}'+\vec{r})}{\delta} \frac{\delta_x}{\delta} \\ &= \frac{\delta_x}{\delta^2} (\delta_{\vec{R},\vec{R}'+\vec{\delta}} - \delta_{\vec{R},\vec{R}'}). \end{aligned} \tag{2.33}$$

The second term is ill-defined in our approximation and also does not relate to motion, as it is proportional to occupation number on a particular site. So, we will neglect this term. The first term is what describes the spin-orbit interaction of an electron hopping between lattice sites. As mentioned before, the nearest neighbor hopping will not contribute, so to leading order and putting it all together,

$$\begin{aligned} H_{\rm R} &\sim E_{\rm eff} \sum_{\vec{R},\vec{\delta}} \frac{1}{\delta^2} C^\dagger(\vec{R}) \left(\delta_y\sigma_x - \delta_x\sigma_y\right) C((\vec{R}+\vec{\delta})) \\ &\sim E_{\rm eff} \sum_{\vec{R},\vec{\delta}} \frac{1}{\delta^2} A^\dagger(\vec{R}) \left(\delta_y\sigma_x - \delta_x\sigma_y\right) A((\vec{R}+\vec{\delta})) \\ &+ (-E_{\rm eff}) \sum_{\vec{R},\vec{\delta}} \frac{1}{\delta^2} B^\dagger(\vec{R}) \left(\delta_y\sigma_x - \delta_x\sigma_y\right) B((\vec{R}+\vec{\delta})) \end{aligned} \tag{2.34}$$

where the $\vec{\delta}$ sum runs over all second nearest neighbors to the Mn at site $\vec{R}$, and in the second line, the sum is explicitly broken into contributions from A and B sites, which are always hopping A to A and B to B [see Fig. 2.1(b). Note that due to the $\mathcal{PT}$ symmetry, the electric field along the

path from A to A must be exactly equal and opposite of that along the path from B to B, hence E_{eff} must change sign between A to A and B to B. Now, Fourier transforming the operators, this becomes

$$\begin{aligned} H_{\text{R}} &\sim E_{\text{eff}} \sum_{k,\vec{\delta}} \frac{1}{\delta^2} A^\dagger(\vec{k}) \left(\delta_y \sigma_x - \delta_x \sigma_y\right) A((\vec{k}) \exp(i\vec{k}\cdot\vec{\delta}) \\ &- E_{\text{eff}} \sum_{k,\vec{\delta}} \frac{1}{\delta^2} B^\dagger(\vec{k}) \left(\delta_y \sigma_x - \delta_x \sigma_y\right) B((\vec{k}) \exp(i\vec{k}\cdot\vec{\delta}). \end{aligned} \tag{2.35}$$

As mentioned above for next nearest neighbor hopping, $\vec{\delta} = (\pm a, 0)$ and $(0, \pm a)$. So, computing the sum over $\vec{\delta}$ explicitly, the Rashba spin-orbit coupling becomes

$$\begin{aligned} H_{\text{R}} &= \lambda \sum_k A^\dagger(\vec{k}) \left(\sigma_y \sin(k_x a) - \sigma_x \sin(k_y a)\right) A((\vec{k}) \\ &- \lambda \sum_k B^\dagger(\vec{k}) \left(\sigma_y \sin(k_x a) - \sigma_x \sin(k_y a)\right) B((\vec{k}) \qquad (2.36) \\ &= \sum_k \psi^\dagger(\vec{k}) \lambda \tau_z \left(\sigma_y \sin(k_x a) - \sigma_x \sin(k_y a)\right) \psi(\vec{k}), \qquad (2.37) \end{aligned}$$

where λ defines the strength of the spin-orbit interaction, and in equation 2.37, the pseudospin representation is used.

Finally, putting equations 2.24, 2.28, and 2.37 into equation 2.22 the full minimal Hamiltonian for the Mn atoms in CuMnAs becomes

$$\begin{aligned} H &= \sum_k \psi^\dagger(\vec{k}) h_k \psi(\vec{k}) \\ &= \sum_k \psi^\dagger(\vec{k}) \Big(- 2t\tau_x\sigma_0 \cos(\frac{a}{2}k_x)\cos(\frac{a}{2}k_y) - t'(\cos(k_x a) + \cos(k_y a))\tau_0\sigma_0 \\ &+ \lambda\tau_z(\sin(k_x a)\sigma_y - \sin(k_y a)\sigma_x) + \tau_z J_n \vec{\sigma}\cdot\vec{n}\Big)\psi(\vec{k}). \end{aligned} \tag{2.38}$$

The above defines h_k that is the same as H_k in equation 1 of [1], where they defined $a = 1$ and let the identity matrices, τ_0 and σ_0 be implicit. There is also an implicit and distinct index on each ψ running over spin, and all of the σ matrices would have both indices on them. The pseudospin space can be diagonalized via Mathematica, and defining $a = 1$, the energy spectrum is equation 2

of [1]:

$$E_{\vec{k}\pm} = -t'(\cos k_x + \cos k_y) \pm \left[4t^2 \cos^2 \frac{k_x}{2} \cos^2 \frac{k_y}{2} + (J_n n_x - \lambda \sin k_y)^2 + (J_n n_y + \lambda \sin k_x)^2 + J_n^2 n_z^2\right]^{\frac{1}{2}}. \tag{2.39}$$

This is plotted for $\vec{n} \parallel [1,0,0]$, $[1,1,0]$, and $[0,1,0]$ in Fig. 2.3 for $\lambda = 0.8t$, $J_n = 0.6t$, and $t' = 0.08t$ [1]. There are Dirac points wherever the term in "[ ]" goes to zero, which happens twice in the smaller shaded Brillouin zone at $\vec{D}_1 = [\pi, \arcsin(J_n/\lambda)]$ and $\vec{D}_2 = [\pi, \pi - \arcsin(J_n/\lambda)]$ [see Fig. 2.3].

Inspired by Young et al. [12] who studied an identical Hamiltonian to Eqn 2.38 but without the AFM exchange, Šmejkal et al. [1] go on to explicitly show the symmetry that protects the 4-fold Dirac crossing is $\mathcal{G}_x = \{M_x : 1/2, 0, 0\}$, which is the combined mirror along the (1,0,0) plane, M_x, and a translation by half a unit cell along [1,0,0]. Young et al. considered the more general set of mirror plus translation symmetries, $\{g, t\}$, which includes $\mathcal{G}_x$ that is present in CuMnAs. Young et al. pointed out that for momenta invariant under g, the Bloch states are eigenvectors of $\{g, t\}$. For $\mathcal{G}_x$, $g = M_x$, and $M_x\vec{k} = \vec{k}$ for $k_x = \pm\pi, 0$. Therefore, if a band crossing occurs on these lines/planes for states with different eigenvalues under $\mathcal{G}_x$, hybridization is forbidden and the crossing is protected. In CuMnAs, there is also a $\mathcal{PT}$ symmetry that enforces Kramers pairs, allowing the possibility of a 4-fold crossing, if the two states of a Kramer's pair have the same eigenvalue under $\mathcal{G}_x$, i.e. $[\mathcal{PT}, \mathcal{G}_x] = 0$, which is true for $k_x = \pm\pi$. Finally, each Kramer's pair must have distinct eigenvalues under $\mathcal{G}_x$ to prevent hybridization, which Šmejkal et al. show is true by $\vec{k} \cdot \vec{p}$ perturbation theory. They show that the Kramer's pairs have distinct eigenvalues of $\pm i$, shown in the inset of Fig. 2.3(c), and the fact that there is a crossing along $k_x = \pm\pi$ ($X \to M$) can also be seen explicitly in the dispersion for $\vec{n} \parallel [1,0,0]$.

Following the work of Yang et al. [13], Šmejkal et al. go on to define a topological index for the Dirac points: $N(k_y) = [N^C_{+i}(k_y) - N^V_{+i}(k_y)] - [N^C_{-i}(k_y) - N^V_{-i}(k_y)]$, where $N^{C(V)}_{\pm i}$ is the number of conduction (valence) bands with eigenvalue $\pm i$ under $\mathcal{G}_x$. Looking at the inset of Fig. 2.3(c), it is clear that each side of the Dirac point has an integer value for N, which changes sign discontinuously

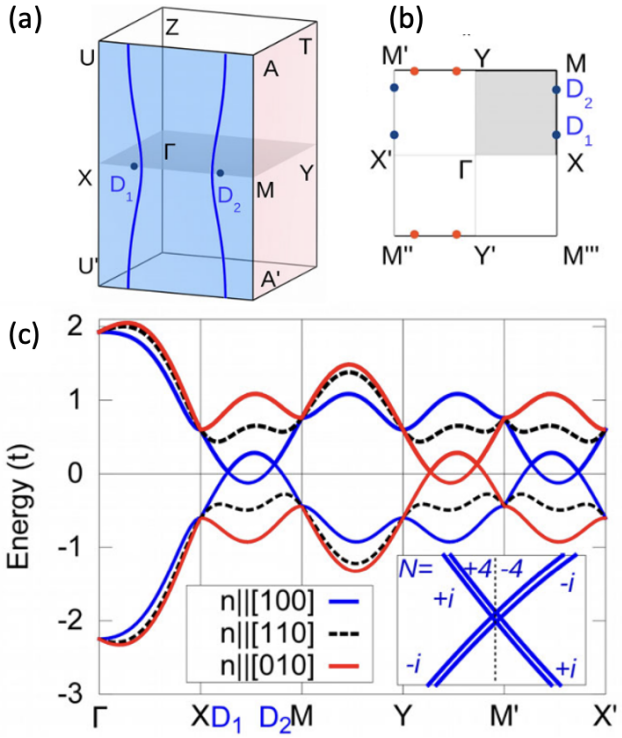

Figure 2.3: CuMnAs Minimal Model Dispersion: a) Depicts the shaded region in (b) expanded to 3D, showing the Dirac points dispersing as Nodal lines. (b) the 2D Brillioun zone, indicating the Dirac points that can be present depending on Néel vector orientation. (c) The dispersion in equation 2.39 plotted for several Néel vector orientations. Inset depicts the topology of D_1 with degenerate bands shifted for clarity. Figure Copied from [1]

at the Dirac point, meaning the Dirac point has a topological charge of -1, showing that the Dirac point has nontrivial topology.

Finally, the critical point here is that the Dirac points are protected by the $\mathcal{G}_x$ symmetry, which is only present for $\vec{n} \parallel [1,0,0]$. By the overall C_4 symmetry of the system, when $\vec{n} \parallel [0,1,0]$ an analogous $\mathcal{G}_y$ symmetry protects Dirac points on $k_y = \pm\pi$ lines/planes. However, for intermediate orientations of the Néel vector, the Dirac points are not protected, meaning the Dirac points pick up a mass and the topology changes because the states are no longer eigenstates of the glide mirror plane symmetries. Thus, control over the Néel vector would offer control over the Dirac quasiparticle masses and potentially the topology of the system. The next section discusses a means to control the Néel vector.

2.2 Spin-Orbit Torque (SOT)

In physics, we often want to both find new phenomena and new ways to control and exploit these phenomena. For example, controlling magnetism enabled us to make hard drives for our computers. These hard drives had spinning disks with little regions of magnetization that could be flipped by applying a large magnetic field, and then the magnetization could be read out. The moving parts required to do this made these less reliable and slower than more favorable modern day solid state drives. However, the physics community has been finding new ways to control magnetic order that do not require the moving parts. The method we will discuss is called Spin-Orbit Torque (SOT).

Spin-orbit torques are torques applied on underlying magnetic moments in a material due to the motion of electrons through the material, i.e. a current. There are primarily two means by which a current can apply a torque on magnetic moments: 1) the current naturally induces a magnetic field, which can then apply a torque that generally makes magnetic moments precess around the direction of the magnetic field. 2) The current could be spin polarized, i.e. have a net magnetic moment, and this moment can couple into the magnetic moment of the material under the standard exchange interaction. (As an aside, it is important to remember that the exchange

interaction generally causes two spin moments to be parallel or anti-parallel depending on the details of the material.) Type 1) is generally referred to as a field-like torque with $\vec{\tau} \sim \vec{m} \times \hat{y}$, where $\vec{B}$ is along $\hat{y}$ and perpendicular to the current direction, $\hat{x}$, and $\vec{m}$ is the magnetic moment in the material. This field like torque can be seen to induce a precession, because this torque will never bring the field and moment parallel. Type 2) is called the damping like torque with $\vec{\tau} \sim \vec{m} \times (\vec{\sigma} \times \vec{m})$, where $\vec{\sigma}$ is the net spin moment of the current. This torque eventually brings the moment to be parallel/anti-parallel to the spin moment of the current and then stops applying a torque, presumably this is why the name "damping like torque" was chosen. See figure 2.4 for an illustration of the two types of torques and the coordinate system used above.

There are actually many mechanisms to generate the spin polarization required to apply a damping like torque (see figure 2.5, which also shows the many materials, dynamics of the bulk switching, and many interesting applications). Let's briefly discuss a few of the mechanisms.

In the spin Hall effect, non-spin-polarized current is sent through a material with a large spin Hall coefficient, which analogously to the Hall effect deflects electrons with spin perpendicular to their motion. In the case of the spin Hall effect, the direction is opposite for spins of opposite direction. This creates a net spin moment accumulation on the surfaces of the material with opposite directions for opposite surfaces. This is depicted in figure 2.5. The spin accumulated on the interface then applies the damping like torque on the material sharing the interface.

The Rashba effect is more relevant to the case of CuMnAs, but before we worry about antiferromagnetism, let's focus on the simpler ferromagnetic case. In general, the Rashba effect stems from broken inversion symmetry. If inversion symmetry were present, then there could not be a net electric field in the crystal, because under inversion, $\vec{E} \rightarrow -\vec{E}$, and since the system was symmetric under inversion, $\vec{E} = 0$. However, once inversion symmetry is broken, there can exist a net electric field. Recall, electrons moving in an electric field experience a magnetic field, $\vec{B} \sim \vec{p} \times \vec{E}$ due to the Lorentz transformations of the electric field. This $\vec{B}$ couples into the spin of the moving electrons, giving rise to a Rashba term in the Hamiltonian, $H_{\mathrm{R}} \sim (\vec{p} \times \vec{E}) \cdot \vec{\sigma}$. Obviously, for electrons moving parallel to $\vec{E}$ this term has no effect, but restricting our interest to the plane

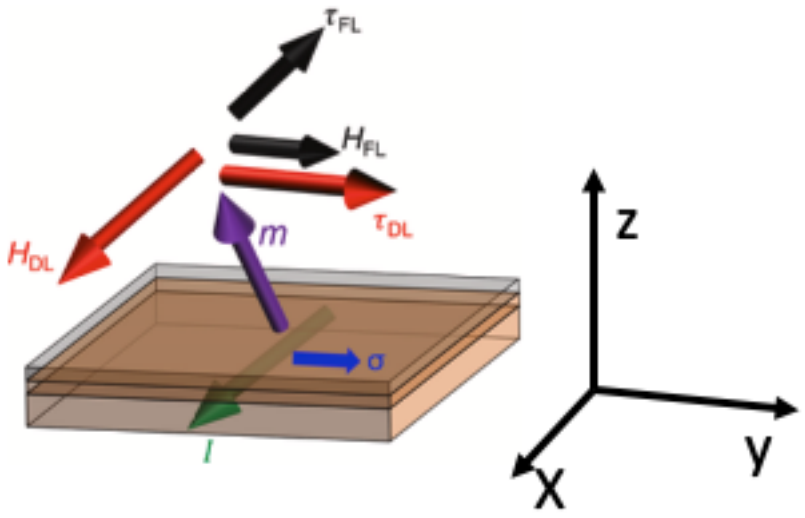

Figure 2.4: Illustration of Field Like (FL) and Damping Like (DL) torques from spin polarized currents on a layer with magnetization. Copied from [14].

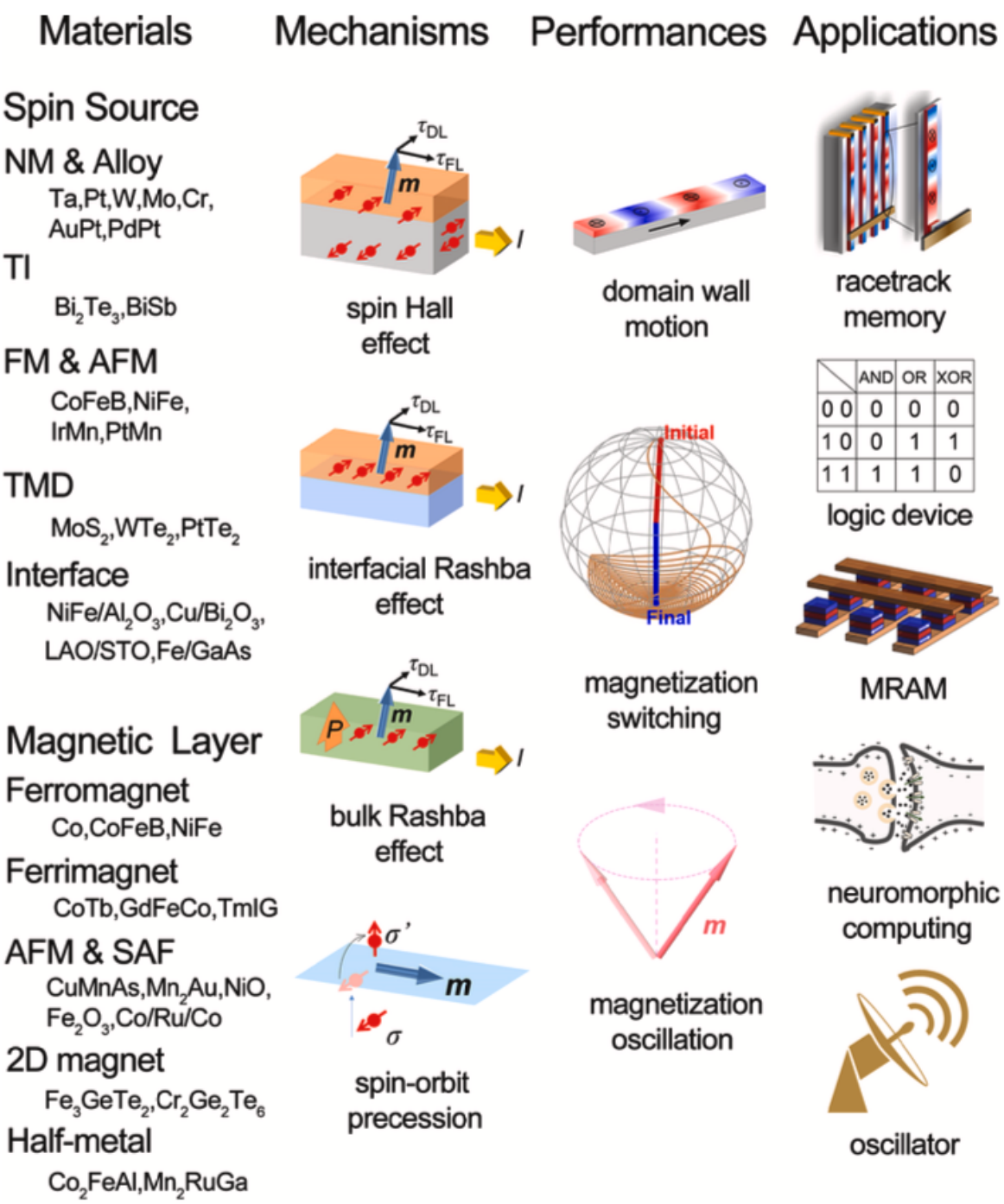

Figure 2.5: An overview of the materials, mechanisms, performances, and applications in the field of spin-orbit torques. Copied from [14].

perpendicular to $\vec{E}$, it can be seen that this term will be minimized for spin lying in the plane and perpendicular to the momentum. This gives rise to a spin texture as shown in the upper panel of figure 2.6. Provided this underlying spin texture exists, it can be seen that when a net current is traveling through the sample, i.e. electrons are scattered from one side of the Fermi surface to the other, there will arise a net magnetic moment owing to the asymmetry of the nonequilibrium Fermi surface. Thus, it can be seen that broken inversion symmetry can give rise to spin polarization of a current, which finally can apply a damping like torque on any nearby magnetic moments. As can be seen in figure 2.5 the inversion symmetry may be broken by the presence of an interface or can be intrinsically broken in the bulk of the crystal, giving rise to the interfacial and bulk Rashba effects, respectively. It is worth noting that this Rashba effect is also sometimes referred to as the inverse spin galvanic effect.

Ultimately, all of the above methods apply torques on the magnetic moment present in either neighboring or the same material. These torques then can either completely rotate the magnetic moments, say from up to down, or they can cause domain walls to move, growing or shrinking domains of various magnetic orientations. In either case, the net result is to rotate magnetic moments, providing control over the magnetization of materials. Then, there are various ways that this control can be used to make devices, and this is all very much an active area of research.

As we can see, there are actually many methods to manipulate the ferromagnetic magnetization of a material by applying currents, but what about antiferromagnets? First of all, none of the above work for antiferromagnets, because the torques from these methods would all cause the alternating magnetic moments to cant, that is move towards being ferromagnetic, rather than rotate the Néel vector. Second, to rotate the Néel vector, the induced magnetic field or the spin polarization of the current would have to alternate with the alternating spin moments of the antiferomagnet, which is generally on spatial scales of the order of $\mathring{A}$. That is not trivial. In fact, people have wanted to use AFM order in memory devices for some time, because they would have many advantages: 1) there are way smaller fringing fields since there is no net magnetization. In ferromagnets, the fields produced by one bit can cause another to flip, limiting the bit density,

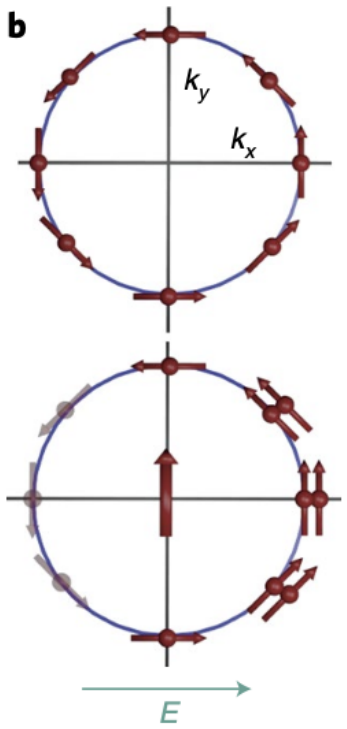

Figure 2.6: Depiction of the spin momentum locking due to the Rashba effect (top), and the net magnetic moment from a net current (bottom). Copied from [15].

but for AFM the bit density could be significantly higher. 2) The magnetic dynamics of AFM are faster, because again no net magnetic moment means a much smaller torque is required to reorient the Néel vector. In fact, the intrinsic frequency is THz instead of GHz. And 3) again owing to no net magnetic moment in AFM, they are less susceptible to magnetic fields destroying the saved data, i.e. the data is safer. But unfortunately, owing to the above mentioned difficulties, there was not much success switching AFM until the last decade! CuMnAs is one of the few AFM that has been electrically switched [16].

2.2.1 Microscopic Physical Description of SOT in AFM CuMnAs

To see how currents apply a torque on the Néel vector in CuMnAs, at a microscopic level, notice the combined parity and time-reversal symmetry, $\mathcal{PT}$, present in the unit cell of CuMnAs (see Fig. 2.7). It can be seen that the $\mathcal{PT}$ symmetry connects the Mn A and Mn B sublattices. Note, under $\mathcal{PT}$, $\vec{\sigma} \to -\vec{\sigma}$ and $\vec{E} \to -\vec{E}$. This implies that their is neither a **net** electric field nor a **net** magnetic moment. Hence the presence of AFM order, which does not have a net magnetic moment. Furthermore, although there cannot be a net electric field, there can be and is an electric field present on each Mn sublattice, which by $\mathcal{PT}$, are equal and opposite. Thus, for the same reasons discussed above during the Rashba effect, the electrons living on Mn A or B sublattice will have the spin texture shown in panels A and B, respectively of Fig. 2.7. Because of the $\mathcal{PT}$ symmetry, the textures are opposite, and when a current is applied in the plane, the net magnetic moments induced on the two Mn sublattices are equal and opposite. That is, the spin polarization of the current is alternating with exactly the same spatial frequency as the equilibrium AFM order present! Finally, the spin polarization will apply a damping like torque on the **Néel vector**, enabling electrical switching of the AFM CuMnAs! (Actually, it is called an antidamping torque, presumably because of the antiferromagnetism it acts on.)

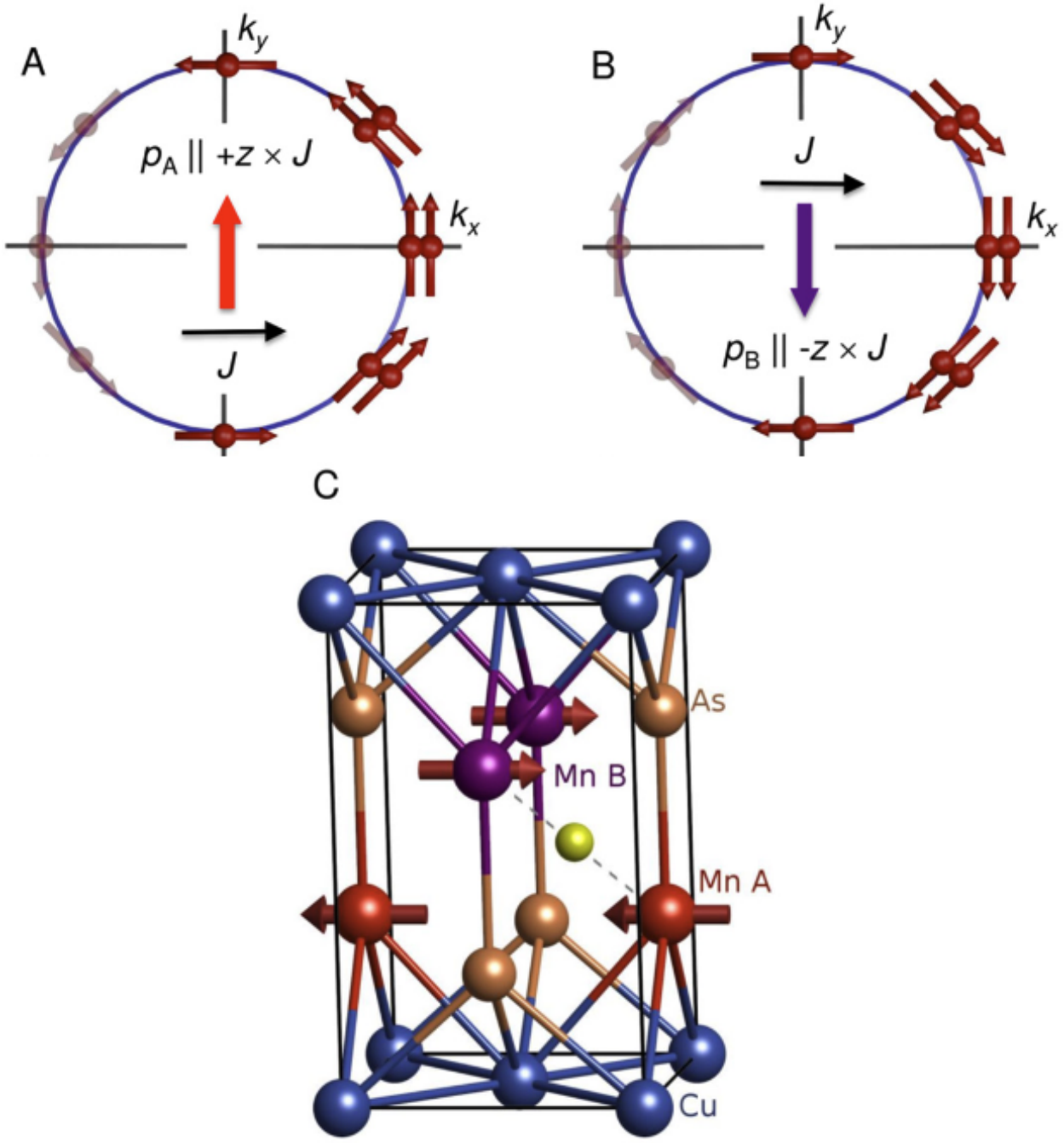

Figure 2.7: Illustration of the spin polarization on the Mn A and B sublattices, panel A and B respectively, in CuMnAs. C) Depiction of the unit cell in CuMnAs, illustrating both the AFM order present and the point about which the crystal is $\mathcal{PT}$ symmetric, yellow ball. Copied from [16].

2.2.2 Symmetry Derived Susceptibilities

The previous section covered the microscopic origin of the torque on the Néel vector in CuMnAs, which in some sense is even better than a group theoretic argument, but it is aesthetically appealing to see how symmetries alone can predict an AFM spin polarization in CuMnAs, and these arguments being so general are far reaching. There is an amazing paper by Železný et al. [17] where they work out the allowed components of the current induced susceptibility for all globally and locally noncentrosymmetric crystal structures. Fortunately, the scope here is much more narrow, focusing on only CuMnAs. Thus, this section will just walk through the symmetry allowed components of the lowest order Current Induced Spin Susceptibility (CISP). That is, what are the allowed components of the following susceptibility:

$$\delta\vec{S} = \chi\vec{E} \tag{2.40}$$

There are two important details worth mentioning before diving in [17]: 1) in an AFM system, the symmetries in question are not the global symmetries of the crystal but instead are the site symmetries of the magnetic atoms. Hence, above the presence of inversion symmetry forbid a Rashba type ferromagnetic CISP, but the presence of inversion symmetry did not forbid an AFM CISP, provided the inversion point was not centered on the magnetic atoms, as was the case in CuMnAs. 2) The CISP will be determined by the electronic structure. Although spin-orbit coupling does couple the magnetic moments into the electronic structure, the spin-orbit coupling is generally weak. So, this motivates an expansion of the susceptibility in terms of magnetic moment present in the crystal. Thus, to first order, we can just focus on the symmetries of the crystal without magnetism present.

Finally, here is the physics: if the system and the forcing field have a symmetry, then the response of the system must preserve the symmetry. Intuitively, the symmetry could be broken in several ways, but how would the system choose if there is nothing to distinguish these options? Figure 2.8 shows the site symmetries of the Mn atoms in CuMnAs, which are two mirror planes passing through both Mn sublattices in the ac and bc planes. Recall, $\vec{E}$ is unchanged (reversed) by

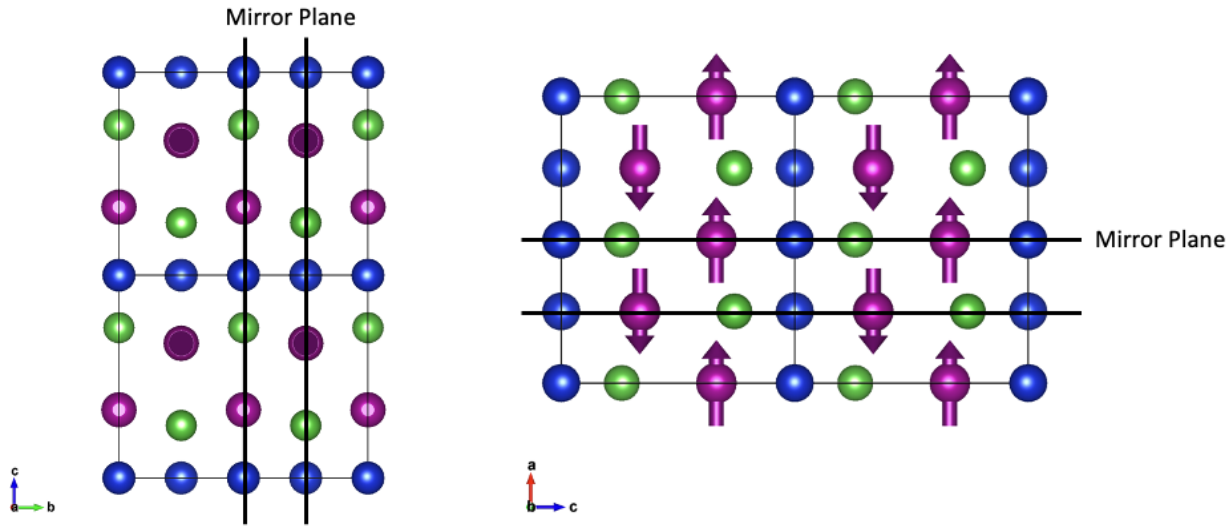

Figure 2.8: Depiction of CuMnAs's site symmetries for the magnetic Mn atoms. That is two mirror planes that pass through the Mn atoms: ac (left) and bc (right).

a mirror plane that is parallel (perpendicular) to the direction of $\vec{E}$. On the other hand, magnetic vectors are axial vectors, which means they do the opposite under reflection. That is, $\vec{S}$ is reversed (unchanged) by a mirror plane that is parallel (perpendicular) to $\vec{S}$. So, for example, we see that the depicted AFM order in Fig. 2.8 breaks the ac mirror plane symmetry, but preserves the bc mirror plane, but again to first order, we can ignore the antiferromagnetic order and thus consider the implications of both the ac and bc mirror planes.

Now let's consider applying an $\vec{E}$ field along a, b, and c. $\vec{E}$ along a breaks the bc mirror plane while preserving the ac mirror plane. The only $\vec{S}$ direction that does the same is along b. Applying the same logic, $\vec{E}$ along b induces $\vec{S}$ along a, and since $\vec{E}$ along c preserves both mirror planes and no direction of $\vec{S}$ preserves both mirror planes, applying $\vec{E}$ along c does not induce a CISP. That is, the nonzero components of the susceptibility are χ_{12} and χ_{21}, to first order. Note that the Mn atoms sit in the 2c Wyckoff position of the CuMnAs lattice, which has 4mm site symmetry. The

CISP susceptibility can then be found in table I of [17] and is

$$\chi = \begin{pmatrix} 0 & -x_{21} & 0 \\ x_{21} & 0 & 0 \\ 0 & 0 & 0 \end{pmatrix}$$

This is consistent with both the above symmetry argument and the microscopic picture discussed above, namely that the spin polarization of the current is in the ab plane. Note that this is the spin susceptibility of each Mn sublattice, but the susceptibilities on each Mn sublattice can be related to each other by the $\mathcal{PT}$ that connects the two sublattices. Since $\mathcal{PT}$ reverses spin, the response of each Mn atom will be equal and opposite.

2.3 Anisotropic Magnetoresistance

For device applications, one needs to not only control the magnetic order but also be able to read out the magnetic state. Exploiting the anisotropic magnetoresistance is one way to do this. Broadly speaking, Magnetoresistance (MR) is the effect of magnetic fields or magnetic order on the resistance of a material. It should be no surprise that a magnetic field impacts the resistance, since electrons obviously respond to the Lorentz force, which causes their path through a material to be curved, and these longer paths naturally provide more opportunity for scattering events and thus lead to higher resistivity. This physics is also responsible for the famous Hall effect.

The Anisotropic Magnetoresistance (AMR) stems from a difference in resistance when travelling parallel or with some angle to a magnetic field or magnetization vector—let's focus on magnetization as this is the case in CuMnAs. The strength of the AMR effect is characterized by the ratio

$$\frac{\Delta\rho}{\rho} = \frac{\rho_\perp - \rho_\parallel}{\rho_\perp}, \tag{2.41}$$

where ρ is the resistivity with $\perp$ ($\parallel$) denoting the component perpendicular (parallel) to the magnetization.

Before diving in, note that from a symmetry point of view, the presence of a magnetization vector breaks rotational symmetry, and thus it is unsurprising that the conductivity tensor would

reflect this broken symmetry. However, there are more detailed microscopic models, and although the details are beyond the scope, let's highlight the salient features to see how AMR emerges (for a more full discussion, including a purely symmetry based argument for the functional form of $\frac{\Delta\rho}{\rho}$, see [18–20]).

The basic physics of AMR in ferromagnetic materials stems from differential scattering of electrons propagating with an angle with respect to the magnetization due to spin-orbit coupling. To see how this occurs, there are several basic ingredients: First, consider the two current model proposed by Mott [21] where the overall resistivity is

$$\frac{1}{\rho} = \frac{1}{\rho^{\uparrow}} + \frac{1}{\rho^{\downarrow}}. \tag{2.42}$$

That is, in the absence of magnetic impurities and without spin-orbit coupling, the two spin channels—along the magnetization, $\uparrow$, and anti parallel, $\downarrow$—conduct electricity independently and the overall resistivity is found from equation 2.42.

Second, a prototypical magnetic metal, a Ni alloy, well below the Curie temperature has the density of states is shown in figure 2.9. The important feature is that there are no spin $\uparrow$ d-states at the Fermi surface, in the absence of spin-orbit coupling. Furthermore, d-states are heavier/more localized, i.e. less conductive, so conduction is dominated by the s-states. Additionally and for related reasons, the resistance to the conduction is dominated by s-d scattering [20, 22]. All of this means that the dominant contribution to the resistivity stems from the $\uparrow$ channel, specifically the s $\uparrow$ states.

Third, spin-orbit coupling ($\sim \vec{L} \cdot \vec{S}$) mixes spin states. The important part being that some d $\uparrow$ states are mixed into the d $\downarrow$ states at the Fermi surface. This then generates some s-d scattering for the s $\uparrow$ states that was otherwise not present. Finally, since there is a net magnetic moment, $\vec{S}$ has a defined direction and thus a preferred direction for the spin-orbit perturbation, which leads to anisotropic mixing of the d $\uparrow$ and d $\downarrow$ states. This anisotropy leads to an anisotropy in the s $\uparrow$ to d $\uparrow$ scattering, which then provides the dominant contribution to the AMR.

Since the AMR depends on spin-orbit coupling, which is generally a sub-dominant energy

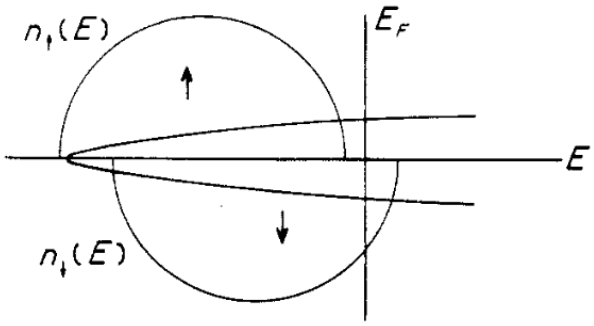

Figure 2.9: Schematic of the density of states in Ni alloys well below the Curie temperature, showing both spin up and spin down, along and anti-parallel to the magnetization, respectively. d-states are shown with semi-circles, while s-states are the other curve. Copied from [20].

scale, and the mechanism only relates to scattering rates, rather than say changes in density of states, it is not surprising that the effect is fairly weak. In Ni alloys, $\frac{\Delta\rho}{\rho}$ is no higher than 20%, depending on the impurity and usually only a few percent [20].

It is worth noting that AMR can be used to make magnetic sensors, because a change in magnetic field will increase and/or rotate the magnetization, yielding a detectable change in resistance. Additionally, magnetic computing devices can exploit the before mentioned SOT to control the magnetic moments, while using AMR to read out the different magnetic states, creating a memory device. In general, the higher the $\frac{\Delta\rho}{\rho}$ the better these devices could be, because they would be more sensitive to changes in magnetization, yielding more sensitive magnetic sensors and higher contrast memory states.

2.3.1 Topological Anisotropic Magnetoresistance

CuMnAs has the chance to produce a much larger AMR signal than the type described above, because as we saw in Sec. 2.1.1, changing the Néel vector orientation does not just change scattering rates, it changes the density of states in CuMnAs by opening and closing a gap at the Dirac points. If the Dirac points are at the Fermi energy without other trivial bands crossing the Fermi energy, then changing the Néel vector orientation can change the system from a Dirac semimetal to an insulator state, i.e. driving a metal-insulator transition (MIT), which would be a topological MIT due to

the nontrivial topology of the Dirac point in the minimal model. The transport counterpart to the topological MIT transition would be a topological AMR. For temperatures below the maximum gap size at the Dirac points, the conductivity should be exponentially suppressed towards 0 as the Néel vector is rotated to open a gap larger than k_BT. Whenever the gap closes, the conductivity should reach a maximum value that is not exponentially suppressed. Therefore, the contrast of the topological AMR signal as a function of Néel vector angle, ϕ, measured from the $[1, 0, 0]$ direction should peak sharply at angles $(0, \pi/2, \pi, 3\pi/2, 2\pi)$, corresponding to the gap being closed, while showing minimal conductivity at temperatures below the gap for other angles. A schematic example of this topological MIT and topological AMR is shown in Fig. 2.10(a-c).

The potentially large contrast between different Néel vector orientations can be compared to the much weaker, mΩ, change in resistance demonstrated in devices made of CuMnAs by Wadley et al. [16] [see Fig. 2.10 (d&e)]. The exact source of the change in resistance observed in this case is still under investigation but likely involves the more traditional changes in scattering rates and possibly heating effects; however, it does not include the above mentioned topological MIT due to the chemical potential lying away from the Dirac points.

2.4 Conclusion

As we have seen in this chapter, CuMnAs is an extremely interesting material at the heart of several exciting areas of research: 1) electron topology, especially in the presence of magnetic order and 2) the quest for much higher contrast and faster magnetic memory devices—i.e. materials that show a strong AMR signal for readout and control over AFM order, which has intrinsically THz speed spin dynamics as opposed to GHz speed in ferromagnetic materials. That is, CuMnAs hosts the appropriate symmetries to enable electric currents to reorient the Néel vector, and that Néel vector reorientation controls Dirac masses and also possibly topology, enabling a topological MIT and topological AMR.

Šmejkal et al. go on to show that the presence of the Dirac points and their protection under the $\mathcal{G}_{x/y}$ symmetries is present in DFT calculations as well. However, DFT does not always provide

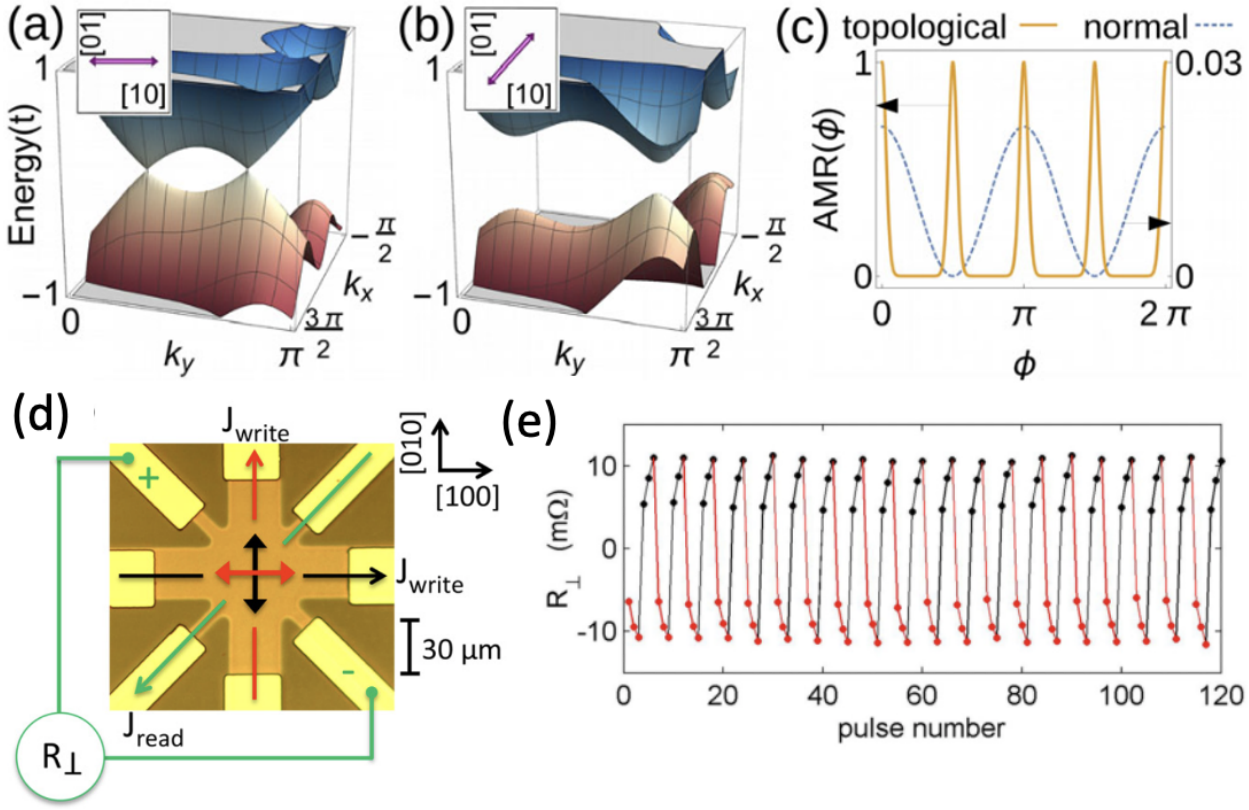

Figure 2.10: Depiction of the topological MIT in the minimal model of CuMnAs vs. traditional AMR in CuMnAs: Schematic of the band structure in the minimal model for (a) $\vec{n} \parallel [1,0]$, which is gapless due to the symmetry protection of the Dirac points by $\mathcal{G}_x$, and (b) $\vec{n} \parallel [1,1]$, which is gapped everywhere because neither $\mathcal{G}_x$ nor $\mathcal{G}_y$ exist at this orientation of the Néel vector. c) Schematic of the corresponding AMR signal as a function of Néel vector angle ϕ for the topological AMR (yellow) and normal scattering based AMR (blue). (d) Schematic of device made by Wadley et al. out of CuMnAs. (e) Change in $R_\perp$ after successive write pulses, demonstrating multilevel switching of CuMnAs. Subfigures (a-c) copied from [1] and (d&e) copied from [16].

an accurate representation of the true electronic structure, particularly when strong correlations are present, which the magnetic Mn has the potential to introduce. Testing the validity of the DFT, finding an accurate description of the electronic structure of tetragonal CuMnAs, and confirming whether the Dirac points persist in the experimentally validated electronic structure is the primary focus of my work presented in this dissertation. The method of experimentally measuring the electronic structure is the focus of the next chapter.

Chapter 3

Introduction to ARPES

Angle Resolved Photoemission Spectroscopy (ARPES) has become a prominent technique to study the electronic structure of solid-state crystals. ARPES is one experimental technique in the broader class of photoemission spectroscopies, where photons of sufficient energy are used to emit an electron from a material. (A process first theoretically described by Einstein, affording him his **only** Nobel Prize.) The emitted electrons can subsequently be studied to learn about properties of the materials they came from. In the specific case of ARPES, the emitted electron's energy and emission angles are measured, and by exploiting various conservation laws, this data reveals the emitted electron's prior momentum and energy when residing inside the material. That is, ARPES measures the distribution of electrons in energy and momentum inside of the material, revealing not only the electronic band structure but also the full many-body physics of the electrons. See Fig. 3.1 for an example of ARPES data.

In this chapter, we will first discuss the theoretical description of ARPES, including what specifically ARPES measures. Then, we will explore experimental details, such as resolution effects and data analysis. And finally, we will briefly discuss time-resolved ARPES and the effects of adding an excitation.

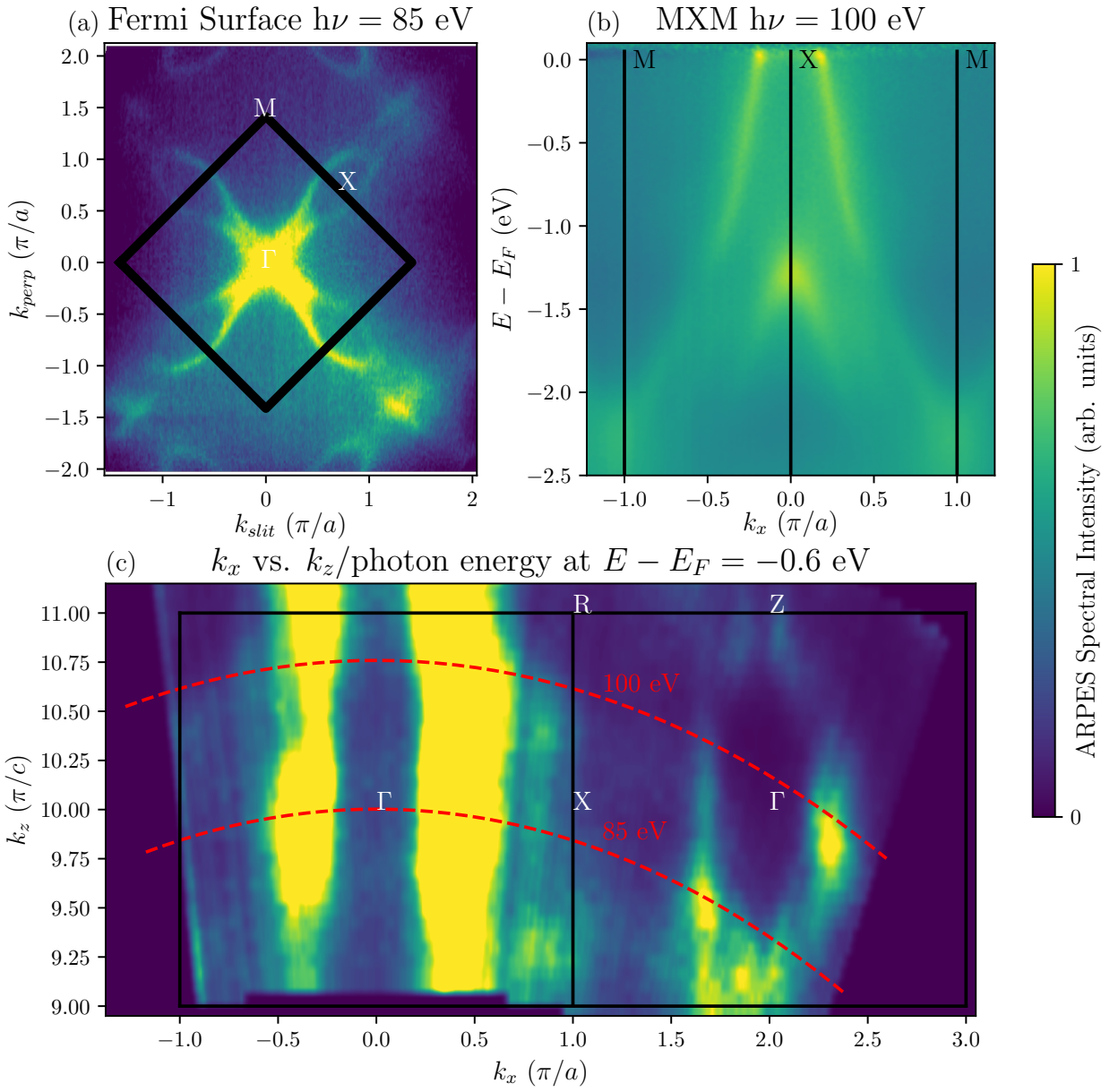

Figure 3.1: Example of ARPES Data set from tetragonal CuMnAs converted to energy and momentum. (a) Fermi Surface plot. One momentum is along the hemispherical analyzer entrance slit, and the other is from rotating the sample, rotating the surface normal through angles perpendicular to the slit. This 2D data is a slice of the 3D data at the Fermi energy. (b) Single ARPES image (E vs. k), with the slit aligned along the MXM cut in momentum space. Here the data is normalized by total intensity at a each energy. (c) k_z scan. One momentum is along the slit of the analyzer, aligned along XΓX, while the other comes from sweeping photon energies. This 2D image is a slice through the 3D data at a binding energy of −0.6 eV. Red dashed lines show constant photon energies.

3.1 Theoretical Description

3.1.1 Overview

In a photoemission process, Einstein taught us that electrons are ejected from a material by a photon of energy $h\nu$, provided that $h\nu$ is greater than the work function, Φ. Using energy conservation, electrons emitted from a binding energy, $E_B = E_\mathrm{i} - E_\mathrm{F}$, (where E_i is the initial state energy and E_F is the Fermi energy) will be emitted with a kinetic energy, $E_{\vec{k}} = h\nu - \Phi + E_B$. Or turning this around, by measuring the kinetic energy of the photoelectron ejected by a photon source of a known energy, the energy conservation tells us that the electron came from a binding energy, $E_B = E_{\vec{k}} - h\nu + \Phi$, and by making repeated measurements, the density of states (DOS) of the material may be measured, up to resolution effects. The DOS of a material and the ejected photoelectrons are shown schematically in 3.2. This is already a powerful technique referred to as Photoemission Spectroscopy (PES).

ARPES adds to PES the measurement of the angle of the photoelectron's momentum with respect to the sample normal (see Fig. 3.3). Since the electrons are ejected into a vacuum in ARPES experiments, the electron states obey the free-space dispersion relation, $E_{\vec{k}} = \frac{\hbar^2 k_\mathrm{f}^2}{2m}$, where m is the mass of the free electron. Then, by energy conservation

$$\begin{aligned} k_\mathrm{f} &= \frac{\sqrt{2mE_{\vec{k}_\mathrm{f}}}}{\hbar} \\ &= \frac{\sqrt{2m(h\nu - \Phi + E_B)}}{\hbar}. \end{aligned} \tag{3.1}$$

Since we know the angle of the electrons motion and the magnitude of the electron's wave vector, it is easy to find the components:

$$\begin{aligned} k_{\mathrm{f},x} &= k_\mathrm{f} \sin(\theta)\cos(\phi) \\ k_{\mathrm{f},y} &= k_\mathrm{f} \sin(\theta)\sin(\phi) \\ k_{\mathrm{f},z} &= k_\mathrm{f} \cos(\theta), \end{aligned} \tag{3.2}$$

where k_f is given in equation 3.1 and the angles are defined in Fig. 3.3. But, we are interested in

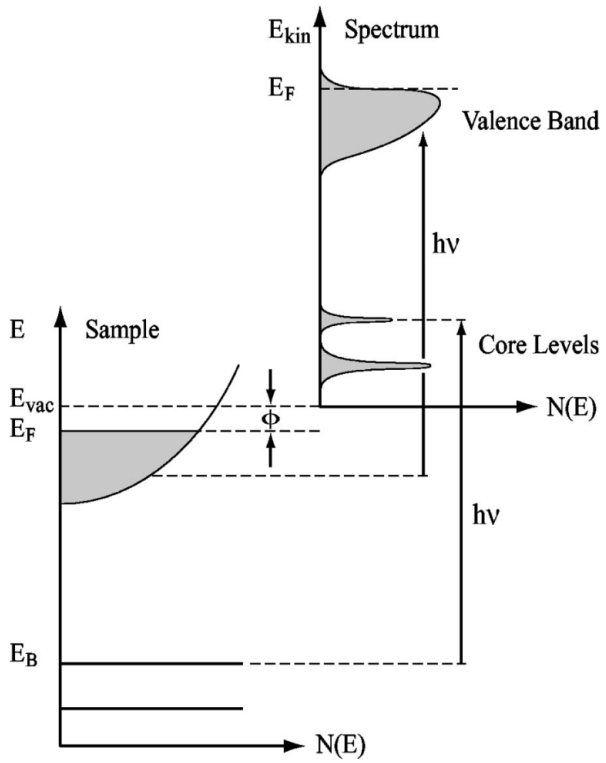

Figure 3.2: Schematic of the energetics of a photoemission process: Left shows the density of states as a function of energy for a material. Right shows the density of states of the photoelectrons after photoemission by photons of energy $h\nu$. Copied from [23].

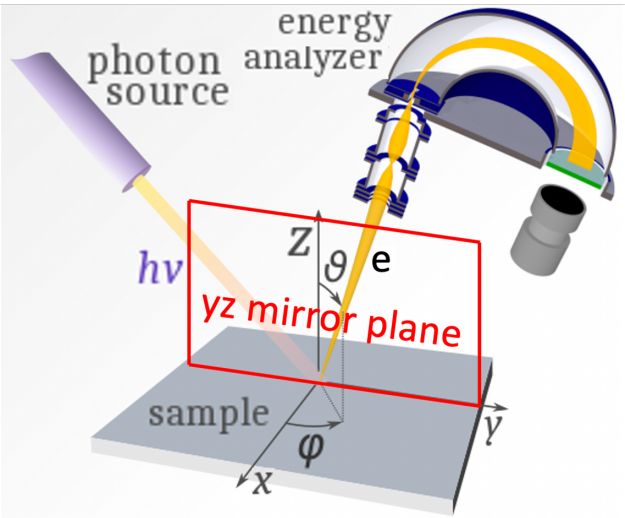

Figure 3.3: Example geometry of a typical ARPES experiment. Adapted from [24].

properties of the material, not the electron in vacuum. Just like energy conservation allowed us to relate the DOS of the photoelectrons to the DOS of the electrons in the material, momentum conservation allows us to relate the momentum of the photoelectron to the momentum of the electron before photoemission. Namely, the translational symmetry of the surface conserves the in plane momentum of the electron as it leaves the surface, i.e. $(k_{\mathrm{i},x}, k_{\mathrm{i},y}) = (k_{\mathrm{f},x}, k_{\mathrm{f},y})$. Of course, the light also imparts momentum to the electron in the material; so, the true momentum of the initial electron state would have to subtract away the momentum of the light. However, for many ARPES experiments, $h\nu \sim 100$ eV; so, the photons carry momentum 100 eV/c, and the ~ 95 eV electrons in free space have momentum ~ 9800 eV/c, where c is the speed of light. Furthermore, an overall shift in momentum is not important, so it is only the relative change in momentum imparted from the light due to rotating the sample that matters, which is even smaller than 1%. Thus the photon momentum may be neglected at low energies.

The out of plane momentum, $k_{\mathrm{i},z}$, is actually much more complex, because in general the out-of-plane momentum is not conserved by the photoemission process, due to the lack of translational symmetry across the surface. However, it has been noted that $k_{\mathrm{i},z}$ may be found by accounting for the energy difference between the bottom of the valence band and the free electron band in

vacuum, V_0, referred to as the inner potential, which is usually on the order of 15 eV [25]. Since the in-plane momentum is conserved, this energy difference only shows up between $k_{\mathrm{i},z}$ and $k_{\mathrm{f},z}$ as

$$\begin{aligned} k_{\mathrm{i},z} &= \frac{1}{\hbar}\sqrt{2m(\frac{\hbar^2 k_{\mathrm{f},z}^2}{2m} + V_0)} \\ &= \frac{1}{\hbar}\sqrt{2m(E_{\vec{k}}\cos(\theta)^2 + V_0)} \\ &= \frac{1}{\hbar}\sqrt{2m[(h\nu - \Phi + E_B)\cos(\theta)^2 + V_0]} \end{aligned} \tag{3.3}$$

Thus, $k_{\mathrm{i},z}$ may be scanned by scanning the photon energy used for photoemission while measuring the same $(k_{\mathrm{i},x}, k_{\mathrm{i},y})$. In practice, V_0 is used as a fitting parameter to offset the periodic dispersion in $k_{\mathrm{f},z}$ to match the Brillouin zone periodicity in $k_{\mathrm{i},z}$. In general, this approximation uses crude assumptions that do not always hold. Thus, in practice, one measures the $k_{\mathrm{f},z}$ dispersion, and if there is no clear dispersion (the bands may be broadened in k_z so much as to be indistinguishable), that is not surprising, but if there is dispersion, then it can be related to $k_{\mathrm{i},z}$ in the above fashion and studied, with a grain of salt. For an example of k_z data see Fig. 3.1(c), where the curvature in k_z for a constant photon energy implied by Eqn. 3.3 is readily seen, and the lack of dispersion in the first zone can be compared to that of the second zone, showing that sometimes there is dispersion and other times not.

Therefore, using energy and momentum conservation, a photoelectron energy and emission angle can be converted into the energy and momentum of the electron inside the material. By taking many successive measurements of lots of photoelectrons, the electronic DOS inside a material may be measured, since the number of electrons emitted from an initial energy and momentum will be proportional to the number of electronic states at that energy and momentum.

3.1.2 Modeling ARPES: 3-Step vs. 1-Step Model

As an initial step to calculating the full ARPES photocurrent, $I(\vec{k}, E)$, the transition probability, $w_{\mathrm{f,i}}$, between the initial N-body ground state, $|\psi_i^N\rangle$ and one particular N-body final state, $|\psi_{\mathrm{f}}^N\rangle$, can be calculated using Fermi's golden rule:

$$w_{\mathrm{f,i}} = \frac{2\pi}{\hbar}|\left\langle\psi_{\mathrm{f}}^N\right| H_{\mathrm{int}} \left|\psi_{\mathrm{i}}^N\right\rangle|^2 \delta(E_{\mathrm{f}}^N - E_{\mathrm{i}}^N - h\nu), \tag{3.4}$$

where E_{i}^N (E_{f}^N) is the total energy of the initial (final) N-electron states, and H_{int} describes the interaction with the incident light. In general, using minimal coupling,

$$H_{\mathrm{int}} = \frac{-e}{2mc}(\vec{A}\cdot\vec{p}+\vec{p}\cdot\vec{A}) + \frac{e^2}{2mc^2}A^2 - eV(\vec{r}). \tag{3.5}$$

However, the gauge may be chosen such that the electrostatic potential, $V(\vec{r}) = 0$. Normally, ARPES experiments are carried out at low enough field strength that neglecting the A^2 term is a good approximation. Finally, for ARPES experiments conducted with $h\nu = \mathcal{O}(100\text{ eV})$, the wavelength of the light is $\mathcal{O}(10\text{ nm})$, which is significantly larger than the size of an atom, $\mathcal{O}(0.1\text{ nm})$. Therefore, it is acceptable to treat the fields as constant on the scale of an atom, i.e. $\vec{\nabla}\cdot\vec{A} \approx 0$ (dipole approximation, not Coulomb gauge). Therefore, $[\vec{p},\vec{A}] = -i\hbar\vec{\nabla}\cdot\vec{A} \approx 0$. Thus,

$$H_{\mathrm{int}} \approx -\frac{e}{mc}\vec{A}\cdot\vec{p}. \tag{3.6}$$

At this point, the final and initial state wave functions need to be specified further, which requires a physical picture of the process. In general, it is more accurate to model the process as a single quantum mechanical transition between an electronic state in the material and a free electron state that is damped inside of the material. This is the one-step model [see Fig. 3.4(right)], but it requires that the initial states include both bulk contributions and all of the microscopic details of the surface physics that impact the initial and final states, which are in general complex. So, it is quite common to use the intuitive 3-step model proposed by Spicer [26] [see Fig. 3.4(left)]. In this model, (1) the photon absorption excites an electron to a state inside of the material. (2) This electron then propagates to the surface, and finally, (3) it can transmit through the surface into the vacuum, depending on the work function. Step (1) contains all of the information about the material that is generally the focus of experiments, and it is described by the total probability of optical excitation. Step (2) can be modeled with an effective mean-free path of the electrons, describing the probability that the electron makes it to the surface without scattering, i.e. changing momentum and energy. This accounts for the surface sensitivity in ARPES, and the scattered electrons contribute to a background intensity. Finally, step (3) can be described by the

probability of the electron transmitting through the surface, which depends primarily on the work function Φ.

Returning to Eqn. 3.4, the initial state wave function is the ground state of the bulk system, and the final states we want to consider are the states with the electron removed from the sample, i.e. after step 1-3. Even in the 3-step model, this is still very complicated. In particular, during steps (2&3), i.e. while the excited electron propagates away from the N-1 body system left behind, the electron interacts with the system (e.g. the hole left behind would have some Coulomb attraction to the escaping electron). In principle, this means that after the initial excitation, the final state transitions through many different states while the N-1 and 1 electron systems interact. However, often the excited electrons have large kinetic energy, and so, move away very quickly. Thus, it is reasonable (and oftenly) assumed that the excited electron is instantaneously removed from the system, referred to as the **sudden approximation**. It is worth noting that this is a worse approximation for low kinetic energy photoelectrons; however, even for electrons with kinetic energies of $\approx$ 1-2 eV created with laser excitations, the sudden approximation still appears reasonably faithful [28]. In any case, under this approximation, the initially excited N-electron state can be separated into the initial (N-1)-electron excited state, $|\psi_{\mathrm{f}}^{N-1}\rangle$, and an instantaneously removed photoelectron state, $|\phi_{\mathrm{f}}(\vec{k})\rangle$, with momentum, $\vec{k}$. That is, the final state can be factorized as $|\psi_{\mathrm{f}}^{N}\rangle = \mathcal{A}\,|\phi_{\mathrm{f}}(\vec{k})\rangle\,|\psi_{\mathrm{f}}^{N-1}\rangle$, and $\mathcal{A}$ just ensures antisymmetry of the fermionic state. $|\psi_{\mathrm{f}}^{N-1}\rangle$ may be projected into the excited eigenstate basis, $|\psi_{m}^{N-1}\rangle$, with energy E_{m}^{N-1}. Thus, a sum over m is needed to find the full transition probability. The initial state is approximated in the Hartree-Fock formalism as a single Slater determinant, which means that the initial state may be factorized as $|\psi_{\mathrm{i}}^{N}\rangle = \mathcal{A}\,|\phi_{\mathrm{i}}(\vec{k})\rangle\,|\psi_{\mathrm{i}}^{N-1}\rangle$. Thus, we can write the matrix elements of equation 3.4 as

$$\langle\psi_{\mathrm{f}}^{N}|\,H_{\mathrm{int}}\,|\psi_{\mathrm{i}}^{N}\rangle = \langle\phi_{\mathrm{f}}(\vec{k})|\,H_{\mathrm{int}}\,|\phi_{\mathrm{i}}(\vec{k})\rangle\,\langle\psi_{m}^{N-1}|\psi_{\mathrm{i}}^{N-1}\rangle\,, \tag{3.7}$$

where the final state is taken as only one excited state, m, which will be summed over anyway. $|\,\langle\phi_{\mathrm{f}}(\vec{k})|\,H_{\mathrm{int}}\,|\phi_{\mathrm{i}}(\vec{k})\rangle\,|^2 \equiv |M_{\mathrm{f,i}}(\vec{k})|^2$ can be identified as the single electron dipole transition matrix element, and $|\,\langle\psi_{m}^{N-1}|\psi_{\mathrm{i}}^{N-1}\rangle\,|^2 \equiv |c_{m,i}|^2$ is just the probability that removing the photoelectron

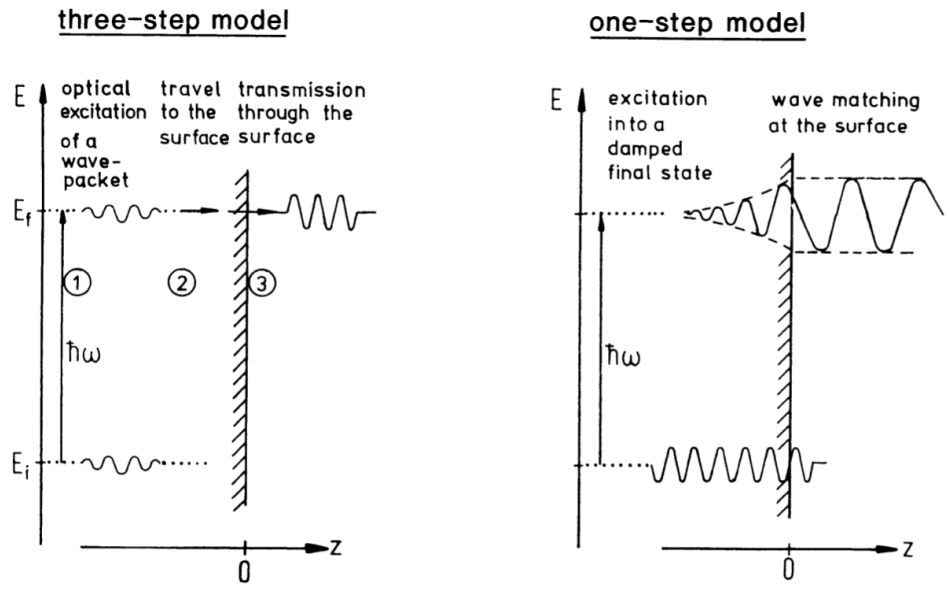

Figure 3.4: Schematic of the one-step vs three-step model: (left) In the three step model, (1) the electron is excited inside of the material, (2) propagates to the surface, and (3) translates through the surface. In the one-step model the electron is excited directly from a Bloch state into a free electron state that is damped at the sample surface. Figure Copied from [27]

from the initial state leaves the remaining N-1 system in the excited state, $|\psi_m^{N-1}\rangle$. Then, the full photocurrent can be written as a sum of transition probabilities, $w_{\mathrm{f,i}}$, over all initial and final states,

$$I(\vec{k}, E) \sim \sum_{\mathrm{f,i}} |M_{\mathrm{f,i}}(\vec{k})|^2 \sum_m |c_{m,i}|^2 \delta(E_{\vec{k}} + E_m^{N-1} - E_{\mathrm{i}}^N - h\nu), \tag{3.8}$$

where $E_{\vec{k}}$ is the energy of the single final state electron.

First, let's consider the non-interacting electron picture. In this case, removal of one electron will leave the (N-1)-electron initial state in exactly one of the excited states, $m = m_0$. Thus, $|c_{m,i}|^2 = \delta_{m,m_0}$. Provided that the matrix element $|M_{\mathrm{f,i}}(\vec{k})|^2$ does not vanish, the photocurrent will be a delta function at $E_{\vec{k}} = \epsilon(\vec{k}) + h\nu$, where $\epsilon(\vec{k})$ is just the energy of the initial single electron at momentum $\vec{k}$, i.e. $\epsilon(\vec{k})$ is the single electron band dispersion [see Fig. 3.5(middle)]. Thus, we see that the band structure can be measured from ARPES experiments. Alternatively, if the electrons are strongly interacting, then the removal of a single electron from the N-electron initial state will strongly affect the remaining (N-1)-electron system, leaving it in a superposition of many excited states, m. In the large N limit, the sum of the delta functions becomes a smooth function. For example, in Fermi-liquid theory the resultant DOS for the photoelectron at momentum $\vec{k}$ looks like that shown in Fig. 3.5(right), where in Fermi liquid theory there is a quasiparticle peak that sharpens near the Fermi energy but also the broader contribution due to the interactions.

3.1.3 The One Particle Spectral Function in ARPES

In quantum many body physics, the most common formalism used to solve problems is the Green's function formalism, and in this section, we will show how the imaginary part of the Green's—the spectral function—function shows up directly in the ARPES photocurrent, $I(\vec{k}, E)$.

The Green's function tells us about the correlations of a quantum state and is most powerful when dealing with many body systems. Specifically, in position space, it tells us about the probability of injecting an electron at position $\vec{r}_1$ at time t_1 and finding it at position $\vec{r}_2$ at time t_2. In the language of second quantization, this is $\langle c(\vec{r}_2, t_2) c^\dagger(\vec{r}_1, t_1)\rangle$ where the expectation value is computed for the state in question, often the ground state. However, to get a proper physical

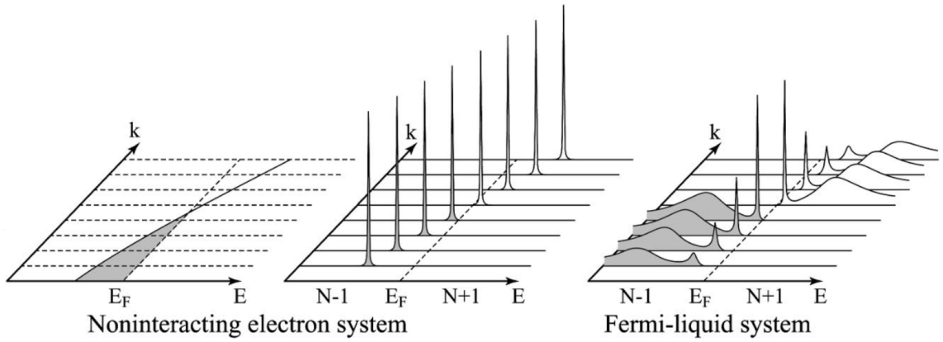

Figure 3.5: Noninteracting vs. interacting picture of DOS: (left) Shows a single band dispersing across E_{F}. (middle) Shows the resultant delta function spike at the band energy, $\epsilon(\vec{k})$, corresponding to the non-interacting DOS at momentum $\vec{k}$. (right) The DOS in the interacting picture at momentum $\vec{k}$, where there is a quasiparticle peak at $\epsilon(\vec{k})$ that sharpens closer to E_{F} but also a broader contribution due interactions. Figure Copied from [23].

observable, this becomes [29]

$$G(\vec{r}_1, \vec{r}_2, t_2 - t_1) = -i\theta(t_2 - t_1) \left\langle \{c(\vec{r}_2, t_2), c^\dagger(\vec{r}_1, t_1)\} \right\rangle , \tag{3.9}$$

where $\theta(x)$ is the Heaviside step function that just ensures that you measure the location of the inserted particle after inserting it. The $\{\}$ denotes the anti-commutator, and implies that the correlation function also takes into account the probability of removing an electron (inserting a hole) at $\vec{r}_1$, t_1 and finding an electron missing (hole) at $\vec{r}_2$, t_2.

Since we are working with a crystal, it makes sense to work in Bloch space, where the Green's function's interpretation becomes the probability of inserting an electron into a Bloch state with momentum $\vec{k}$ at time t_1 and finding it in the same Bloch state at a later time, t_2. Translational invariance guarantees that the position space Green's function only depends on $\vec{r}_2 - \vec{r}_1$ and analogously that there is only one momentum variable. So, in a translationally invariant system, the Green's function can be written in Bloch space as [29]

$$G(\vec{k}, t) = -i\theta(t) \left\langle \{c(\vec{k}, t), c^\dagger(\vec{k})\} \right\rangle , \tag{3.10}$$

where $t_2 \equiv t$ and $t_1 \equiv 0$. To evaluate this operator, one can use the standard identity using the trace of the density matrix operator, ρ: $\langle A \rangle = \mathrm{tr}(\rho A)$, where "tr" denotes the trace. Using a complete basis of energy eigenstates,

$$\begin{aligned}
\langle \{c(\vec{k}, t), c^\dagger(\vec{k})\} \rangle &= \mathrm{tr}(\rho \{c(\vec{k}, t), c^\dagger(\vec{k})\}) \\
&= \frac{1}{Z} \sum_{n,m} \langle n| e^{-\beta H} \left(c(\vec{k}, t) |m\rangle \langle m| c^\dagger(\vec{k}) + c^\dagger(\vec{k}) |m\rangle \langle m| c(\vec{k}, t) \right) |n\rangle \\
&= \frac{1}{Z} \sum_{n,m} \langle n| e^{-\beta E_n} \left(e^{iHt} c(\vec{k}) e^{-iHt} |m\rangle \langle m| c^\dagger(\vec{k}) + \right. \\
&\quad \left. c^\dagger(\vec{k}) |m\rangle \langle m| e^{iHt} c(\vec{k}) e^{-iHt} \right) |n\rangle \\
&= \frac{1}{Z} \sum_{n,m} \langle n| e^{-\beta E_n} \left(e^{iE_n t} c(\vec{k}) e^{-iE_m t} |m\rangle \langle m| c^\dagger(\vec{k}) + \right. \\
&\quad \left. c^\dagger(\vec{k}) |m\rangle \langle m| e^{iE_m t} c(\vec{k}) e^{-iE_n t} \right) |n\rangle \\
&= \frac{1}{Z} \sum_{n,m} \langle n| c(\vec{k}) |m\rangle \langle m| c^\dagger(\vec{k}) |n\rangle e^{i(E_n - E_m)t} \left(e^{-\beta E_n} + e^{-\beta E_m} \right).
\end{aligned} \tag{3.11}$$

$|n\rangle, |m\rangle$ are energy eigenstates and Z is the partition function. Line two computes the trace in the energy basis, uses the operator form of the density matrix, and inserts the identity operator. Line 3 makes use of the time evolution of the electron annihilation operators to propagate the operators into the same time. In the last line, the second term swaps $n \leftrightarrow m$, and in all cases, the Hamiltonian of the system is replaced with the energy eigenvalues of the energy eigenstates it acts on. Now, we would like to work in the frequency basis to draw comparison to ARPES, so $G(t, \vec{k})$ must be Fourier transformed:

$$\begin{aligned} G(\vec{k},\omega) &= \frac{1}{Z}\sum_{n,m} |\langle n| c(\vec{k}) |m\rangle|^2 \left(e^{-\beta E_n} + e^{-\beta E_m}\right)(-i)\int_0^\infty e^{i(E_n - E_m)t} e^{i(w+i\delta)t} dt \\ &= \frac{1}{Z}\sum_{n,m} |\langle n| c(\vec{k}) |m\rangle|^2 \frac{e^{-\beta E_n} + e^{-\beta E_m}}{\omega + E_n - E_m + i\delta}, \end{aligned} \tag{3.12}$$

where the regulator, δ, is inserted to make the integral converge, but when necessary, the limit of $\delta \to 0$ is taken. Next, we can introduce the spectral function $A(\vec{k}, \omega) = -\frac{1}{\pi}\Im G(\omega, \vec{k})$, which can be computed using the identity $\frac{1}{x+i\delta} = \mathcal{P}\frac{1}{x} - i\pi\delta(x)$, where $\mathcal{P}$ is the principal part of the function. Thus,

$$\begin{aligned} A(\vec{k},\omega) &= \frac{1}{Z}\sum_{n,m} |\langle n| c(\vec{k}) |m\rangle|^2 \left(e^{-\beta E_n} + e^{-\beta E_m}\right)\delta(\omega + E_n - E_m) \\ &= \frac{e^{\beta\omega}+1}{Z}\sum_{n,m} |\langle n| c(\vec{k}) |m\rangle|^2 e^{-\beta E_m}\delta(\omega + E_n - E_m) \\ &= \frac{1}{n_{\mathrm{F}}(\omega) Z}\sum_{n,m} |\langle n| c(\vec{k}) |m\rangle|^2 e^{-\beta E_m}\delta(\omega + E_n - E_m), \end{aligned} \tag{3.13}$$

where $n_{\mathrm{F}}(\omega)$ is the Fermi function. Or rearranging a bit,

$$n_{\mathrm{F}}(\omega) A(\vec{k},\omega) = \frac{1}{Z}\sum_{n,m} |\langle n| c(\vec{k}) |m\rangle|^2 e^{-\beta E_m}\delta(\omega + E_n - E_m). \tag{3.14}$$

Finally, we arrive at a quantity that resembles Eqn. 3.8 without the sum over matrix elements but is actually more general. To make the comparison more clear, consider $|m\rangle = |\psi^N\rangle$, an N-electron energy eigenstate, and $|n\rangle = |\psi_{\mathrm{f}}^{N-1}\rangle$, an (N-1)-electron energy eigenstate. Note that $c(\vec{k})|\psi^N\rangle = |\psi^{N-1}\rangle$, i.e. an N-electron eigenstate with one electron suddenly removed. Note, under the above conditions, the spectral function is the single-electron removal spectral function (one

could have considered the overlap with an (N+1)-electron system as well). The additional factors present above and not in Eqn. 3.8 account for thermal effects. In general, measurements are not at T=0, and thus the ground state is a sum of N-electron energy eigenstates weighted by the usual probability$\sim e^{-\beta E_m}$. Alas, we can write the ARPES spectral intensity as

$$I(\vec{k},\omega) = I_0(\vec{k},\omega,\vec{A})n_{\mathrm{F}}(\omega)A(\vec{k},\omega), \tag{3.15}$$

where $I_0(\vec{k},\omega,\vec{A})$ is proportional to the matrix elements $|M_{\mathrm{f,i}}(\vec{k})|^2$, and the Fermi function is accounting for the fact that one can only photoemit from occupied electron states. Thus, we see that under the sudden approximation, the ARPES photocurrent is proportional to the spectral function, and this is generally the primary object of interest in materials and thus ARPES studies.

3.1.4 Interpreting the One-Particle Spectral Function

To see what the spectral function can tell us about a system, let's consider the interacting many-body system. In a general interacting many-body system, one can always write the single particle Green's function as [29]

$$G(\vec{k},\omega) = \frac{1}{\omega - \xi(\vec{k}) - \Sigma(\vec{k},\omega)}, \tag{3.16}$$

where $\xi(\vec{k})$ is the non-interacting band dispersion and $\Sigma(\vec{k},\omega)$ is the electron self-energy. The self-energy is a complex function that captures all of the interactions of the single electrons with the rest of the many-body system, e.g. electron-electron, electron-phonon, etc. $\Sigma(\vec{k},\omega)$ can be calculated in perturbation theory using Feynman's diagrams but is generally difficult to calculate. Σ shows up in the single-electron spectral function for a general many-body system as [29]

$$A(\vec{k},\omega) = -\frac{1}{\pi}\frac{\Im\Sigma(\vec{k},\omega)}{(\omega - \xi(\vec{k}) - \Re\Sigma(\vec{k},\omega))^2 + (\Im\Sigma(\vec{k},\omega))^2}. \tag{3.17}$$

To illustrate the effects of Σ, let's consider two simple cases: a purely imaginary and purely real Σ. Starting with a purely imaginary and constant $\Sigma = i\frac{1}{\tau}$,

$$G(\vec{k},\omega) = \frac{1}{\omega - \xi(\vec{k}) - i\frac{1}{\tau}}. \tag{3.18}$$

This can be easily Fourier transformed by noting that there is a pole in the complex plane at $\omega = \xi(\vec{k}) + i\frac{1}{\tau}$ and that $e^{i\omega t} = 0$ around the boundary of the upper half of the complex plane, except along the real line. Thus,

$$G(\vec{k}, t) \propto e^{-\frac{t}{\tau}} e^{i\xi(\vec{k})t}. \tag{3.19}$$

Had the imaginary part of Σ been zero, then an electron inserted into the Bloch state with energy $\xi(\vec{k})$ would have stayed there indefinitely evolving in the usual manner for an energy eigenstate. However, now the probability of finding the electron in this same state at a later time, t, is exponentially suppressed. In other words, the electronic states now have a lifetime, τ, because it can interact with other excitations, scattering into different states.

The effect of the lifetime shows up in the spectral function as,

$$A(\vec{k}, \omega) = -\frac{1}{\pi} \frac{\frac{1}{\tau}}{(\omega - \xi(\vec{k}))^2 + (\frac{1}{\tau})^2}. \tag{3.20}$$

This is a Lorentzian function in energy, where τ is related to the FWHM of the peaks in energy. With good enough data, the lifetimes of states may be extracted from ARPES data by finding the width of peaks in the data.

Next, consider a purely real self-energy. In this case, the spectral function resumes its delta function form as [29]

$$A(\vec{k}, \omega) = \delta(\omega - \xi(\vec{k}) - \Sigma(\vec{k}, \omega)). \tag{3.21}$$

Thus, instead of having delta function peaks at $\xi(\vec{k})$, the peaks are shifted to $\xi(\vec{k}) + \Sigma(\vec{k}, \omega)$, that is the band structure has been renormalized by the interactions. Therefore, the fully renormalized band structure may be extracted from ARPES data by finding the positions, $(E, \vec{k})$, of peaks in the data.

So, we see that ARPES, by measuring something proportional to the one electron removal spectral function, can tell us about the fully renormalized quasi-particle dispersion and the lifetimes of the states, making ARPES a very powerful probe of many-body electron physics in solid materials.

3.1.5 Matrix Elements

Although the spectral function is of primary interest, the matrix elements play an important role in modulating the ARPES spectral intensity, inspiring some important work in the area: Moser [30] gives an excellent analytical derivation of the matrix element effects under broad assumptions. And Day et al. [31] have produced a computational package for calculating matrix elements from Wannier functions and a tight binding Hamiltonian. Here, I will only demonstrate the matrix element's ability to send the ARPES photocurrent to zero under highly symmetrical and constrained situations.

When the matrix element is purely odd with respect to a mirror plane, the matrix element is zero, because the integral over the full space of an odd function is always zero. To see how this can happen, see Fig. 3.6, where the photon scatters in a mirror plane of the initial state wave function, shown as a $d_{x^2-y^2}$ orbital in the figure. Recall the matrix element, $|M_{\mathrm{f,i}}(\vec{k})|^2 = |\langle\phi_{\mathrm{f}}(\vec{k})|\, H_{\mathrm{int}}\, |\phi_{\mathrm{i}}(\vec{k})\rangle|^2 \rightarrow M_{\mathrm{f,i}} \sim \langle\phi_{\mathrm{f}}(\vec{k})|\, \vec{A}\cdot\vec{p}\, |\phi_{\mathrm{i}}(\vec{k})\rangle$, which can be broken into three parts: $\vec{A}\cdot\vec{p}$, $\langle\phi_{\mathrm{f}}(\vec{k})|$, and $|\phi_{\mathrm{i}}(\vec{k})\rangle$. Since the mirror plane contains the detector in the cases we are interested in, the only portion of the final state that makes it to our detector is the portion symmetric with respect to the mirror plane. The odd component of the final state is zero everywhere in the mirror plane and thus on the detector.

Next, focusing on $\vec{A}\cdot\vec{p}$. First note that for the full electromagnetic Hamiltonian, H, in the dipole approximation where $[\vec{A},\vec{p}] = 0$, $[\mathrm{H},\vec{x}] = \frac{-i\hbar}{m}\vec{p}$. So, we can replace $\vec{p}$ with $[\mathrm{H},\vec{x}]$ up to constants. Next, looking back at the original application of Fermi's golden rule, Eqn. 3.4, and noting that the final and initial states are eigenstates of H with different eigenvalues, the commutator does not vanish, and $[\mathrm{H},\vec{x}] \propto \vec{x}$. Finally, $\vec{A}$ is a constant over the dimension of the initial state wave function in the the dipole approximation. Thus, we can further simplify, $\vec{A}\cdot\vec{p}$ in $M_{\mathrm{f,i}}$ to $\vec{\epsilon}\cdot\vec{x}$ up to constants, where $\vec{\epsilon}$ is the polarization vector of $\vec{A}$. So, when $\vec{\epsilon}$ is in-plane, $H_{\mathrm{int}} \sim \vec{\epsilon}\cdot\vec{x}$ is symmetric about the mirror plane as it only depends on coordinates in the plane, and vice versa (antisymmetric) when $\vec{\epsilon}$ is perpendicular to the mirror plane.

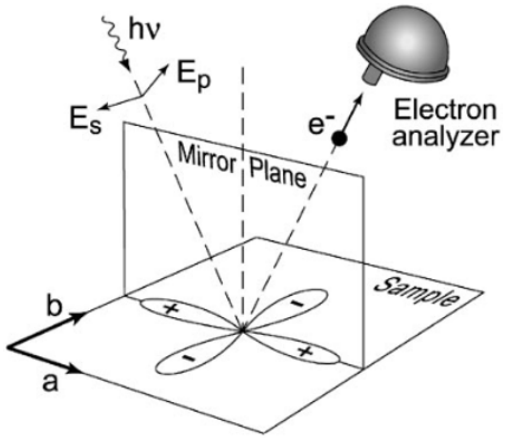

Figure 3.6: Matrix Element Effect: depiction of photoemission in the photon scattering plane that is a mirror plane for a d-orbital, which is odd with respect to the mirror plane shown. Figure Copied from [23].

Since the initial state shown in Fig. 3.6 is symmetric with respect to the mirror plane, the overall matrix element is antisymmetric (vanishes) for $\vec{\epsilon}$ perpendicular to the plane and symmetric (non-vanishing/allowed) for $\vec{\epsilon}$ in the plane. And vice versa for an antisymmetric initial state wave function with respect to the mirror plane. Thus, we arrive at the condition for the allowed and 0 matrix element when the light is incident in a mirror plane of the initial state wave function and the ARPES intensity is measured for electrons emitted in the same mirror plane:

$$\langle\phi_{\mathrm{f}}(\vec{k})|\,\vec{A}\cdot\vec{p}\,|\phi_{\mathrm{i}}(\vec{k})\rangle = \begin{cases} 0 & \begin{cases} |\phi_{\mathrm{i}}(\vec{k})\rangle \text{ antisymmetric, } \vec{\epsilon}\,\mathrm{in-plane} \\ |\phi_{\mathrm{i}}(\vec{k})\rangle \text{ symmetric, } \vec{\epsilon}\,\text{perpendicular} \end{cases} \\ \text{allowed} & \begin{cases} |\phi_{\mathrm{i}}(\vec{k})\rangle \text{ antisymmetric, } \vec{\epsilon}\,\text{perpendicular} \\ |\phi_{\mathrm{i}}(\vec{k})\rangle \text{ symmetric, } \vec{\epsilon}\,\mathrm{in-plane} \end{cases} \end{cases} . \tag{3.22}$$

Note that symmetry allowed matrix elements may still go to zero for other reasons, but symmetry forbidden elements will be 0. Of course, in general the incident light and outgoing electrons are not in mirror planes of the initial state. In this case, the matrix element will not vanish by symmetry but will act as an overall scaling of the ARPES intensity that is angle, energy, and polarization dependent. This more complicated situation can be taken into account by more complicated calculations, such as using Chinook [31].

3.2 Experimental Details

ARPES experiments involve a light source to photoemit electrons, a sorting apparatus that sorts the electrons in emission angle and energy, a detector that measures incident electrons, and a manipulator that controls, among other things, the angle of the sample surface with respect to the electron lens. Experiments must be done in ultra-high vacuum (UHV) (pressures $\lesssim 5 \times 10^{-11}$ torr), because the electrons would ionize the air as they traverse from the sample to the detector. Additionally, UHV prevents layers of particles from depositing on the surfaces, which must be pristine, too quickly to conduct data acquisition.

There are several light sources and detectors available in modern ARPES experiments. For

the light, gas (often He) discharge lamps can generate the UV light but must be monochromatized to remove additional spectral lines and only discrete spectral lines are available. Lasers that upconvert light, using either nonlinear crystals (up to an energy of $\lesssim 7$ eV) or ionization of gas (into the soft X-ray regime), can be employed and will be discussed in chapter 6. And perhaps the most common and versatile sources are those that emit light by causing electrons moving at relativistic speeds to undergo periodic oscillations in a wiggler or undulator. The electrons can move around storage rings (synchrotrons) or are accelerated in a linear trajectory at X-ray free electron sources. In both cases, the light is tunable over a broad spectral range and can be monochromatized to provide better energy resolution. For the detectors, an electrostatic lens is used to sort the electrons in angle space and retard the electrons to a particular energy. Then, the energy may be measured with a time-of-flight detector that exploits the fact that higher energy electrons travel faster to measure the energy. Or more commonly, the electrons are sent through a linear slit that selects one momentum perpendicular to the slit but passes a range of momenta along the slit direction, and energy is measured by sending electrons through a hemispherical capacitor that transmits electrons within a narrow energy range, spreading the electrons of different energy radially. In both cases, the electrons terminate on a position sensitive detector (microchannel plate in series with a fluorescent screen and a camera for a hemispherical analyzer). In the case of a time-of-flight detector two momenta are mapped onto the spatial position, while the time dimension is mapped into energy, allowing 3D data to be acquired directly. For a hemispherical analyzer, one momentum dimension and an energy dimension are mapped onto the two spatial dimensions of the camera, while an additional manipulator rotation or electrostatic deflection must be employed to select different momentum perpendicular to the slit to generate a comparable 3D data set. However, the hemispherical analyzers generally provide higher energy resolution than time-of-flight detectors. See Fig. 3.7 for a schematic of a generic beamline at a synchrotron, employing a Scienta hemispherical analyzer and grating based monochromator.

While the prior section considered an idealized case to illustrate the information available in ARPES experiments, this section deals with practical considerations and limitations of the real

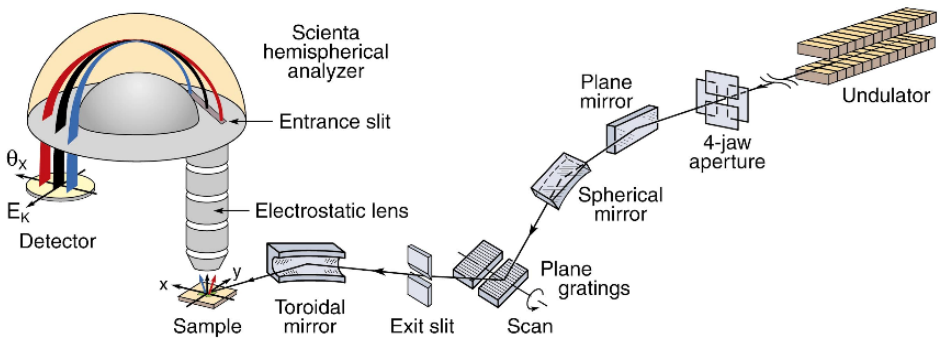

Figure 3.7: Schematic of a general ARPES end station at a beamline that employs a grating based monochromator and Scienta hemispherical analyzer. Figure Copied from [23].

experiments and equipment. In particular, finite resolution effects from light sources and detectors, approaches to data analysis, and the practical limitations of surface sensitivity are discussed. The work done in the present thesis used hemispherical analyzers and synchrotron and laser based light sources. So they will be the focus of this section.

3.2.1 Resolution

In general, measurements are made with a finite resolution that leads to broadening of the data, which is distinct from the intrinsic broadening due to interactions/self-energies. Additionally, electrons that scatter prior to leaving the material, secondaries, contribute to a background intensity. These finite resolutions may be accounted for mathematically by convolving the ARPES spectral intensity in Eqn. 3.15 with resolution functions, and adding a background term, B, that can account for secondaries [23]:

$$I(\vec{k},\omega) = \int d\omega' d\vec{k}' I_0(\vec{k}',\omega',\vec{A}) n_{\mathrm{F}}(\omega') A(\vec{k}',\omega') R(\omega-\omega') Q(\vec{k}-\vec{k}') + B, \tag{3.23}$$

where R (Q) is the energy (momentum) resolution function. R can generally be considered Gaussian, but Q can be more complicated [23]. Note that B is generally a function, and there are several choices one can make, depending on the goals of the analysis.

The energy resolution is a combination of several sources but dominated by three sources: the light, the hemispherical analyzer, and space-charge effects. The light will contain multiple

frequencies, meaning electrons with the same initial energy will be ejected into a range of kinetic energies, corresponding to absorbing different frequencies of light. In general, there is no such thing as a truly monochromatic light source. At best, one has to contend with Heisenberg in the form of the time-bandwidth product, $\Delta t \Delta\omega \approx 2\pi(0.44)$ for a Gaussian pulse of full width half max (FWHM) Δt ($\Delta\omega$) in time (frequency). This limitation plays an important role in time-resolved ARPES that use ultrashort pulses from lasers. However, for synchrotron sources, the time resolution is often not important and is usually on the order of 100 picoseconds(ps) [32] for which the minimum FWHM in frequency space is $\ll 1$ meV, which is not a serious limitation on the energy resolution. Only at a time resolution of around 1 ps would the Heisenberg limit of around 1 meV start to come into play. Instead, undulators that have periodic magnetic fields to drive the electron oscillations that produce the bright radiation in the infrared to X-ray regime are limited in energy resolution by several other factors. Perhaps the most important are the fact that the undulator is finite in size, which means the Fourier transform of the magnetic field is peaked at the oscillation frequency but broadened again by Heisenberg, and the electron beam has a finite emittance, that is spread in the distribution of electrons in position and momentum. Together along with other factors, this constrains the width of the spectral peaks produced by undulators to be much broader than 1 meV. So, to achieve the highest energy resolution, grating based monochromators are used and set the overall limit of the energy resolution of the light, which is limited by the resolving power of the monochromator, $R = \Delta E/E$. Thus, a better energy resolution is generally available for lower energy photons. For example, at the ARPES One-Cube beamline at BESSY in Germany, which has one of the best energy resolutions in the world, $\lesssim 1$ meV energy resolution for photons < 100 eV can be achieved [33]. In practice, photon energy resolution of a few meV is good, and to achieve higher data throughput/photon flux, some energy resolution can usually be sacrificed by changing the input and exit slits of monochromators (see Fig. 3.7).

A significant limitation on the energy resolution of the hemispherical analyzer is the finite size of the entrance slit. The narrow dimension of the slit is along the dimension that the energy is projected onto, which effectively leads to a finite spread of the electrons for any given energy,

limiting resolution. For a straight slit, the long dimension of the slit departs from the circumference of the hemispherical analyzer leading to additional resolution affects. In general, the energy resolution of the hemispherical analyzer is given as $\Delta E = E_{\text{pass}}(w/R_0 + \alpha^2/4)$ [23], where w is the width of the slit, R_0 is the radius of the hemispherical analyzer, α is the acceptance angle into the hemisphere, and E_{pass} is the center energy that transmits through the hemispherical capacitor. The electrostatic lens retards electrons of a selectable kinetic energy to this pass energy. The pass energy and slit may be chosen to optimize energy resolution, with narrower widths and lower pass energies yielding better energy resolution. However, the smaller the pass energy the smaller the window in energy on the detector, but the selected kinetic energy may be scanned to measure large energy ranges. For scale, Scienta's DA30-L can achieve < 1.8 meV energy resolution [**noauthor˙da30-l˙nodate**], and at low kinetic energies (< 3 eV), their DA30-L-8000 can achieve < 1 meV energy resolution [**noauthor˙da30-l-8000˙nodate**].

Finally, the space-charge effect comes from the fact that the electrons interact with each other as they move through space to the detector. The faster moving electrons get ahead of the charged electron cloud and are accelerated forward by the electrostatic repulsion from the charged cloud, causing electrons emitted from E_{F} to have higher kinetic energies than expected. In general, electrons at different energies and emission angles will be in different locations of the electron cloud and thus feel different electrostatic forces. These energy and angle dependent electrostatic forces will cause broadening in energy and angle, limiting resolution. Since the coulomb force falls off as $1/r^2$, clearly the space-charge effect is highly dependent on the electron density and thus photon flux on the sample. So, in practice, one can measure the amount of space charge by looking at the change in E_{F} with changing photon flux. If increasing the flux does not shift E_{F} higher in kinetic energy, then there is negligible space charge. Otherwise, one can reduce the photon flux at the cost of electron counts and thus data throughput, optimizing the trade-off based on the needs of the experiment. For non-time-resolved experiments with quasi-continuous light, the electrons can be spread over time, yielding little space-charge at high electron counts. However, for time-resolved experiments, where the electrons are emitted within the $\lesssim 1$ ps pulses, the space-charge can be

quite severe, often requiring one electron per pulse of light, severely limiting data throughput.

The overall energy resolution of the experiment must account for all of the above energy resolutions, which generally add in quadrature. To optimize the trade-off between data throughput to energy resolution, it is best practice to make measurements with the various energy resolutions approximately equal. To date, some of the best overall energy resolutions achieved in ARPES are ~ 1 meV [34, 35].

The momentum resolution stems from several factors as well, but it is dominated by the aberrations of the electrostatic lens, which are reduced by emitting from a small spot size on the sample along the axis of the lens. Additionally, the finite width of the slit allows a range of momentum perpendicular to the slit through, which are not resolved, i.e. this width contributes to momentum resolution in the direction along the slit width. Scienta's DA30L can achieve an angle resolution of $< 0.1^\circ$ [**noauthor˙da30-l˙nodate**], which means that momentum resolution will be better at lower kinetic energies, since the uncertainty is in angle.

3.2.2 Surface Sensitivity

Perhaps the greatest limitation of ARPES (or power depending on your experimental goals) is the extreme surface sensitivity. As mentioned before, this stems from the fact that we are interested in the electrons that escape from the surface without scattering. This means electrons that are excited within roughly the mean-free path of an electron for a given kinetic energy, which is generally quite short (see Fig. 3.8). For ARPES measurements carried out with light in the 10 to a few hundred eV, the mean-free path is $\lesssim 1$ nm, which is less than or on the order of a single lattice constant. Even for laser ARPES experiments that are carried out at 6 eV and are thus much more bulk-sensitive, the mean free path is still only a few nm. Alternatively, really high energy photons can be used to probe further into the bulk, but at the sacrifice of energy resolution, as mentioned above. Additionally, it should be obvious that an extremely rough or dirty surface no longer posses the translational invariance along the surface that leads to the conservation of in-plane momentum, which is critical to the angle-resolved part of ARPES. Together, these facts mean that

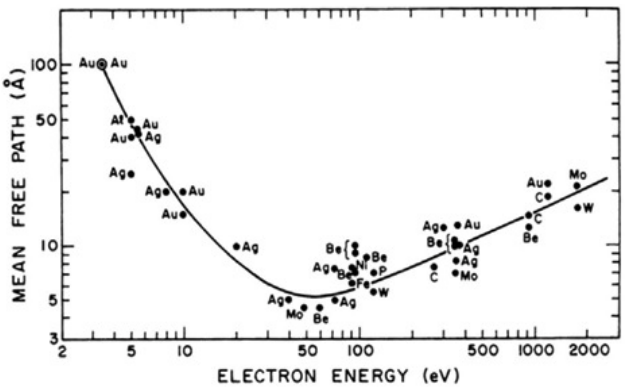

Figure 3.8: The dots represent measured mean-free paths at various electron kinetic energies, while the line is a fit, representing the "universal" mean-free path of electrons. Figure Copied from [36].

ARPES requires extremely clean, flat, and uniform surfaces. Note that the surfaces usually must be prepared in vacuum, because exposure to atmosphere for even a few seconds renders surfaces too disordered to study with ARPES.

There are several common ways to achieve the surface quality required for ARPES. First and most common, a rod may be glued to the surface of the sample, which can be hit with an in vacuum, moveable arm to remove the post. If you are lucky, this will cause the sample to cleave along a particular plane, revealing a pristine surface. However, it is common for this process to pull the entire sample off of the sample mount or to reveal a rough surface that is not suitable for ARPES. In general, the success of this process depends on the chemistry of the sample and a bit of luck. For example, layered materials bound by Van der Waals forces come apart easily, while 3D materials with ionic bonds holding together the material often cleave very poorly. Second, surfaces may be prepared by successive rounds of sputtering to remove the top layers exposed to atmosphere and annealing to relax the surfaces back into uniform and flat surfaces. However, this method usually requires a significant amount of trial and error to develop a material specific recipe and does not always work. Third and most relevant to the present thesis, the sample may be grown with a pristine surface using molecular beam epitaxy. However, exposure to air would destroy the surface. So, either the material must be grown in a chamber attached to the ARPES chamber, or the material must be capped with a protective layer of material. In the latter case, the cap must

then be removed somehow, prior to measuring. So, it is common to use a material like amorphous As that boils off of the surface at a temperature low enough to leave the material and its surface undisturbed.

In general, the need for a pristine surface renders ARPES measurements on many materials completely impossible.

3.2.3 ARPES Data Analysis

The primary goal of ARPES data analysis is to extract the spectral function and/or its components, namely the fully renormalized band structure and the lifetimes/scattering rates of the states. As we discussed before, the band structure is related to peak positions, while the lifetimes are related to the widths in energy of the peaks.

There are many approaches to extracting this information from ARPES data, but I will discuss the primary three methods. Note, although ARPES can be a 4-dimensional data set (intensity as a function of 3 momenta and energy), it is acquired as a series of 2D images (intensity as a function of momentum along the slit and energy), so it is natural to perform analysis on each 2D image individually. Furthermore, to perform peak fitting, it is convenient to break 2D ARPES images up into a series of 1D line cuts along either energy at a constant momentum (energy distribution curve or EDC) or momentum at a constant energy (momentum distribution curve or MDC) (see Fig. 3.9 for an example of an MDC and EDC extracted from a 2D ARPES image). It is easier to perform the peak fitting on 1D EDCs or MDCS; however, the brave among us have engaged in the third approach, "2D fitting", where an ARPES image (intensity as a function of one momentum and energy) is fit directly all at once. In fact, I even once attempted to fit a full 3D map at constant photon energy (intensity as a function momentum along the slit, momentum perpendicular to the slit, and energy) all at once, but this is very complicated due to the matrix element effect.

In all cases, one usually tries to fit their data using a model based on Eqn. 3.23, but the level of detail of the model used depends on what is being studied. For example, if one just wants to extract peak locations, then the details of the self-energy are less important; however, if one wants

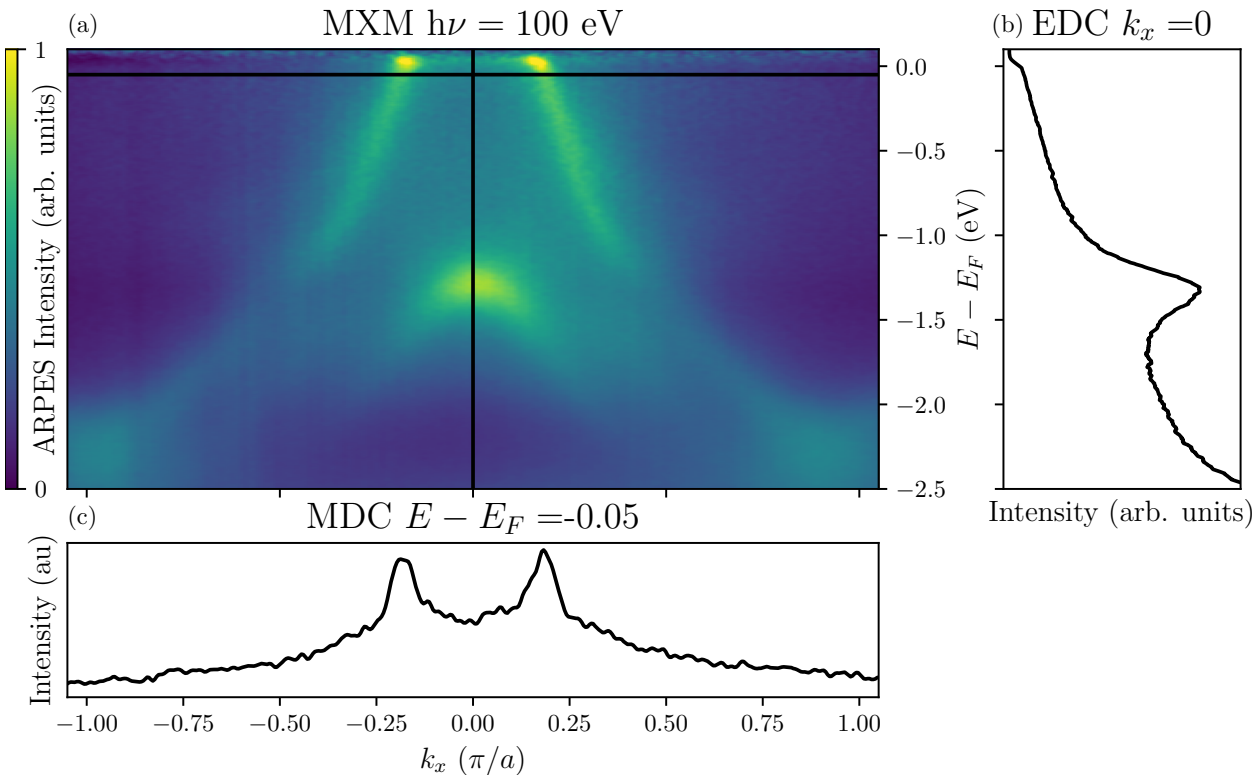

Figure 3.9: ARPES image with an EDC and MDC shown: a) ARPES data taken along the MXM cut from CuMnAs at hν=100eV [same data as 3.1(b)] but with different min and max color scale. All MDCs are normalized by their intensity in this data. Black lines show locations of EDCs and MDCs. b) EDC through the ARPES image without normalization by MDC intensity. c) MDC through the ARPES image without the normalization by MDC intensity.

to study lifetimes and other more subtle effects, then a more detailed model must be put forth. In my opinion, the hardest factor to account for is the matrix element effect, because there is no universal model for this, and while it can be simulated numerically with a good theoretical model of the band structure, one is often trying to extract and understand the band structure in the first place. So, in practice, the matrix element is often either assumed to be constant or modeled ad hoc to capture the observed spectral intensity changes ascribed to a matrix element effect. Meanwhile the Fermi function is easily added to a model, and Gaussians can be convolved with the model to capture the resolution effects; however, distinguishing between the widths from the resolution effects and those of intrinsic broadening due to self-energies can be a challenge. Therefore, one ideally knows the resolution of their measurements, rather than fitting these parameters. Often a linear background is enough, but a Shirley background [37] can be used when being more precise.

Finally, the object of primary interest: the spectral function (Eqn. 3.17). When fitting line cuts, MDC fitting is often preferred because the self-energies, Fermi function, and background are usually not very momentum dependent, while they are highly energy dependent. This means that when fitting an EDC, one must come up with a suitable functional form that accounts for the variation with energy; however, for MDC fitting, these complex functions are converted to simpler constants at a given momentum (e.g. a constant width of a peak). However, to relate the width in momentum to a width in energy that corresponds to a lifetime, $\Delta E = \frac{\partial E(k)}{\partial k}\Delta k = v(k)\Delta k$, where $E(k)$ is the fully renormalized band structure. This means one must take the additional step of extracting band velocities, but this is not too difficult. Due to the energy dependent terms, the Lorentzian shape in energy is often obscured, and the MDC peaks actually follow a Lorentzian more closely (as seen in Fig. 3.9); however, the line shape of an MDC peak should only truly be Lorentzian for a linearly dispersing band. When performing 2D fits, one must come up with a full model of the band structure and self energy, with suitable fitting parameters. Although more challenging, when done correctly one extracts directly the self-energy and the band structure all at once, usually with far fewer fitting parameters.

The above highlights the primary goals of ARPES data analysis, but it should be said that

ARPES contains more information than just lifetimes and dispersion. For example, matrix element effects can reveal orbital content of the bands. Superconducting gaps can also be measured as discussed in Ch. 5, and surface reconstruction and/or CDW periodicity can be extracted via the q-vector of replicated bands in ARPES. Therefore, ARPES data can reveal quite a bit of information about a material.

3.3 Time-Resolved ARPES

Time-resolved ARPES is an experimental technique in the broader class of pump-probe spectroscopies. Pump-probe spectroscopies utilize a pump to disturb a system and a probe that measures the system. By making measurements with a probe at many times, the dynamics of the system as it recovers from the pump can be studied. In time-resolved ARPES measurements, we are interested in the dynamics of electrons in materials, which are $\mathcal{O}(fs - ps)$, which is way too fast for even modern electronics. This problem has been solved with ultrafast lasers that provide pulses of light with widths in time of $\mathcal{O}(fs - ps)$, which are used for the pump and the probe in ultrafast pump-probe techniques, including our time-resolved ARPES system. The pulses are sent along different spatial paths to a sample being studied, where one path has a variable delay, allowing the relative arrival time of the pulses to be swept from the probe arriving first ($t < 0$) through simultaneous arrival ($t = 0$) to the probe arriving after the pump ($t > 0$). The lasers put out many nearly identical pulses at regular intervals that are much longer than the relaxation time of the material, allowing data acquisition at each relative arrival time to average over many pulses and thus times long enough to make measurements. By making measurements at many relative arrival times (variable delays), the dynamics can be reconstructed.

The time-resolution of these ultrafast pump-probe techniques is related to how far the pulses must be separated in time to distinguish them from overlapping, which is related to the full-width at half-max (FWHM) of the pulses in time. Due to Heisenberg, the FWHM in time is inversely proportional to the FWHM in energy, meaning very good time resolution comes at the cost of poor energy resolution. That is, a fast pump might excite many modes of the system, and a fast probe

sacrifices energy resolution of the ARPES measurement. Therefore, one must choose the energy resolution and time-resolution based on the dynamics one wants to study. We are interested in resolving superconducting gaps $\mathcal{O}(10$ meV), which exist for $\mathcal{O}$(ps), which is challenging but in-principle doable, fortunately. Another limitation of energy resolution when using ultrashort pulses is space-charge, which can limit the number of photoemitted electrons per laser pulse to $\mathcal{O}(1)$. This makes data acquisition times very long.

In a time-resolved ARPES experiment, one needs a high photon energy ultrafast probe to conduct the experiment. This is quite challenging. Nonlinear optics techniques can be used to upconvert laser light, but these process fall of as $|\vec{E}|^n$ for the n-th harmonic created, making bright high photon energy sources from lasers a challenge. Nevertheless, nonlinear crystals can be used to create bright enough sources, but the highest photon energy attainable at reasonable fluxes is limited by the band gap of the material, $\mathcal{O}(7eV)$, after which reabsorption greatly limits the photon flux achievable. These lower energy probes restrict the region of momentum space that can be studied to less than the full Brillouin zone in most materials. Higher photon energies are available by nonlinear conversion in gas (HHG); however, since a gas is much less dense than a solid and this represents higher harmonics (larger n), the fluxes are usually quite small, which are further reduced by monochromatization if one wants to achieve good energy resolution, making these systems a challenge as well. Finally, one can try to use sources generated by electron oscillations for the probe. However, normal synchrotron electron bunches are pretty long in time $\mathcal{O}(10ps)$, limiting their time resolution. X-ray free electron sources improve the time resolution, but they struggle to maintain constant photon flux pulse to pulse, which makes space charge effects difficult to deal with. All of the above techniques present pros and cons, but we chose a 6 eV probe that is a fourth harmonic of our laser, because it provides high flux and good energy resolution, making it suitable for our experiments that do not require access to the full zone.

Another challenging aspect of time-resolved ARPES is due to the practical requirement that the laser pulses overlap in space and in time on the material. Since our time delay stage is $\mathcal{O}(100$ mm) and our laser paths are around 10 m, we need the paths to be the same to within

1% to ensure that $t = 0$ is on our delay stage. That is a pain in the ass. However, by carefully measuring and then taking long scans of our stage with a sample that has a strong signal, this can be done. Spatial overlap of the beams is also a challenge, but it can be achieved by aligning the pump and the probe to the same $\mathcal{O}(100\ \mu\text{m})$ scratch in a dagged copper puck. The pump photoemits from the copper due to multi-photon absorption, which is strongly suppressed by the dag. multi-photon absorption also enhances the UV probe photoemission. So, although a pain, this can be accomplished, but it becomes exceedingly difficult when the pump pulse becomes weak (see discussion of window in a window in Ch. 6).

In terms of interpreting time-resolved ARPES data, the discussion of this chapter continues to apply, at least to first order. Although, of course, now we are measuring a spectral function from a non-equilibrium system at a time defined relative to the perturbing pulse. However, often after a very fast thermalization time [$\mathcal{O}$(fs)], the electronic system can be considered to be in thermal equilibrium, even if it is not in equilibrium with the rest of the system, e.g. phonons.

3.4 Conclusion

We have seen that ARPES is a powerful tool that reveals lots of rich information about the electronic structure of materials, particularly the one-electron removal spectral function. Time-resolved ARPES promises the chance to gain similar information about the dynamics of materials, although it remains a technically very difficult experiment, limiting the number of successful high impact experiments to date.

Chapter 4

Electronic Structure of CuMnAs, a Candidate Antiferromagnetic Dirac Semimetal

4.1 Introduction and Review of Prior Work

CuMnAs has emerged as an exciting material, both for spintronic applications [16, 38] and the study of anti-ferromagnetic (AFM) Dirac materials [1, 39, 40]. CuMnAs has a combined inversion and time reversal symmetry, $\mathcal{PT}$, that connects two oppositely oriented magnetic Mn sublattices with a Néel temperature ∼480 K [see Fig. 4.1(a)] [4, 41]. As we discussed in Ch. 2, Sec. 2.2, current driven through CuMnAs can efficiently reorient the Néel vector via a spin orbit torque. This was theoretically predicted [1, 42] and experimentally confirmed in CuMnAs and in another $\mathcal{PT}$ symmetric antiferromagnet, Mn_2Au [16, 43–46]. It has also been suggested that heating effects may assist the switching by helping to overcome energy barriers [46]. Additionally, current induced thermal gradients add not only heat but strain, which caused thermomagnetoelastic switching to dominate in an insulating AFM [47]. In any case, the Néel vector reorientation in CuMnAs was directly imaged using photoemission electron microscopy with x-ray magnetic linear dichroism providing contrast [43].

Control over the Néel vector allows manipulation of some electronic properties of CuMnAs. First, the presence of magnetic order gives rise to an anisotropic magnetoresistance (AMR). Therefore, the resistivity along the a lattice direction can be modulated by orienting the Néel vector to be perpendicular or parallel to a, for example. Wadley et al. made such a device out of a thin film of tetragonal CuMnAs and used the AMR signal to demonstrate the electrical switching of

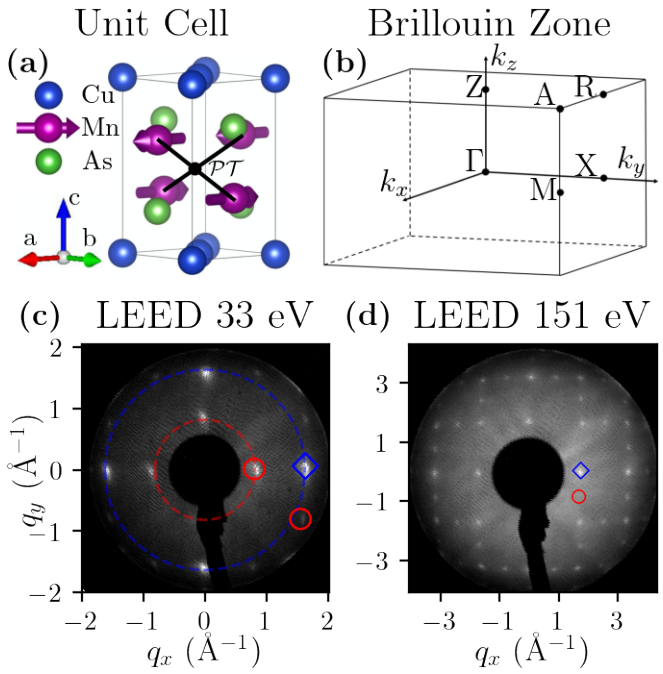

Figure 4.1: CuMnAs unit cell, Brillouin zone, and LEED: (a) Real space unit cell depicting the magnetic moments on the Mn atoms with arrows. (b) Tetragonal Brillouin zone, labeling high symmetry points. (c&d) LEED patterns from a decapped sample taken with 33 eV and 151 eV electrons, respectively. The blue diamond encloses an expected peak from tetragonal CuMnAs, while the red circles enclose extra peaks from 2x1 and 1x2 surface reconstruction domains. (c) The blue (red) dashed circle is drawn with a radius of $\frac{2\pi}{a}$ ($\frac{2\pi}{2a}$) where a is the in-plane lattice constant of CuMnAs.

the Néel vector [16]. The electrical switching was even shown to be scalable to THz speeds [44]. However, the true origins of the observed resistance changes in similar devices has been shown to include or even be dominated by electromigration and the Seebeck affect due to large thermal gradients [48–50]. Additionally, in multidomain AFMs like CuMnAs, domain migration can impact the observed changes in resistivity due to domain wall magnetoresistance [51]. Second, as we discussed in Ch. 2, Sec. 2.1.1, Šmejkal et al. pointed out that the $\mathcal{PT}$ symmetry provides doubly degenerate bands, which allows for the existence of antiferromagnetic Dirac fermions close to or at the Fermi level [1]. Additional off-centered or nonsymmorphic crystallographic symmetries can protect the massless Dirac fermions. The presence or absence of these symmetries can be controlled by reorienting the Néel vector resulting in tunable masses of the Dirac fermions. And, as discussed in Ch. 2, Sec. 2.3, opening and closing of the Dirac mass gap allow a much stronger topological AMR [1, 45], which has yet to be demonstrated because the Fermi energy is not at the Dirac points in tetragonal CuMnAs.

Both the tetragonal and orthorhombic phases of CuMnAs have been studied theoretically and experimentally. All of the above interesting properties are believed to be present in both structural phases. Additionally, the orthorhombic phase is proposed to host a new topological metal-insulator transition, due to the predicted presence of a bulk Dirac point at E_F and lack of other bands crossing E_F [1].

Density Functional Theory (DFT) has been critical to the development of the above theoretical predictions, but it has only been experimentally tested to a limited extent in tetragonal CuMnAs: the AC permittivity (determined from ellipsometry) and UV photoemission spectroscopy were studied [52]; neutron diffraction and x-ray magnetic linear dichroism were used to study the magnetic ordering [3]; and, more recently, experiments using scanning tunneling microscopy elucidated the surface termination of thin films of tetragonal CuMnAs, discovering the existence of As step edges which may host surface reconstructions [53]. These experiments were compared to DFT predictions; however, there exist no direct comparisons to the band structure calculated from DFT. Furthermore, DFT is known fail in the presence of strong correlations, because we only have

approximations to the electronic exchange correlation functional. Since we are interested in the AFM phase of CuMnAs, the correlations will be critical to the electronic structure, meaning standard DFT will fail; however, in some cases, it is possible to account for the correlations using an ad hoc parameter, U, to account for on-site repulsion between electrons. Although this works in some cases, it does not work in all cases, and even if it does work for CuMnAs, quantitative predictions would depend on the precise value of U, which is unknown a priori. Therefore, a thorough comparison of the electronic band structure of CuMnAs from DFT and experimental measurements is needed to ensure the applicability of DFT and extract a U value, if applicable.

We directly measure the band structure with high resolution ARPES measurements and provide a detailed comparison to DFT. Additionally, we find surface reconstructions and a chemical potential shift.

4.2 Theory Selection

We show the crystallographic and magnetic structure of the tetragonal phase of CuMnAs in Fig. 4.1(a). The nonmagnetic space group is nonsymmorphic (P4/nmm). Since the magnetic Mn atoms are light, the effects of spin-orbit coupling on the band-structure are highly perturbative and smaller than our resolution can detect, unlike in strongly relativistic $\mathcal{PT}$ antiferromagnet Mn_2Au [54]. Therefore, in the antiferromagnetic state the nonrelativistic spin group ($P14/^2n^2m^2m$) describes the main energy scales of our measured band structure, including Fermi surfaces [55]. However, within $\sim$10 meV of a Dirac point, the fermion masses are required to accurately describe the electronic dispersion, and to calculate the Dirac fermion masses, spin-orbit coupling must be included and the relativistic magnetic symmetry group (Pm'mn) with generators $\{C_{2x}|\frac{1}{2}00\}$, $\{M_y|0\frac{1}{2}0\}$, and $\mathcal{PT}$ must be employed.

To model the electronic structure of tetragonal CuMnAs, my labmate Peipei Hao and I performed DFT+U calculations, using the Generalized Gradient Approximations (GGA) with the Coulomb interaction U applied to the Mn 3d orbitals, using Dudarev's implementation [56–58] (see Sec. 4.5 for a complete description of our DFT). To illustrate the effects of including spin-orbit

coupling (SOC) on the Fermi surface, 3D Fermi surfaces are plotted with PyProcar [59] in Fig. 4.2 with and without SOC included in the DFT calculations. The Fermi surfaces are plotted at the stoichiometric Fermi energy determined from DFT and at our experimental E_F, hole doped by 388 meV relative to DFT. The Fermi surface has no visibly discernible distinction between the calculations with and without SOC, which is to be expected for the light magnetic Manganese atoms, because there are no Dirac crossings at the Fermi energy. This explicitly supports the above argument that it is only necessary to account for SOC when calculating fermion masses. Therefore, spin-orbit coupling was turned off for all DFT shown, except in Fig. 4.12(a,b,&c) and Fig. 4.2.

To try to determine the U value that most accurately describes our experimental data, a full comprehensive study similar to what follows in the rest of this chapter was conducted for $U = 0$ (pure GGA) to $U = 10$ eV, but the best chance of bounding the acceptable values of U quantitatively lied in studies of the band dispersing across E_{F} in the $X\Gamma X$ cut, where the bandwidth is quite sensitive to U. Everywhere else, the bands are only slightly perturbed by a changing U, maintaining good qualitative and quantitative agreement with the data. To quantitatively compare DFT to experiment for this cut, I conducted several studies: 1) comparison of the Fermi velocity, 2) comparison of extracted and DFT dispersions, and 3) full 2D Fitting of the $X\Gamma X$ ARPES image. Before diving into the studies, note that $U \lesssim 2$ eV can be ruled out on qualitative grounds, because the band top does not even cross the Fermi energy, as it clearly does in the data. Fig. 4.3(b) includes $U = 1$ eV, which can be seen to not cross E_{F}, while also not capturing the band bottom.

Since there is no Fermi velocity for $U < 2$ eV, I studied v_{F} for $U = 2$ to 5 eV. When extracting v_{F} from DFT, one must study a slice along k_x through k-space at a particular (k_y, k_z). The k_z value corresponding to the photon energy studied was selected by tuning the inner potential to match the dispersion seen in photon energy scans (see. Sec. 4.3.1), and the k_y value was chosen by studying Fermi maps. Next, one has to determine the Fermi energy of experiment in the DFT, which as we will see is not the same as the Fermi energy determined from DFT. To make the shift quantitative and consistent, the chemical potential was shifted to bring the band top at Z in the DFT to the corresponding maximum intensity in the experimental energy distribution cut

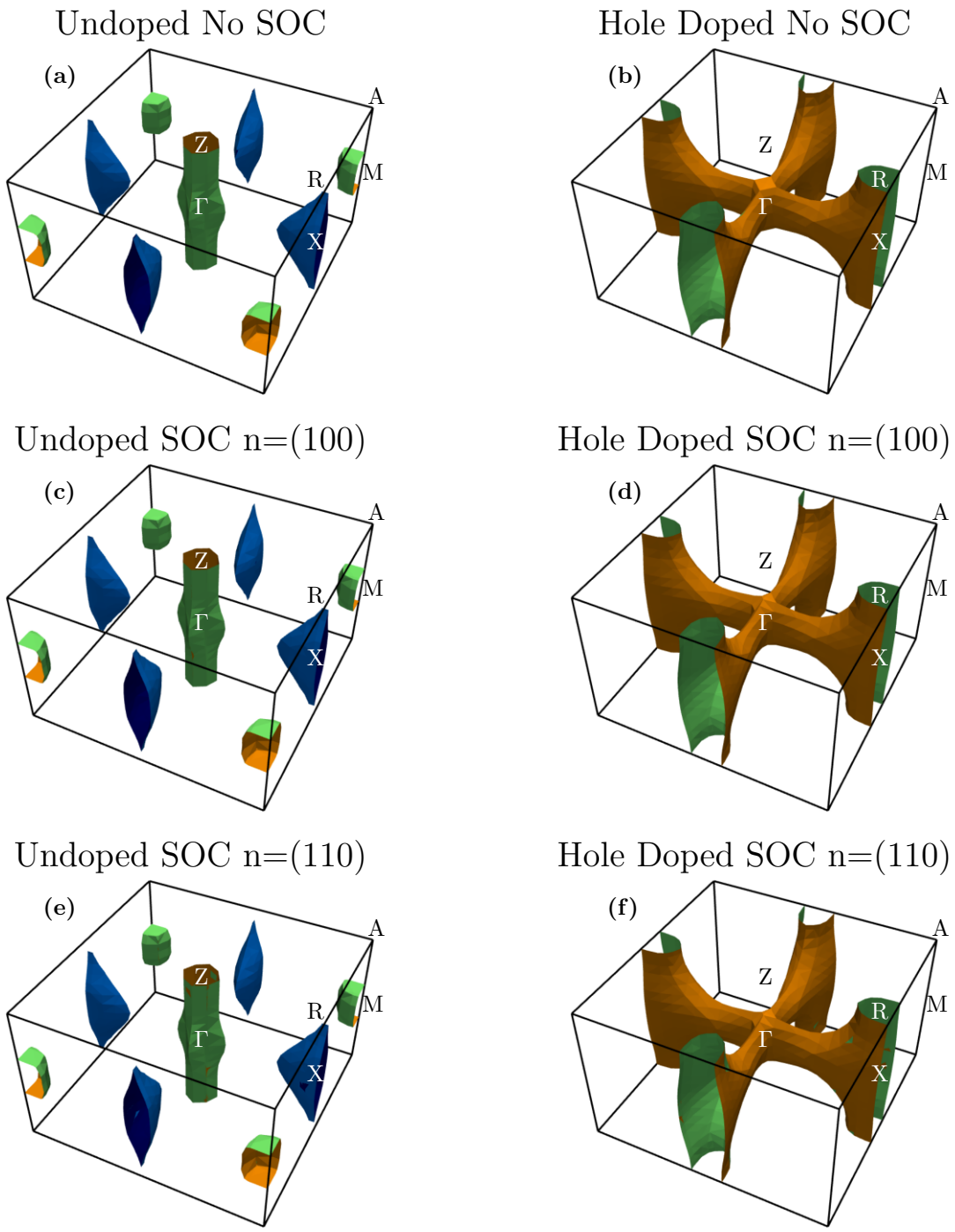

Figure 4.2: Our calculated Fermi surfaces with and without SOC: Three dimensional Fermi surfaces are plotted at the stoichiometric Fermi energy calculated with DFT (a,c&e) and at an energy 388 meV below (hole doping) this energy (b,d,&f), corresponding to our experimental E_F. The Fermi surfaces are from DFT calculations with no spin-orbit coupling (a&b) and with spin-orbit coupling and the Néel vector fixed to the (1,0,0) direction (c&d) and the (1,1,0) direction (e&f). All calculations use GGA+U=2.25 eV, consistent with all other DFT shown, meaning that (a&b) are the same as shown in Fig. 4.7.

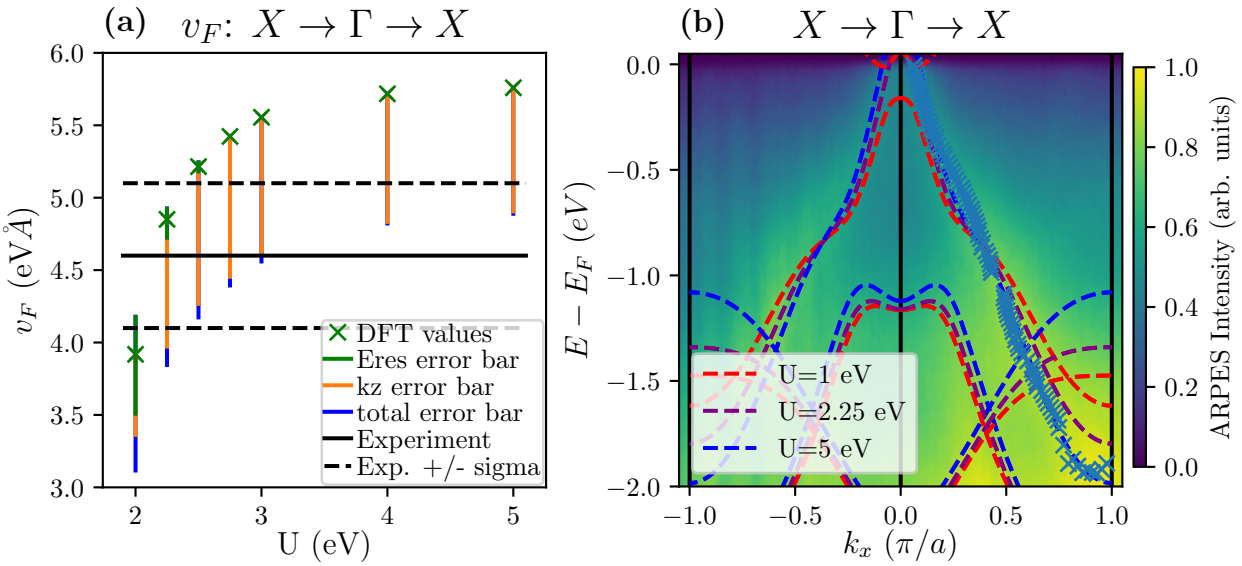

Figure 4.3: Comparison of DFT U to $X\Gamma X$ ARPES data: a) The Fermi velocity extracted from DFT as a function of U as compared to experiment. The black line represents the value extracted experimentally, with the dashed lines representing $\pm\sigma$, where σ is determined from error propagation through the fitting (see. Sec. 4.5.2). The green "x" mark the value at $v_{\mathrm{F}}(k_z, E_{\mathrm{F}})$, where k_z is determined from inner potential fitting and E_{F} is determined from fitting the location of the band top through Z. The green error bars span $v_{\mathrm{F}}(k_z, E_{\mathrm{F}} \pm \sigma_E$. The orange error bars span $v_{\mathrm{F}}(k_z \pm \sigma_{k_z}, E_{\mathrm{F}}$. And, the blue error bars span from min to max of $v_{\mathrm{F}}(k_z \pm \sigma_{k_z}, E_{\mathrm{F}} \pm \sigma_E$. See the text for σ_{E/k_z}. b) Shows the $X\Gamma X$ data with peak positions extracted by piecewise MDC and EDC fitting shown as blue "x's" and DFT dispersion plotted as dashed lines.

(EDC) through Z. In the case of $U = 2.25$ eV, this resulted in the experimental Fermi energy, $E_{\mathrm{F}}^{\mathrm{exp.}} = E_{\mathrm{F}}^{\mathrm{DFT}} - 0.388\mathrm{eV}$, where $E_{\mathrm{F}}^{\mathrm{DFT}}$ is the Fermi energy from the DFT at the corresponding U value, which implies our samples are hole-doped compared to the stoichiometric $E_{\mathrm{F}}^{\mathrm{DFT}}$. Note, the precise shift did depend on the specific value of U used. Finally, with k_y, k_z, and $E_{\mathrm{F}}^{\mathrm{exp.}}$, I can extract the corresponding Fermi velocity from DFT, $v_{\mathrm{F}}(k_y, k_z, E_{\mathrm{F}}^{\mathrm{exp.}})$, which is plotted as the green "x's" in Fig. 4.3(a). This implies that $U = 2.25$ eV is the only U value studied that is consistent with the experimental Fermi velocity extracted from the cut (see Sec. 4.5.2 to see how the Fermi velocities and uncertainty are found). It would be really tempting to conclude that $2 < U < 2.5$ eV; however, one needs to consider the uncertainty in the determined values of k_y, k_z, and $E_{\mathrm{F}}^{\mathrm{exp.}}$ to rigorously bound U. It would be quite challenging (if not impossible) to rigorously propagate the errors through our analysis; so, I simply illustrate the effect of the corresponding uncertainties. For $E_{\mathrm{F}}^{\mathrm{exp.}}$ uncertainty, I used $2\sigma_E = 4k_B T_{eff} = 0.037$ eV extracted from Fermi fitting the edge in the $X\Gamma X$ data studied [see Fig. 4.3(b)] away from any bands, and the corresponding E_{res} error bars span the min/max of $v_{\mathrm{F}}(k_y, k_z, E_{\mathrm{F}}^{\mathrm{exp.}} \pm \sigma_E)$. The energy uncertainty results in a larger uncertainty for v_{F} at lower values of U when the band top is still close to E_{F}. At higher values of U, the top is well above E_{F}, and the band is much more linear near E_{F}. k_z uncertainty is much more subtle and difficult to pin down. I can only put an order of magnitude lower bound on it by considering the Heisenberg uncertainty, $\hbar\Delta k_z \Delta z \geq \hbar/2 \rightarrow \Delta k_z \geq \frac{1}{2\Delta z} \approx 0.2\pi/c = 2\sigma_{k_z}$, where the approximation makes use of the universal curve of the inelastic mean free path to estimate Δz at the photon energy studied. Then, the k_z error bars span the min/max of $v_{\mathrm{F}}(k_y, k_z \pm \sigma_{k_z}, E_{\mathrm{F}}^{\mathrm{exp.}})$. Finally, k_y uncertainty is subdominant and thus ignored, and the total error bars span the min/max of $v_{\mathrm{F}}(k_y, k_z \pm \sigma_{k_z}, E_{\mathrm{F}}^{\mathrm{exp.}} \pm \sigma_E)$. So, we see that the Fermi velocity favors $U = 2.25$ eV but cannot be used to exclude the range of $U > 2$ eV studied, because the error bars, particularly due to k_z uncertainty, cause overlapping of the experimental v_{F} uncertainty range and the theoretical v_{F} range.

To extend the quantitative comparison between DFT and experiment to the full range of binding energies available, I extracted the full band dispersion from the $X\Gamma X$ ARPES data by

piecewise MDC and EDC fitting the data [see Fig. 4.3(b)]. MDC fitting was performed everywhere except near the band bottom, where EDC fitting was required. The MDC fitting was done separately in several regions to allow the model to be adjusted to account for qualitative changes in the data, e.g. the appearance of additional bands near $E - E_{\mathrm{F}} = -1$ eV. With the full dispersion, i.e. a set of peak positions and uncertainties in peak position, σ, I was able to compare the experimental dispersion to the DFT [see Fig. 4.4(a)]. I quantified the difference between the experiment and theory by summing the difference of the peak position in k (E) with the band position in k (E) from DFT at the E (k) where MDC (EDC) fitting was performed. I normalized the difference by the uncertainty in the peak position, σ, found during the fitting process. Since the theoretical bands do not cross E_{F} for $U < 2$ eV, this comparison can only be made for $U \gtrsim 2$ eV as shown. Smaller values of this sum correspond to more similar dispersion between experiment and theory. This metric shows that the band dispersion from larger U values is a better description of the data, which can also be seen qualitatively by inspecting Fig. 4.3(b), where it is clear that the improvement comes primarily from the better agreement in band bottom position. However, again the comparison with theoretical dispersion is made by choosing a slice along k_x at a particular k_y, k_z, and chemical potential shift. The expected values and uncertainties of these parameters are the same as described in the comparison of the Fermi velocity above, and the error bars are generated in the same manner. So, while comparison of the full dispersion favors larger U values, it is not possible to rule out $U > 2$ eV, because the error bars strongly overlap over the full region studied.

In yet another attempt to bound the acceptable values of U, I performed 2D fitting of the $X\Gamma X$ ARPES image, using the dispersion from DFT for both bands present in the ARPES data. Naturally, I based my model off of Eqn. 3.23, using a constant matrix element and a self-energy from Fermi liquid theory. In this case, I was not interested in the widths, nor a perfect fit, but rather just a quantitative comparison of the dispersion from DFT and experiment. Figure 4.5 shows an example of a 2D fitting process for $U = 5$ eV. Clearly there remains systematic sources of error—i.e. features in the data that cannot be captured by my model, namely intensity to the left of the blue curve. This systematic error is largely due to the fact that the data comes from a

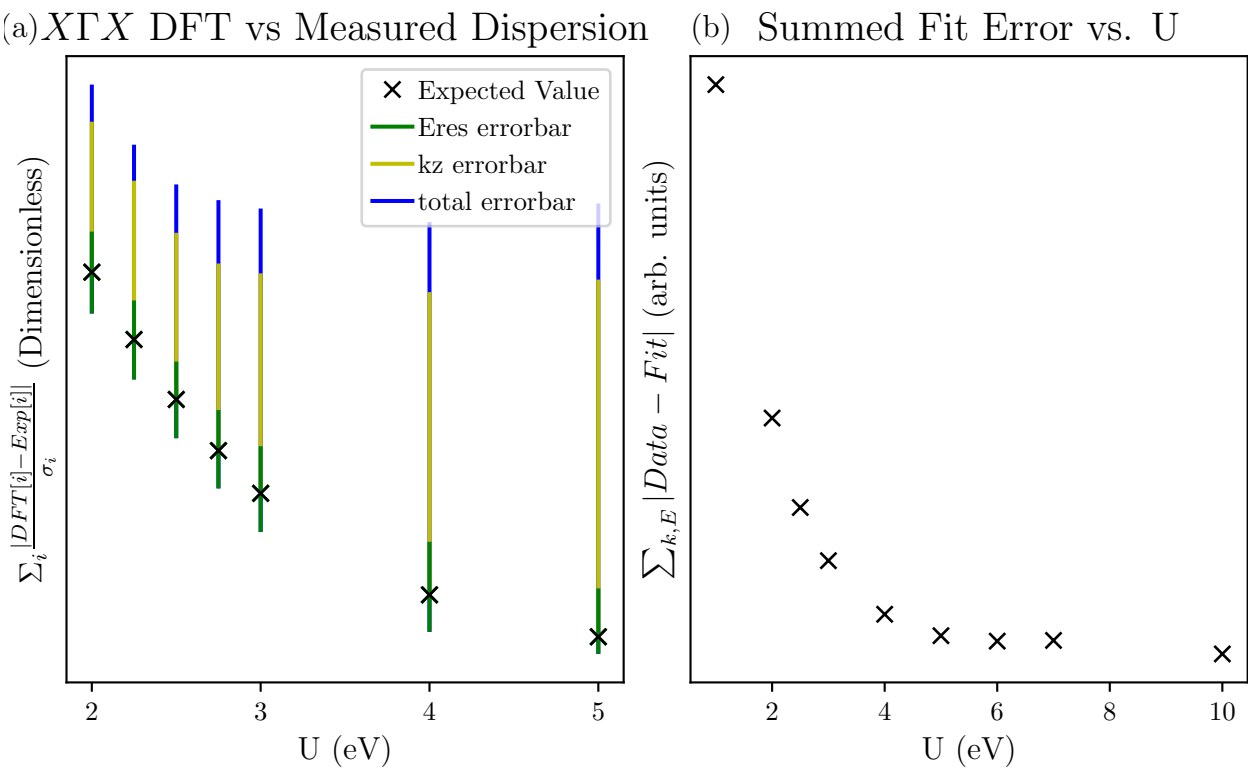

Figure 4.4: Comparison of DFT and experimental $X\Gamma X$ dispersion. a) Comparison of the dispersion extracted by piecewise MDC and EDC fitting of the band in the $X\Gamma X$ ARPES cut [see Fig. 4.3(b)] and the corresponding band from DFT. The y-value is the sum of the absolute value of the difference between the peak position in k (E) determined from MDC (EDC) fitting and the band position at the corresponding energy (momentum) from DFT normalized by the uncertainty of the peak position determined from the fitting process. Lower values correspond to better agreement for the experimental and theoretical dispersion. Error bars are determined in the same manner as in Fig. 4.3. b) The sum of the difference in the absolute value of the data and a full 2D fit of the data, using both bands from the DFT to simulate the $X\Gamma X$ ARPES data.

distribution of k_z values due to k_z uncertainty, while my model again takes only one cut through the DFT. As these bands disperse in k_z they largely sweep through the regions to the left of the blue curve. Additionally, the upper right corner of the orange band sweeps along the position of high intensity to the left of the orange curve, probably also explaining the apparent mismatch here. In any case, I am just after a quantitative comparison of the DFT that I can explore as a function of U, which is shown in Fig. 4.4(b). This is a sum over images similar to 4.5(d) for each U value. Unsurprisingly this shows a qualitatively similar distribution as a function of U to Fig. 4.5(a), favoring higher U values primarily to capture the lower seeming band bottom in the data. This type of analysis does not require that the band cross the Fermi energy, so I include $U = 1$ eV, which is unsurprisingly significantly worse, and I also extended the values of U to 10 eV to try to find a turning point and plausible upper bound, but this did not happen. Again there is uncertainty in the choice of k_y, k_z, and chemical potential shift, which is not shown in this figure since it is so similar to Fig. 4.5(a), which again precludes a tighter bound on U than $U \gtrsim 2$ eV. Also, although I do not show the results, a similar 2D fitting scheme for a crop region of the image around just the Fermi energy actually favors $U = 2.25$ eV, consistent with the Fermi velocity comparison study.

After all of this analysis, we can safely rule out $U \lesssim 2$ eV for failing to even qualitatively capture the dispersion. Furthermore, comparison of v_{F} favors $U \sim 2.25$ eV, while the bandwidth/band bottom location favors larger $U \gtrsim 4$ eV. However, accounting for reasonable uncertainty, particularly in k_z, leaves us with $U \gtrsim 2$ eV as the best experimental bound that we can place on U, with all values yielding good qualitative agreement with experiment. Perhaps an upper bound based on physical grounds is possible, but this would not be a very tight, nor rigorous, bound, since U is a phenomenological parameter. This is perhaps why most studies do not go to the lengths that I did to bound the U value quantitatively in the first place. Instead, it is common to put forth the best U value on more qualitative grounds.

Nevertheless, it is useful to put forth the "best" single theory. To this end, one needs to consider which metric is most robust and most important. Naturally, the electronic structure near the Fermi energy is vastly more important than the structure ~ 2 eV below the Fermi energy,

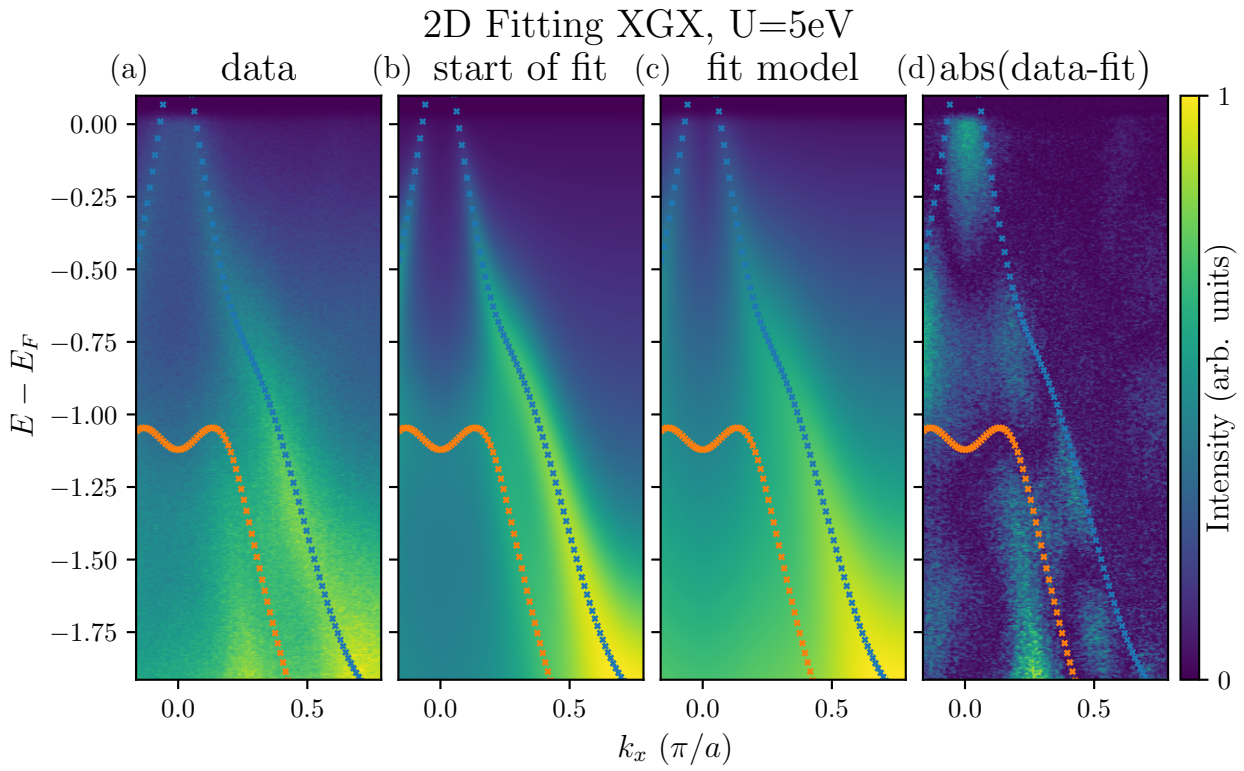

Figure 4.5: Example of 2D fitting of the $X\Gamma X$ ARPES data at $U = 5$ eV: a) Shows the data. b) Shows the model at the starting parameters of the fit. c) Shows the resulting best fit model. d) shows the absolute value of the data-fit, which was also the objective that was minimized. a-d) blue and orange curves show the dispersion from DFT.

because the structure within k_BT ($\sim$ 25 meV for room-temperature) of E_F dominates much of the physics, e.g. transport. Furthermore, as we will see shortly, bands are replicated due to a 2x1+1x2 surface reconstruction, and in the $X\Gamma X$ cut, the replicated bands would skew the band-bottom lower than from just the non-replicated bands in the cut. Since the band broadening is large at the deep binding energies near the band bottom, it is hard to distinguish primary from replicated bands and rule out this possibility. Thus, the band bottom location of the primary band is hard to determine conclusively, making the 2D fitting and comparison of the full dispersion less reliable, since they primarily preferred larger U values due to the band bottom position extracted from EDC fitting.

Therefore, the best and most reliable agreement with DFT was found for $U = 2.25$ eV, which relies primarily on the more robust and important comparison of Fermi velocities in the $X\Gamma X$ cut. It was necessary to apply ≈ 390 meV of rigid hole doping to the chemical potential from theory, i.e. the experimental Fermi energy was found to be equal to the theoretical Fermi energy -390 meV. Possible origins of the energy shift will be discussed. Therefore, unless explicitly discussed, all of the DFT shown in the rest of this chapter is from $U = 2.25$ eV and has been plotted after applying the above mentioned rigid chemical potential shift.

4.3 Experimental Results and Comparison with DFT

After decapping, LEED was performed **in situ**, revealing a well ordered surface with reconstructions [see Fig. 4.1(c&d)]. The (001) surface of tetragonal CuMnAs should produce a square reciprocal lattice with edge lengths of $2\pi/a$, where a is determined from XRD to be 3.85 Å. This is seen in the LEED patterns; however, there are additional spots at the midpoints along the edges of the squares, suggesting the presence of 2x1 and 1x2 surface reconstruction domains. The reconstruction is confirmed by observing that the first order Bragg peaks occur at a radius of $2\pi/2a$, where without a reconstruction they would occur at $2\pi/a$ [see Fig. 4.1(c)]. Despite the surface reconstruction, the LEED pattern is sharp, indicating a successful decap. Samples were subsequently transferred into the ARPES chamber, maintaining an ultra-high vacuum environment from decap

to ARPES data acquisition.

4.3.1 k_z Dispersion

To find the photon energies that represent the symmetry planes of the Brillouin zone, the k_z dispersion was acquired by measuring along the $X \rightarrow \Gamma \rightarrow X$ high symmetry line while scanning the photon energy, $h\nu$, over the range 70-125 eV in steps of 1 eV, using p-polarized light. At these energies, the photon momentum may be neglected, yielding [23]

$$k_z = \sqrt{\frac{2m_e}{\hbar^2}(h\nu - \Phi - E_b + V_0) - k_x^2 - k_y^2}, \tag{4.1}$$

where $\Phi = 4.5$ eV is the work function, E_b is the binding energy, k_x (k_y) is the in-plane momenta along the a (b) direction of the lattice, and V_0 is the inner potential. The series of spectra over the photon energy range may be stitched together to yield the k_z-dispersion in the plane containing the $X \rightarrow \Gamma \rightarrow X$ cut (Fig. 4.6). From Eqn. 4.1, it can be seen that changing V_0 offsets the spectrum in k_z. Thus, the inner potential was tuned to produce the expected k-space periodicity in k_z, yielding $V_0 = 15$ eV.

With the appropriate k_z dispersion, the DFT can be overlaid onto the data as seen in Fig. 4.6(b). The fundamental DFT captures the diamond-like structure enclosing Γ quite nicely; however, there are additional features near $k_x \approx 1.8$ and $2.2\pi/a$ that do not disperse in k_z. These 1D features are nicely explained by the same 2x1 replication seen in the LEED, Fermi surfaces, and the $R \rightarrow Z \rightarrow R$ symmetry cut (see Sec. 4.3.4). This is visually illustrated in Fig. 4.6(b) by overlaying the replicated DFT in red. The non-dispersing feature can be identified as the replication of the $k_y = \pi/a$ plane of k-space onto the $k_y = 0$ plane. The circular pieces of the DFT are from the bands that make the tips of the ellipses in the $k_z \approx \pi/c$ Fermi surface, which for the polarization shown are suppressed by the matrix elements (see Sec. 4.3.2).

In addition to testing the DFT against dispersion in k_z, determining the inner-potential, as done here, determines the k_z value of any particular photon energy at k_x,k_y. In this way, the k_z values of the data are labeled, using an "$\approx$" to acknowledge that the k_z value is not constant

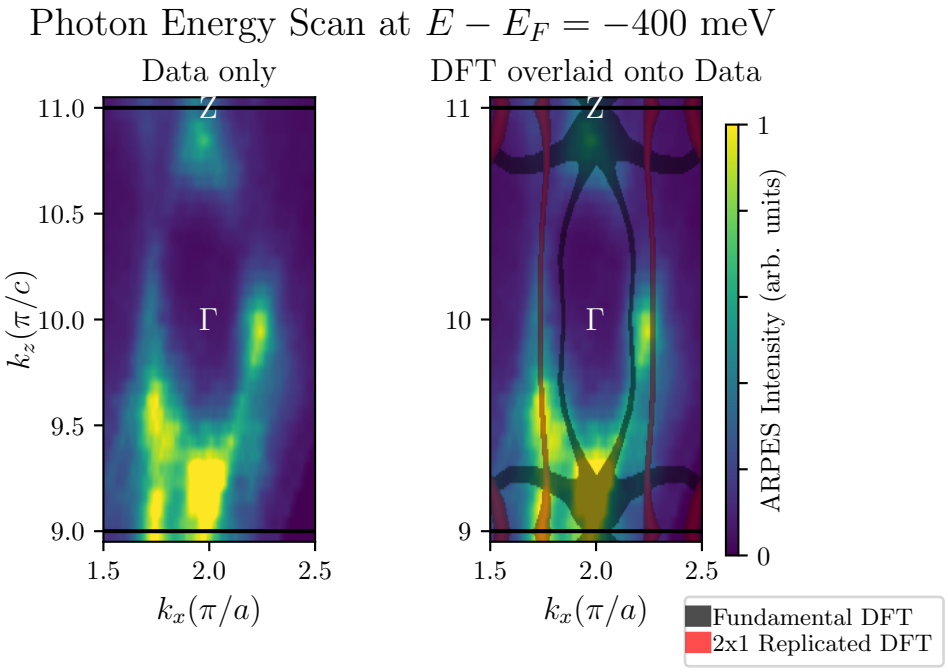

Figure 4.6: k_z dispersion: (a&b) Experimental data taken at ALS MERLIN ARPES. Using p-polarized light, photon energies were scanned between 70-125 eV while taking the $X \to \Gamma \to X$ cut; however, the data shown here is cropped to a single Brillouin zone (black box). Photon energies and angles are converted to k_z and k_x using an inner potential of 15 eV. High symmetry points are labeled in white text. (b) Same data as (a) but with the fundamental DFT overlaid in black transparency and the 2x1 replicated DFT overlaid with red transparency.

across a cut nor Fermi surface and that the precise value from Eqn. 4.1 is not exactly 0 or π/c for the photon energies used. The k_z values used to plot the DFT are labeled as approximate when the value from Eqn. 4.1 is used, yielding a slightly different value from the representative value listed. Furthermore, the exact distribution of k_z values that contribute with varying strength to the spectral weight depends on the matrix elements and the details of the sample surface, yielding crisp dispersion in some zones for some bands and not for others. That is to say that determining the precise k_z uncertainty for any particular cut is not practical. Hence a regular appeal to contributions from multiple k_z values to explain spectral weight in various E-k cuts and Fermi surfaces.

4.3.2 In-plane Fermi Surfaces

The in-plane Fermi surface was measured at $k_z \approx 0$ [see Fig. 4.7(c)] and $k_z \approx \pi/c$ [see Fig. 4.7(d)], which may be selected by tuning the photon energy (see Sec. 4.3.1). In this case, the zone center data were taken with 85 eV photons, whereas the zone edge data were taken at 100 eV. For comparison, the undoped and doped Fermi surfaces from the DFT are shown in Fig. 4.7(a) and Fig. 4.7(b), respectively. It is clear that the undoped Fermi surface does not agree with experiment. For example, there are no pockets near the M points. However, after lowering the chemical potential of the DFT by ≈ 0.390 eV (rigid hole doping), all of the qualitative and even quantitative features of the experimental Fermi surface are consistent with the bulk DFT calculations. To illustrate the qualitative agreement, the hole doped Fermi surface is overlaid on the data in Fig. 4.7(e&f). They both show a propeller-shaped Fermi surface in the $k_z \approx 0$ plane and ellipses at the R points in the $k_z \approx \pi/c$ plane, with the experiment and theory displaying a very similar shape and size of these features.

There are, however, three subtle effects that might naively appear as qualitative discrepancies between the experiment and theory: First, unlike the DFT, the data shown in Fig. 4.7(d&f) does not have C_4 symmetry. While turning on spin-orbit coupling and a Néel vector orientation in the DFT would break this symmetry, the effect is too small to explain the data or even detect (see Fig. 4.2). Instead, it is primarily the transition matrix element that is known to modulate the

ARPES spectral intensity that is responsible for breaking the C_4 symmetry in the data, which will be discussed in detail below, and in fact, a detailed analysis of this matrix element effect reveals the orbital character of the Fermi surface. Second, due to the inherent surface sensitivity of ARPES and lack of translational symmetry perpendicular to the surface, ARPES spectra from any photon energy can contain contributions from multiple k_z values. This explains the closed ellipses near the X points in Fig. 4.7(c) and some of the weight at $k_x = 0$ near the Z point in Fig. 4.7(d). This point is visually illustrated in Fig. 4.7(e) by overlaying the DFT from a second k_z value (orange transparency) that is $0.35\pi/c$ away from the anticipated k_z value (red transparency). Third, there is extra spectral weight near the Z point in Fig. 4.7(f) indicated by white text, which is identified as a replica of the vertical ellipses enclosing the zone edges at $k_x = 0$. The back-folding of this ellipse onto Z is the analogue of the 2x1 surface reconstructions observed in the LEED and will be analyzed quantitatively in Sec. 4.3.4.

As discussed in Ch. 3, Sec. 3.1.5, the matrix element can send the ARPES spectral intensity to 0 for measurements made in a mirror plane. This effect can be seen in the experimental Fermi surface in the $k_z \approx \pi/c$ plane (see Fig. 4.8). Building off of the selection rules derived and summarized in Eqn. 3.22, we can use the suppression of the spectral weight in the Fermi surface to determine the orbital content of the bands. Taking the yz plane as the mirror plane, s-polarized light, $\boldsymbol{\epsilon} = \hat{\boldsymbol{x}}$, is polarized perpendicular to the mirror plane, and therefore, only initial state wave functions with odd symmetry (antisymmetric) with respect to the yz mirror plane may be emitted. On the other hand, p-polarized light lies in the yz plane, and thus initial state wave functions that are odd will not be emitted in this mirror plane. With this in mind, the data clearly implies that the bands at $k_x \approx 0$ must be odd with respect to the yz plane, which includes the p_x, d_{xy}, and d_{xz} orbitals.

The DFT can be further scrutinized by comparing the orbital projection from the DFT to the polarization dependence of the experimental data. In Fig. 4.8(b), the Fermi surface is projected onto the odd orbitals with respect to the yz plane from the DFT. In Fig. 4.8(d), the same plot is shown but for the even orbitals: s, p_y, p_z, d_{yz}, d_{z^2}, and $d_{x^2-y^2}$. The DFT clearly shows the states

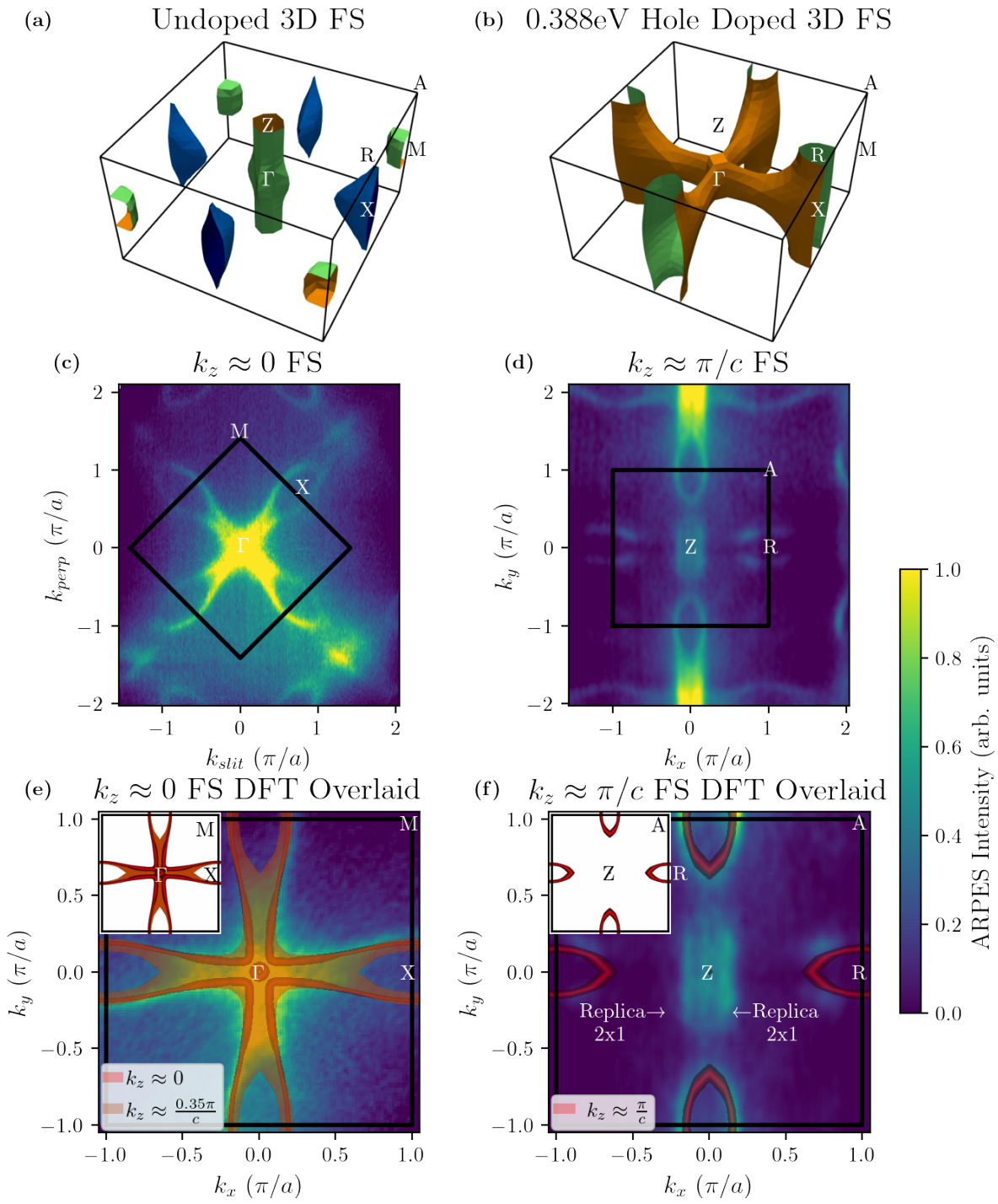

Figure 4.7: Fermi surface: (a&b) 3D Fermi surfaces from the DFT plotted with PyProcar [59]: (a) undoped and (b) hole doped. Unsymmetrized Fermi surface data taken with 85 eV (c&e) and 100 eV (d&f), linear vertically polarized photons. (c-f) The same data is shown twice. The black box depicts the Brillouin zone boundary. The data is from the CuMnAs01 sample. (e&f) Because the undoped DFT does not match the experimental data, the hole doped DFT is overlaid with a transparency. The insets show only the hole doped DFT.

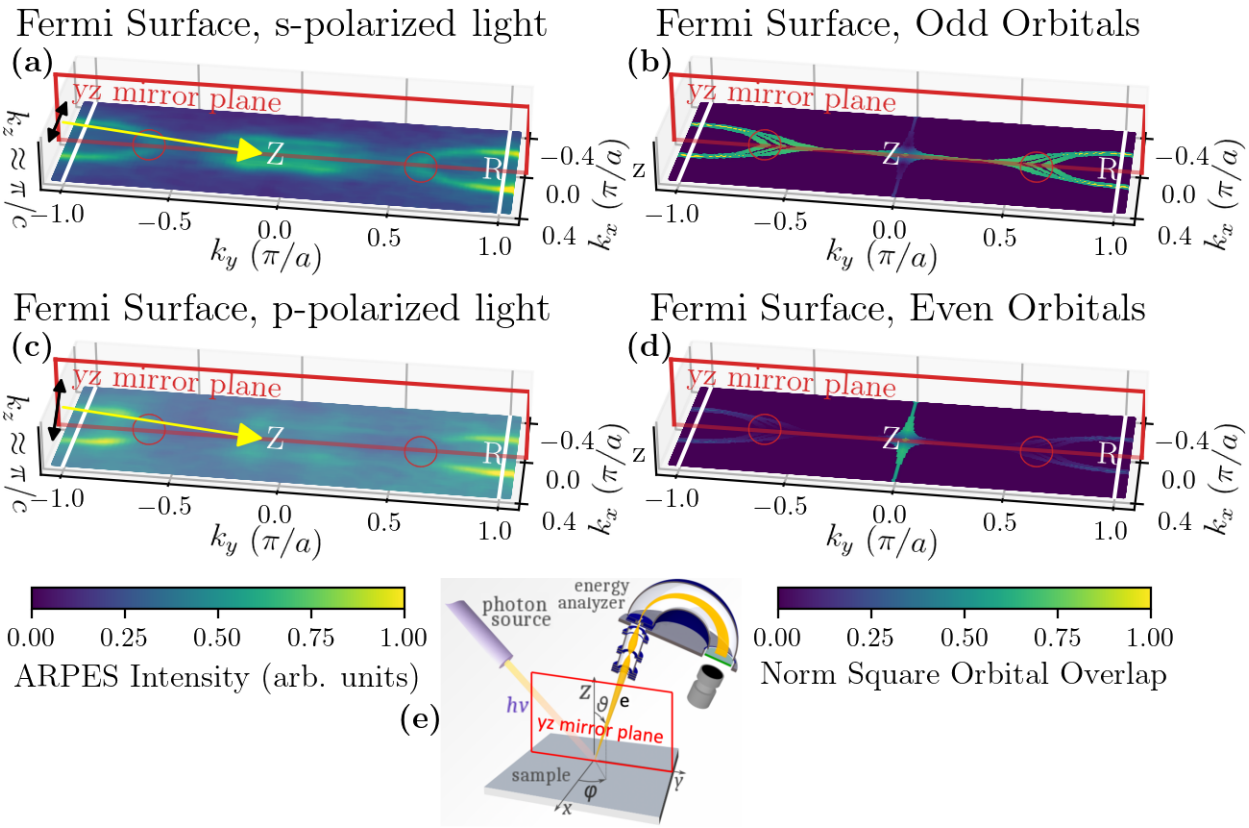

Figure 4.8: Orbital decomposition: (a) Fermi surface data taken with 100 eV photons linearly polarized along $\hat{\boldsymbol{x}}$ [same data as Fig. 2(b) of the main text]. (c) Same as (a) but with the photon polarization lying in the yz mirror plane. (a&c) Yellow arrow indicates incoming light, while black double arrows indicate the polarization of the light. (b&d) Superimposed Fermi surface plots of the DFT at $k_z \approx \pi/c$, $\pi/c - 0.16\pi/c$, and $\pi/c - 0.28\pi/c$ projected onto the odd orbitals (p_x, d_{xy}, and d_{xz}) and even orbitals (s, p_y, d_{yz}, d_{z^2}, and $d_{x^2-y^2}$) with respect to the yz mirror plane, respectively. (a-d) White text labels symmetry points of the BZ. BZ boundaries indicated by white lines. (e) Experimental coordinate system adapted from [24]. (a-e) Red box indicates the yz mirror plane that contains incoming photon beam.

at $k_x \approx 0$ are odd, with vanishing contributions from even states, which is consistent with the experimentally observed polarization dependence. Further examination of the DFT data indicates that all three odd states contribute comparably to the tips of the ellipses enclosed in the red circles. And for the states near the Z point along the red line, the p_x and d_{xz} states have comparable strength, while the d_{xy} state's contribution is weak and vanishing at Z.

In Fig. 4.8, the DFT is plotted for three k_z values—$k_z \approx \pi/c$, $\pi/c - 0.16\pi/c$, and $\pi/c - 0.28\pi/c$—because the precise location of the tips of the ellipses and their sizes are dependent on the precise distribution of the k_z values that contribute spectral weight. Additionally, the presence of the line through Z is explained by the multiple k_z values contributing. Fortunately, the parity of the orbital character of the bands is not as sensitive to k_z.

4.3.3 Symmetry Cuts and Fermi Velocities

With the aid of Fermi surface plots and k_z dispersion (see Sec. 4.3.1), E-k dispersion for the high symmetry cuts in the Γ-X plane are readily acquired using 85 eV, LV polarized photons [see Fig. 4.9(a&f)]. To quantitatively compare the experimental data to DFT, momentum distribution cuts (MDCs) are fit [see Fig. 4.9(c&e)] to extract the low energy experimental dispersion, which is overlaid with corresponding dispersions from the hole doped DFT in Fig. 4.9(b&d). Additionally, the MDC peak locations may be fit to a line to extract the Fermi velocity. The $X \to \Gamma \to X$ MDCs are fit with two Voigt functions, and the extracted Fermi velocity is 4.6 eV Å, which to within the experimental error bars is the same as the Fermi velocity from the hold doped DFT, $v_{\mathrm{F}} = 4.8$ eV Å. The $M \to X \to M$ symmetry cut contains the $A \to R \to A$ bands near E_F, due to the same k_z uncertainty mentioned above. Therefore, the extracted MDCs were fit with four Voigt functions, representing four bands. The Fermi velocity of the bands corresponding to the $M \to X \to M$ cut is 6.0 eV Å. Again to within experimental precision, this is the same as the Fermi velocity from the hole doped DFT, $v_{\mathrm{F}} = 6.4$ eV Å. The error on the extracted Fermi velocities from MDC fittings scales as $\sim {v_{\mathrm{F}}}^2$. So, for these large Fermi velocities, the relative error is found to be $\sim 10\%$ (see Sec. 4.5.2).

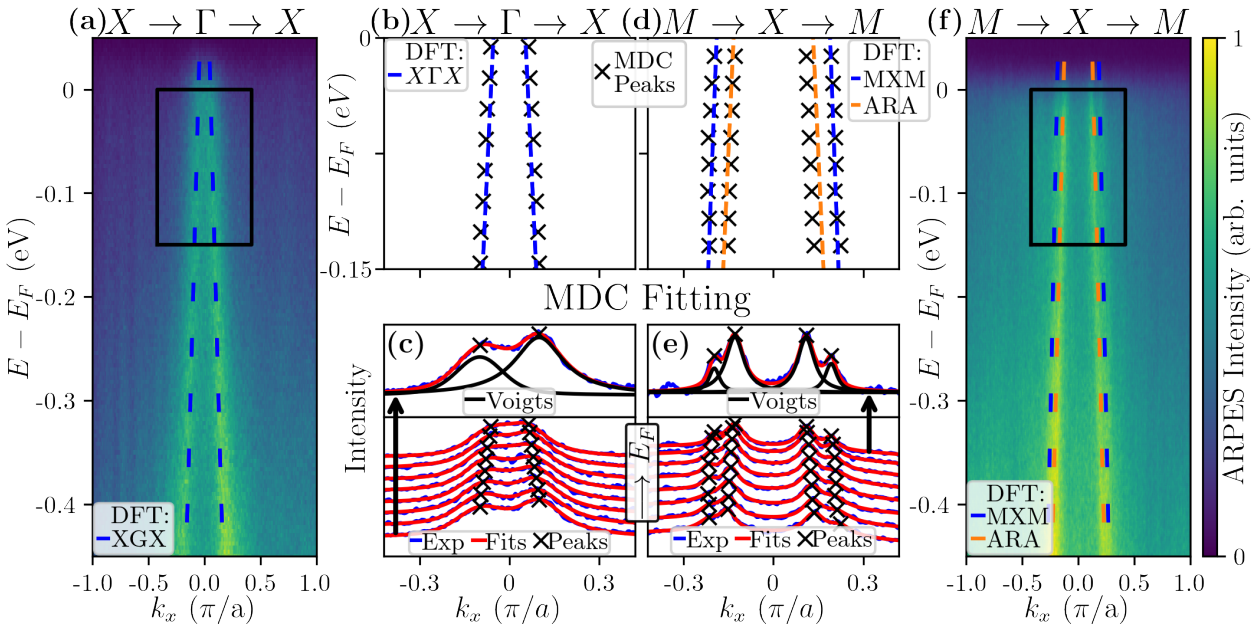

Figure 4.9: Symmetry Cuts: (a&f) ARPES images with hole doped DFT overlaid as dashed lines. Black boxes in (a) and (f) depict the region shown in (b&c) and (d&e), respectively. (b&d) Comparison of the dispersion from the hole doped DFT and experiment. (c&e) Waterfall plots of MDCs with fits overlaid. Upper panels depict a single MDC, highlighting the individual Voigt functions used for each peak in the fit. (a-f) The $X \to \Gamma \to X$ and $M \to X \to M$ symmetry cuts—(a-c) and (d-f), respectively—were acquired with 85 eV, LV polarized photons. The $X \to \Gamma \to X$ data comes from the CuMnAs01 sample and the $M \to X \to M$ data from the CuMnAs02 sample.

To explore the comparison qualitatively to deeper binding energies, Fig. 4.10(a&b) shows the $X\Gamma X$ and ARA cuts to almost 1.5 eV in binding. The symmetry cuts are seen to exhibit excellent qualitative agreement with the DFT. The band crossing E_F in the $X \to \Gamma \to X$ cut tracks the DFT very well. The strong lines crossing E_F in the $A \to R \to A$ cut are nicely tracked by the bands shown (the lack of a gap and subtle difference in k_F is due to contributions from other k_z values). Additionally, the band-top at $k_x = 0$ in the $A \to R \to A$ cut shows good agreement.

However, the $X \to \Gamma \to X$ and $A \to R \to A$ cuts are missing bands from the DFT, which reveal matrix element effects demonstrated in Fig. 4.10. In both cases, the relevant mirror plane to consider is the yz plane, which contains the final states (even) for **only** $k_x = 0$, and thus this argument only applies for the states near the vertical solid red line in the figures. The data was taken with polarization along $\hat{x}$—perpendicular to the mirror plane; so the matrix element sends the spectral intensity to zero for even initial states with respect to the yz mirror plane. The portion of the band-top near $k_x \approx 0$ and $E - E_F \approx -1.2$ eV in the $X \to \Gamma \to X$ cut is suppressed in the data. Additionally, the band bottom at $k_x = 0$ in the $A \to R \to A$ cut is suppressed. Both are consistent with the prediction from the DFT that these bands at $k_x = 0$ consist entirely of even orbitals.

4.3.4 Replicas and Chemical Potential Shift

Having demonstrated the strong agreement between the DFT and experiment, it is time to address two issues raised previously in detail—the replication and doping. First, to quantitatively test the hypothesis that the extra structure near the Z point of the Fermi surface is the replication of the ellipses near the R point [see Fig. 4.11(a)], the dispersion along the $R \to Z \to R$ cut is compared to the dispersion along the $A \to R \to A$ cut. MDC fitting is used to extract the experimental dispersion along the $R \to Z \to R$ cut [see Fig. 4.11(b)]. The MDCs are fit with three Voigt functions—two to capture the bands in question and one to capture a band top at $k_x = 0$ that disperses across E_F as a function of k_z. The extracted dispersion from the $R \to Z \to R$ cut is overlaid with the DFT dispersion along the $A \to R \to A$ cut, showing excellent qualitative

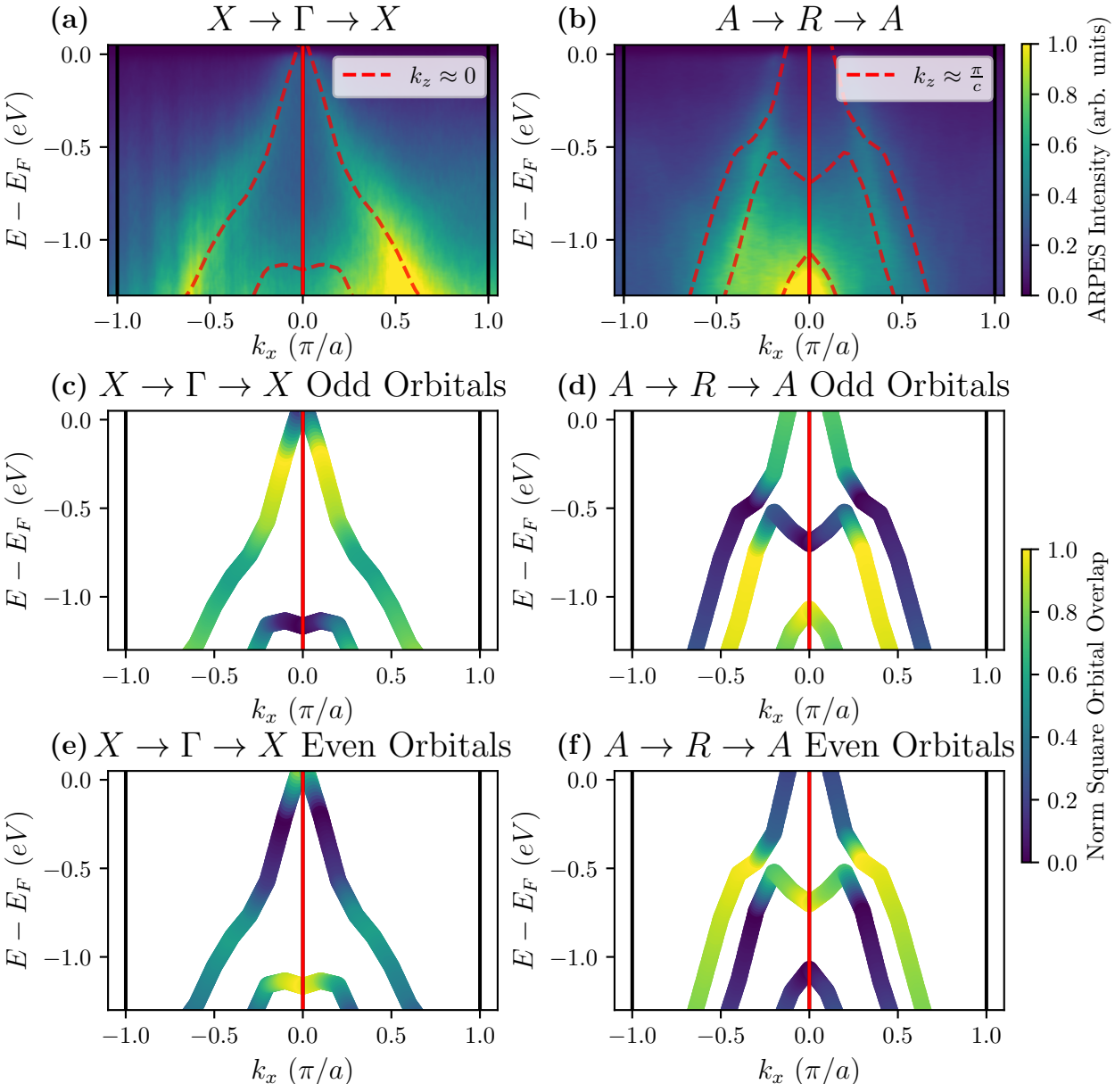

Figure 4.10: Matrix elements in symmetry cuts: (a) $X \to \Gamma \to X$ taken with 85 eV s-polarized ($\epsilon = \hat{x}$) photons. (b) $A \to R \to A$ symmetry cut was taken with 102 eV s-polarized photons. (a&b) Red dashed lines show DFT. (c&e) $X \to \Gamma \to X$ cut through the DFT projected onto odd (c) and even (e) orbitals with respect to the yz plane, which contains only $k_x = 0$. (d&f) Same as (c&e) but for the $A \to R \to A$ cut through the DFT. (all) The solid red line indicates the states contained in the yz mirror-plane.

agreement [see Fig. 4.11(c)]. From MDC analysis, the Fermi velocity of the bands in the $R \to Z \to R$ cut is determined to be 5.1 eV Å. The Fermi velocity of the $A \to R \to A$ cut extracted from the DFT is 5.2 eV Å, which is within 2% of the experimental value.

Second, to determine if the $\approx$ 390 meV chemical potential shift is reasonable, necessary concentrations of likely defects are calculated. It turns out that two effects allow this relatively large energy shift to be explained by reasonably small defect concentrations. First, CuMnAs is a semimetal. According to the DFT, $\approx$ 390 meV of hole doping corresponds to only 0.27 holes per unit cell. Second, the most likely defects all bring a substantial number of holes with each defect. According to Máca et al., the most energetically favorable defects are Cu and Mn vacancies followed by Mn substitutions for Cu [60]. One reasonably suspects that the non-magnetic copper will have 10 valence electrons, i.e. will be [Ar] $3d^{10}$, and the magnetic Mn will be [Ar] $3d^5$ with 5 valence electrons, naively leaving As with a full valence shell. The atomically projected Density Of States (DOS) from the DFT mostly agrees with this intuition, finding 10 valence electrons on Cu and 5.4 on Mn, which would mean that each Mn for Cu substitution brings 4.6 holes. Therefore, taking into account the 222 stoichiometry of the unit cell, the 388 meV shift would result from only 1.3%, 2.4%, and 2.9% of pure Cu or Mn vacancies or Mn for Cu substitutions, respectively. Furthermore, there could be combinations of these defects, yielding very reasonable defect levels. Specifically, the defect concentrations in the few percent range give, according to Máca et al. [60], DFT resistivities of CuMnAs consistent with experiment.

4.4 Discussion

In-plane Fermi surfaces, k_z dispersions (see Sec. 4.3.1), and symmetry cuts as E-k dispersions for tetragonal CuMnAs are reported for the first time. After shifting the chemical potential by ≈ -390 meV (hole doping), DFT calculations—using GGA+U with $U = 2.25$ eV applied to the Mn-3d orbitals—are found to be in excellent qualitative and quantitative agreement with the experimental data. In particular, the DFT predicts accurate Fermi velocities and an orbital character for the bands that is consistent with the experimental results. Additionally, surface reconstruction and

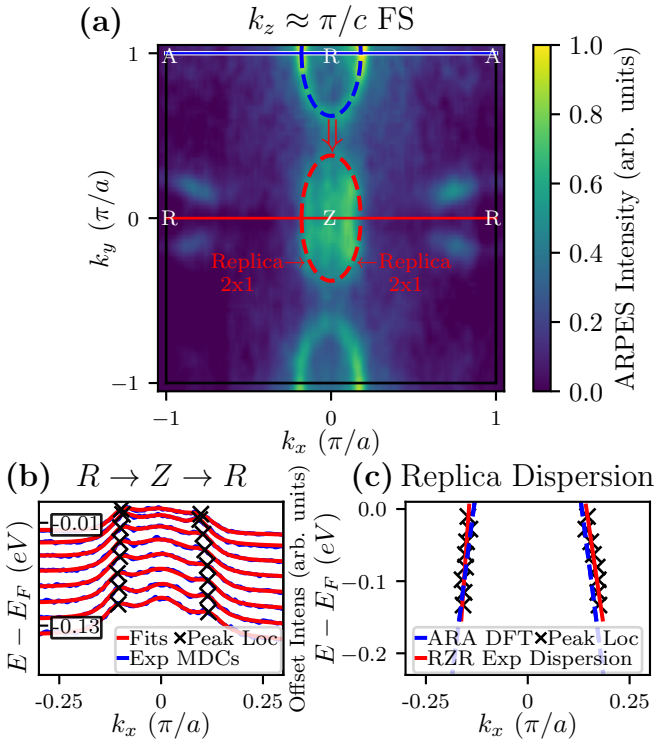

Figure 4.11: Replica band: (a) The same Fermi surface data as shown in Fig. 4.7(b). The blue dashed ellipse represents a primary pocket that replicates as the red dashed ellipse due to the 1x2 surface reconstructions. (b) Waterfall plot of MDCs extracted from the $R \to Z \to R$ symmetry cut [red line in (a)]. (c) Comparison of the experimental $R \to Z \to R$ dispersion and the $A \to R \to A$ dispersion from the DFT. The blue line in (a) shows the $A \to R \to A$ symmetry cut.

replicated bands are found.

Furthermore, the extracted value of U is consistent with that of other studies. Veis et al. found that $U_{eff} = (U - J) \approx 2$ eV fit their angle-integrated photoemission data best [52]. In the GGA+U scheme used for the calculations in this paper, U and J values are not separate, and what really enters the total energy is the "$U - J$" value. So, the $U = 2.25$ eV term in this manuscript corresponds to the U_{eff}. Guyen et al. used $U = 2$ eV to explain emergent edge states on their surface reconstructed CuMnAs thin films [53]. $U < 2$ eV fails to even qualitatively capture the ARPES experimental results, primarily because the bandwidth of the band in the $X \rightarrow \Gamma \rightarrow X$ is too small. The strongly constrained and appropriately normed (SCAN) functional [61] increased this bandwidth compared to pure GGA, yielding a similar bandwidth to $U = 1$ eV. Nevertheless, SCAN still did not produce a large enough bandwidth for the $X \rightarrow \Gamma \rightarrow X$ cut. $U = 2.25$ eV within GGA was primarily chosen because it reproduces the Fermi velocity in the $X \rightarrow \Gamma \rightarrow X$ cut most accurately.

Much of the interest in CuMnAs stems from the predicted Dirac fermions with an electrically tunable mass gap. After tuning the DFT to match the experimental data, these Dirac crossings are still present [see Fig. 4.12(a-c) where spin-orbit coupling is added to show the changing Dirac fermion masses]. There are Dirac crossings deep below the Fermi energy that were studied. Figure 4.12(d) shows data along the $M \rightarrow X \rightarrow M$ edge of the Brillouin zone taken with 100 eV LV photons with hole doped DFT overlaid. However, because the Dirac points are so deep in binding and the data is broadened in k_z due to surface sensitivity, the Dirac points cannot be resolved to compare directly to the DFT. Nevertheless, the qualitative agreement is strong. This raises the confidence in the existence of the Dirac crossings only 180 meV above the stoichiometric and defect free Fermi energy [see the red circle in Fig. 4.12(b)]. Note, moving E_F to this Dirac point should enable band topology switching. Additionally, this would enable electrically controllable anisotropic changes in the DOS near E_{F}, which one would expect to produce a larger AMR signal than the traditional type that depends on anisotropic scattering rates. Indeed, anisotropic changes in the band gap of $EuMnSb_2$ played a crucial role in the discovered colossal AMR signal [62].

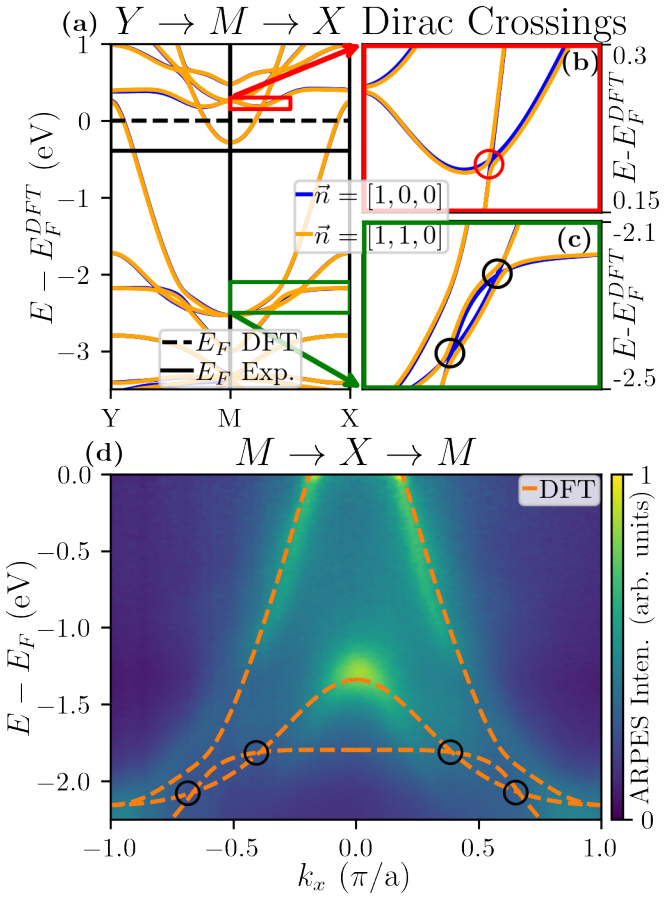

Figure 4.12: Dirac fermions with electrically tunable mass gaps: (a) Shows the $Y \rightarrow M \rightarrow X$ cut near E_F from DFT on the undoped energy scale with spin-orbit coupling included. (b&c) Zoom in on the dispersion in the red and green boxes shown in (a), respectively, highlighting nearby Dirac fermions. The red circle in (b) shows the closest Dirac point to E_{F}. (d) ARPES image with hole doped DFT overlaid. Data comes from the CuMnAs01 sample, which has AFM domains with the Néel vector along $[1,1,0]$ and $[1,\bar{1},0]$. The black circles highlight the same Dirac points in both (c&d).

More generally, the strong agreement between the DFT and experiment shown throughout this paper lend credence to the predictions from the DFT beyond the ones directly verified. For example, this applies to the atomic character of the bands predicted by the DFT. The atomic character of the bands predicted by the DFT are plotted with PyProcar [59] in Fig. 4.13). There is strong hybridization of the bands near the experimental Fermi surface, $E - E_{\mathrm{F}}^{\mathrm{DFT}} \approx -0.390$ eV on this unshifted energy scale (red line). This is in contrast to the pure GGA calculation where Mn dominated the Fermi surface. The application of $U = 2.25$ eV to the Mn 3d orbitals has pushed the primary contribution from the Mn atoms above the Fermi surface and leveled the playing field between the three atomic species.

By showing that DFT accurately captures the electronic structure of tetragonal CuMnAs, more weight is given to the growing interest in CuMnAs as a candidate AFM topological Dirac material. Furthermore, the low DOS near E_F provides hope that tetragonal CuMnAs can be electron doped moving E_F into the proximity of the electrically switchable Dirac points above E_F in the studied films. According to the DFT, the Dirac points are 570 meV or $\sim$0.38 electrons per unit cell above the chemical potential in the current films or only 180 meV/$\sim$0.12 electrons per unit cell above the defect free chemical potential. Alternatively, orthorhombic CuMnAs was suggested to be a pristine antiferromagnetic Dirac semimetal with only Dirac fermions at the Fermi level without any trivial bands. Considering the reliability of DFT in the description of tetragonal CuMnAs presented here, studying orthorhombic CuMnAs appears as a promising direction in research of antiferromagnetic Dirac semimetals.

4.5 Methods

4.5.1 ARPES

High resolution ARPES measurements were made at the MERLIN ARPES endstation of beamline 4.0.3 at the Advanced Light Source and at the HR-ARPES branch of beamline i05 at the Diamond Light Source. Data were taken below 50 K with photon energies in the range 75-125 eV,

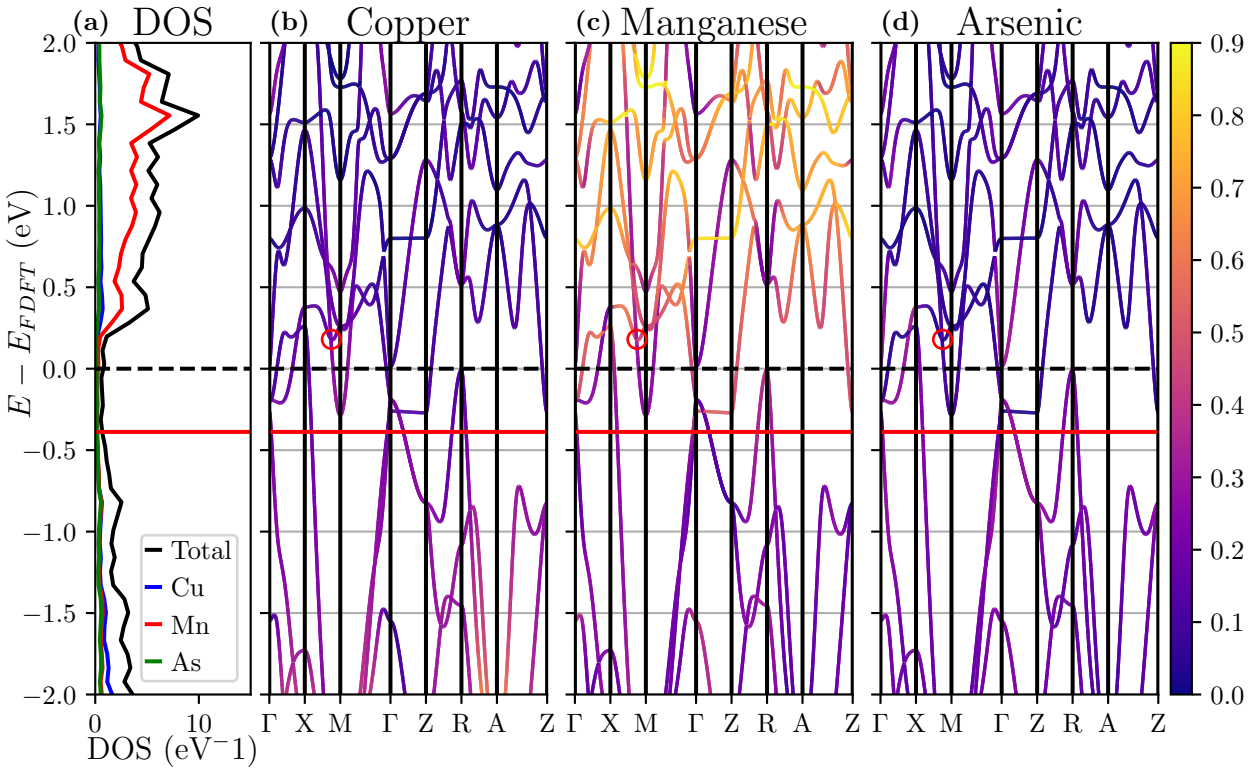

Figure 4.13: Atomic projected density of states and dispersion: (a) The Cu, Mn, As, and total DOS. (b,c,&d) The electronic dispersion along high symmetry cuts with the color scale depicting the projection of the Bloch states onto Cu, Mn, and As atomic orbitals, respectively. In all figures, the black dashed lines indicate the Fermi energy from DFT, while the red lines show the experimental Fermi energy.

using both linear vertical and linear horizontal polarization. The base pressure was $\lesssim 5 \times 10^{-11}$ Torr.

4.5.2 Extracting Fermi Velocity Uncertainty from MDC Fitting

General Intuition In MDC fitting, the energies, $\{E\}$, of the MDCs are assumed to be precisely the measured values. However, there will be uncertainty in the extracted peak positions, $\{k\}$, related to instrument resolution and uncertainty in the fitting due to noise in the data. This uncertainty will lead to an uncertainty in the Fermi velocity. The scaling of the uncertainty in v_F can be illustrated by considering

$$\begin{aligned} v_F &= \left.\frac{dE}{dk}\right|_{k_F} \\ &\approx \left.\frac{\Delta E}{\Delta k \pm \sigma_{\Delta k}}\right|_{k_F} \\ &= \left.\frac{\Delta E}{\Delta k}\right|_{k_F} \pm \sigma_{v_F} \end{aligned} \tag{4.2}$$

where Δk (ΔE) is just the difference between the two k (E) points closest to the Fermi energy and $\sigma_{\Delta k}$ is the uncertainty in the difference of the two k-points. For small $\sigma_{\Delta k}$, the resulting uncertainty in v_{F}, σ_{v_F}, can be found by transforming the variance in Δk under the Jacobian:

$$\sigma_{v_F}^2 \approx \frac{dv_{\mathrm{F}}}{d\Delta k}\sigma_{\Delta k}^2\frac{dv_{\mathrm{F}}}{d\Delta k} \tag{4.3}$$

$$\begin{aligned} \sigma_{v_F} &= |\Delta E(\Delta k)^{-2}\sigma_{\Delta k}| \\ &= |v_{\mathrm{F}}^2\frac{\sigma_{\Delta k}}{\Delta E}|. \end{aligned} \tag{4.4}$$

So, the uncertainty in v_F scales as v_{F}^2.

Particulars of Our Method First, the $\{E\}$, $\{k\}$, and $\{\sigma_k\}$ that correspond to a band must be extracted. Since the bands within 150 meV of E_F are highly linear, the ARPES spectral intensity from a band along an MDC can be approximated as a Voigt function in k. So, MDCs for all energies, $\{E\}$, between E_F and $E_F - 150$ meV are fit using a linear combination of Voigt functions to represent the bands. The center locations of the Voigt functions are the $\{k\}$. Although

the $\{\sigma_k\}$ can be acquired from the non-linear least squares fitting directly, a better estimate for $\{\sigma_k\}$ can be found by using a Markov chain Monte Carlo simulation. This algorithm explores the parameter space nearby the best fit solutions to calculate the posterior distribution of the model parameters. Using the calculated probability distributions, $\{\sigma_k\}$ can be estimated as half the distance between the 15.8 and 84.2 percentiles of the marginal probability distribution of the peak location, k. All of this fitting is done in Python using Lmfit [63].

Second, the uncertainty in v_{F} from the derivative method given above can be improved by fitting polynomials to the pairs of $\{E\}$ and $\{k\}$ corresponding to a band. In particular, linear polynomials are fit to extract $k(E) = b * E + c$ where k is treated as the dependent variable for technical reasons, including that E varies more than k for large Fermi velocities. $k(E)$ is fit with standard least squares fitting, using Numpy's Polyfit function [64], which calculates the covariance matrix over b and c taking into account $\{\sigma_k\}$.

Finally, $v_{\mathrm{F}} = 1/b$. Using σ_b from the covariance matrix of b and c, the uncertainty in v_{F} can be found by again transforming σ_b under the Jacobian:

$$\sigma_{v_F}^2 \approx \frac{dv_{\mathrm{F}}}{db}\sigma_b^2\frac{dv_{\mathrm{F}}}{db} \tag{4.5}$$

$$\begin{aligned}\sigma_{v_F} &= |\frac{1}{b^2}\sigma_b| \\ &= |v_{\mathrm{F}}^2\sigma_b|.\end{aligned} \tag{4.6}$$

Again, $\sigma_{v_{\mathrm{F}}} \propto v_{\mathrm{F}}^2$.

In this way, the Fermi velocities of the bands in the experimental ARPES cuts are determined: $X \to \Gamma \to X$ has $v_F = 4.6 \pm 0.5$eVÅ, $M \to X \to M$ has $v_F = 6.0 \pm 0.7$eVÅ, and $R \to Z \to R$ has $v_F = 5.1 \pm 0.5$eVÅ. Hence, the reported relative uncertainty in the main text of $\sim 10\%$. Note, that the uncertainty in the $M \to X \to M$ cut cannot be reliably found from the Markov chain Monte Carlo simulations due to the lack of convergence in a reasonable amount of time. This is caused by the presence of four partially overlapping peaks. Therefore, the uncertainty found in the same manner outlined above, except using $\{\sigma_k\}$ acquired directly from the non-linear least squares fitting of the MDCs, is reported.

4.5.3 LEED Analysis

To extract the lattice constant from LEED, LEED images must be converted to q-space. Because the electron probe depth at the energies studied is less than the c-axis lattice constant, it is standard to assume that the electrons reflect at the surface, thus only experiencing a 2D lattice. The implication being that only the in-plane scattering vector is needed to determine the lattice constants. Assuming only elastic collisions, the magnitude of the scattered electron momentum, k, can be found from the free electron dispersion and the known incident electron's energy, E:

$$k = \frac{\sqrt{2mE}}{\hbar}, \tag{4.7}$$

where m is the mass of the electron. Since LEED was acquired at normal incidence, the momentum of the reflected electron in the plane perpendicular to our incident electron beam is the in-plane scattering momentum, $\vec{q}$. Defining the line from the sample back along the incident beam as our z-axis, we can find $\vec{q}$:

$$q_x = k \sin\theta \cos\phi \text{ and} \tag{4.8}$$

$$q_y = k \sin\theta \sin\phi, \tag{4.9}$$

where θ is the polar angle and ϕ is the azimuth angle. In practice, θ can be found as the ratio of the length from the origin of a LEED image to a particular point, ρ, to the distance from the origin to the edge of the LEED screen, l, which is at a known polar angle defined by the LEED field of view, 42° for the LEED used here:

$$\sin\theta = \frac{\rho}{l} \sin 42^\circ. \tag{4.10}$$

Finally, the x-axis and thus ϕ are chosen arbitrarily for convenience, allowing LEED images to be converted to q-space.

The lattice constant is then extracted using Bragg's law in the plane of the surface,

$$\begin{aligned} \vec{G^{\|}} &= \vec{k_f^{\|}} - \vec{k_i^{\|}} \\ &= \vec{q}, \end{aligned} \tag{4.11}$$

where $\vec{G}^{\parallel}$, $\vec{k}_f^{\parallel}$, and $\vec{k}_i^{\parallel}$ are the in-plane components of the reciprocal lattice vectors, the final electron momentum, and the incident electron momentum, respectively. For the present case of a tetragonal unit cell with the (001) surface exposed and x defined along the "a" lattice direction,

$$\vec{G}^{\parallel} = \frac{2\pi}{a}(h\hat{x} + k\hat{y}) \text{ and} \tag{4.12}$$

$$|\vec{G}^{\parallel}| = \frac{2\pi}{a}\sqrt{h^2 + k^2}. \tag{4.13}$$

Since $|\vec{G}^{\parallel}| = |q|$, Eqn. 4.13 can be solved for a:

$$a = \frac{2\pi}{|\vec{q}|}\sqrt{h^2 + k^2}, \tag{4.14}$$

where $\vec{q}$ corresponds to the location of a Bragg peak in q-space with Miller indices h,k.

It is possible to then label the observed peaks under two hypothetical schemes: 1) no surface reconstruction, treating all peaks as fundamental and thus $h, k \in \mathbb{Z}$ for all peaks, and 2) one with 2x1 and 1x2 surface reconstructed domains, treating the peaks on the corners of squares as primary with $h, k \in \mathbb{Z}$ and the peaks on the edges as replicas with h or k a half integer. Under these two schemes, one can extract a, and we find that scheme "1)" yields twice the value of the known lattice constant, while scheme "2)" produces the correct lattice constant, confirming the presence of the suspected 2x1 and 1x2 surface reconstructed domains. Note that the lack of peaks in the centers of the squares rules out a full 2x2 surface reconstruction.

4.5.4 Sample Preparation

The 45 nm thick films of single-crystalline tetragonal CuMnAs were grown by molecular beam epitaxy on GaP(001) with the (001) face of CuMnAs exposed. The films were capped with 30 nm of As to protect the surfaces from contamination from the ambient environment. Decapping was performed in an environment with pressures $\lesssim 10^{-8}$ Torr, reaching a max temperature reading of 340 °C on a pyrometer, emissivity = 0.1 (see Fig. 4.14).

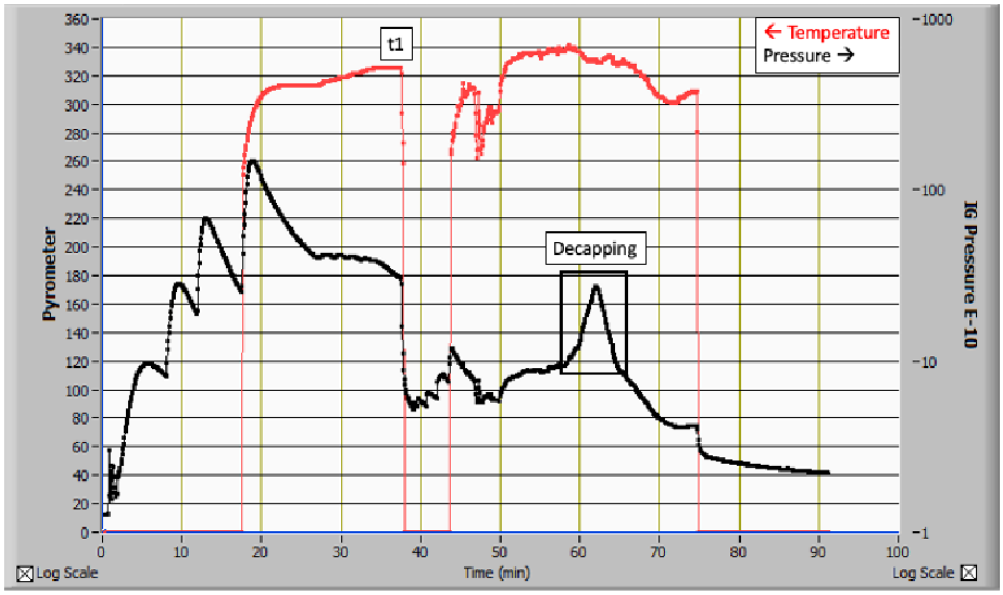

Figure 4.14: Decapping. Time series data of the temperature (red data on left axis) and pressure (black data on right axis). At time t1, the filament heater was switched to an e-beam heater, which was turned up slowly. The decapping period is highlighted by the black box.

4.5.5 Density Functional Theory Calculations

The DFT calculations were performed with Vienna Ab-initio Simulation Package (VASP) [56–58], based on a plane wave basis set. The interaction between ions and electrons is described by the projector-augmented wave (PAW) method [65, 66]. GGA+U scheme was applied, with the exchange-correlation functional being the Perdew-Burke-Ernzerhof generalized gradient approximation functional [67], and an on-site Coulomb potential of 2.25 eV was applied to the Mn-3d electrons, using Dudarev's implementation. A full relaxation of the lattice structure was carried out with the energy and force breaking condition set to 10^{-6} eV and 10^{-3} eV/Å. The cut off energy was taken as 550 eV. A dense k-mesh of 31*31*19 was used in the static calculation of the electronic structure. The calculations were carried out with each of the Mn atoms having a magnetic moment of 3.67 μB with the Néel vector along the [010] orientation. Finally, the chemical potential was shifted to bring the band top at Z in the DFT to the corresponding maximum intensity in the experimental Energy Dispersion Cut (EDC) through Z. In the case of $U = 2.25$ eV, this was 388 meV, but the precise shift did depend on the specific value of U used, with all U values

requiring some shift.

Chapter 5

Motivation To Study Light Induced Superconductivity

The focus of this chapter is to motivate our intended time-resolved ARPES experiments on light induced superconductivity. I will begin with an introduction to superconductivity, followed by an overview of some of the prior work by Cavalleri et al. measuring possible light induced superconductivity, and conclude with a discussion of what we might hope to measure with our experiments.

5.1 Introduction to Superconductivity and Its History

At exactly 4pm on 8 April 1911, Kamerlingh Onnes notebook's indicate that the resistance of Mercury at about 3K was "practically zero" [68]. He and his team had discovered superconductivity for the first time, measuring the sudden drop in resistance to zero at T_c that is characteristic of a superconductor (see Fig. 5.1). Incidentally, they had also observed the superfluid transition in Helium as well but did not realize it, foreshadowing the development of a theoretical framework that would unify the two. This work sparked a fascinating development in low-temperature physics, including breakthroughs in the areas of phase transitions, Bose-Einstein Condensates, superfluids, and superconductivity, affording Onnes a Nobel prize [69].

5.1.1 Meissner-Ochsenfeld Effect and the London Equation

Although superconductors get their name from their zero resistance property, the defining characteristic of superconductors is actually their perfect diamagnetism, which causes them to expel

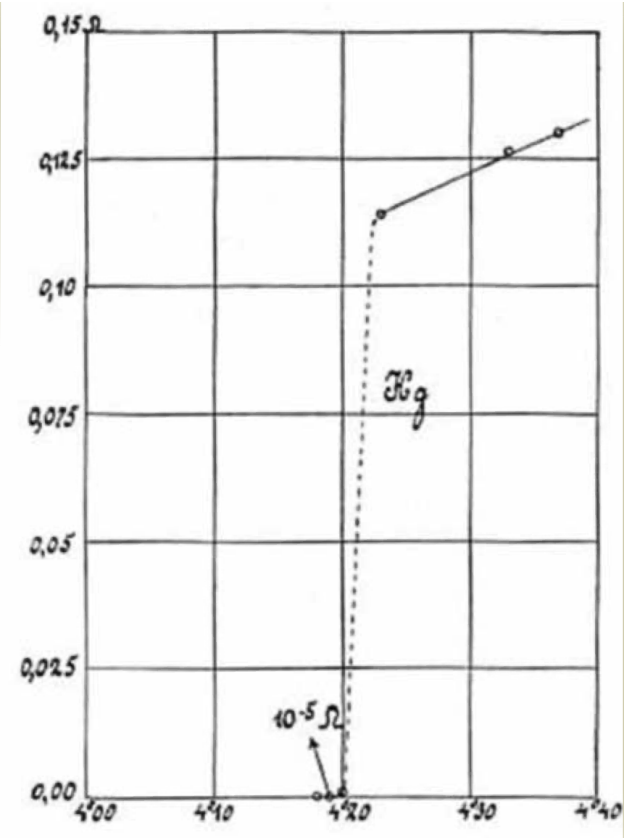

Figure 5.1: Historical resistance plot from Kamerlingh Onnes studies on superconducting Mercury. The plot is of resistance with respect to temperature in Kelvin, showing a $T_c \approx 4.25$ K. Figure Copied from [68].

magnetic fields at all costs. This effect was first discovered in 1933 by Meissner and Ochsenfeld, giving the property its name, the Meissner-Ochsenfeld effect [70]. There are many reasons that this is considered the defining characteristic over zero-resistance: 1) the Meissner-Ochsenfeld effect is a property of the equilibrium state rather than a transport property, 2) the Meissner-Ochsenfeld effect implies zero resistance and not vice-versa (consider a field cooled perfect conductor), and 3) it is considered a more reliable measurement.

The first theoretical description that could describe the electrodynamics in a superconductor and thus account for the Meissner-Ochsenfeld effect came in 1935 from two brothers, Heinz and Fritz London [71]. Inspired by the Meissner-Ochsenfeld effect, they considered the possibility that magnetic fields could sustain the currents, and thus they replace the electric field with the magnetic vector potential in Ohm's law. Also taking inspiration from the two fluid model proposed by Laszlo Tisza [72] in the context of superfluid He, they replaced the overall density with a superfluid density, n_s—the density of electrons in the superconducting state. Thus, they wrote down the London equation,

$$\vec{j}_s = -\frac{n_s e^2}{2m_e}\vec{A}, \tag{5.1}$$

where $\vec{j}_s$ is the superconducting current. Using this equation and Drude theory with infinite lifetime between scattering events, they were able to show that circulating (screening) currents on the surface of a superconductor create an equal and opposite magnetic field, canceling the external magnetic field, yielding zero magnetic field in the material, thus explaining the Meissner-Ochsenfeld effect. Furthermore, they showed that the magnetic field inside the sample goes to zero exponentially, $B(z) = B_0 e^{-z/\lambda}$ in distance from the sample surface, z. The characteristic length of the exponential decay, λ, is called the London penetration depth.

Although this theory began as a purely phenomenological theory to describe the Meissner-Ochsenfeld effect, it had profound implications that were not lost on F. London [73]. The London theory implies that the electron's mean momentum is the same over very large distances—a deeply important concept in the theory of thermodynamic phases formalized into off-diagonal long range

order in the density matrix by Penrose much later in 1951 [74]. London was an important theorist to the developing theory of superfluid ^{4}He, and at the time, quantum mechanics was still young and thought to only apply to microscopic phenomena like atoms. So, it was deeply puzzling that at very low temperatures a system would tend towards a liquid state at all, since in classical mechanics a system should tend towards a state with no motion that orders itself in position space to minimize the interaction energy, i.e. towards a crystal. The fact that superfluids and superconductors seemed to crystallize in momentum space instead was a hint not lost on F. London that quantum mechanics was at play. Quantum mechanics would help explain the long range order in average momentum too, since for a well defined momentum state there would be a large position uncertainty due to Heisenberg. Together, these insights lead London to suspect that Bose-Einstein Condensation (BEC) was involved in the description of superfluid ^{4}He, leading him to a close prediction of the superfluid transition temperature, because in a BEC the particles crystallize in momentum space, i.e. a macroscopic number of particles condense into the 0 momentum state. At this point, the de Broglie wavelength becomes larger than the intermolecular spacing, necessitating the need for a macroscopic quantum wave function. However, it is not enough to just assert that there is a macroscopic quantum wave function that describes either superconductors or superfluids and apply the standard Schrödinger equation, because as Landau would point out, there needs to be a term proportional to $|\psi|^4$ in the free energy to ensure thermodynamic stability in the superconducting/superfluid phase where the term proportional to $|\psi|^2$ has a negative coefficient. That is, without a positive term proportional to $|\psi|^4$, $|\psi|$ would tend towards infinity with the energy tending towards negative infinity, which is clearly not allowed physically.

5.1.2 Landau-Ginzburg Theory and Type-II Superconductors

Type-II superconductors were discovered in 1935 by Rjabinin and Shubnikow [75]. Type-II superconductors allowed discrete magnetic flux to penetrate the sample at intermediate fields between H_{c1} and H_{c2} (See Fig. 5.2). Like type-I superconductors, the field is fully expelled at fields below H_{c1}, and the superconductors become normal materials at fields above H_{c2}, because in an

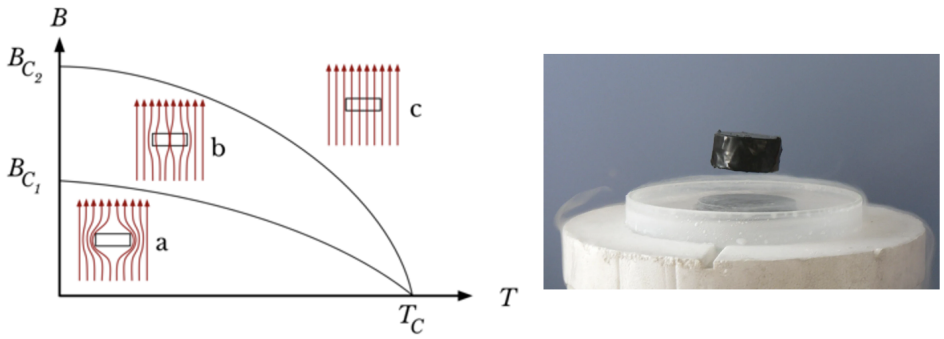

Figure 5.2: Meissner-Ochsenfeld effect in a type II superconductor: Left, shows a plot of the critical fields, B_{c_1} and B_{c_2}, as a function of temperature, depicting the magnetic field expulsion of a superconducting material in the fully superconducting state, state with vortices, and normal state as insets. Right a superconductor levitating in a magnetic field due to the Meissner-Ochsenfeld effect. Left Copied from [76]. Right Copied from [70].

attempt to expel the magnetic field, the screening currents exceed the critical current, I_c, driving the system into a normal dissipative state.

A theoretical description of type-I and type-II superconductors was put forth by Landau and Ginzburg [77], expanding on Landau's earlier work on phase transitions where he introduced the idea of an order parameter [78]. In this theory, they used a complex function, ψ, which represents a macroscopic quantum wave function, as the order parameter. They put forth the Landau-Ginzburg free energy density for superconductors coupled to a vector potential through the usual minimal coupling as

$$f_s(T) = f_n(T) + \frac{\hbar^2}{2m^*}|(\frac{\hbar}{i}\vec{\nabla} + 2e\vec{A})\psi|^2 + a|\psi|^2 + \frac{b}{2}|\psi|^4, \tag{5.2}$$

where $f_s(T)$ is the free energy density of the superconductor, $f_n(T)$ is the free energy density of the normal state, m^* is the effective mass, and a and b are constants. Although, in their original formulation of the free energy, they used e instead of $2e$, which reportedly Ginzburg suggested fit the data better [71]. Perhaps this is because Landau pushed back against the notion that superfluidity had anything to do with a BEC, since he like Kapitsa correctly thought superconductors and superfluids were analogous and superconductors involved electrons that are fermionic not bosonic [72].

In any case, the Landau-Ginzburg theory of superconductivity is a very successful theory that applies to all known superconductors, even those that we do not understand well microscop-

ically. And, as promised, it leads to a nonlinear Schrödinger equation, suggesting further that superconductivity is a macroscopic quantum state.

5.1.3 BCS Theory

In hindsight, it is almost surprising that it took until 1957 for the first microscopic theory to describe superconductivity to be put forth by Bardeen, Cooper, and Schrieffer, referred to as BCS theory [79], because as early as 1938 London was suggesting that superfluidity was akin to some sort of Bose-Einstein Condensation and should be described by a macroscopic quantum wave function [72], and upon the discovery of superfluid ^{4}He by J.F. Allen and A.D. Misener and independently by P. Kapitza, Kapitza coins the term superfluid by proposing, "by analogy with superconductors, ... the helium below the λ-point enters a special state which might be called superfluid." [72]. Indeed there were even treatments of superconductors as charged bosonic systems, where the bosons were electron pairs [80]. However, though many of the important intuitions about superconductivity were circulating in the minds of physicists, there remained several puzzles: how are the electrons bound into pairs, and how to write a macroscopic quantum coherent state of fermion pairs.

The first problem of bound electron pairs is obviously confusing, since electrons should repel each other. However, it was already shown by Frölich in 1950 that there could be an attractive interaction between electrons near the Fermi surface [81], which BCS built upon to come up with an effective attractive interaction between electrons. There are two main ingredients: First, it was already known that in a material the Coulomb repulsion between electrons is screened. That is, the electrons are really quasiparticles of electrons dressed by a cloud of positive charge from the ions, which causes the Coulomb force between these quasiparticles to decay exponentially, i.e. be screened by the lattice. So, the Coulomb force between electronic quasiparticles can be considerably less intense. Second, electronic interactions with the lattice can create an effective attraction between electrons, because an electron can scatter off of an ion creating a lattice distortion, which causes an accumulation of positive charge where ions are now closer to each other due to the lattice

distortion. This positive charge then attracts another electron, creating an effective attractive interaction between electrons. Or, in the language of field theory and Feynman diagrams, the electrons exchange a phonon (quantum of lattice vibration), creating a momentum transfer between electrons (see Fig. 5.3, representing the lowest order correction to the electron-electron interactions due to phonons). Furthermore, the electrons move much faster than the ions, meaning that the attraction is retarded in time, reducing further the role of the Coulomb repulsion. The full derivation of the interaction is much more complex, and in some cases, the interaction can even be repulsive. In fact, the electron-phonon interaction was expanded to the strong coupling regime later by Migdal [82] and then Éliashberg [83] using the Green's function formalism in what is now known as Migdal-Éliashberg theory. Nevertheless, the important point is that BCS put forth a reasonably justified approximation of the electron-electron interaction mediated by phonons that is weakly attractive between electrons within about the Debye energy, $\hbar\omega_{\mathrm{D}}$, of the Fermi surface in conditions relevant to low-temperature superconductors.

It is not enough to show that there is a weakly attractive interaction between electrons in 3D, because in 3D, the attraction generally has to exceed a threshold to yield a bound-state unlike in lower dimensions. However, Cooper in the famous Cooper problem, showed that an arbitrarily weak interaction between electrons in the presence of a Fermi sea would lead to a bound state. The key here is that due to Pauli exclusion electrons can only scatter around the 2D Fermi surface, because the bulk of the 3D Fermi sea is filled by electrons, unperturbed by the electron-phonon interaction put forth by BCS. That is, the electrons that participate in the weak electron-phonon interaction near the Fermi surface are effectively in 2D, meaning an arbitrarily weak interaction does create a bound state. Thus, the Fermi surface is said to be unstable to attractive interactions, since they lead to pairing of the electrons near the Fermi surface at sufficiently low temperatures.

The pieces are coming together; however, it is simply inaccurate to consider the electron pairs as bosons that then condense into a superfluid, because while an electron pair does have bosonic commutation relations for pair separations much greater than the pair size, the BCS state has strongly overlapping electron pairs. However, Schrieffer, looking for a translationally invariant

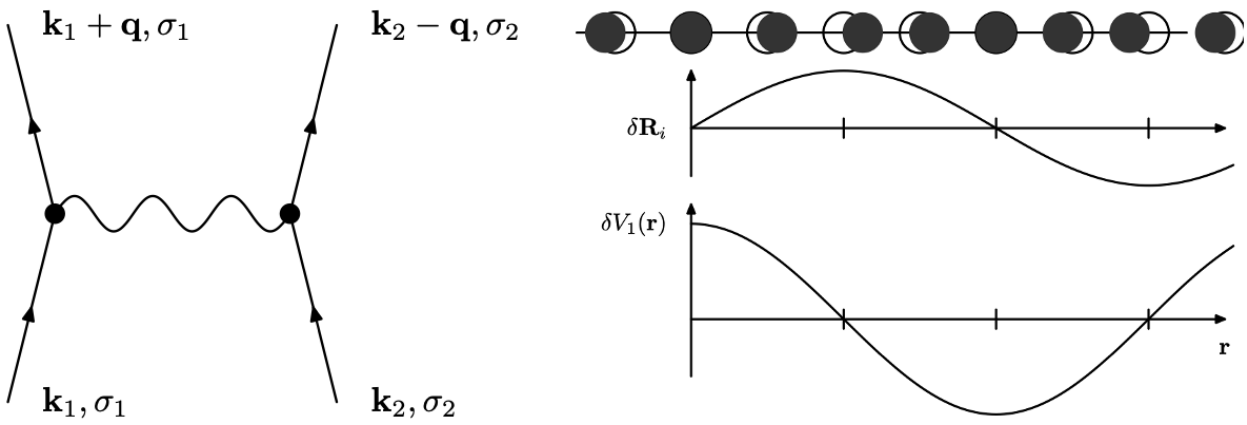

Figure 5.3: The electron phonon interaction. Left shows a Feynman diagram for the lowest order correction to the electron-electron interaction due to the electron-phonon coupling. In this diagram, two electrons exchange a phonon of momentum $\vec{q}$. Right depicts the effective potential due to a phonon excitation of the lattice. Upper panel shows a periodic crystal displacement from rest positions (open circles). Middle shows the displacement vector amplitude, $\delta\vec{R}_i$, for atom at position $\vec{R}_i$. Finally, the lower panel shows the change in the potential energy of the lattice potential, $\delta V_1(\vec{r})$, as function of position, which is due to the net accumulation of positive (negative) charge where ions are now closer together (farther apart) due to the phonon. Figure Copied from [71].

ground state, was able to write down a coherent state of zero center-of-mass electron pairs:

$$|\text{BCS}\rangle = (\text{constant})\Pi_{\vec{k}} \exp(\alpha(\vec{k})P^\dagger(\vec{k}))\,|0\rangle\,, \tag{5.3}$$

where $\alpha(\vec{k})$ is a coherence factor and $P^\dagger(\vec{k}) = c^\dagger_\uparrow(\vec{k})c^\dagger_\downarrow(-\vec{k})$ is the pair creation operator. Through the normal commutation relation for the fermionic operators, this can be related to the BCS wave function with the more common $u(\vec{k})$ and $v(\vec{k})$, but the above representation makes the connection with a normal quantum mechanical coherent states more obvious. Although this is not a condensate of bosons, it does possess the off-diagonal long range order of the BEC and superfluid. Also, it does have a definite phase while not having a definite particle number, as it should to be a coherent state.

Finally putting it all together, BCS were able to write down a mean-field Hamiltonian that included the effective electron-phonon interaction as

$$H_{\text{BCS}} - \mu N = \sum_{\vec{k},\sigma}(\xi(\vec{k}) - E_{\text{F}})c^\dagger_\sigma(\vec{k})c_\sigma(\vec{k}) + \sum_{\vec{k}}\left(\Delta c^\dagger_\uparrow(\vec{k})c^\dagger_\downarrow(-\vec{k}) + \Delta^* c_\downarrow(-\vec{k})c_\uparrow(\vec{k})\right), \tag{5.4}$$

where $\Delta = -|g_{\text{eff}}|^2 \sum_{\vec{k}} \langle c_\downarrow(-\vec{k})c_\uparrow(\vec{k})\rangle$ is the superconducting gap and g_{eff} characterizes the strength of the electron-phonon interaction. Additionally, it makes sense to work in the grand canonical ensemble framework, accounting for the chemical potential energy, μN. The gap shows up in the above from the standard mean-field decoupling of the 4-electron operator interaction term, with the average being over the pair annihilation operator, which would normally be 0 but not for the BCS state, instead of the number operator. The above Hamiltonian is quadratic in electron operators, which can always be diagonalized by a Bogoliubov transformation, yielding

$$H_{\text{BCS}} = \sum_{\vec{k}} E(\vec{k})b^\dagger_\uparrow(\vec{k})b_\uparrow(\vec{k}) - E(\vec{k})b^\dagger_\downarrow(-\vec{k})b_\downarrow(-\vec{k}), \tag{5.5}$$

where the $b^\dagger$ operators create the Bogoliubov particles that are linear combinations of electrons and holes with opposite spin and momentum. And their energies are

$$E(\vec{k}) = \sqrt{(\xi(\vec{k}) - E_{\text{F}})^2 + |\Delta|^2}. \tag{5.6}$$

Then, the ground state of this Hamiltonian may be found by the variational method, minimizing H_{BCS} with $|\mathrm{BCS}\rangle$ as the trial wave function. This, yields solutions for the $\alpha(\vec{k})$ or $u(\vec{k})$ and $v(\vec{k})$, depending on the representation used. These can then be used to find a self-consistent solution for the gap, which BCS showed at T=0 is

$$2\Delta(T=0) = 3.52 k_{\mathrm{B}} T_{\mathrm{c}}, \tag{5.7}$$

relating the gap at T=0 to the superconducting transition temperature, T_{c}. They also showed by taking the limit of $\Delta \to 0$ that T_{c} is

$$k_{\mathrm{B}} T_{\mathrm{c}} = 1.13 \hbar \omega_{\mathrm{D}} \exp(-1/(|g_{\mathrm{eff}}|^2 g(E_{\mathrm{F}})), \tag{5.8}$$

where $g(E_{\mathrm{F}})$ is the density of states at E_{F}. The important and disappointing point of the above being that T_{c} is exponentially suppressed, making a high T_{c} difficult to achieve.

BCS theory was eventually accepted because it predicted all of the important aspects of superconductors. The isotope effect was accounted for by the fact that the interaction range was the Debye energy, which changed with the changing mass of the ions. The BCS ground state also possessed a gap 2Δ around the Fermi energy, which can be seen by setting $\xi(\vec{k})$ to the Fermi energy in Eqn. 5.6. The gap was experimental measured around the same time that BCS produced their theory. Additionally, eqn. 5.7 was closely satisfied for a large number of superconductors. And, as we can see from $|\mathrm{BCS}\rangle$, the theory satisfied the long held intuition that the physics of superconductivity was related in some way to superfluids and BECs, although distinct.

5.1.4 Nambu Green's Function and ARPES as a Probe of Δ

From BCS theory, we saw that the Fermi surface is gapped in the superconducting state, and so, intuitively we should expect to be unable to photoemit from energies within Δ of the Fermi surface, i.e. directly observing the superconducting gap in ARPES. However, we can describe the effect of superconductivity on ARPES spectra more precisely by recalling Eqn. 3.23 of chapter 3, which illustrates the role of the imaginary part of the Green's function, $A(\vec{k}, \omega)$. Thus, we want to consider the Green's function of a superconductor.

Nambu showed [84], working in the particle ($(1,0)^T$) hole ($(0,1)^T$) basis, that the Green's function for the superconductor, including self-energies—Σ, could be written as

$$G^{-1} = \begin{pmatrix} \omega - \xi(\vec{k}) + E_{\mathrm{F}} - \Sigma & Z\Delta \\ Z\Delta^* & \omega + \xi(\vec{k}) - E_{\mathrm{F}} - \Sigma \end{pmatrix}, \tag{5.9}$$

where $Z = 1 - \Re\Sigma/\omega$ is the quasiparticle renormalization factor due to interactions in the system. For ARPES, we are only interested in the electronic portion of the Green's function, since we cannot photoemit holes (nor electron pairs in normal ARPES). This corresponds to G_{11}, which can be found by inverting the above to give

$$G_{11} = \frac{\omega + \xi(\vec{k}) - E_{\mathrm{F}} - \Sigma}{(\omega - \Sigma)^2 - (\xi(\vec{k}) - E_{\mathrm{F}})^2 - Z^2|\Delta|^2}. \tag{5.10}$$

The imaginary part of this function can be used to simulate the ARPES spectral intensity. The imaginary portion of this is in general a messy function. However, if we examine the limit when $\Sigma \to 0$ (only pairing interaction included), then we can examine the much simpler spectral function, recalling that a regulator must be used. Then, using the same identity to get the imaginary part of the Green's function in Eqn. 3.13, the spectral function can be written

$$\begin{aligned} A(\vec{k},\omega) &\propto \delta(\omega^2 - (\xi(\vec{k}) - E_{\mathrm{F}})^2 - |\Delta|^2) \\ &\propto \left(\delta(\omega - E(\vec{k})) + \delta(\omega + E(\vec{k}))\right), \end{aligned} \tag{5.11}$$

where $E(\vec{k})$ is given in Eqn. 5.6. This is unsurprising, because the non-interacting situation is exactly diagonalizable with Bogoliubov quasiparticles having energies $\pm E(\vec{k})$, of which the electron's are a part of both branches. So, the electron single particle spectral function also picks up a pole at these energies. Noting that $\xi(\vec{k}) \geq 0$, $E(\vec{k}) \geq |\Delta|$. Thus, the arguments of the delta function can only be 0 for $|\omega| \geq |\Delta|$, meaning the density of states develops a 2Δ gap around $E = E_{\mathrm{F}}$, since $\omega = 0$ is already defined as E_{F}. Note, from Eqn. 3.23, the ARPES intensity is cut off by the Fermi function, so only $\omega \leq E_{\mathrm{F}}$ (or 0 in the above Green's functions) are accessible to ARPES. Thus, we confirm our intuition that ARPES can directly measure the superconducting gap, but we continue to show that it can also probe the full many-body physics present through Σ.

However, it should be noted that ARPES alone cannot confirm superconductivity! Recall from the prior discussion that it is the Meissner-Ochsenfeld effect that defines a superconductor, not the superconducting gap. After all, there can be other states of matter that exhibit a gap in the density of states, e.g. a trivial insulator. Nevertheless, ARPES is still useful for measuring a superconducting gap. Additionally, we have thus far implicitly only discussed s-wave superconductors with an isotropic gap. However, this formalism can be expanded to consider pairing in different angular momentum channels, yielding momentum dependent gaps. In this case, as far as ARPES is concerned, we simply replace $\Delta \to \Delta(\vec{k})$ in the above Green's function. Then, we see that ARPES is a powerful tool to directly measure the superconducting gap symmetry.

5.2 Search for Room-Temperature Superconductors

From the very beginning, it was obvious that a zero resistance state would have many technological implications. In fact, many are realized already today, e.g. MRI machines use superconductors to generate high magnetic fields. However, many more applications will only be economical if a superconductor with a T_c well above room-temperature is found, since cryogenically cooling the entire electrical grid is not feasible, for example. However, over 100 years later, a room-temperature superconductor still does not exist; however, much progress has been made. See the Fig. 5.4 for a plot of materials and their T_c plotted against the year they were discovered.

One exciting development was the discovery of so-called high-T_c superconductors (blue diamonds in Fig. 5.4), which are generally not described by BCS theory. However, they are described by Ginzburg-Landau theory. The announcement of this discovery at APS's March Meeting in 1987 is referred to by the old-timers as the Woodstock of physics, although I cannot imagine it was anything like Woodstock. The huge jump in T_c created a lot of hope that a room-temperature superconductor was in reach, but unfortunately, this has not panned out.

Another exciting area of research in the last couple of decades is superconductivity under extremely high pressures (not shown on the plot). Here the interest is in hydride materials. Hydrogen is very light and thus has a high Debye energy, and it is a positive ion without screening

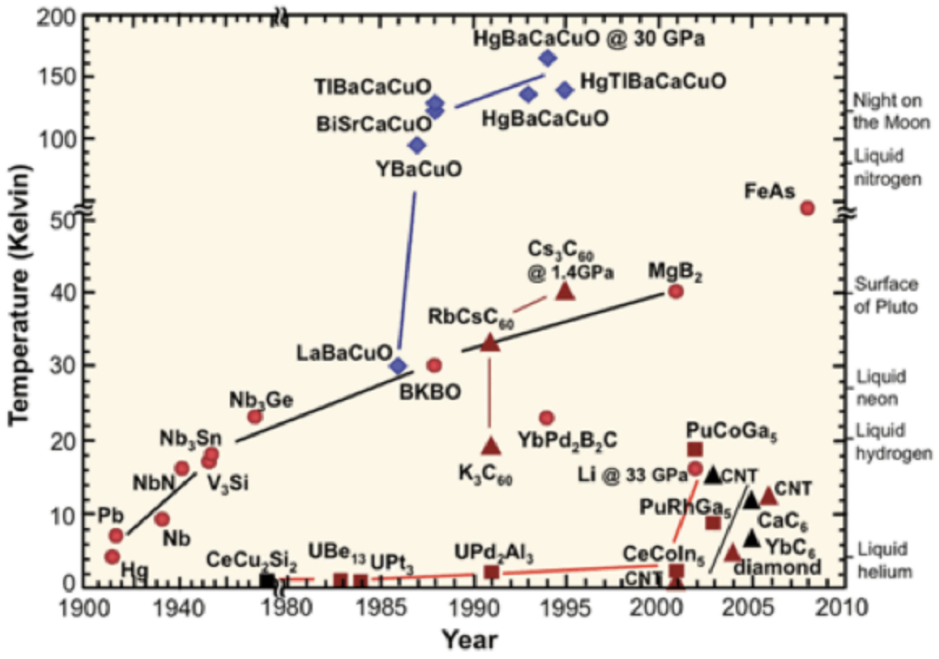

Figure 5.4: Superconducting T_c vs. time for many materials. Figure Copied from [85].

from core electrons and so strongly couples to electrons. Thus, the idea is to use hydrogen based phonons to mediate the pairing and drive up T_c as high as possible. The only problem with that is that hydrogen does not crystallize at room pressure, hence the need for very high pressures to create crystalline hydride materials. There has been a lot of very solid scientific work showing that this can indeed happen [86]. However, there have also been recent claims of room-temperature superconductors at around 160 GPa and then at around 1 GPa, which are still largely impractical pressures but impressive sounding feats nonetheless. However, it seems highly likely that both of those reports are based on fabricated data, hence I will not cite them here. At least, the first report at 160 GPa has already been proven to, at least, use highly unusual background subtraction and likely fabricated data, for which it was retracted. At the time of writing, the results at 1 GPa has not existed long enough to know, but issues with this result have already emerged. Nevertheless, the field as a whole is still an active and sound area of research, but for now, I think it is still very safe to say that no room-temperature superconductors have been created in the field of high-pressure superconductivity.

Finally, we arrive at the area of ongoing research relevant to the present thesis, which is also new within the last two decades: light induced superconductivity, where reports of superconductivity at room-temperature have also been made but not verified independently. This will be the focus of this section.

5.2.1 Overview of Prior Work on Light Induced Superconductivity

The field of light induced superconductivity has been pioneered primarily by Cavalleri and his massive teams, but the field has gained attention from other groups of theorists and experimentalists, and it is now too big to review in its entirety. Instead, I will just highlight the salient points relevant to our experiments.

Cavalleri et al. have been pumping materials with very intense mid-IR pulses and probing the response of the systems with several techniques but primarily the optical conductivity with THz reflectivity measurements. Using this technique, they have seen signatures of superconductivity

up to temperatures, T^*, far above their equilibrium T_c in several materials of relevance to our ambitions: K_3C_{60} [87] (150 K$\approx T^* > T_c$ = 20 K, but with signs up to 300 K), YBCO [88, 89] (310 K$\approx T^* > T_c$ = 50 K), and $\kappa-(BEDT-TTF)_2Cu[N(CN)_2]Br$ [90] (50 K$\approx T^* > T_c$ = 12 K). This work has been expanded on, leading to many articles [2, 91–95] to name just a few.

To see what kind of experimental evidence exists, let's focus on the material with the most evidence, K_3C_{60}, summarized by Budden et al. [93]. The THz reflectivity measurements have three primary signatures of the possible superconductivity: The superconducting gap makes (**1**) the reflectivity go to 1 and (**2**) the real part of the conductivity go to 0 for sub gap frequencies. There is a delta function in the real part of the conductivity at 0 frequency, signifying the dissipationless current flow in the DC limit; however, this cannot be directly probed by the THz optical pulse. Nevertheless, due to the Kramers-Kronig relationship, this delta function singularity in the real part of the conductivity leads to (**3**) a $1/\omega$ divergence in the imaginary part of the conductivity. Naturally, all of these signals are present in the measurements of the non-excited K_3C_{60} at $T<T_c$; however, surprisingly, they are also present after photoexcitation with an intense mid-IR pulse at T= 100 K (see Fig. 5.5). Cavalleri et al. mapped out the temperatures, showing the signs were strongly present at temperatures up to 150 K$\approx T^*$ with some weak signs up to 300 K. Initially, they only saw signs of this transient state for up to about 1 ps; however, by stretching their IR pulses to $\mathcal{O}$(ns), they were able to see the signatures of the superconductivity for up to $\mathcal{O}$(ns). The longer lifetime enabled resistivity measurements to be made with standard electrical contacts via a 2-point measurement. They had to calibrate the contact resistance with a 4-point measurement, which was subtracted from their transient 2-point measurement, yielding a value for the resistivity consistent with 0 after background subtraction; however, their uncertainty range is $\mathcal{O}(\Omega)$, which is quite large considering that copper wire often has a resistance $< 1\Omega$ (see Fig. 5.6). Additionally, they made pressure dependence measurements on the transient state that were consistent with superconductivity [92]. Together, this is suggestive that they are seeing a transient superconducting state.

The evidence for the superconductivity in $\kappa-(BEDT-TTF)_2Cu[N(CN)_2]Br$ is based off of

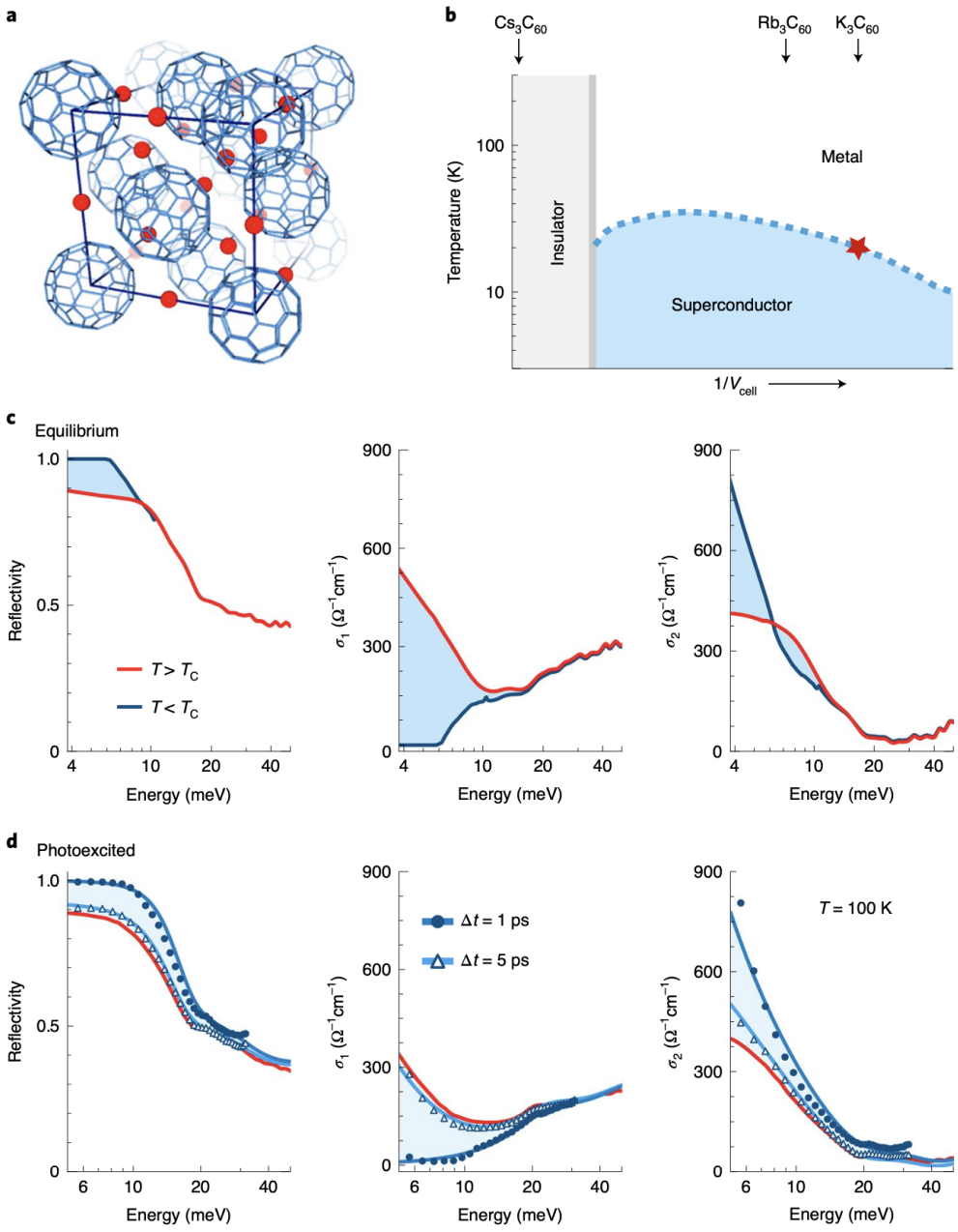

Figure 5.5: K_3C_{60} light induced superconductivity: a) depiction of the unit cell of K_3C_{60}. b) Phase diagram of C_{60} family of compounds as a function of unit cell volume, with K_3C_{60} T_c shown as the red star. c) the optical reflectivity, real conductivity, and imaginary conductivity as measured by THz reflectivity measurements (left to right) at temperatures above and below T_c without optical excitation. d) The same as (c), but now the equilibrium measurements at T= 100 K are compared to measurements made at 1 ps and 5 ps after excitation by an intense mid-IR pump pulse. Figure Copied from [93].

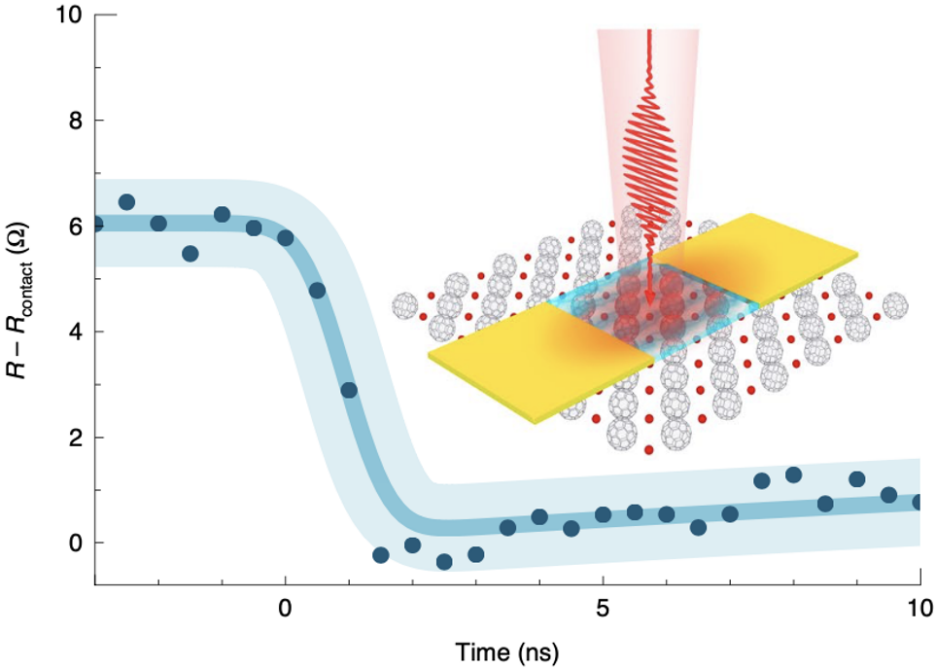

Figure 5.6: Transient 2-point resistance measurement of K_3C_{60}: Time series depicts sharp drop in resistance to a value consistent with 0 after excitation with mid-IR pump pulse. Shaded region depicts uncertainty estimate. Inset depicts schematically the excitation followed by resistance measurement. Figure copied from [93].

similar interpretations of the THz reflectivity measurements as K_3C_{60}. The evidence in YBCO is also based off of THz reflectivity measurements, showing a similar enhancement of the low frequency imaginary part of the conductivity. Additionally, in the transient state a plasmon edge emerges in the THz measurements, which is associated with the Josephson plasmons present when the system is in a superconducting phase. The phase diagram was mapped out by Kaiser et al. [89] and shown in fig. 5.7. Note that their transient superconducting state was only observed for underdoped YBCO but with T^* reaching well above room temperature.

Much effort has been made to understand the origins of these transient states. From an experimental point of view, the frequency of the pumping pulse has been swept in these experiments. Initially, in K_3C_{60} the pump was thought to resonate with a $T_1U(4)$ phonon mode; however, the response is probably too broad ($\sim 6-15$ μm) to be strongly associated with this phonon mode. However, the $\kappa-(BEDT-TTF)_2Cu[N(CN)_2]Br$ superconducting like response was only observed for pump wavelengths $\sim 6.8-8$ μm, which is near to C=C vibrational modes of the ET molecule. Additionally, in YBCO the superconducting response is only seen for frequencies that resonate with one of two apical oxygen modes ($\sim$ 17.6 and 15 μm). The latter situations point to the importance of phonons, while the results with K_3C_{60} suggest the phonons may not play a critical role. Meanwhile, much theoretical work has been done [96, 97]. Some have explored the role of phonons. Some have proposed that an initial fluctuating pair density wave state when driven will yield similar experimental signatures.

While the field has continued to progress and gained much attention, there remains many open issues. There has been no widely accepted microscopic theory put forth to explain the transient states being studied. Additionally, while the experimental signatures are suggestive of a transient superconducting state, they have not measured the Meissner-Ochsenfeld effect, nor a 4-point DC resistance of 0, leaving open the possibility that this is some other phenomena that is not superconductivity. For example, it has been proposed that other mechanisms may account for their data (e.g. charge density waves (CDW)] [98] or an induced polarization on the surface [99]). However, I can personally attest that there is still strong debate in the community about what is being ob-

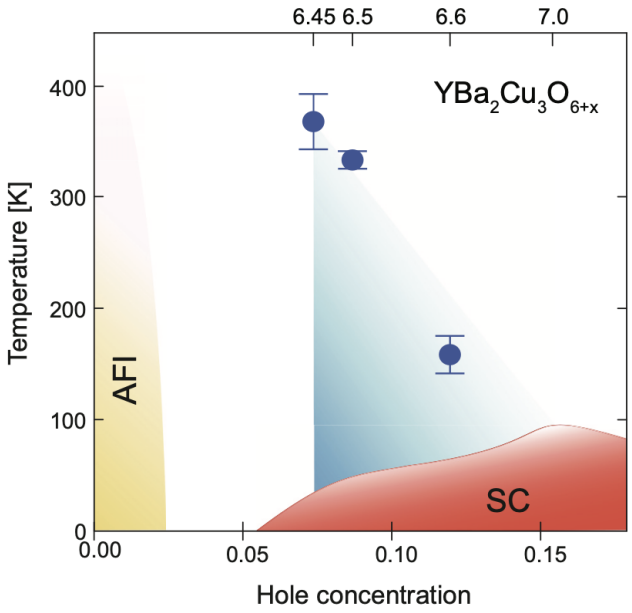

Figure 5.7: Schematic phase diagram for YBCO. The blue shaded region shows the photo induced superconductivity transition temperature, T^*. Figure Copied from [89].

served with no alternative theory being accepted either, making the field an exciting area of ongoing research, especially with the prospect of superconductivity occuring at room temperature!

Chapter 6

Towards Measuring Light Induced Superconductivity: Laser Systems Overview and Upgrades

In an effort to better understand the transient superconducting like state, we are interested in conducting time-resolved ARPES experiments. As already shown, if the system becomes superconducting, we should generally see a superconducting gap and be able to determine the pairing symmetry, adding new information and additional evidence that the transient state is in fact superconducting. While this would just add more circumstantial evidence, time-resolved ARPES might also be able to directly rule out some alternative scenarios. A leading alternative explanation involves charge density waves (CDWs), and it was shown theoretically that time-resolved ARPES should be able to distinguish between a CDW and a superconducting state [100], which could rule out CDWs. On the other hand, some of the theories could be addressed directly with time-resolved ARPES. A driven pair density wave state would introduce an additional periodicity into the system, potentially replicating bands (similar to what we saw from surface reconstructions in CuMnAs), which would be detectable directly in ARPES. If any replicated bands could be associated with a pair density wave periodicity, that might be a smoking gun. Alternatively, if the superconductivity results from strong enhancement of a phonon mediated pairing mechanism, it is possible to directly measure the phonon coupling strength to the electronic structure [101], potentially revealing this enhancement. Therefore, time-resolved ARPES could provide extremely valuable, potentially conclusive, information about the transient state in these systems.

Naturally, we would like to be able to study all of the materials that exhibit the superconduct-

ing like response, but ARPES is a challenging measurement with limitations, particularly surface sensitivity. YBCO is notoriously difficult to cleave, and while $\kappa-(\mathrm{BEDT-TTF})_2\mathrm{Cu[N(CN)_2]Br}$ is layered, the layers are ionically bound making cleaving unlikely. However, high resolution angle integrated photoemission experiments on the material have been done, opening the possibility of measuring a transient superconducting gap [102], although resolving the gap would require better energy resolution than they had. Meanwhile, $\mathrm{K_3C_{60}}$ is highly reactive to air, meaning that a single crystalline sample of $\mathrm{K_3C_{60}}$ must be grown in the same UHV system as the ARPES measurements are made, which is not our specialty, making that more difficult for us, although it is a work in progress. In the short term, the easiest material for us to study is underdoped BSCCO, which cleaves very well, and although Cavalleri and his team have not been able to measure a superconducting like response in this system (primarily due to technical difficulties that make their measurement infeasible), it has very similar physics, including apical oxygen modes near 17 μm pump wavelength, and so we expect it could have the same phase. However, BSCCO presents the most difficult experimental parameters for our optical system, namely the conversion efficiency of our difference frequency generation (DFG) at 17 μm is very poor, making strong pulses difficult for us to achieve. Therefore, I have upgraded the time-resolved ARPES system around the requirements of BSCCO, which will also enable studies of $\mathrm{K_3C_{60}}$ as soon as we have a sample and $\kappa-(\mathrm{BEDT-TTF})_2\mathrm{Cu[N(CN)_2]Br}$, at least measuring the angle integrated spectra.

Our newly improved system is built upon the time-resolved ARPES system built by several members of my group that came before me, primarily Stephen Parham [103]. This system has a broadly tunable IR pump pulse, courtesy of optical parametric amplification (OPA) ($\sim 1.2-2.5\ \mu$m) and DFG ($\sim 4-20\ \mu$m) from light conversion, and a variable bandwidth 6 eV probe pulse designed by Parham [103]. To take full advantage of the available IR pump wavelengths with as much power as possible, I designed and built a purge system. Additionally, the weak pump at 17 μm makes the extremely difficult problem of finding spatiotemporal overlap of the pump and probe on the sample, highlighted by Parham [103], even more challenging; however, we built a special first-of-its-kind window in a window to make this problem easier. Finally, maintaining that spatial

overlap for the long times required to make measurements sensitive enough to study light induced superconductivity is a real challenge, which I solved by implementing a custom pointing stabilization system. Finally, the system continues to use the ARPES chamber that was primarily designed, built, and maintained by Justin Griffith, allowing long lived sample surfaces due to the special cryogenic shields that achieve a pressure of $< 1 \times 10^{-12}$ Torr. Additionally, our studies will make use of a high-resolution 7 eV laser ARPES system, which does not have time resolution, for initial maps and very good energy resolution data. The 7 eV system uses the same ARPES system, and prior to my upgrades shared a beam path with the 6 eV system, making switching between the two difficult. My new system uses different ports for these systems, making switching trivial.

In this section, I will discuss the optical setups, including some of the physics involved, and the upgrades to the system that I made. This work will enable future measurements of light induced superconductivity with time-resolved ARPES, potentially answering many open and important questions in the field.

6.1 Brief Theoretical Background

6.1.1 Ti:Sapphire Lasers

Titanium doped Sapphire (Ti:Sapphire) based lasers have played an important role in the development of ultrafast lasers, because these materials have a large gain bandwidth, allowing the fast pulses (typically $10 - 100$ fs). To create the pulses in an oscillator, Ti:Sapphire is placed in a cavity with tunable frequency dependent dispersion (typically prisms), tunable beam divergence (translatable curved optics), and pumped with a 532 nm laser, which creates the population inversion. This system will lase in continuous wave (CW), but as mentioned broadband ultrashort pulses from "mode locked" operation are the goal. The broadband pulses require that the round trip phase accumulation in the cavity is close to the same for a large range of frequencies, which is achieved by the controlling the insertion of prisms into the beam path. Next, the CW efficiency needs to be worse than the mode locked efficiency to prefer mode locked operation. This is achieved

by detuning the beam divergence in the cavity, making CW lasing less efficient. Meanwhile, the Ti:Sapphire crystal exhibits a nonlinear refractive index, $n(I)$, that depends on the intensity of the field propagating through the crystal. Therefore, for a spatial profile with more intensity towards the center and less on the edges (e.g. a Gaussian), the center of the pulse will travel slower than the edges, which is a lensing affect called Kerr lensing. The mode locked pulses are short in time and thus higher in peak intensity than the CW, thereby experiencing more Kerr lensing than the CW mode. The extra lensing of the mode locked pulse compensates for the intentional detuning of the beam divergence in the cavity, making mode locked operation more efficient than CW operation. This process is called Kerr lens mode locking. Finally, all that is needed is something to equalize the offset phase (time=0) of each frequency component in the cavity, which is achieved by a quick impulse to one of the prisms that all of the frequencies will agree happened at the same time. This kicks the laser into mode locked operation, yielding ultrafast pulses of $\mathcal{O}$(nJ) at $\mathcal{O}$(MHz) repetition rates typically centered around 800 nm ($\sim$ 1.55 eV).

While these pulses are incredibly short in time, they are still not strong enough to drive many of the nonlinear processes required to make the UV probe and IR pumps desired for time-resolved ARPES. Therefore, these pulses are amplified; however, the amplified ultrashort pulses are so intense that they would burn optics instantaneously. Therefore, to avoid this, a Chirped Pulse Amplification (CPA) scheme (see Fig. 6.1) is used. CPA works by introducing a frequency dependent phase across the pulse bandwidth that spreads the pulse in time by making redder and bluer components spread in time, reducing the peak intensity of the pulse. After amplification, the frequency dependent phase is removed from the spectrum in a compressor, which recompress the pulse in time to an ultrafast pulse. The stretcher and compressor use dispersive elements (typically gratings), which cause the different frequency components to traverse different spatial paths of varying length, introducing the frequency dependent phase. Ideally the compressor perfectly removes the phase introduced by the stretcher. Notice that the stretcher includes a telescope that images the first grating behind the second grating, effectively making the stretcher the mirror image of the compressor, guaranteeing that the phase introduced by the stretcher is perfectly removed

by the compressor. However, in practice aberrations in the imaging system introduce phase that is not perfectly removed, particularly at higher orders of the polynomial expansion of the frequency dependent phase across the spectrum (think terms $\propto \omega^4$ or higher); however, for our pulse width in time of $\sim$ 70 fs these higher order contributions are not a limiting factor. This is called CPA because a chirping sound is also due to a phase delay of different frequency components in an audio pulse. CPA was first introduced by Donna Strickland and Gérard Mourou [104], affording them the 2018 Nobel prize in physics.

The amplification process involves another Ti:Sapphire crystal pumped by a 532 nm laser, which allows the oscillator pulse to steal the power through stimulated emission, amplifying the pulse. There are generally two schemes for this: a multi pass process where the pulse passes through the Ti:Sapphire many times but never quite along the same path, eventually leaving the amplification stage. Alternatively, a regenerative (regen) cavity can be used, which is preferred for time-resolved ARPES due to the higher repetition rates achievable. A regen cavity works by using an electrically controllable wave plate (a Pockel's cell) in conjunction with static wave plates and polarizers to electrically switch the cavity between an open and closed cavity. That is, in one state, the polarization changes in the cavity such that a polarizer ejects pulses before they can traverse the cavity many times; however, in the other state, light is reflected back into the cavity by a polarizer, allowing many round trips in the cavity. During the period where round trips are forbidden, the cavity has very high loss and lasing is not preferred. This allows the 532 nm pump time to build a large population inversion in the Ti:Sapphire crystal. Once the inversion is approaching saturation, the Pockel cell injects the oscillator pulse and closes the cavity, allowing the pulse to make many round trips, stealing power through stimulated emission from the Ti:sapphire crystal on each pass. Eventually, the pulse would dump power back into the crystal, recreating the population inversion. However, before this happens, the Pockel cell switches the cavity back to an open state, allowing the pulse to leave at its peak power.

The above is just a crude outline of how a Ti:Sapphire oscillator and CPA based regen amplifier work to create intense ultrafast pulses. For a more complete discussion of the physics,

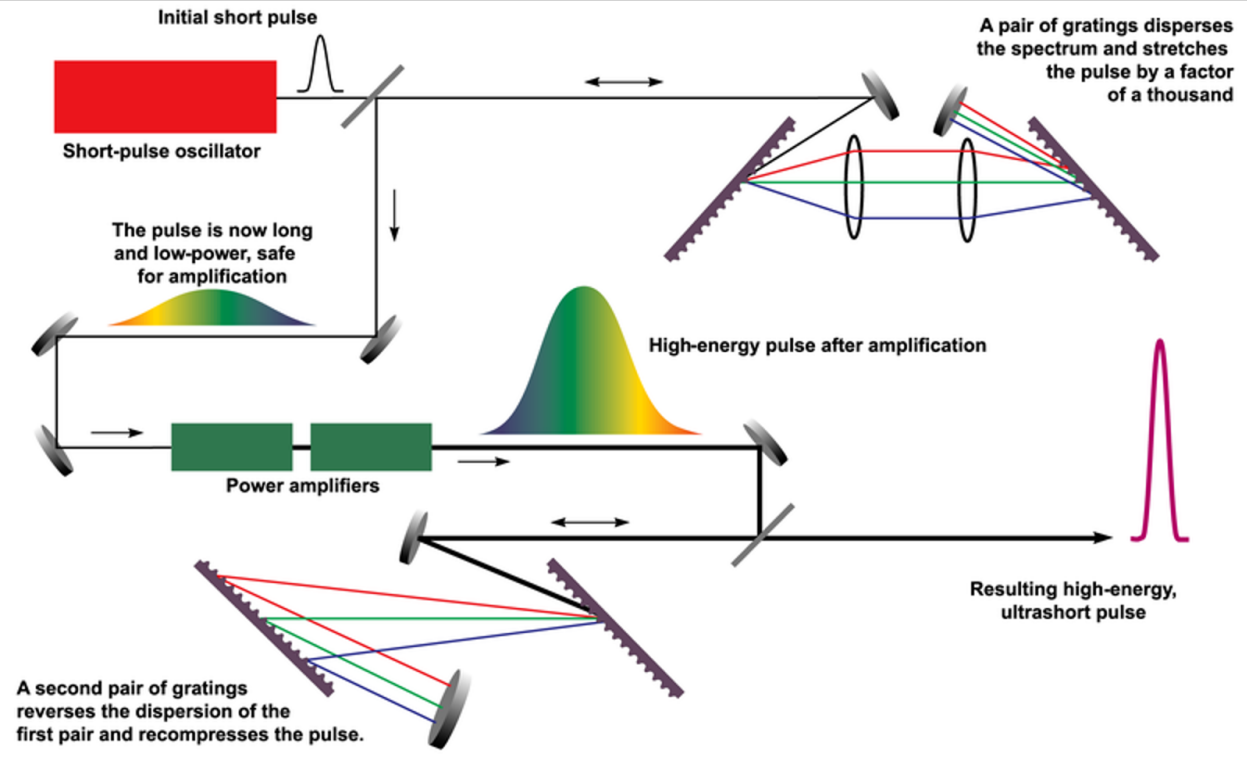

Figure 6.1: Chirped Pulse Amplification scheme. File Copied from [105].

the reader should explore one of the many text books on ultrafast pulse generation, e.g. Weiner's book is excellent [106].

6.1.2 Nonlinear Optics

All physicists are introduced to linear optics in textbooks that describe the physics of electromagnetism extremely well like Griffith's [107] and those that focus on mathematical methods to solve more complicated problems in electromagnetism (i.e. Jackson [108]), yielding nightmares in many first year physics graduate students. In either case, in linear optical media, the electromagnetic field couples to the polarization of the material linearly:

$$\vec{P} = \epsilon_0 \chi^{(1)} \vec{E}, \tag{6.1}$$

where ϵ_0 is the permittivity of free space and $\chi^{(1)}$ is the linear susceptibility of the material, which characterizes the strength of the dipole response of the material to an external electric field. This provides an excellent description of how electromagnetic waves interact with many materials due to several approximations/assumptions: 1) many materials are non-magnetic, meaning the interaction with the magnetic field is not as important. 2) Most materials are not charged, so in a multipole expansion, the monopole does not contribute, and therefore, the dipole term is of leading order. And, 3) materials are made of atoms, which pick up a polarization for displacements of the charged particles from their equilibrium positions due to $\vec{E}$. A small displacement around an equilibrium position is characterized by a harmonic oscillator, which oscillates at the driving frequency. In this case, the dipoles oscillate at the frequency of the electric field, reemitting light of the same frequency. The above linear susceptibility means that for $\vec{E}(\omega)$, $\vec{P}$ also oscillates at ω, meaning that the linear term captures this harmonic oscillator physics. In reality, this linear term is just the first of the series expansion of $\vec{P}$ in powers of $\vec{E}$, which is a good approximation because $\vec{E}$ is usually much less than the electric field in the atoms.

However, the advent of the laser made it possible to create electric fields with a strength comparable to that of the atom, opening up the field of nonlinear optics. These strong electric

fields require our perturbative expansion of $\vec{P}$ to be extended to the nonlinear terms in $\vec{E}$, which is generally

$$\vec{P} = \epsilon_0(\chi^{(1)}\vec{E} + \chi^{(2)}\vec{E}^2 + \chi^{(3)}\vec{E}^3 + ...), \tag{6.2}$$

where $\chi^{(n)}$ is the n-th order susceptibility tensor. This leads to all kinds of interesting physics, like Kerr lensing, but I wish to focus on $\chi^{(2)}$ processes, which encompasses all of the nonlinear processes used to convert our Ti:Sapphire pulses to laser pulses for time-resolved ARPES.

To see the effect of $\chi^{(2)}$ on the frequency components of the polarization vector, let's assume for simplicity that $\chi^{(2)}$ is diagonal, i.e. the polarization vector points along $\vec{E}$ and thus ignore polarization. Furthermore, let's focus on two frequency components of $E(t)$, $E(t) = E_1 \exp(-i\omega_1 t) + E_2 \exp(-i\omega_2 t) + c.c.$. The second order dipole response, $P^{(2)}$, is given by Eqn. 6.2 as

$$\begin{aligned} P^{(2)}(t) &= \epsilon_0\chi^{(2)}\left(E_1^2 e^{-2i\omega_1 t} + E_2^2 e^{-2i\omega_2 t} + 2E_1E_2e^{-i(\omega_1+\omega_2)t} + 2E_1E_2^* e^{-i(\omega_1-\omega_2)t} + c.c.\right) \\ &\quad +2\epsilon_0\chi^{(2)}(E_1E_1^* + E_2E_2^*). \end{aligned} \tag{6.3}$$

Notice that due to the second order susceptibility, the dipoles now oscillate with frequencies $2\omega_1$, $2\omega_2$, $\omega_1 + \omega_2$, and $\omega_1 - \omega_2$, and there is also a frequency independent term. The oscillating dipoles will reemit light at the same frequency that they oscillate at, meaning that light passing through a crystal with a second order nonlinear susceptibility can generate light at the sum of the frequency components, sum frequency generation (SFG), and the difference of the frequencies, difference frequency generation (DFG). The special case of $\omega + \omega = 2\omega$ is called second harmonic generation (SHG), while the case where $\omega - \omega = 0$ is called optical rectification (OR).

The conversion of frequencies of light to different frequencies stems from the large displacements of the charge due to the larger field intensities. These larger displacements notice the non-quadratic terms of the potential energy landscape as a function of displacement. In the language of quantum field theories, the terms $\propto x^{(n+1)}$ correspond to terms with $(n+1)$ ladder operators, which correspond to $(n+1)$-point vertices in Feynman diagrams. For example, $n + 1 = 3$ allows for processes where two quanta of dipole oscillation at frequencies ω_1 and ω_2 are destroyed and create one frequency of ω_3 and also the time-reversed process where one dipole oscillation quanta

of frequency ω_3 splits into two photons of frequencies ω_1 and ω_2. So, we see that the nonlinear conversion of light stems from the anharmonic terms of the potential energy as a function of displacement, and we see that second order nonlinear process come from a cubic term in the potential energy landscape. In general, the susceptibility will be related to this potential energy landscape, which is constrained by symmetries of the system, which in our case is symmetries of the crystals. The most relevant symmetry to us is whether the crystal is centrosymmetric—symmetric under inversion, because if this is true, then the energy landscape cannot have odd powers, and $\chi^{(2)}$ is zero along with all other odd powers.

As always conservation laws constrain the nonlinear processes. Energy conservation is the reason that the frequencies add the way that they do. The above discussion of vertices for the dipole oscillation will ultimately lead to an effective theory for the photons that will also have 3-point vertices. At the vertex, energy will be conserved, requiring the sum of created photon energies to equal the sum of destroyed photon energies. So two photons being destroyed to create one is an SHG process where energy conservation requires the new photon energy to have $\omega_3 = \omega_1 + \omega_2$. Meanwhile, one photon splitting into two photons leads to a DFG process, with $\omega_2 = \omega_1 + (\omega_2 - \omega_1)$, creating photons at the difference frequency, $\omega_3 = \omega_2 - \omega_1$ (notice that the term proportional to the difference frequency oscillation of the dipole in Eqn. 6.3 has an E and an E^* component, corresponding to creation of ω_1 and annihilation of ω_2 giving $\omega_3 = \omega_2 - \omega_1$). This process is also called Optical Parametric Amplification (OPA), because one of the input frequencies, ω_1 above, is actually amplified during the difference frequency generation.

Momentum conservation is also required and leads to phase matching conditions. That is the momentum of destroyed photons must equal that of created photons, for SFG $\vec{k}_1 + \vec{k}_2 = \vec{k}_3$. Using the dispersion relation of the material this can be converted to $n(\omega_1)\omega_1/c + n(\omega_2)\omega_2/c = n(\omega_3)\omega_3/c$ for collinear beams. Physically, if the above conditions are not satisfied, then the conversion efficiency is drastically limited, because if the momentums are not the same, then the driving field can get out of phase with the fields created by the nonlinear processes, which allows the created fields to induce the time-reversed nonlinear process, leaking power back into the original driving

field frequency. Thus, to have efficient nonlinear processes, one must satisfy the phase matching condition. However, this is not trivial. For example considering SHG, $\omega_1 = \omega_2 = \omega = \omega_3/2$, which reduces the momentum conservation requirement to $n(\omega) = n(2\omega)$, which is generally not true for materials. However, one can take advantage of uniaxial crystals that have rotational symmetry about one axis but not around the two orthogonal axes (e.g. a tetragonal crystal structure). Light polarized along the axis of rotational symmetry (ordinary rays) will propagate at a different velocity than light polarized orthogonal to that (extraordinary rays). One can often achieve phase matching between different frequencies of ordinary and extraordinary light beams by choosing the propagation direction of the light through the crystal with respect to the rotational axis of symmetry of the crystal. There are two types of phase matching that exploit this: Type I makes an extraordinary ray from two ordinary rays (o+o=e), while Type II utilizes ordinary plus extraordinary to make an extraordinary ray (o+e=e). Type I is utilized in our systems.

The last thing to consider in nonlinear optics is that our light is made of broad bandwidth pulses. In general, one cannot achieve phase matching perfectly over a range of frequencies, but instead, one tries to phase match as close as possible over as broad a range of frequencies as possible. That is, one tries to match the refractive index at a point and as many derivatives of the refractive index as possible. The slight mismatch is captured by mismatched derivatives, leading to temporal walk off of the pulses involved in the conversion. This means that the driving pulse might get ahead in time of the pulses created through the nonlinear process. This in turn means that the driving pulse creates more nonlinear light that destructively interferes with the light originally created. This limits the length over which light can be coherently generated by nonlinear processes before the power starts to decrease. That is, the better the phase matching, the longer the distance over which power can be driven into the pulses generated by the nonlinear conversion, allowing more powerful pulses generated by nonlinear conversion.

There is much more to say about nonlinear optics than the overview given here. The interested reader should refer to a comprehensive book on the subject, e.g. Boyd [109].

6.2 Overview of Optical Systems

The laser based ARPES systems in our lab are shown in Fig. 6.2. There are two separate systems, the 7eV ARPES system and the time-resolved ARPES system.

The 7eV laser system offers the best energy resolution $\sim$ 1 meV on a good day (normally $\lesssim$ 5 meV), and it has high data throughput, making this system extremely useful for a fast Fermi map and high resolution data. The system starts with a Coherent Paladin laser, which produces 355 nm, $\sim$ 15 ps pulses at 80 MHz repetition rate. The relatively long pulses and high repetition rates enable the high data throughput with minimal space-charge and narrow bandwidth due to the time-bandwidth product. The 355 nm pulses are directed into a pure nitrogen purge box where the pulses are frequency doubled (SHG) in a KBBF crystal, which has a very high band gap, allowing the generation of 7 eV pulses without reabsorption by the crystal. The pure nitrogen environment is required to avoid atmospheric absorption of 7 eV by Oxygen. The 7 eV pulses are directed through a beam tube into a smaller box attached to the ARPES chamber. In this box, the 7 eV is focused with a CaF_2 lens through a CaF_2 UHV window into the chamber and onto the sample.

The time-resolved ARPES system enables the electronic dynamics of materials to be studied, and it is built off of a KM Labs Wyvern laser system. This system starts with a Ti:Sapphire oscillator (KM Labs Griffin), which produces ultrafast ($\lesssim$ 40 fs), $\mathcal{O}$(nJ) pulses centered at 800 nm. These pulses then enter a Ti:Sapphire regenerative amplifier (KM Labs Wyvern) that is pumped by a Coherent Lee laser at 532 nm, producing $\sim$ 70 fs, 600 μJ pulses centered at 800 nm at a 20 kHz repetition rate (12 W average power). The output of the Wyvern goes through a pointing stabilization system before being split into two branches, creating an IR pump and a UV probe. The IR is generated by an OPA that seeds a DFG, and the output of the DFG goes through a pointing stabilization system. To avoid atmospheric absorption, the IR is kept in a pure nitrogen environment from generation to transmission into the UHV ARPES chamber. The UV system is a fourth harmonic generation system that produces $\sim$ 6 eV light, which is put through a time-compensated monochromator to control the trade off between time and energy resolution of the

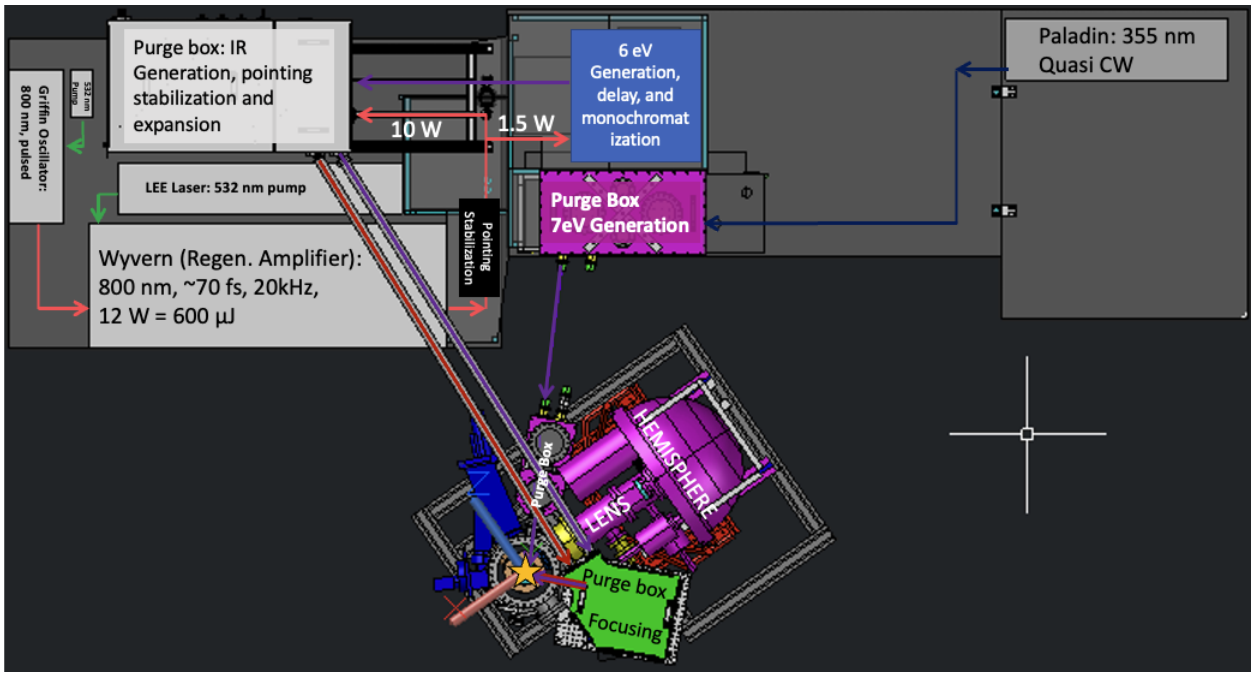

Figure 6.2: Full Laser ARPES System Layout drawn in CAD (view from above): UHV Chamber with ARPES Analyzer shown towards the center bottom, with the sample shown as the gold star. A KM Labs Wyvern laser system provides 70 fs pulses for the time-resolved ARPES system. The pulses are split into 10 W to seed the IR pump generation and 1.5 W for the 6eV probe generation. The 6eV is sent into a nitrogen purge box, where the IR is generated. Both beams traverse beam tubes to a smaller purge box, which combines and focuses the beams onto the sample. Separately, a Coherent Paladin laser provides 355 nm quasi-CW [$\mathcal{O}(10ps)$, $\mathcal{O}$(100MHz) repetition rate] light that is frequency doubled inside of another nitrogen purge box, generating 7eV light. The 7eV is sent through a beam tube (not shown) to a smaller puge box that focuses the 7eV onto the sample. Full system CAD drawing from Justin Griffith. I drew the IR purge boxes and Wyvern laser systems (the latter not to scale).

probe. The 6 eV light is also subject to a variable path length delay that controls the time between the pump and probe pulse arrival on the sample. The IR is expanded and then both the 6eV and IR are focused then made collinear before entering the chamber through our special window inside of a window. In the following sections, I will describe these various systems in more detail.

6.2.1 6eV Probe Generation and Monochromatization

Stephen Parham designed the ~ 6 eV generation scheme, utilizing a fourth harmonic process that he describes excellently in his thesis [103]. Therefore, I will just give a quick overview of the system here. The process consists of three successive Type I SFG processes in β-barium borate (BBO) crystals. The first process takes two $\sim$ 800 nm ordinary (H-polarized) photons from the fundamental pulse and makes one extraordinary (V-polarized) $\sim$ 400 nm photon, creating a 400 nm pulse [800 nm(o)+800 nm(o)$\rightarrow\sim$ 400 nm(e)]. Due to the small mismatch in group velocity between the 400 nm and 800 nm pulses, the two pulses are no longer perfectly overlapping in time. So, a Calcite time plate is used to restore temporal overlap of the pulses. Additionally, a dual wave plate rotates the fundamental pulse polarization to vertical and leaves the 400 nm pulse vertically polarized after a full π rotation. Next, one ordinarily polarized photon (V-polarization) is taken from each of the pulses to create a 3rd harmonic extraordinarily polarized (H-polarization) pulse [400 nm(o)+800 nm(o)$\rightarrow\sim$ 267 nm(e)]. Again the pulses are delayed in time, but in this case, there is no suitable time-delay plate for these wavelengths. So the fundamental and third harmonic light are split by dichroic mirrors. The fundamental light is rotated to horizontal polarization by a half-wave plate and subjected to a tunable delay stage to allow temporal overlap in the final BBO crystal. The first and third harmonic are recombined with another dichroic mirror and sent collinearly through the final BBO. Finally, an ordinary (H-polarization) photon is taken from each of the fundamental and third harmonic pulses and combined to make an extraordinary (V-polarization) pulse of fourth harmonic [267 nm(o)+800 nm(o)$\rightarrow\sim$ 200 nm(e)]. Lenses can be (but are not) added to focus the beams into the final BBO to enhance conversion efficiency. After separation with dichroic mirrors, we are left with a fourth harmonic ($\approx 6.2eV$) pulse of light.

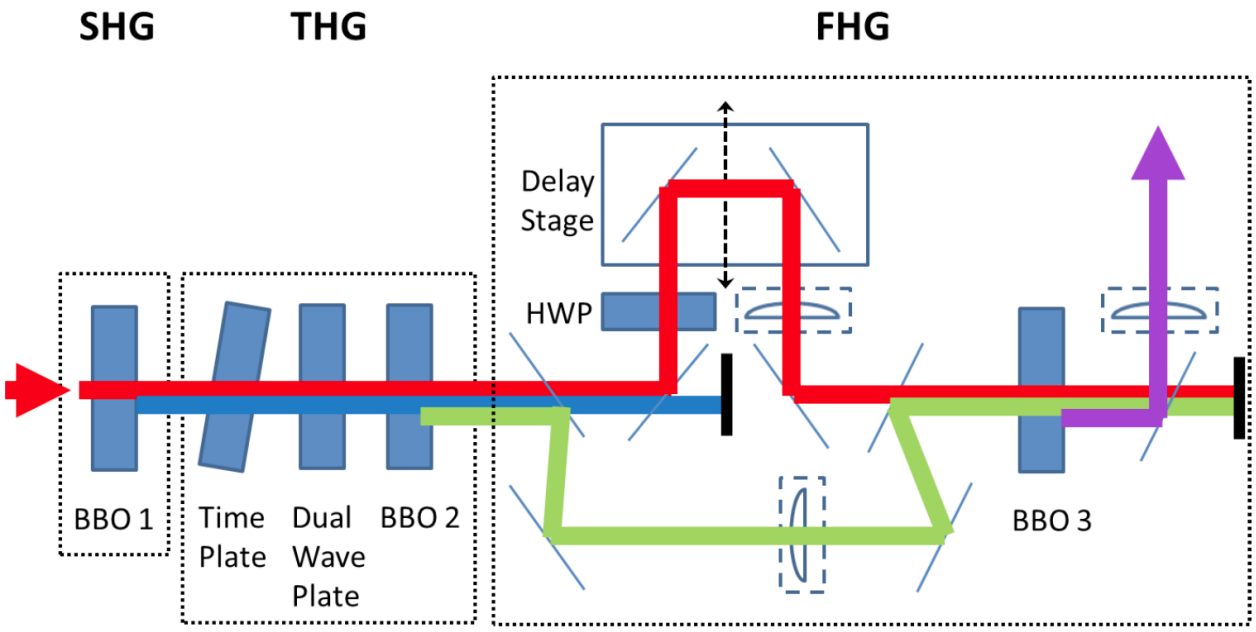

Figure 6.3: Fourth Harmonic Generation Scheme: The Fourth Harmonic is generated by three successive Type I SFG processes each involving the fundamental in BBO crystals. The final result is ~ 6 eV photon pulses. Figure Copied from [103].

This pulse of light has a time width of $\mathcal{O}$(100fs), which is faster than the $\mathcal{O}$(ps) dynamics that Cavalleri saw. The excess time-resolution yields unnecessarily poor energy resolution via Heisenberg. Additionally, to resolve superconducting energy gaps, we want the best energy resolution possible. So, to make a better measurement, we use a time-compensated monochromator (see Fig. 6.4). This is essentially a stretcher designed to introduce no phase at all. The setup consists of identical plane gratings placed 4f apart with a telescope placed in between. The first lens brings the frequency propagation vectors parallel while focusing the spatial mode. Thus, at the focal plane, the frequencies are mapped onto spatial coordinates, allowing a variable slit to block unwanted frequencies. Larger slits allow larger bandwidth (better time resolution and worse energy resolution), and can be translated in the focal plane to control the center wavelength, to an extent (see Fig. 6.5). The inverse process reconstructs the pulse without introducing unwanted phase, except for the minimal dispersion in the CaF_2 lenses, which is not so critical for a $\mathcal{O}$(ps) pulse.

The end result is a variable bandwidth ~ 6.2 eV pulse that can induce photoemission from a sample, acting as a suitable probe pulse in time-resolved ARPES experiments.

6.2.2 Mid-IR Pump Generation

Our IR pump is generated in a Light Conversion Topas-C OPA that feeds a Light Conversion n-DFG (non-collinear DFG), where the DFG can be bypassed, allowing tunability of the pump wavelength over $\sim 1.2 - 2.5$ μm and $\sim 4 - 20$ μm (see Fig. 6.6 for a plot of power vs wavelength) More regions of the spectrum can be covered with additional crystals and configurations.

The OPA is a three stage nonlinear process. First a small amount of pump light is focused into a sapphire plate to generate a white light continuum (this is not an SHG process and is quite a bit more complex). This white light then overlaps in a BBO crystal with more of the pump laser to generate a small amount of signal light through a DFG process (also called an optical parametric amplification process). The DFG process is variably phase matched by motorized mounts with a selectable signal wavelength, allowing selective amplification of a narrow region of the broad white

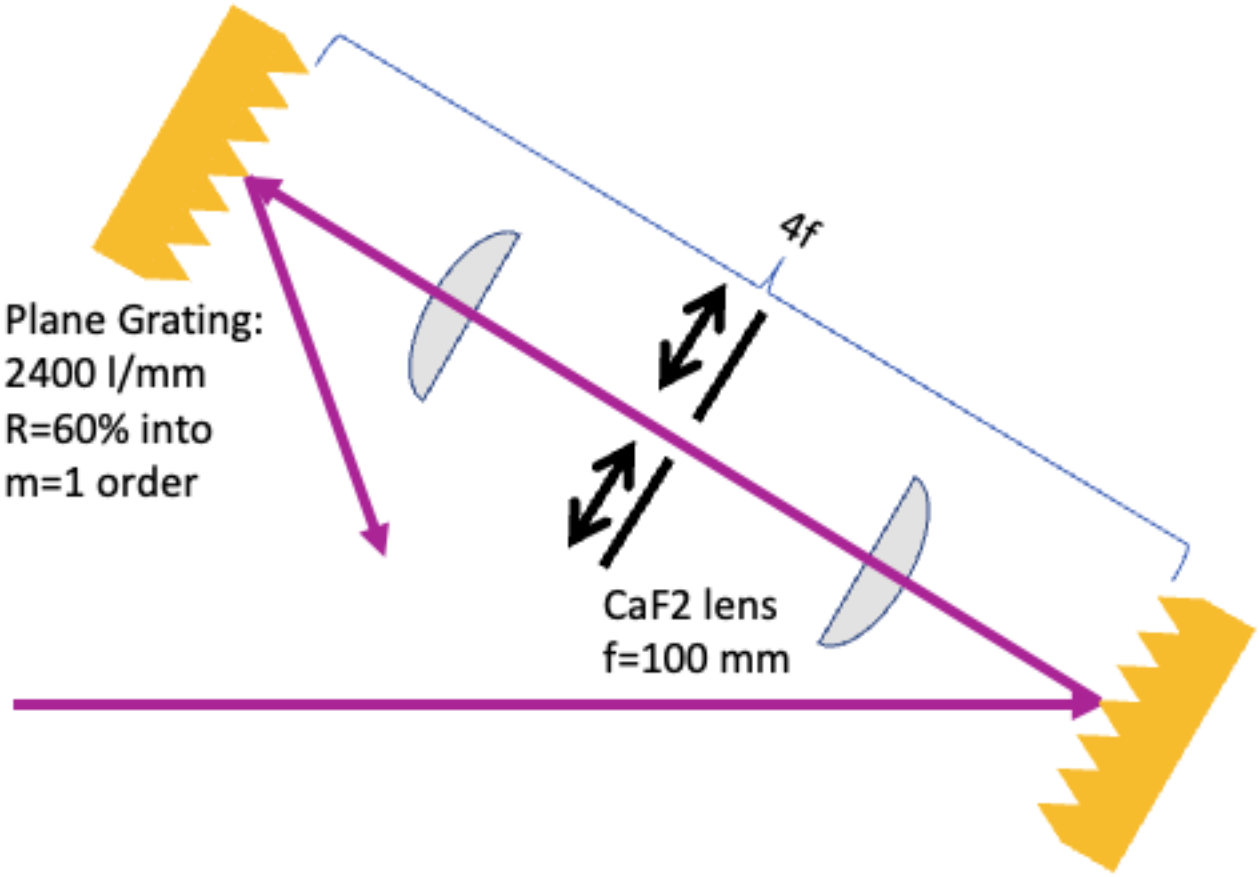

Figure 6.4: Time compensated monochromator for the 6 eV probe pulse. Two plane gratings are separated by 4f with a telescope made of CaF_2 lenses in between. In this configuration, the lenses focus the spatial mode while bringing the frequency propagation vectors parallel, mapping the frequencies onto spatial coordinates at the focal plane of the lenses. A variable slit is placed in this plane to control the transmitted bandwidth of the pulse before it is reconstructed by the inverse process, resulting in an outgoing pulse of variable bandwidth without introducing unwanted phase.

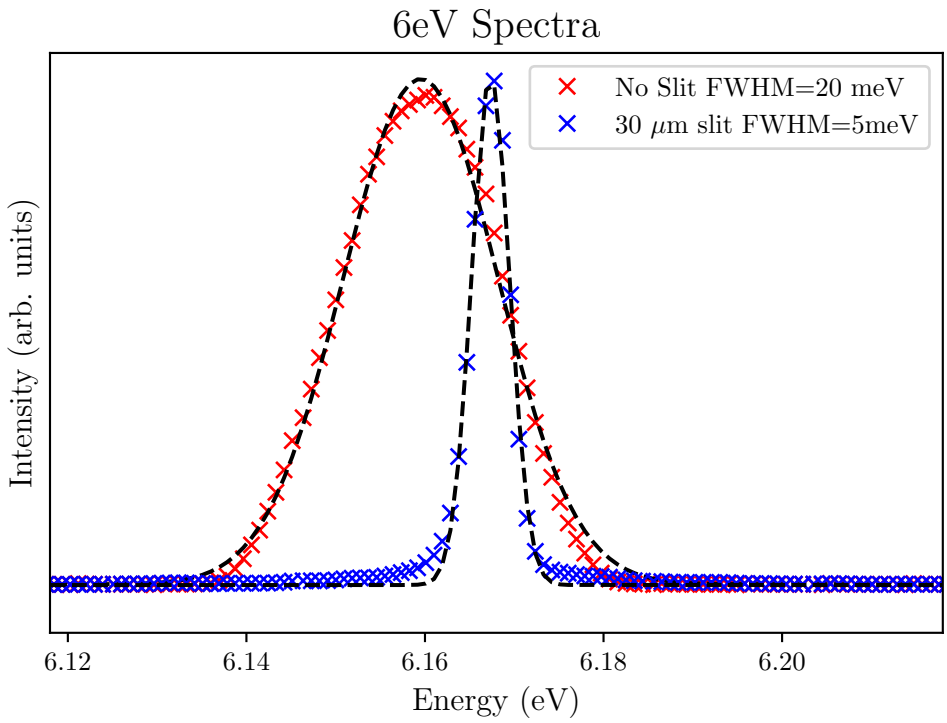

Figure 6.5: 6eV spectra acquired after the mono. Full bandwidth of the 6eV pulse with no slit in the mono and a narrowed spectrum of only 5meV with a 30μm slit are shown. Spectra are acquired with Ocean Optics HR4000 UV spectrometer.

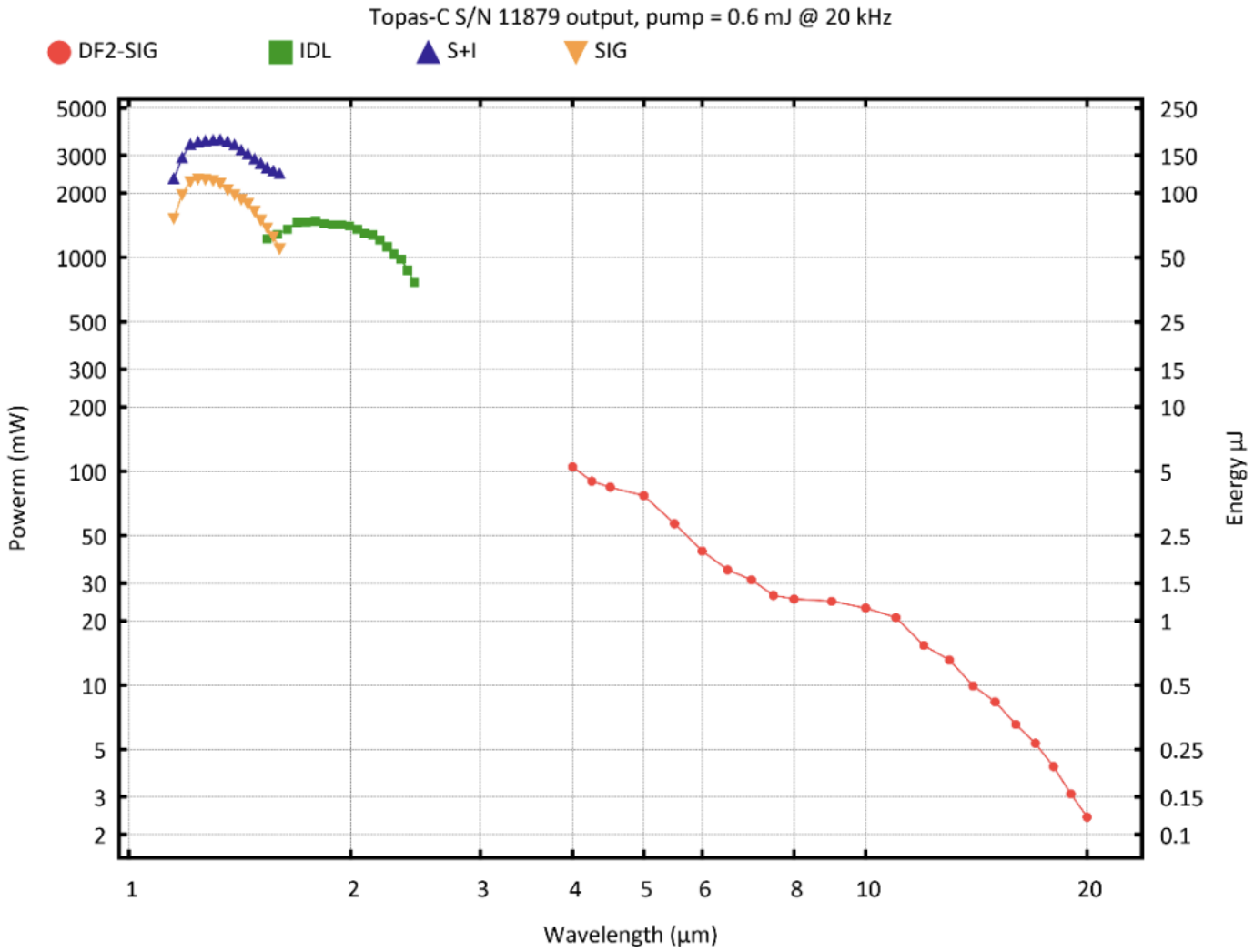

Figure 6.6: IR power vs wavelength: The figure shows the power of the output IR light as a function of wavelength over the OPA tuning range ($\sim 1.2 - 2.5$ μm) and DFG tuning range ($\sim 4 - 20$ μm). Figure courtesy of light support service tech. Note that our system has been reconfigured since this plot was made; however, the qualitative trends are similar. My improvement of the laser combined with better alignment of the system now allows us to achieve 3.5 W of signal+idler at 1.3μm and 10 mW at 17 μm, despite only pumping with 10 W (0.5 mJ pump).

light generated in the first process. The small signal generated in this process is then sent through a final BBO crystal with the majority of the pump beam, amplifying the signal in a final OPA/DFG process, creating the idler wavelength in the process. Again this process has motorized mounts for selective phase matching to control the overall output wavelengths of the signal and idler, which combined span wavelengths $\sim 1.2 - 2.5$ μm.

The nDFG is a much simpler process, where the signal and idler are crossed in a GaSe nonlinear crystal that can be rotated to selectively phase match for a specified DFG process between the signal and idler. The end result is much longer wavelengths over $4 - 20$ μm, where the non-collinear geometry allows isolation of the DFG pulse.

The combined system gives us access to a broad range of IR wavelengths to use as a pump in time-resolved ARPES experiments.

6.2.3 IR Purge System

Atmospheric absorption of the IR light by gas molecules such as CO_2 (see Fig. 6.7) not only introduces power loss but also reshaping of the pulse in time due to frequency dependent absorption, which further reduces the peak field in addition to reducing time-resolution. Additionally, our primary goal was to use ~ 17 μm pump light, which is already low power due to the phase matching conditions of the generation scheme, and the demanded intensity on the sample is already at the limits of what we can achieve (see Fig. 6.8). Therefore, it was essential to keep losses and reshaping to a minimum.

To mitigate atmospheric absorption, the IR would need to be both generated in and transmitted through a pure nitrogen environment to the UHV ARPES chamber. Therefore, two airtight boxes were made with beam tubes connecting them: one box lives on the optical tables while the other is attached to the ARPES chamber (see Figs. 6.9 and 6.10). The optics table box was much larger, because it housed the OPA and DFG, the IR stabilization system (see Sec. 6.3), and a beam expander for the IR. Additionally, the 6eV laser pulse enters the purge system at the large box. Both the 6eV and the IR pump leave this box through custom made KF ports that are used to

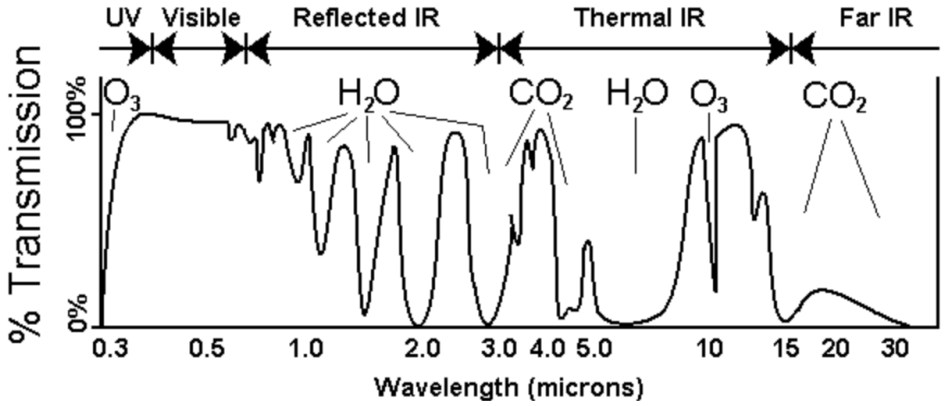

Figure 6.7: Transmission of infrared electromagnetic spectrum in atmosphere. Chart highlights gas molecules that contribute to absorption in regions of low transmission. Figure Copied from [110].

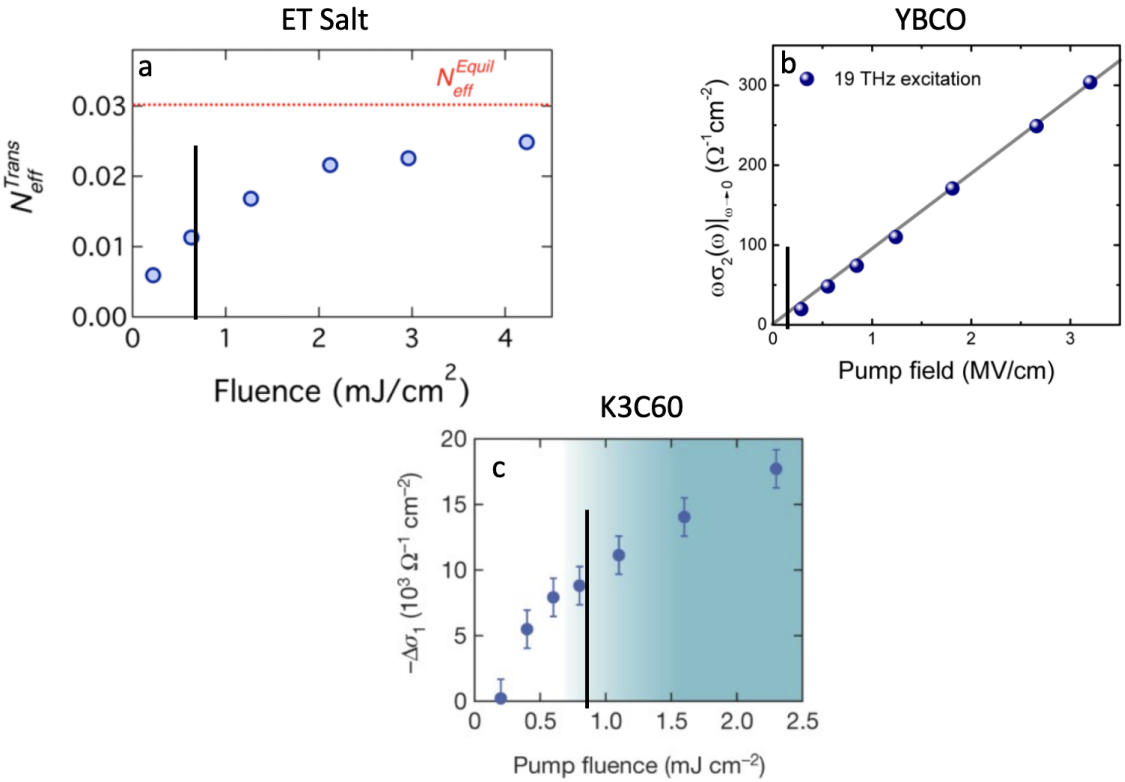

Figure 6.8: Pump intensity requirements to induce transient superconducting like state: (a) Number of "condensed" carriers as a function of pump fluence (blue circles) in $\kappa-(BEDT-TTF)_2Cu[N(CN)_2]Br$. Red dashed line shows the equilibrium value. Adapted from [90]. (b) $\omega\sigma_2(\omega)|_{\omega\to 0}$ as a function of the pump electric field strength in YBCO. Adapted from [94]. (c) The integrated loss in spectral weight of σ_1 from 0.75-2.5 Thz as a function of pump fluence in K_3C_{60}. The blue shaded region indicates parameter ranges where a superconducting model was used to fit the data. Adapted from [87]. (a-c) The black vertical line indicates the the maximum pump strength that we can achieve with our systems, highlighting the need to minimize absorption.

connect the two boxes through two long KF-40 tubes (see Fig. 6.11). The smaller box attached to the chamber houses only the focusing setups for both the UV and IR.

The primary design pattern of the boxes consisted of bolting together 3/8" Aluminum sheets to create a box. The airtight seal was made by adding a layer of Torr seal around all of the permanent connections. For the larger box, this was all of the joints between sheets except the lids. However, the larger number of geometric constraints on the small box in addition to supply chain issues from Covid, meant that the small box needed to sit on top of its breadboard instead of containing it inside. The lids/walls and walls/breadboard seals were made with custom Viton gaskets cut from large sheets of gasket material. The gaskets were compressed with C-clamps for the lids and optics clamps to the breadboard. With the exception of the connection to the special window inside a window, all other ports (electrical, optical, and gas feedthroughs) were machined with bolt patterns for standard KF and Conflat flanges to allow commercially bought feedthroughs to be used. There were 18 (10) such ports on the large box (small box). A custom mounting flange had to be made to attach the small box to the window in a window to allow for sufficient error tolerance in measurements and machining. The seals here consisted of two commercially bought Viton gaskets to seal to the box walls and separately the window flange. I designed the full system, had the components machined by Xometry, and assembled the boxes myself.

The purge system worked beautifully as designed. By flowing a small amount of nitrogen into the purge system, the system can be maintained at a positive pressure in the box for many months or even a year, allowing more than sufficient time for measurements at close to pure nitrogen levels. The single biggest contribution to the leak rate of the boxes is that the "sealed hole" breadboard is only sealed to fluid not air, because apparently, people spill coffee on expensive and sensitive optical systems. In any case, as mentioned above, at the time the breadboard could not be placed inside of the box, but now that the supply chain issues have been solved, Thorlabs could easily make a custom breadboard to live inside of the box, if ever greater purity/longer times for the purges were needed.

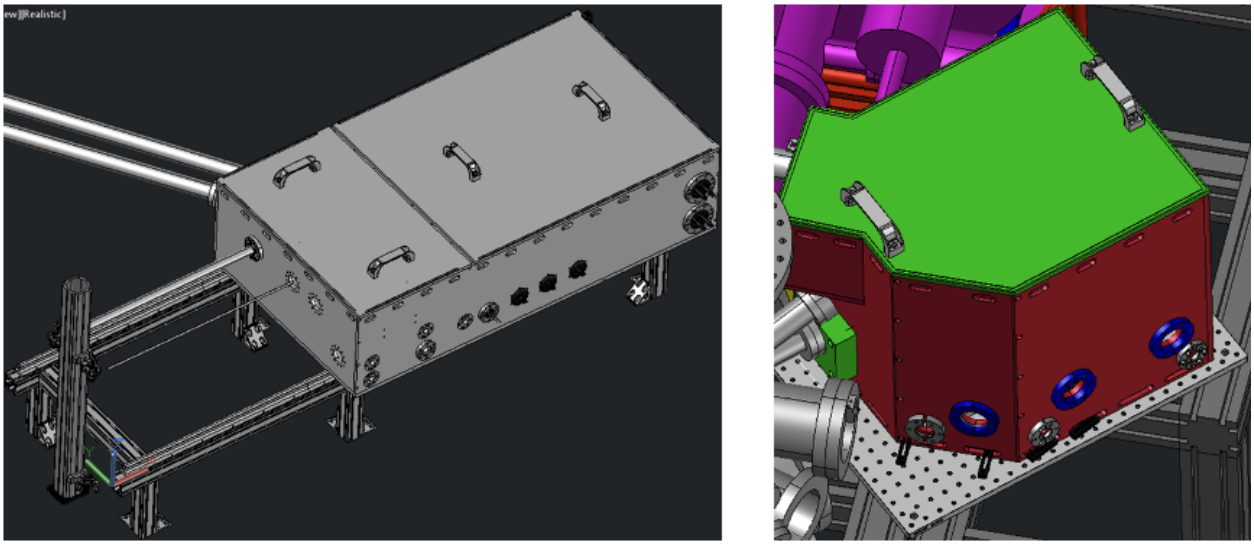

Figure 6.9: IR Purge Boxes in CAD: Left shows the larger purge box on the optics table (see Fig. 6.2). This box houses a breadboard, the OPA and DFG that generate the IR Pump, the IR laser pointing stabilization system, and IR beam expander. The purge box rests on a high-precision rail translation system. Removable lids allow access to the internals. Many ports were added for optical, electrical, and gas feedthroughs. 195 nm and 800 nm laser light traverses periscopes and enter the box through separate conflat mounted windows on the left wall. Laser light leaves through KF tubes on the back wall that connect to the small box. Right, the small purge box is attached to the ARPES chamber and rests on an optics breadboard with sealed holes (mock breadboard shown). The box houses focusing and beam combining systems. This box also has a removable lid (green top) and many feedthroughs for gas and electrical connections. Additionally, a small mounting flange (green box) creates the airtight seal with the port that the special window in a window is mounted on (see Sec. 6.13).

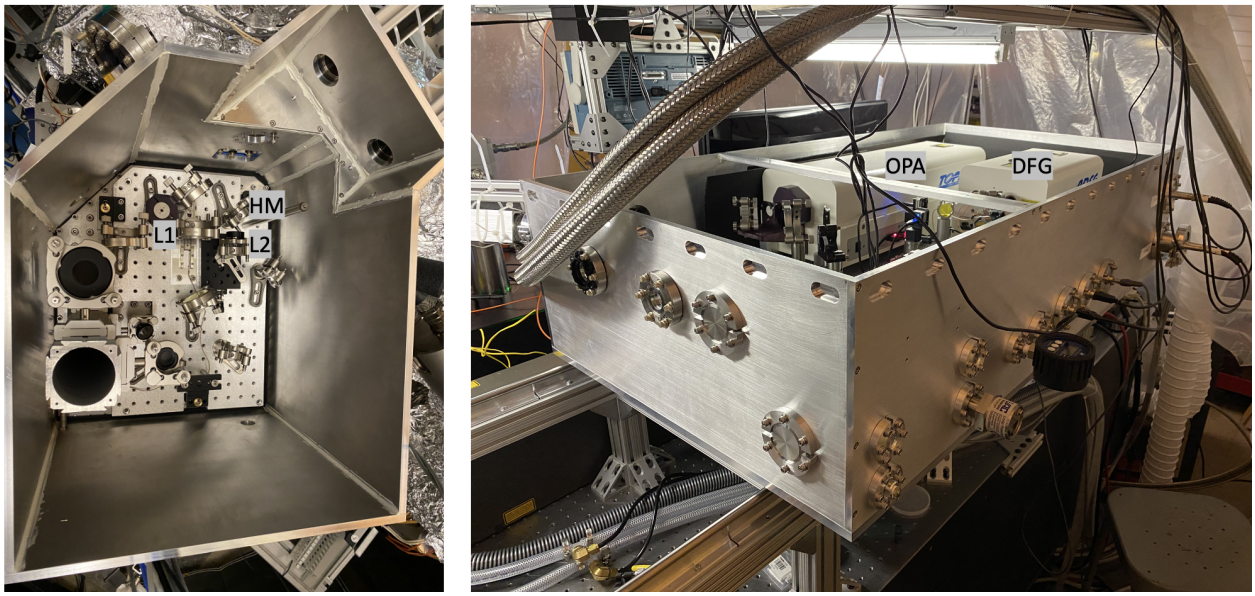

Figure 6.10: Deployed purge boxes: left) The smaller purge box with the lid removed to show internals. HM highlights the holey mirror. L1 is the IR lens on a motorized stage to compensate for chromatic aberrations. L2 is the 6eV lens on a manual stage. Notice the white torr seal along the edges to provide a UHV quality seal. right) The large purge box with the lid removed to show the internals. The large white box is the OPA and the smaller white box is the DFG.

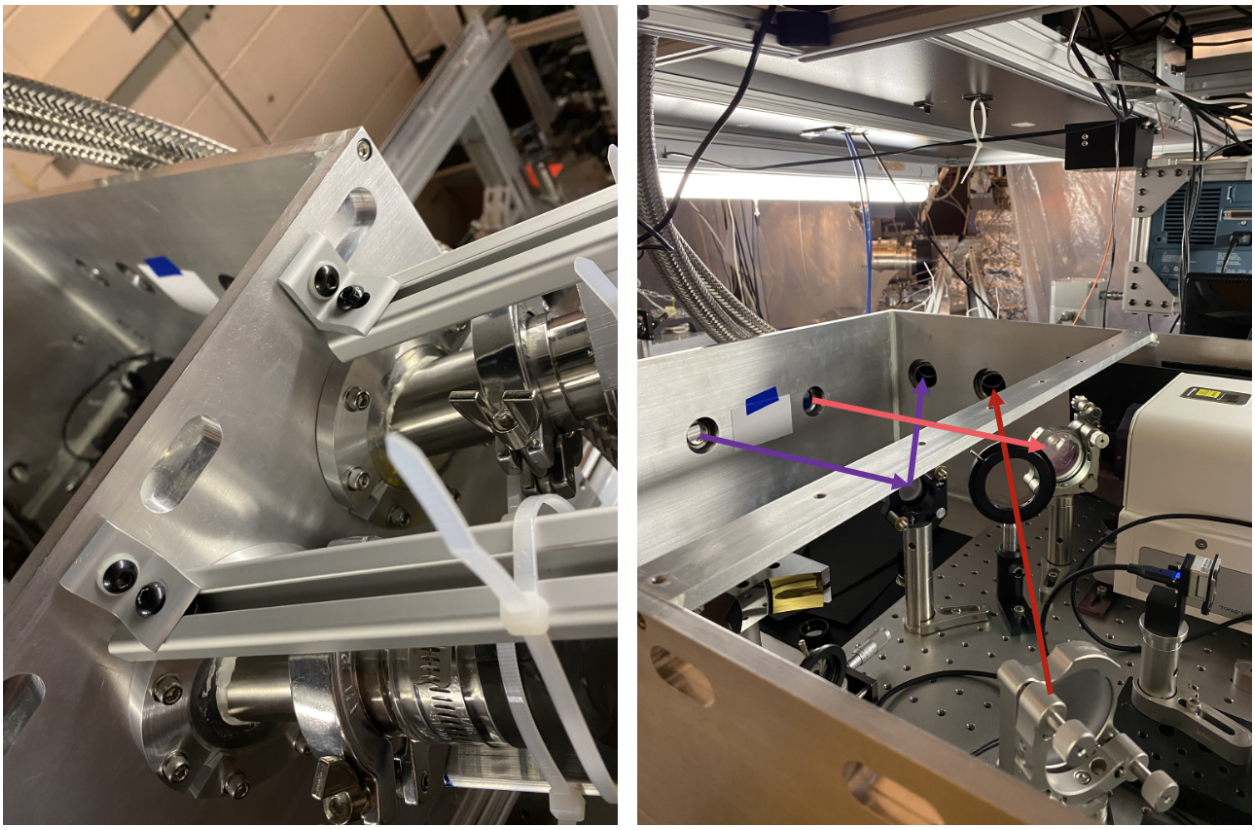

Figure 6.11: Beam tubes connecting the purge boxes: left) The custom KF ports that mate the beam tubes to the box are shown. Notice the white torr seal around the perimeter of the intersection of the tubes with the box. right) The beam tubes connecting the two boxes can be seen along with the smaller box off in the distance. The purple arrows highlight the 6eV path through the big box. The light red arrow shows where the 800nm fundamental light enters the box, and the dark red arrow shows how the IR beam leaves the large box.

6.2.4 Focusing Into the ARPES Chamber: A Window Inside a Window

As noted by my predecessor [103], perhaps the most difficult aspect of a time-resolved ARPES system is finding spatiotemporal overlap of the two beams on the sample inside of a UHV environment. This task is especially difficult because no material transmits both the UV and the IR lasers, requiring the use of two distinct vacuum ports, allowing spatial overlap at only one point in space, making spatial overlap difficult to find and harder to maintain on the sample during ARPES mapping motions. However, we solved this problem by gluing a tiny UV window inside of a larger IR window, maintaining a UHV seal between the windows that could survive a UHV bake out, which to our knowledge is the first time this has ever been done. This enables a collinear geometry where spatial overlap can be confirmed outside of the chamber and exists for the entire beam path through the ARPES chamber, simplifying spatial overlap in time-resolved ARPES significantly (see Fig. 6.12). We used CaF_2 (ZnSe) windows for the UV (IR), epoxying them together with FO-EPXY-UHV from Accuglass (see Fig. 6.13). To mount the window in a UHV flange and achieve a UHV seal, a Viton seal was compressed with a 12-bolt pattern onto the window, compressing the window into a tin gasket that ultimately made the UHV seal.

Maintaining a UHV seal at the window-window joint through baking to 90°C was nearly impossible, requiring many attempts. Finally, a procedure that worked required that the bubbles in the epoxy be removed by curing the epoxy under vacuum. However, even this was not enough. So, Vacseal was also applied to the joint while pulling a vacuum on the window to plug any residual leaks. After this procedure, the window passed the leak test. The leak test was performed using an RGA in a UHV chamber with the window mounted to the chamber. There was no perceptible increase in the partial pressure of Helium even when dousing the window with Helium gas. However, a small diffusive (slow) leak was detectable by enclosing the window in a bag that was fully inflated with He (see Fig. 6.14). Nevertheless, the window was affixed to the ARPES chamber and baked to 90° C, achieving a base pressure in the main chamber of $\lesssim 5 \times 10^{-12}$ Torr. No perceptible drift in the pressure of the chamber was noted on a many month time scale.

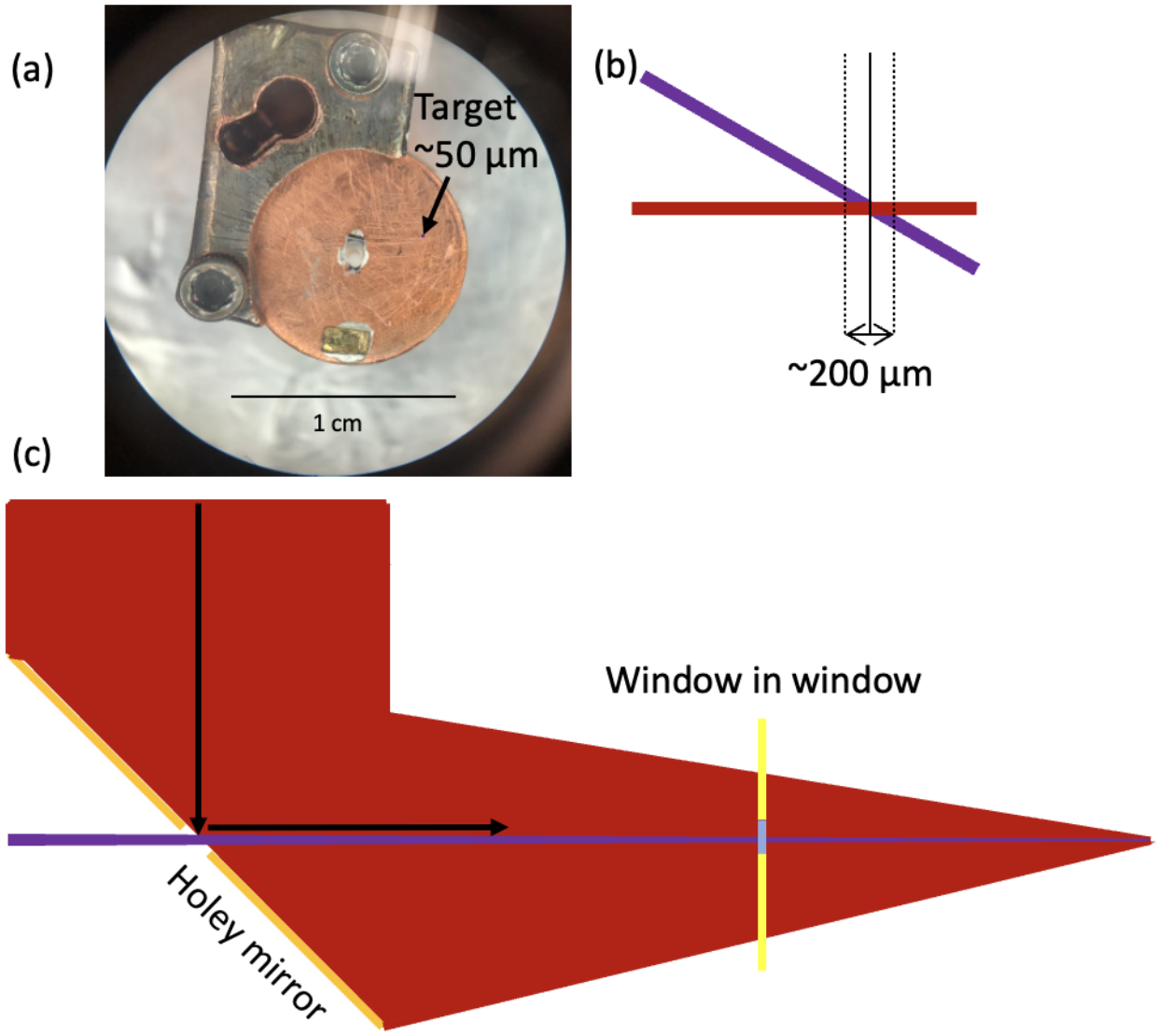

Figure 6.12: Illustration of collinear vs. noncollinear geometry in time-resolve ARPES: (a) Shows a sample holder with a tiny dot indicating the to scale size of the overlapping region in the sample surface plane. (b) Shows the depth of the overlap in the direction normal to the surface due to noncollinear geometry. (c) Schematic of how the IR and UV are combined with a mirror that has a hole in it and transmit through our window in a window, allowing collinear geometry.

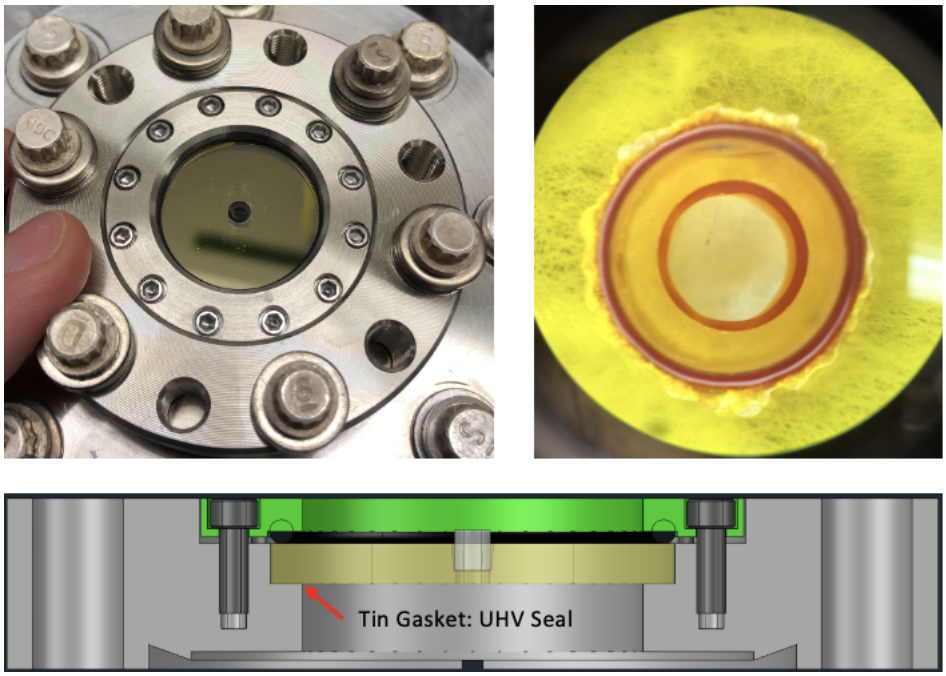

Figure 6.13: Window in a window: Upper left shows the assembled window mounted in a conflat flange. Upper right figure shows the window under a microscope, highlighting the central CaF_2 window (3 mm diameter) and the seal with the ZnSe window. Bottom figure shows shows a cross section of the cad drawing. The red arrow points to where the UHV seal is made by compressing the ZnSe window (yellow) into a tin gasket that rests on the ledge.

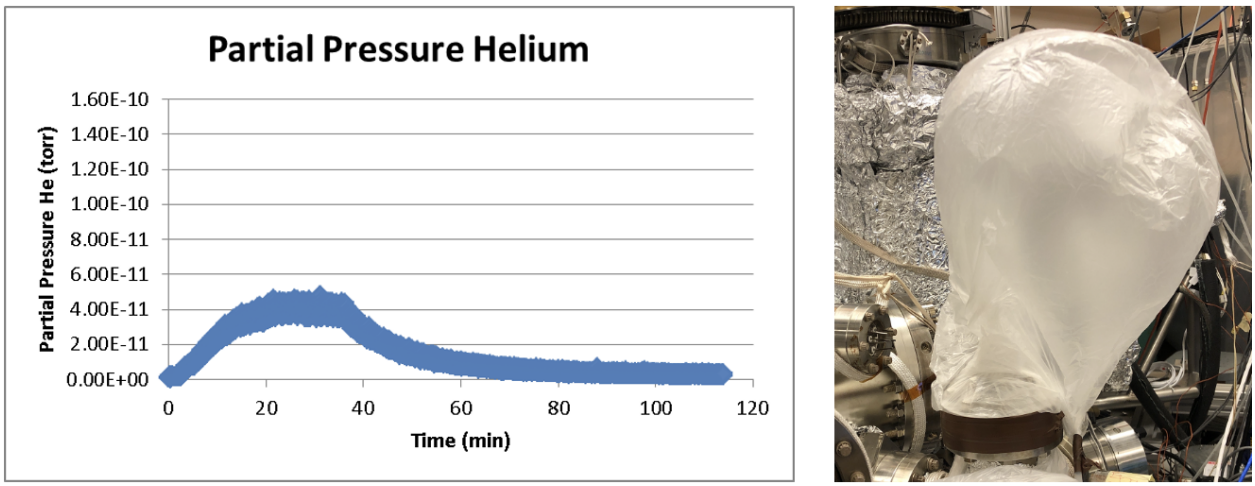

Figure 6.14: Leak testing the window in a window: Left shows the partial pressure of Helium measured with an RGA after enclosing the port in a bag filled entirely with Helium (right).

With a suitable window for collinear transmission of the UV and IR into an UHV ARPES chamber, a focusing system needed to be designed. Naturally, the IR beam needed to be expanded significantly to make use of the transmissible ZnSe window and minimize the flux on the non-transmissible CaF_2 window. To select the magnification, I came up with a crude model for the transmission of the beam. I assumed that the beam was a Gaussian beam and measured the beam waist of the IR. Then, I assumed that the magnification simply expanded the waist. Next, the transmission through the window was modeled as 0 for any part of the beam incident on the CaF_2 or regions outside of the ZnSe window. Otherwise, the average transmission value of ZnSe was used. Then, I created a plot of this transmission as a function of the magnification, indicating the magnification value that maximized this transition (see Fig. 6.15). After trying a few beam expansion options, I settled on Edmund Optics Canopus beam expander with a 5x beam expansion, because 5x was close to the optimal value, while their expander was easy to align and designed to minimize aberrations. This indeed worked quite well, producing a tight focus and similar power transmission as expected!

Finally, my focusing setup included a KBr lens that focused the IR into the chamber after reflection off of a mirror with a hole in it. The UV was made collinear with the IR beam by transmitting through the hole in the mirror (see Fig. 6.10). The KBr lens was placed on a motorized stage to correct for chromatic aberrations. KBr was chosen to maximize transmission and because custom and long focal length off axis parabolics suitable for focusing from outside of the ARPES chamber were not readily available. After combination of the beams with the holey mirror, the beams transmitted through the special window (see Fig. 6.16).

Although a final ARPES measurement studying light induced superconductivity has eluded me, the overall focusing system has been tested and works wonderfully. That is, a time=0 signal was measured on BSCCO. Due to the simplicity of the collinear setup, the wavelength was changed easily and rapidly between 4μm and 17μm, maintaining spatial overlap and demonstrating the superior ease of operation of a collinear time-resolved ARPES system, enabled by our novel window in a window.

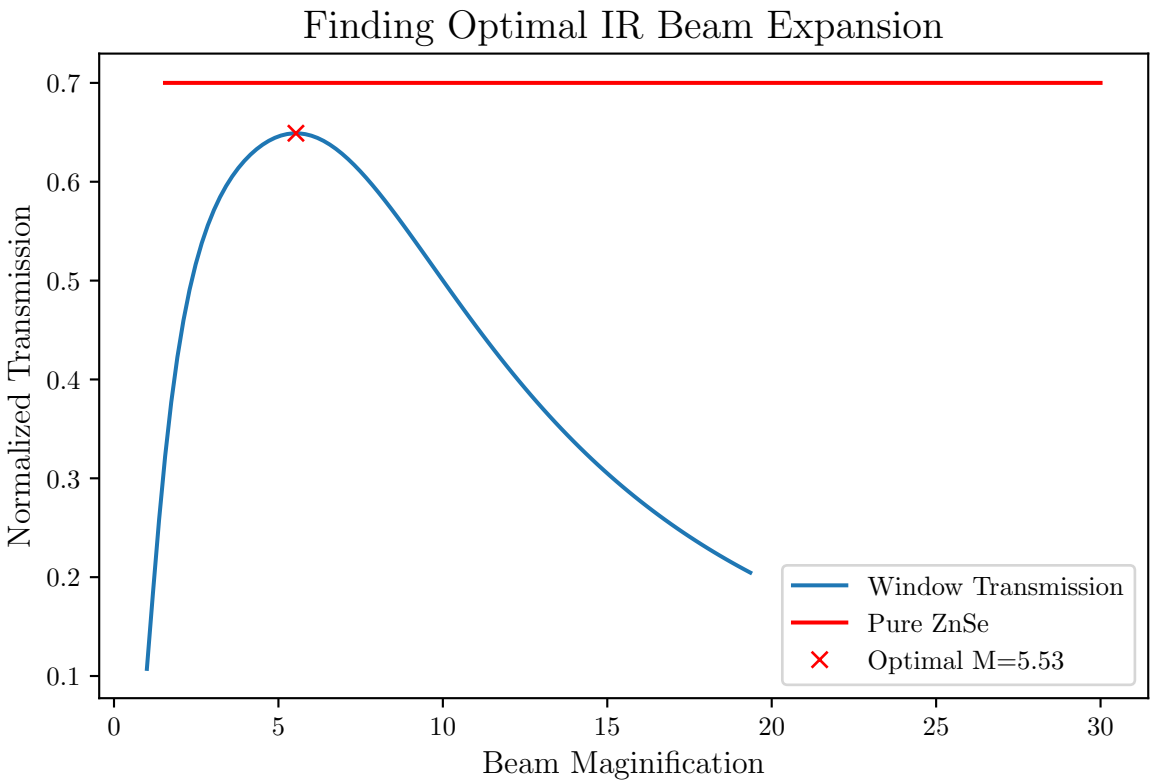

Figure 6.15: IR transmission through the window in a window for a given magnification of the beam.

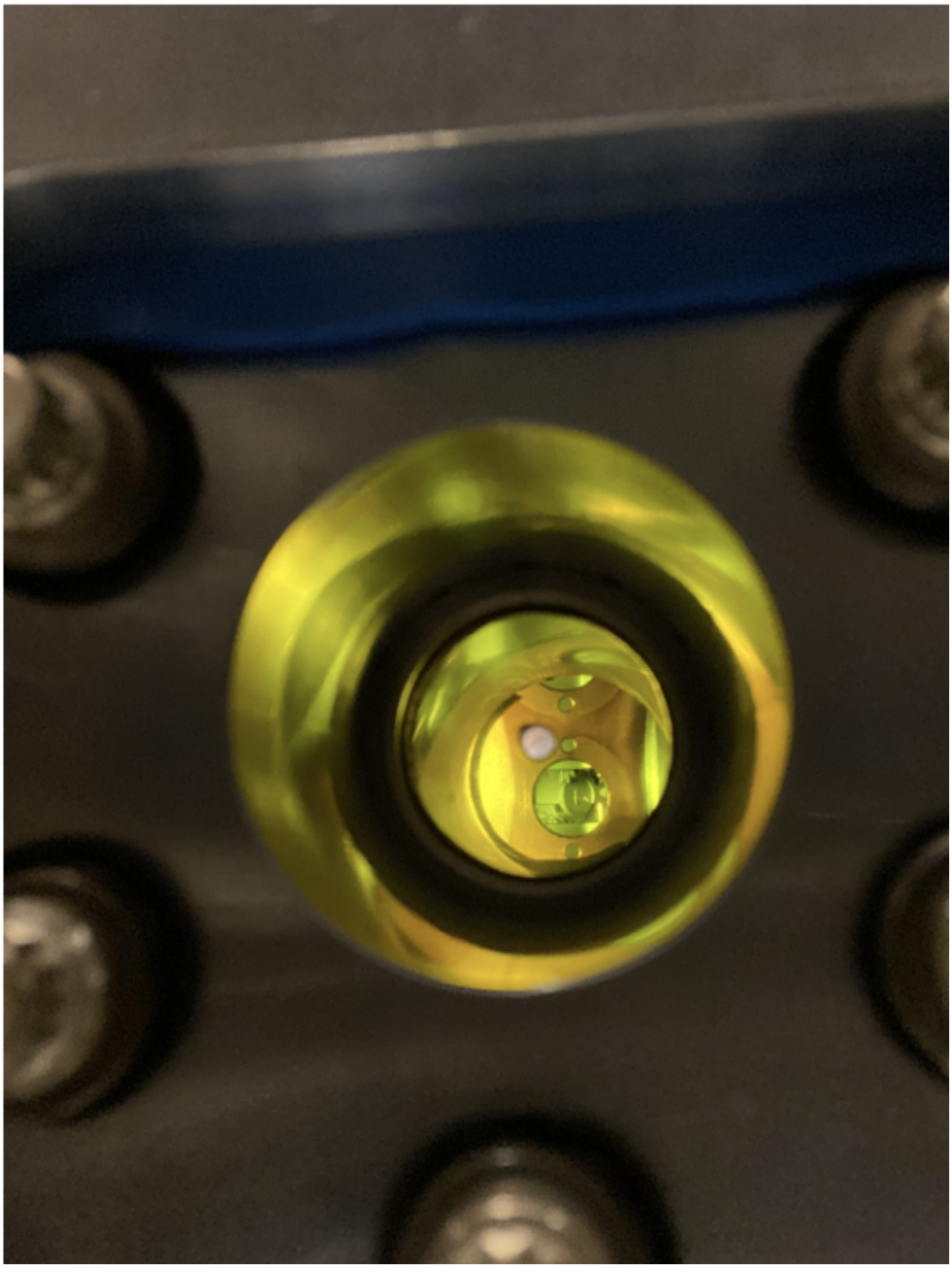

Figure 6.16: Window in a window on the ARPES chamber: The image is taken from slightly off the axis of focusing into the chamber. The optical axis goes through the smaller, clear CaF_2 window, through the center of the hole in the copper shield, and intersects the sample that lies on the circular black puck in the image. Going the other way, this optical axis goes through the center of the hole in the holey mirror. The yellow region of the window is the ZnSe that the IR goes through. The blue sheet near the top of the image is the gasket that mates the flange to the small box. The gasket mating the flange to the window is not visible.

6.3 Pointing Stabilization and Alignment Systems

Time-resolved ARPES has very low data throughput due to space-charge effects limiting the number of electrons that can be photoemitted per light pulse to around one electron per pulse, making data acquisition over long periods of time essential to successful studies. However, free-space Ti:Sapphire lasers are notoriously difficult to work with, and their pointing can be unstable on both fast and slow time-scales, with the former often related to vibrations from pumps or air currents and the latter largely driven by thermal fluctuations. Additionally, our broadly tunable IR pump source has moving parts in it to offer the tunability, and while the pointing drift is minimal when changing the wavelength, it is not zero, and our ARPES chamber is several meters away, making our sensitivity to pointing drift from our Ti:sapphire source and tunable mid-IR pump very sensitive. This created a problem for our time-resolved ARPES system, which I solved with a combination of cameras for measuring the pointing, piezo actuated mirrors for active control, and a custom software system implemented in Python [111] to operate the system and provide logic for the active control.

It should be mentioned that the pointing stabilization system may also be used for alignment of the laser after large drifts of the pointing, which I find is at least required every time the laser is turned off and on, using the coarse adjustment on the piezo mirrors. Of course, there are other methods of aligning the beam after large drifts in the pointing (e.g. using irises), but in my experience, these are usually only rough, requiring reoptimization of some signal to restore optimal alignment. However, the pointing stabilization system measures the pointing of the beam so precisely that when aligning the laser to this system, I find that all down stream systems are aligned as well as before, requiring no further optimization. Therefore, aligning the pointing stabilization system is a quick and highly accurate way to restore previous alignment of all downstream setups even days or weeks later, saving a tremendous amount of time.

6.3.1 Selecting Core System Components

To create a solution, I reviewed commercial options available from Thorlabs, Newport, and MRC systems; however, they did not offer detectors that would work with our long wavelength IR pump ($4 - 20$ μm), in addition to being quite costly. Thus, a custom solution would be required, meaning I needed to find position detectors and piezo controllers. There are primarily two options for position detectors: quadrant photodiodes and cameras. Quadrant photo detectors are usually preferred over cameras for their larger bandwidths, allowing for correction of faster instabilities; however, the primary concern for us is correcting slow thermal drifts to allow long-time data acquisition. Furthermore, cameras clearly acquire vastly more data than just the center of mass of the beam, which could allow for more sophisticated data processing layers to be applied in the future. Additionally, we had a legacy camera based system for the Ti:Sapphire laser, which I knew that I could expand upon. Therefore, I found some suitable IR cameras from FLIR systems, FLIR Bosons, which had spectral responsivity out towards 20 μm, which is rather difficult to find in general. The cameras use an uncooled VO_x microbolometer array for pixels. The Ti:Sapphire laser system initially used Mightex cameras, but I ultimately switched to newer FLIR Blackfly S cameras. Thorlabs MDT693B piezo controllers with Thorlabs Polaris piezo actuated mirrors were used for active control of the laser pointing. Thus, I acquired all of the core hardware components necessary to build the system.

6.3.2 Operating Theory

Optical Setup: Acquiring Pointing Information In both cases, the optical setup for measuring and controlling the pointing is the same and depicted in Fig. 6.17, where the beam pointing through BS1 is measured by cam 1 and cam 2 and controlled by PM1 and PM2. The pointing direction is measured by focusing the laser onto cam 2, because the focal position is only dependent on the angle of the beam into the lens and thereby into BS1. This is due to the fact that a lens Fourier transforms a laser beam. Meanwhile, cam 1 captures the beam before the focal

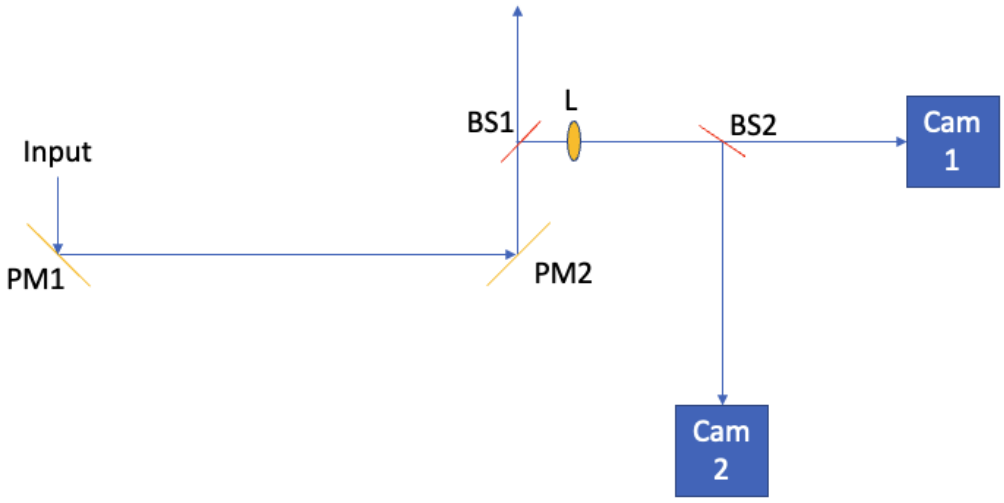

Figure 6.17: Pointing measuring system: PM1 and PM2 are piezo actuated mirrors. BS1 and BS2 are beam splitters. L is a lens. The pointing through BS1 is ultimately measured by the two cameras, Cam 1 and Cam 2, and stabilized by PM1 and PM2.

position, which is sensitive to the offset of the beam on the lens and thereby BS1. The sensitivity to the offset outside of the focus is obvious by visualizing intersecting a ray headed towards the focus from a location off-axis of the lens. Therefore, this system captures the pointing direction and offset at BS1, and by stabilizing these parameters with PM1 and PM2, the beam that transmits BS1 will also be stabilized, which is the beam used in experiments.

Of course, the vastly different wavelengths between the mid-IR and the Ti:Sapphire laser require not only different cameras but also different transmissive materials. For the Ti:Sapphire beam, anti-reflection coated UV Fused Silica is used for BS1, which reflects $\lesssim 1\%$. UV Fused Silica was also used for the plano-convex lens, f=250 mm, and BS2 (50/50). Additionally, although not shown, neutral density filters are used to avoid over saturating the camera. For the mid-IR, no coatings are broad enough to cover our spectral range. Therefore, uncoated KBr is used for BS1 to have the lowest reflection possible ($\sim 10\%$). And a ZnSe lens, f=250 mm, and beam splitter (BS2) are used. Again, neutral density filters are used as needed.

Update Logic The laser stabilization system is built around a core update logic that has

three steps: 1) calculate the position on the cameras, 2) find the displacement vector between this position and the desired position, and 3) map that displacement vector onto a new voltage to apply. For step 1, multiple options are available, but the most robust choice is actually a simple center of mass calculation. Obviously step 2 is just the difference between the set position and the new center of mass, $\vec{d}$, which is a 4-d displacement vector (2 coordinates on each camera); however, at this stage one can implement a PID controller by putting the displacement through a PID formula:

$$\vec{d}_n^{\text{pid}} = P\vec{d}_n + I\sum_{i=0}^{n}\vec{d}_i + D(\vec{d}_n - \vec{d}_{n-1}), \tag{6.4}$$

where P, I, and D are constants that control the strength of the proportional, integral, and derivatives, respectively. The parameters, P, I, and D are often just chosen manually to optimize stability of the pointing.

Finally, the key logical component of the update is the mapping from $\vec{d}_n^{\text{pid}}$ to some change in the voltages, $\delta\vec{V}_n$, to apply to the mirrors to remove this displacement, restoring the pointing to the desired positions. This mapping is found by sweeping the voltages on the mirror and looking at the change in position, which can in general be fit by a polynomial expansion in powers of $\delta\vec{V}_n$. However, it is theoretically justified to use only a linear fit because 1) the hysteresis of the piezos is small, making the displacement of the piezos linear in voltage, and 2) under small angle approximations, the position displacements (offset and angle) are linear in displacement of the piezos. To illustrate this, see Fig. 6.18. Neglecting the shift in the surface position due to the piezo expansion, the changing beam pointing in 1D can be accounted for by the changing surface normal of the mirror, which shifts by $\delta\theta$. From basic trig, $\delta x/M = \tan(\delta\theta)$, where M is the distance between the pivot point and piezo stack for the mirror mount. However, $M = \mathcal{O}(1")$ for a 1" mirror, and $\delta x = \mathcal{O}(10\mu m)$ for the full range of the piezo. Therefore, $\delta x/M = \mathcal{O}(10\mu m/1") = \mathcal{O}(10^{-3})$ is small enough to justify the small angle approximation for the resulting $\delta\theta$, i.e. $\tan(\delta\theta) \approx \delta\theta$, making $\delta\theta \approx \delta x/M = \mathcal{O}(10^{-3})$ radians. Therefore, $\delta\theta \propto \delta x \propto \delta V$. As mentioned before, the camera in the focus is directly sensitive to the angle of the beam pointing, thus the position on this camera is linearly proportional to δV on the piezo. As for the displacement of the beam in the

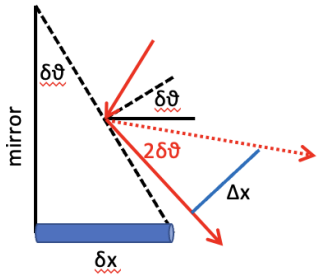

Figure 6.18: Illustration of linearity of displacement of the piezo (δx) to the angle (2δ) and displacement (dx) of the beam leaving the mirror in 1 dimension. The mirror surface (black line) is displaced about a pivot point to a new surface (dashed black line) by the piezo displacement (blue cylinder). This shifts the surface normal (black line) to a new normal (dashed black line). Finally, the original beam path (solid red arrows) is shifted to a new beam path (dashed red arrow) due to the deflection by the piezo. Note, nothing is drawn to scale—figure is only illustrative. Furthermore, the shift in the position of incidence on the mirror surface is not shown for simplicity.

direction perpendicular to the original propagation, Δx, $\Delta x = \tan(2\delta\theta)D \approx 2D\delta\theta \propto \delta V$, where D is the distance of propagation from the mirror to where the displacement is measured (i.e. the lens) and the small angle approximation is again employed. Note, the neglected contribution to the displacement of the beam from the displaced position of the mirror surface and thus position of incidence of the beam on the surface is also linear in voltage for similar reasons. Clearly, the 2 degrees of freedom (DOF) (displacement and angular change) is the reason we need 2 mirrors (with 2 DOF each to handle the vertical and horizontal planes) to fully control the laser pointing. Systems that only control the angle and neglect displacement are also possible with only one mirror. In any case, the point of the above is that $\vec{d} \approx A\delta\vec{V}$, where $A_{i,j} = d_i/\delta V_j$, and A is found in the calibration process that sweeps voltages and measures changes in position. Finally,

$$\delta\vec{V}_n = A^{-1}\vec{d}_n^{\text{pid}} \tag{6.5}$$

is the mapping that we need to stabilize the pointing. Here, $\delta\vec{V}_n$ is the voltage change that would have induced the change in pointing based on the calibration process. Therefore, subtracting $\delta\vec{V}_n$ from the current voltages will restore the pointing.

Unfortunately, the finite range of the piezos means that sometimes the pointing drift is too large to fully restore. So, the update logic must decide how to handle this case. My algorithm

first looks to additional DOF (if present or skips this step if not), then if the pointing cannot be restored, based on the user input, quits locking or shifts to locking only the angle of the pointing allowing drift of the offset. My system allows the user to use additional mirrors to compensate the drift enough to allow the fast mirrors to continue updating as described above. If used, there are more than 4 DOF for 4 positions, and the full matrix mapping from position to voltages that is found during the calibration may not be inverted. So, I separate the DOF into 4 DOF used for fast updates as described above, which has an invertible matrix, and 2 DOF for slow updates whenever the 4 fast DOF are not enough. When the update voltage is found to be outside of the allowed voltages, I look for a step along the null vectors of the full matrix with all DOF that brings all motors to a voltage inside of their allowed ranges. I check for the existence of such a step by breaking the 6 inequalities ($0 \leq V_i \leq 150$ V) for the 6 voltages into pairs, which have 2 DOF for 2 equations (step-size along each of two null vectors). Thus, the inequality equations may be solved for the step-sizes, which then defines a parallelogram that bounds the step-sizes that bring the voltages into their bounds. Repeating this for all 6 equations gives 3 parallelograms, and I look for their overlapping region using Shapely [112]. If an overlapping region exists, then I look for the smallest step size in the region and add this step to the initially out of bounds update. Since the step is along null-vectors, this still restores the pointing by virtue of the initial calculation of update voltages, and now all voltages are in bounds. If there is no overlapping region of the parallelograms, then no solution exists that restores the pointing; so, I take the step that brings the pointing closest to restoration. Then, I proceed with the steps described above where the offset center of mass is allowed to drift as minimally as possible, while the angular coordinate of the pointing is fully restored, which is more important. However, the user may require the system to quit locking in this case. In any case, if the angular pointing cannot be fully restored, locking is forcibly stopped, requiring coarse adjustment by the user before continuing.

6.3.3 Software Architecture

The software can be broken into three primary functions: communication with the hardware (cameras and piezo motor controllers), implementation of the update logic, and communication with the user through a Graphical User Interface (GUI). The hardware communication handles tasks such as grabbing frames and setting voltages, using the hardware's respective SDKs, and it is handled by 4 objects, two camera and two piezo motor objects. The control logic is implemented by an object that is constantly listening for new frames, using them to calculate update voltages, which are then sent to the piezo control objects that apply the voltages. Finally, the GUI is used to change parameters (e.g. exposure time of the camera), update the GUI with information (e.g. position on the cameras), and initiate the stabilization process. The GUI functions are all implemented in another object.

The software is implemented in Python, primarily using PyQt5 [**noauthor˙pyqt5˙nodate**], which is a python implementation of Qt. Qt is an event based programming package that implements and runs a GUI and allows communication between objects via sending signals that trigger slots (methods). Qt also allows easy multithreading, allowing each of the above mentioned objects to be on their own thread with independent event loops. A thread's event loop is essentially an infinite loop that peels off and processes events received in order or executes an efficient wait command until new events arrive. For example, the cameras send a signal indicating a new frame has arrived along with sending the actual frame. This signal then queues on the UpdateManager's event loop, and when the UpdateManager's event loop gets to this event, it triggers the UpdateManager to run its frame processing function (or in Qt lingo it calls the process frame slot). By running individual event loops and using queued connections between objects on different threads, Qt avoids any race conditions in the multithreading process. Although python has a global interpreter lock that prohibits python from running on multiple threads simultaneously, many python packages, including Qt, call external (non-pythonic) code that releases the global interpreter lock, allowing other threads to run concurrently during the execution of external code. Thus, multithreading in

python does still vastly improve the overall speed of the update loop—time to grab new frames and apply a new voltage ($\sim$ 500 ms $\rightarrow\sim$ 30 ms, where the latter is limited by the frame rate of the camera). However, the global interpreter lock is still a limitation to multithreading efficiency in python at times.

6.3.4 GUI Overview

The application's GUI is broken into a set of controls that are always visible and four different tabs: camera view, pointing view, piezo view, and unlock report. The ever present controls include a "Lock" button that initiates/stops the locking algorithm, a "Define New Home" button that captures and stores a new set position, an "Align" button that brings the piezos to their center voltage for alignment. Additionally, the user may decide whether the program should quit locking when the piezos go out of bounds after a settable time in seconds by checking the "Force Unlock" checkbox, or they can allow the program to continuously attempt to restore the pointing as best it can. I have noticed that sometimes the pointing will drift out of piezo bounds for only a short period before returning into bounds. The user can also choose to suppress various image, pointing, and piezo plots, which can be useful if the computer is struggling to keep up with the demands of the application, which can happen with cheaper computers. Finally, a file drop-down menu allows the user to initiate the calibration process, save the state of the system (all of the settings such as cameras to use, exposure times, etc.), load the home/set position by date, and load the state by date (allowing faster startup).

Figure 6.19 shows the GUI with the camera view tab displayed. On startup, this tab displays a "load recent visible" and "load recent IR" button, which when clicked loads the most recent state of the visible and IR systems for immediate use without selecting each parameter again. Alternatively, one can select the visible or IR system with the drop-down menu at the top of the tab, which then loads a view similar to that displayed in the figure. This view allows the user to select the cameras with a drop-down menu showing available cameras on the computer. Then, the user may set relevant parameters to the type of camera shown. For the visible, this includes

exposure time, gain, threshold for background subtraction, possibly averaging over frames, and generating and selecting a ROI on the camera graphically. Setting an ROI can increase the frame rate of the camera. The controls are set with an update button. Importantly, this view also allows the user to view a live stream of the incoming frames from each camera, with yellow cross-hairs showing the center of mass, and a green (locked)/red (unlocked) circle showing the set position. The color scheme of the images may be controlled as well.

Figure 6.20 shows the GUI view of the pointing view and piezo view tabs, which show a time series of all four degrees of freedom of the center of mass and piezo voltages, respectively. The pointing view tab also provides control over how many points are plotted in the figures, and gives the user the ability to acquire the piezo and/or center of mass data for a time in "[days, hours, minutes, seconds]." The piezo view tab also allows the user to select the motors to be used with the system. Additionally, the PID parameters may be set on this tab. Finally, the user must specify four channels on the motors to use for updating the voltages on each update. Additionally, the software allows the user to select two additional channels/DOF to change whenever the fast motors cannot restore the pointing, allowing longer stabilization times.

Finally, Fig. 6.21 displays a log of incidents when the pointing could not be fully restored due to the drift exceeding the compensation range. This report displays the time that the incident first began, how long the pointing stayed outside of the control range, and how far outside of the control range the pointing drifted.

6.3.5 Characterizing the System

Fig. 6.22 shows 10 minutes of laser pointing data when locked (actively stabilized) and unlocked. The figure shows both time series and frequency data. From the data, it is clear that the algorithm achieves its primary purpose—removing slow thermal drifts that are large in amplitude and thus more disruptive. This can be seen directly in the time series, and it is also clear in the frequency data that low frequency noise has been suppressed. Furthermore, when there is significant drift over long timescales, it is clear that the standard deviation of the pointing is significantly

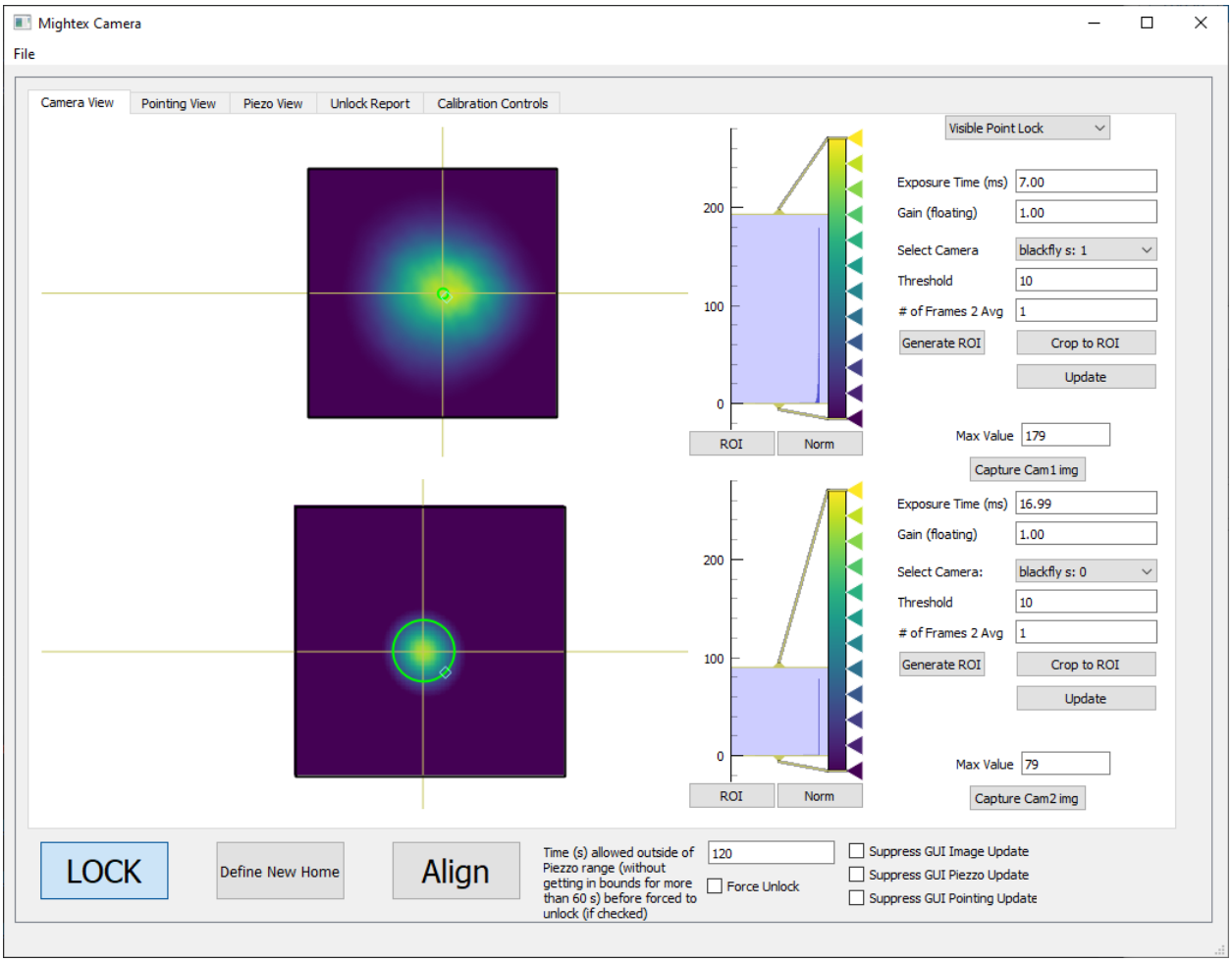

Figure 6.19: Point lock GUI Camera View: Figure displays the full window of the application GUI with the camera view tab selected. User can choose whether an IR or visible system is used, and then choose the cameras and set relevant camera settings in this view, as well as see returned images.

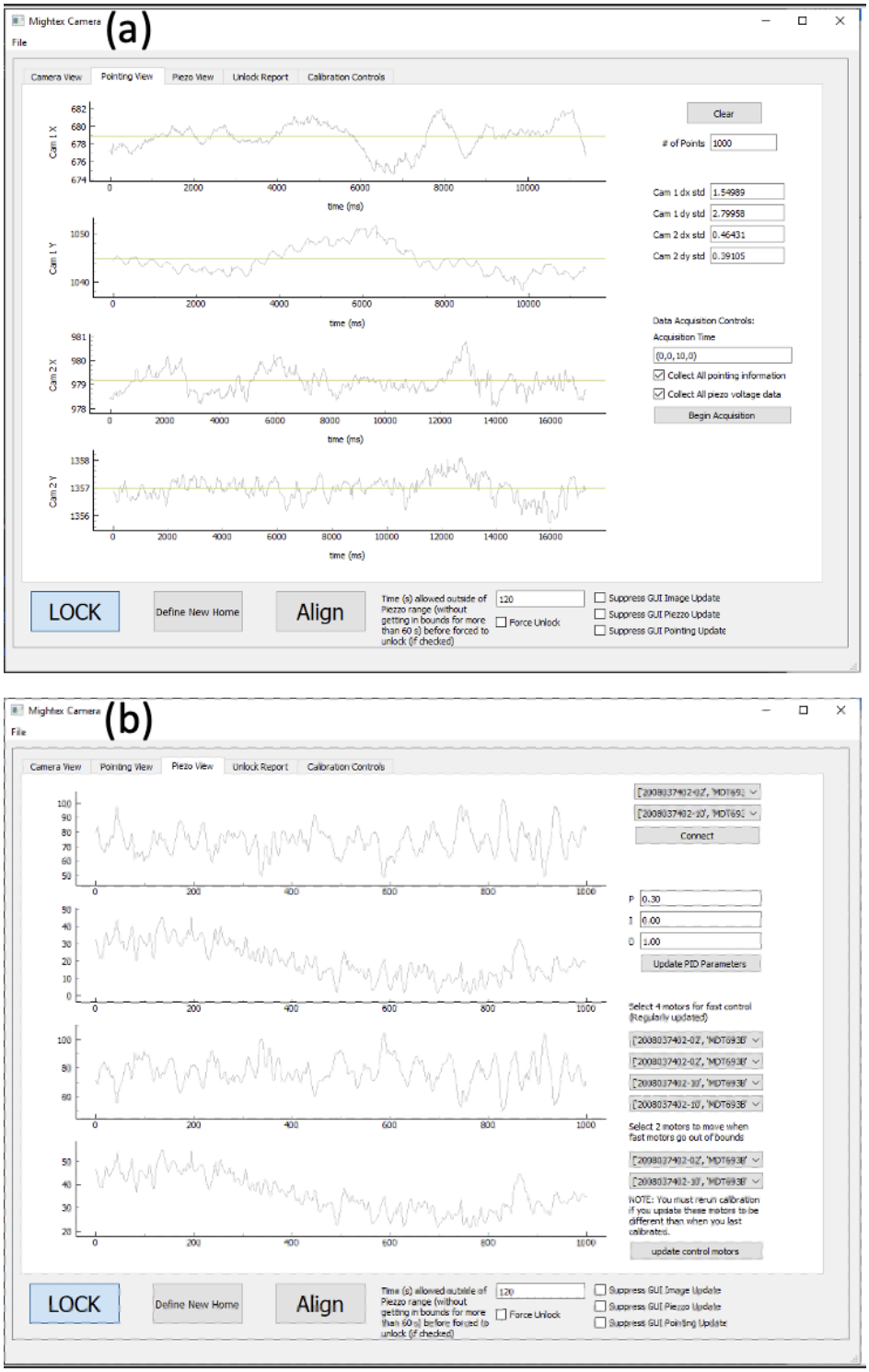

Figure 6.20: Point lock GUI line plots: a) Shows the GUI view of the pointing view tab. In this tab, the user can see line plots of the center of mass coordinates, controlling the number of points plotted. User can also initiate data acquisition. b) Shows the GUI view of the piezo view tab. This shows plots of the Voltages (Volts) vs time plotted as index of voltage applied (right current, left past). The user can also select the motors and what channels to use for control (fast) vs. slow adjustments.

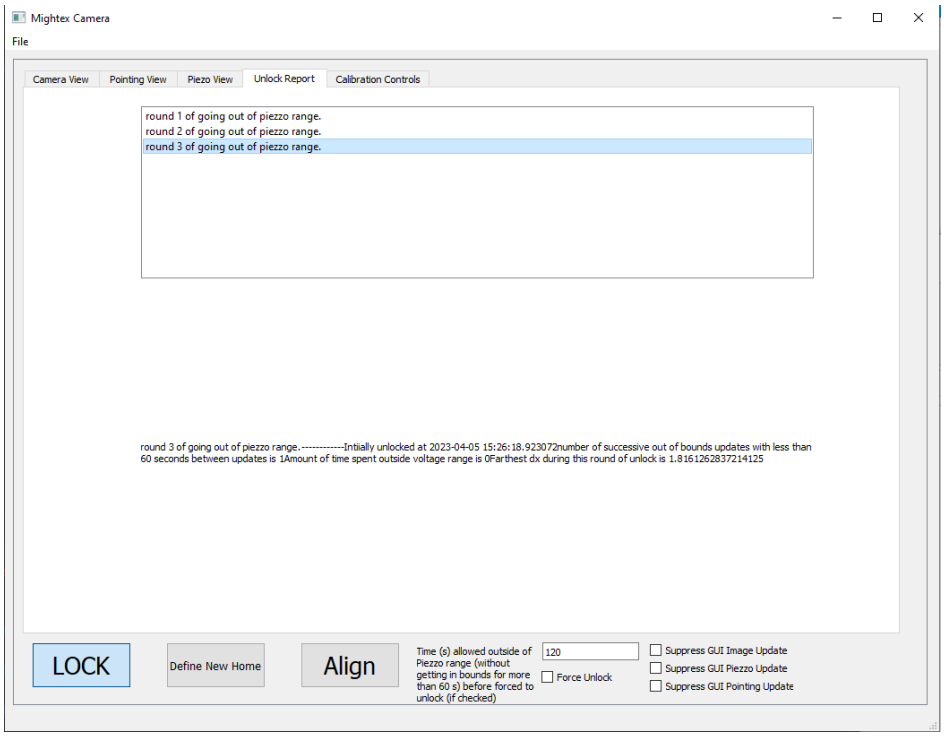

Figure 6.21: Unlock Reporting: Figure shows the GUI view of the unlock report tab. This tab displays a log of instances where the update voltages went out of bounds, forbidding a complete restoration of the pointing. Logs include information about when this occurred, for how long, and how far out of bounds the pointing drifted.

reduced. However, it is also apparent that the system really does not improve noise above about 125 mHz, which is because the data shown is from when the system was forced to average over many frames, reducing the bandwidth of the stabilization. This was to reduce the introduction of unwanted high frequency noise, while continuing to stabilize low frequencies. This is an effective quick and dirty trick; however, a better approach would be to tune the PID parameters more carefully, which will be implemented in the future.

6.3.6 Limitations

While the system performance is excellent, there are limitations that should be kept in mind. First and foremost, the piezos have very little throw! This means that they can only correct for a narrow range of pointing drift, limiting how long the system can stabilize the pointing. Therefore, longer throw piezos are more desirable; however, there is a limit to what is commercially available. Unfortunately, the pointing drift depends on many many factors and can exceed this limit. To an extent, this can be overcome by daisy chaining together multiple mirror actuators with integrated piezo stacks (see Fig. 6.23). We have done this, and it works great, but our laser is so unstable that even 2x the throw is not enough for multiday scans. An ideal solution would be a slow but long range motor with an integrated piezo motor, but these are not available; so, I came up with my slow motor algorithm described above, but I have not implemented it with a different type of long-range motor yet, allowing only additional piezos to be used thus far, which still does not overcome the pointing drift of my laser. Second, it is important to note that what we really care about is the true laser pointing, and our system uses the center of mass of the beams as a proxy for this. In fact, most systems employ a quadrant detector that is also using the center of mass as a proxy for the pointing information. However, the laser beam mode also changes with time! This can be caused by natural changes in the laser and also by the beam clipping on an optic upstream of the stabilization system as it drifts. It can also be caused by the beam drifting onto a defect on the optic. All of these will change the calculated center of mass coordinates even if the beam pointing does not change at all. Therefore, correcting for this “pointing drift” will actually induce

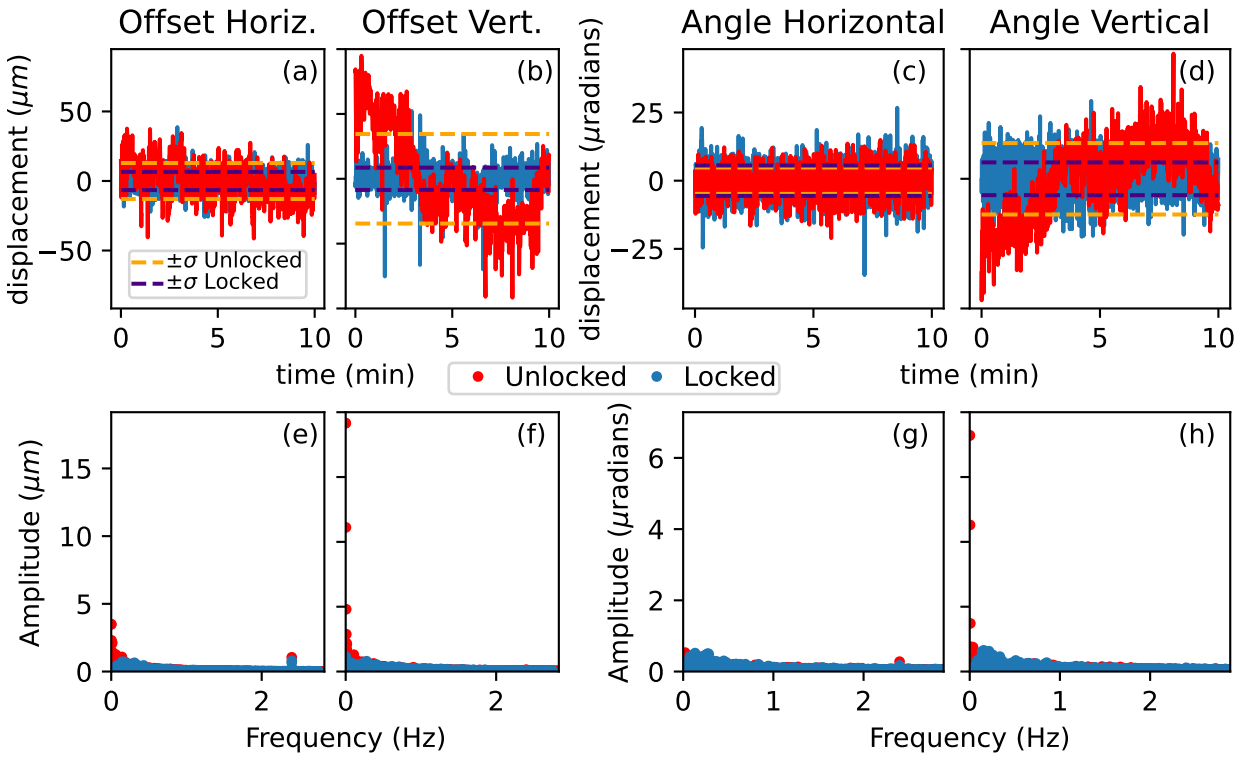

Figure 6.22: Point locking characterization: a-d) time series of the displacement of the center of mass on each camera, and the dashed lines represent the standard deviation of the data. e-f) Magnitude of the Fourier transforms of a-d, respectively. a,b,e,&f) Come from the camera outside of the focus, and thus, the displacement is converted from pixels to microns using the pixel size of the camera. c,d,g,&h) Come from the camera in the focus, which can be converted to a change in angle, $\Delta\theta = \arctan(\Delta x/2f)$ [113], where $f = 200$ mm is the focal length of the lens and Δx is the displacement of the center of mass on the camera.

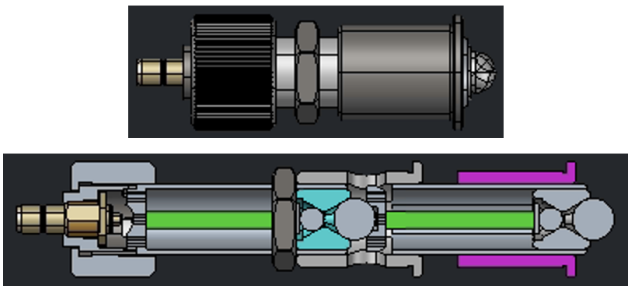

Figure 6.23: Daisy chain of multiple piezo stacks to double effective throw. Top is a single Thorlabs Polaris-P20 mirror actuator with an integrated piezo stack. These can be screwed into a Polaris mirror mount to make a piezo adjusted mirror. Bottom shows a cross section of two Polaris-P20s in series, doubling the effective piezo throw. Piezos are the green rectangles. Cad drawings of Polaris-P20 is downloaded from Thorlabs website.

unwanted pointing changes, and therefore what looks more stable to your measured system can be less stable at the systems that really matter. This is an unfortunate limitation of the system design; however, this is where a camera based system can shine, because it is possible to account for mode changes. For example, a Gaussian mixture model might be employed to detect different modes of operation that the laser is moving between, applying a different pointing target and/or calibration matrix A^{-1} for each operating mode of the laser. Regardless of the details, the point is that more information is available to account for this limitation using more advanced algorithms, possibly including machine learning algorithms. However, time limitations have rendered these ambitions projects for a future date.

6.4 Conclusion

Our time-resolved ARPES system provides a unique opportunity to test the purported light induced superconductivity seen in many systems by Cavalleri et al. My upgrades to the system make these experiments practical and improve the data quality attainable. The new window in a window and point locking systems allow a collinear geometry and precision alignment and stabilization, enabling easier initial alignment and long-time, higher quality data acquisition. The new purge system will yield higher pump intensities with less distorted pulses over a much broader frequency range.

Having completed the upgrades and optimized the systems, we are poised to make the desired experimental measurements on light induced superconductivity, and with a much more user friendly experiment, I hope that many more experiments on a broader class of materials will follow, not just studies of light induced superconductivity.

Bibliography

1. Šmejkal, L., Železný, J., Sinova, J. & Jungwirth, T. Electric control of dirac quasiparticles by spin-orbit torque in an antiferromagnet. **Physical Review Letters 118,** 106402 (2017).

2. Cavalleri, A. Photo-induced superconductivity. **Contemporary Physics 59.** Publisher: Taylor & Francis _eprint: https://doi.org/10.1080/00107514.2017.1406623, 31–46. ISSN: 0010-7514 (2018).

3. Wadley, P. **et al.** Antiferromagnetic structure in tetragonal CuMnAs thin films. **Scientific Reports 5,** 17079 (2015).

4. Máca, F. **et al.** Room-temperature antiferromagnetism in CuMnAs. **Journal of Magnetism and Magnetic Materials 324,** 1606–1612 (2012).

5. Haldane, F. D. M. Model for a Quantum Hall Effect without Landau Levels: Condensed-Matter Realization of the "Parity Anomaly". **Physical Review Letters 61.** Publisher: American Physical Society, 2015–2018 (1988).

6. Kane, C. L. & Mele, E. J. Quantum Spin Hall Effect in Graphene. **Physical Review Letters 95.** Publisher: American Physical Society, 226801 (2005).

7. Semenoff, G. W. Chiral Symmetry Breaking in Graphene. **Physica Scripta T146,** 014016. ISSN: 0031-8949, 1402-4896. arXiv: `1108.2945[cond-mat,physics:hep-th]` (2012).

8. **The Nobel Prize in Physics 1913** NobelPrize.org. `https://www.nobelprize.org/prizes/physics/1913/summary/` (2023).

9. **tutorial 1—Graphene** https://www.weizmann.ac.il/condmat/oreg/sites/condmat.oreg/files/uploads/2015/tutorial_1.pdf (2023).

10. ProfM. **Answer to "How to understand the time-reversal symmetry in graphene?"** Matter Modeling Stack Exchange. https://mattermodeling.stackexchange.com/a/1602 (2023).

11. Fuchs, J.-N. & Goerbig, M. O. Introduction to the Physical Properties of Graphene.

12. Young, S. M. & Kane, C. L. Dirac Semimetals in Two Dimensions. **Physical Review Letters 115.** Publisher: American Physical Society, 126803 (2015).

13. Yang, B.-J., Bojesen, T. A., Morimoto, T. & Furusaki, A. Topological semimetals protected by off-centered symmetries in nonsymmorphic crystals. **Physical Review B 95.** Publisher: American Physical Society, 075135 (2017).

14. Song, C. **et al.** Spin-orbit torques: Materials, mechanisms, performances, and potential applications. **Progress in Materials Science 118,** 100761. ISSN: 0079-6425 (2021).

15. Železný, J., Wadley, P., Olejník, K., Hoffmann, A. & Ohno, H. Spin transport and spin torque in antiferromagnetic devices. **Nature Physics 14,** 220–228 (2018).

16. Wadley, P. **et al.** Electrical switching of an antiferromagnet. **Science 351,** 587–590 (2016).

17. Železný, J. **et al.** Spin-orbit torques in locally and globally noncentrosymmetric crystals: antiferromagnets and ferromagnets. **Physical Review B 95,** 014403 (2017).

18. Tumanski, S. **Thin Film Magnetoresistive Sensors** 576 pp. ISBN: 978-0-429-14604-6 (CRC Press, Boca Raton, 2001).

19. Thomas, G., Marsocci, V. A. & Lin, P.-k. On the theory of the spin-orbit interaction in the magnetoresistivity effects in ferromagnetic metals. **Physica 45,** 407–417 (1969).

20. Campbell, I. A., Fert, A. & Jaoul, O. The spontaneous resistivity anisotropy in Ni-based alloys. **Journal of Physics C: Solid State Physics 3,** S95. ISSN: 0022-3719 (1970).

21. Mott, N. F. The resistance and thermoelectric properties of the transition metals. **Proceedings of the Royal Society of London. Series A - Mathematical and Physical Sciences 156.** Publisher: Royal Society, 368–382 (1997).

22. Gomes, A. A. Electronic structure of iron based alloys. **Journal of Physics and Chemistry of Solids 27,** 451–463. ISSN: 0022-3697 (1966).

23. Damascelli, A., Hussain, Z. & Shen, Z.-X. Angle-resolved photoemission studies of the cuprate superconductors. **Reviews of Modern Physics 75,** 473–541 (2003).

24. Ponor. **English: setup of an ARPES experiment: light source provides photons that eject electrons from the sample; the electron emission angle and energy are measured by the hemispherical electron analyzer.** 2020.

25. Chiang, T. .-., Knapp, J. A., Aono, M. & Eastman, D. E. Angle-resolved photoemission, valence-band dispersions $E(\vec{\mathrm{k}})$, and electron and hole lifetimes for GaAs. **Physical Review B 21.** Publisher: American Physical Society, 3513–3522 (1980).

26. Berglund, C. N. & Spicer, W. E. Photoemission Studies of Copper and Silver: Theory. **Physical Review 136.** Publisher: American Physical Society, A1030–A1044 (1964).

27. Hüfner, S. **Photoelectron Spectroscopy** ISBN: 978-3-642-07520-9 978-3-662-09280-4 (Springer, Berlin, Heidelberg, 2003).

28. Koralek, J. D. **et al.** Laser Based Angle-Resolved Photoemission, the Sudden Approximation, and Quasiparticle-Like Spectral Peaks in $Bi_2Sr_2CaCu_2O_{8+\delta}$. **Physical Review Letters 96.** Publisher: American Physical Society, 017005 (2006).

29. Giamarchi, T., Iucci, A. & Berthod, C. **Introduction to many body physics** 2013.

30. Moser, S. An experimentalist's guide to the matrix element in angle resolved photoemission. **Journal of Electron Spectroscopy and Related Phenomena 214,** 29–52. ISSN: 0368-2048 (2017).

31. Day, R. P., Zwartsenberg, B., Elfimov, I. S. & Damascelli, A. Computational framework chinook for angle-resolved photoemission spectroscopy. **npj Quantum Materials 4.** Number: 1 Publisher: Nature Publishing Group, 1–10. ISSN: 2397-4648 (2019).

32. Byrne, W. E. **et al. Bunch Diffusion Measurements at the Advanced Light Source** in. Proceedings of EPAC (Edinburgh, Scotland, 2006).

33. Energie, H.-Z. B. f. M. u. **ARPES One-Cube** HZB Website. `https://www.helmholtz-berlin.de/pubbin/igama_output?modus=einzel&sprache=en&gid=1679&typoid=75136` (2023).

34. Iwasawa, H. **et al.** Development of laser-based scanning μ-ARPES system with ultimate energy and momentum resolutions. **Ultramicroscopy 182,** 85–91. ISSN: 0304-3991 (2017).

35. Yokoya, T. **et al.** Ultrahigh-Resolution Photoemission Spectroscopy of Ni Borocarbides: Direct Observation of the Superconducting Gap and a Change in Gap Anisotropy by Impurity. **Physical Review Letters 85.** Publisher: American Physical Society, 4952–4955 (2000).

36. Seah, M. P. & Dench, W. A. Quantitative electron spectroscopy of surfaces: A standard data base for electron inelastic mean free paths in solids. **Surface and Interface Analysis 1.** _eprint: https://onlinelibrary.wiley.com/doi/pdf/10.1002/sia.740010103, 2–11. ISSN: 1096-9918 (1979).

37. Shirley, D. A. High-Resolution X-Ray Photoemission Spectrum of the Valence Bands of Gold. **Physical Review B 5.** Publisher: American Physical Society, 4709–4714 (1972).

38. Stamenova, M., Mohebbi, R., Seyed-Yazdi, J., Rungger, I. & Sanvito, S. First-principles spin-transfer torque in CuMnAs—GaP—CuMnAs junctions. **Physical Review B 95,** 060403 (2017).

39. Šmejkal, L., Mokrousov, Y., Yan, B. & MacDonald, A. H. Topological antiferromagnetic spintronics. **Nature Physics 14,** 242–251 (2018).

40. Tang, P., Zhou, Q., Xu, G. & Zhang, S.-C. Dirac fermions in an antiferromagnetic semimetal. **Nature Physics 12,** 1100–1104 (2016).

41. Wadley, P. **et al.** Tetragonal phase of epitaxial room-temperature antiferromagnet CuMnAs. **Nature Communications 4,** 2322 (2013).

42. Železný, J. **et al.** Relativistic Néel-order fields Induced by electrical current in antiferromagnets. **Physical Review Letters 113,** 157201 (2014).

43. Grzybowski, M. J. **et al.** Imaging current-induced switching of antiferromagnetic domains in CuMnAs. **Physical Review Letters 118,** 057701 (2017).

44. Olejník, K. **et al.** Terahertz electrical writing speed in an antiferromagnetic memory. **Science Advances 4,** eaar3566 (2018).

45. Bodnar, S. Y. **et al.** Writing and reading antiferromagnetic Mn_2Au by Néel spin-orbit torques and large anisotropic magnetoresistance. **Nature Communications 9,** 348 (2018).

46. Meinert, M., Graulich, D. & Matalla-Wagner, T. Electrical switching of antiferromagnetic Mn_2Au and the role of thermal activation. **Physical Review Applied 9,** 064040 (2018).

47. Meer, H. **et al.** Direct imaging of current-induced antiferromagnetic switching revealing a pure thermomagnetoelastic switching mechanism in NiO. **Nano Letters 21,** 114–119 (2021).

48. Chiang, C. C., Huang, S. Y., Qu, D., Wu, P. H. & Chien, C. L. Absence of Evidence of Electrical Switching of the Antiferromagnetic Néel Vector. **Physical Review Letters 123,** 227203 (2019).

49. Zhang, P., Finley, J., Safi, T. & Liu, L. Quantitative study on current-induced effect in an antiferromagnet insulator/Pt bilayer film. **Physical Review Letters 123,** 247206 (2019).

50. Churikova, A. **et al.** Non-magnetic origin of spin Hall magnetoresistance-like signals in Pt films and epitaxial NiO/Pt bilayers. **Applied Physics Letters 116,** 022410 (2020).

51. Bodnar, S. Y. **et al.** Magnetoresistance Effects in the Metallic Antiferromagnet Mn_2Au. **Physical Review Applied 14,** 014004 (2020).

52. Veis, M. **et al.** Band structure of CuMnAs probed by optical and photoemission spectroscopy. **Physical Review B 97,** 125109 (2018).

53. Nguyen, G. D. **et al.** Emerging edge states on the surface of the epitaxial semimetal CuMnAs thin film. **Applied Physics Letters 116,** 061603 (2020).

54. Fedchenko, O. **et al.** Direct observation of antiferromagnetic parity violation in the electronic structure of Mn_2Au. **Journal of Physics: Condensed Matter 34,** 425501 (2022).

55. Šmejkal, L., Sinova, J. & Jungwirth, T. Beyond conventional ferromagnetism and antiferromagnetism: a phase with nonrelativistic spin and crystal rotation symmetry. **Physical Review X 12,** 031042 (2022).

56. Kresse, G. & Hafner, J. Ab initio molecular dynamics for liquid metals. **Physical Review B 47,** 558–561 (1993).

57. Kresse, G. & Furthmüller, J. Efficiency of ab-initio total energy calculations for metals and semiconductors using a plane-wave basis set. **Computational Materials Science 6,** 15–50 (1996).

58. Kresse, G. & Furthmüller, J. Efficient iterative schemes for ab initio total-energy calculations using a plane-wave basis set. **Physical Review B 54,** 11169–11186 (1996).

59. Herath, U. **et al.** PyProcar: A python library for electronic structure pre/post-processing. **Computer Physics Communications 251,** 107080 (2020).

60. Máca, F. **et al.** Physical properties of the tetragonal CuMnAs: a first-principles study. **Physical Review B 96,** 094406 (2017).

61. Sun, J., Ruzsinszky, A. & Perdew, J. P. Strongly constrained and appropriately normed semilocal density functional. **Physical Review Letters 115,** 036402 (2015).

62. Sun, Z. L. **et al.** Field-induced metal-to-insulator transition and colossal anisotropic magnetoresistance in a nearly Dirac material $EuMnSb_2$. **npj Quantum Materials 6,** 1–8 (2021).

63. Newville, M., Stensitzki, T., Allen, D. B. & Ingargiola, A. **LMFIT: non-Linear Least-Square minimization and curve-fitting for python** version 0.8.0. 2014.

64. Harris, C. R. **et al.** Array programming with NumPy. **Nature 585,** 357–362 (2020).

65. Blöchl, P. E. Projector augmented-wave method. **Physical Review B 50,** 17953–17979 (1994).

66. Kresse, G. & Joubert, D. From ultrasoft pseudopotentials to the projector augmented-wave method. **Physical Review B 59,** 1758–1775 (1999).

67. Perdew, J. P., Burke, K. & Ernzerhof, M. Generalized gradient approximation made simple. **Physical Review Letters 77,** 3865–3868 (1996).

68. Van Delft, D. & Kes, P. The discovery of superconductivity. **Physics Today 63.** Publisher: American Institute of Physics, 38–43. ISSN: 0031-9228 (2010).

69. **The Nobel Prize in Physics 2010** NobelPrize.org. `https://www.nobelprize.org/prizes/physics/2010/press-release/` (2023).

70. Of Encyclopaedia Britannica, T. E. in **Encyclopædia Britannica** (Encyclopædia Britannica, 2018).

71. Annett, J. F. **Superconductivity, Superfluids, and Condensates** 200 pp. ISBN: 978-0-19-850756-7 (Oxford University Press, Oxford, New York, 2004).

72. Balibar, S. The discovery of superfluidity. **HAL open science** (2006).

73. London, F. **Superfluids** (John Wiley & Sons, 1950).

74. Penrose, O. CXXXVI. On the quantum mechanics of helium II. **The London, Edinburgh, and Dublin Philosophical Magazine and Journal of Science 42.** Publisher: Taylor & Francis _eprint: https://doi.org/10.1080/14786445108560954, 1373–1377. ISSN: 1941-5982 (1951).

75. Rjabinin, J. N. & Shubnikow, L. W. Magnetic Properties and Critical Currents of Supraconducting Alloys. **Nature 135.** Number: 3415 Publisher: Nature Publishing Group, 581–582. ISSN: 1476-4687 (1935).

76. Bobroff, J. & Bouquet, F. **File:Superconductor interactions with magnetic field.png** 2011.

77. in. **Collected Papers of L.D. Landau** (ed Ter haar, D.) 546–568 (Pergamon, 1965). ISBN: 978-0-08-010586-4.

78. Landau, L. The Theory of Phase Transitions. **Nature 138.** Number: 3498 Publisher: Nature Publishing Group, 840–841. ISSN: 1476-4687 (1936).

79. Bardeen, J., Cooper, L. N. & Schrieffer, J. R. Theory of Superconductivity. **Physical Review 108.** Publisher: American Physical Society, 1175–1204 (1957).

80. Schafroth, M. R. Superconductivity of a Charged Ideal Bose Gas. **Physical Review 100.** Publisher: American Physical Society, 463–475 (1955).

81. Fröhlich, H. Theory of the Superconducting State. I. The Ground State at the Absolute Zero of Temperature. **Physical Review 79.** Publisher: American Physical Society, 845–856 (1950).

82. Migdal, A. Interaction between electrons and lattice vibrations in a normal metal. **Journal of Experimental and Theoretical Physics (U.S.S.R.) 34,** 1438–1446 (1958).

83. Eliashberg, G. Interactions between electrons and lattice vibrations in a superconductor. **Journal of Experimental and Theoretical Physics (U.S.S.R.) 38,** 966–976 (1960).

84. Nambu, Y. Quasi-Particles and Gauge Invariance in the Theory of Superconductivity. **Physical Review 117,** 648–663. ISSN: 0031-899X (1960).

85. QuantumLevitation. **The Rise Of High Temperatures Superconductors** Quantum Levitation. `https://quantumlevitation.com/the-rise-of-high-temperatures-superconductors/` (2023).

86. Zhang, X., Zhao, Y., Li, F. & Yang, G. Pressure-induced hydride superconductors above 200 K. **Matter and Radiation at Extremes 6,** 068201. ISSN: 2468-2047 (2021).

87. Mitrano, M. **et al.** Possible light-induced superconductivity in K3C60 at high temperature. **Nature 530.** Number: 7591 Publisher: Nature Publishing Group, 461–464. ISSN: 1476-4687 (2016).

88. Hu, W. **et al.** Optically enhanced coherent transport in YBa2Cu3O6.5 by ultrafast redistribution of interlayer coupling. **Nature Materials 13.** Number: 7 Publisher: Nature Publishing Group, 705–711. ISSN: 1476-4660 (2014).

89. Kaiser, S. **et al.** Optically induced coherent transport far above T_c in underdoped $YBa_2Cu_3O_{6+\delta}$. **Physical Review B 89.** Publisher: American Physical Society, 184516 (2014).

90. Buzzi, M. **et al.** Photomolecular High-Temperature Superconductivity. **Physical Review X 10.** Publisher: American Physical Society, 031028 (2020).

91. Buzzi, M. **et al.** Phase Diagram for Light-Induced Superconductivity in $\kappa-(ET)_2-X$. **Physical Review Letters 127.** Publisher: American Physical Society, 197002 (2021).

92. Cantaluppi, A. **et al.** Pressure tuning of light-induced superconductivity in K3C60. **Nature Physics 14.** Number: 8 Publisher: Nature Publishing Group, 837–841. ISSN: 1745-2481 (2018).

93. Budden, M. **et al.** Evidence for metastable photo-induced superconductivity in K3C60. **Nature Physics 17.** Number: 5 Publisher: Nature Publishing Group, 611–618. ISSN: 1745-2481 (2021).

94. Liu, B. **et al.** Pump Frequency Resonances for Light-Induced Incipient Superconductivity in $YBa_2Cu_3O_{6.5}$. **Physical Review X 10.** Publisher: American Physical Society, 011053 (2020).

95. Von Hoegen, A. **et al.** Amplification of Superconducting Fluctuations in Driven $YBa_2Cu_3O_{6+x}$. **Physical Review X 12.** Publisher: American Physical Society, 031008 (2022).

96. Chattopadhyay, S. **et al. Mechanisms for Long-Lived, Photo-Induced Superconductivity** 2023. arXiv: 2303.15355[cond-mat,physics:physics].

97. Bittner, N., Tohyama, T., Kaiser, S. & Manske, D. Possible Light-Induced Superconductivity in a Strongly Correlated Electron System. **Journal of the Physical Society of Japan 88.** Publisher: The Physical Society of Japan, 044704. ISSN: 0031-9015 (2019).

98. Demsar, J. Light-induced superconductivity. **Nature Physics 12.** Number: 3 Publisher: Nature Publishing Group, 202–203. ISSN: 1745-2481 (2016).

99. Chiriacò, G., Millis, A. J. & Aleiner, I. L. Transient superconductivity without superconductivity. **Physical Review B 98.** Publisher: American Physical Society, 220510 (2018).

100. Paeckel, S. **et al.** Detecting superconductivity out of equilibrium. **Physical Review B 101.** Publisher: American Physical Society, 180507 (2020).

101. Hein, P. **et al.** Mode-resolved reciprocal space mapping of electron-phonon interaction in the Weyl semimetal candidate Td-WTe2. **Nature Communications 11.** Number: 1 Publisher: Nature Publishing Group, 2613. ISSN: 2041-1723 (2020).

102. Sekiyama, A. **et al.** High-resolution photoemission study of metallic, insulating, and superconducting BEDT-TTF salts. **Physical Review B 56.** Publisher: American Physical Society, 9082–9090 (1997).

103. Parham, S. P. **Electron Dynamics in High Temperature Superconductors Studied Using Angle and Time-Resolved Photoemission Spectroscopy** PhD thesis (Univerisity of Colorado Boulder, 2015).

104. Strickland, D. & Mourou, G. Compression of amplified chirped optical pulses. **Optics Communications 56,** 219–221. ISSN: 0030-4018 (1985).

105. **File: Chirped Pulse Amplification** 2019.

106. Weiner, A. **Ultrafast Optics** 1st edition. 598 pp. ISBN: 978-0-471-41539-8 (Wiley, Hoboken, N.J, 2009).

107. Griffiths, D. J. **Introduction to Electrodynamics** 4th edition. 620 pp. ISBN: 978-1-108-42041-9 (Cambridge University Press, Cambridge, United Kingdom ; New York, NY, 2017).

108. Jackson, J. D. **Classical Electrodynamics Third Edition** 3rd edition. 832 pp. ISBN: 978-0-471-30932-1 (Wiley, New York, 1998).

109. Boyd, R. W. **Nonlinear optics** 4th ed. ISBN: 978-0-12-811002-7 (Academic Press is an imprint of Elsevier, San Diego, 2019).

110. Team, T. G. I. S. **TNC Global Invasive Species Team page** `https://www.invasive.org/gist/products/sensing/physics060.html` (2023).

111. Rossum, G. v. & Drake, F. L. **The Python language reference** Release 3.0.1 [Repr.] **Python documentation manual / Guido van Rossum; Fred L. Drake [ed.] Pt. 2.** 109 pp. ISBN: 978-1-4414-1269-0 (Python Software Foundation, Hampton, NH, 2010).

112. Gillies, S. **et al. Shapely** 2022.

113. Shimizu, Y., Matsukuma, H. & Gao, W. Optical Angle Sensor Technology Based on the Optical Frequency Comb Laser. **Applied Sciences 10.** Number: 11 Publisher: Multidisciplinary Digital Publishing Institute, 4047. ISSN: 2076-3417 (2020).